Search for double beta decay of ^{82}Se with the NEMO-3 detector and development of apparatus for low-level radon measurements for the SuperNEMO experiment

James Mott
University College London

Submitted to University College London in fulfilment
of the requirements for the award of the
degree of **Doctor of Philosophy**

September 25th, 2013

Declaration

I, James Mott, confirm that the work presented in this thesis is my own. Where information has been derived from other sources, I confirm that this has been indicated in the thesis.

James Mott

Abstract

The $2\nu\beta\beta$ half-life of ^{82}Se has been measured as $T^{2\nu}_{1/2} = (9.93 \pm 0.14(\mathrm{stat}) \pm 0.72(\mathrm{syst})) \times 10^{19}$ yr using a 932 g sample measured for a total of 5.25 years in the NEMO-3 detector. The corresponding nuclear matrix element is found to be $|M^{2\nu}| = 0.0484 \pm 0.0018$. In addition, a search for $0\nu\beta\beta$ in the same isotope has been conducted and no evidence for a signal has been observed. The resulting half-life limit of $T^{0\nu}_{1/2} > 2.18 \times 10^{23}$ yr (90% CL) for the neutrino mass mechanism corresponds to an effective Majorana neutrino mass of $\langle m_{\beta\beta} \rangle < 1.0 - 2.8$ eV (90% CL). Furthermore, constraints on lepton number violating parameters for other $0\nu\beta\beta$ mechanisms, such as right-handed current and Majoron emission modes, have been set.

SuperNEMO is the successor to NEMO-3 and will be one of the next generation of $0\nu\beta\beta$ experiments. It aims to measure ^{82}Se with an half-life sensitivity of 10^{26} yr corresponding to $\langle m_{\beta\beta} \rangle < 50 - 100$ meV. Radon can be one of the most problematic backgrounds to any $0\nu\beta\beta$ search due to the high $Q_{\beta\beta}$ value of its daughter isotope, ^{214}Bi. In order to achieve the target sensitivity, the radon concentration inside the tracking volume of SuperNEMO must be less than 150 µBq/m^3. This low level of radon is not measurable with standard radon detectors, so a "radon concentration line" has been designed and developed. This apparatus has a sensitivity to radon concentration in the SuperNEMO tracker at the level of 40 µBq/m^3, and has performed the first measurements of the radon level inside a sub-section of SuperNEMO, which is under construction. It has also been used to measure the radon content of nitrogen and helium gas cylinders, which are found to be in the ranges 70 – 120 µBq/m^3 and 370 – 960 µBq/m^3, respectively.

Acknowledgements

First and foremost, I would like to express my extreme gratitude to my supervisor, Ruben Saakyan, without whose guidance this thesis would not have been possible. As annoying as it may be, always knowing the answer to any question I might pose, no matter how obscure, is certainly a very useful trait to have as a supervisor.

In addition, my thanks go to Stefano Torre, David Waters and Adam Davison for many constructive conversations on analysis techniques and software issues - I am sure I would have spent a lot more time groping in the dark without this guiding influence. In the same vein, collaborative work with fellow NEMO-3 students at other institutions, in particular Sophie Blondel and Summer Blot, was also pivotal in producing a coherent analysis.

Away from a computer screen and back in the real world, I am indebted to Derek Attree and Brian Anderson for their technical expertise and for their patience as I attempted to develop basic engineering skills. Without them, none of the real 'screw-driver' physics in this thesis would have been remotely functional. I am also truly appreciative of the camaraderie shared with my fellow lab rats, Cristóvão Vilela and Xin Ran Liu.

Away from phyics, the love and support from my family has been a comforting presence, not just for this PhD but throughout my life. For this, I feely greatly blessed. Finally, special thanks go to Clara for her unflinching support throughout this whole process and for ensuring that my funding lasted as long as necessary with such rigorous budgeting.

Contents

List of Figures **11**

List of Tables **16**

1. Introduction **18**

1.1. NEMO-3 . . . 19
1.2. SuperNEMO . . . 21
1.3. Author's Contributions . . . 22
1.3.1. NEMO-3 Contributions . . . 22
1.3.2. SuperNEMO Contributions . . . 23

2. Neutrino Phenomenology **25**

2.1. Standard Model Neutrinos . . . 25
2.1.1. Discovery of the Neutrino . . . 25
2.1.2. Neutrino Interactions . . . 25
2.1.3. Neutrino Flavours . . . 27
2.2. Neutrino Mixing and Oscillations . . . 28
2.2.1. Oscillation Phenomenology . . . 29
2.2.2. Oscillations in Matter . . . 30
2.2.3. Measurement of Oscillation Parameters . . . 31
2.3. Neutrino Mass . . . 32
2.3.1. Dirac Mass . . . 32
2.3.2. Majorana Mass . . . 33
2.3.3. See-saw Mechanism . . . 34
2.4. Experimental Constraints on Neutrino Mass . . . 36
2.4.1. Tritium Decay . . . 36
2.4.2. Cosmology . . . 37
2.4.3. Neutrinoless double beta decay ($0\nu\beta\beta$) . . . 38

2.4.4. Oscillations 39
2.5. Outstanding questions 39
2.5.1. Number of neutrinos 39
2.5.2. Absolute Mass and Mass Hierarchy 40
2.5.3. CP Violation 41
2.5.4. Nature of the neutrino 42

3. Double Beta Decay **43**
3.1. Beta Decay 43
3.1.1. Allowed and Forbidden Decays 44
3.2. Two Neutrino Double Beta Decay 45
3.3. Neutrinoless Double Beta Decay 46
3.3.1. Neutrino Mass Mechanism 48
3.3.2. Right-handed Current 49
3.3.3. Majoron Emission 51
3.4. Nuclear Matrix Elements 54
3.4.1. Interacting Shell Model 55
3.4.2. Quasiparticle Random Phase Approximation 56
3.4.3. Interacting Boson Model 56
3.4.4. Projected Hartree-Fock-Bogoluibov Method 56
3.4.5. Energy Density Functional Method 57
3.4.6. Comparison of different NME calculations 57

4. Double Beta Decay Experiments **59**
4.1. Detector Design Considerations 59
4.1.1. Maximising Signal 60
4.1.2. Minimising Background 62
4.2. Detector Technologies 63
4.2.1. Semiconductor Experiments 63
4.2.2. Scintillation Experiments 67
4.2.3. Bolometer Experiments 70
4.2.4. Time Projection Chamber Experiments 71
4.2.5. Tracker-Calorimeter Experiments 73
4.3. Double Beta Decay Measurements 74
4.3.1. $2\nu\beta\beta$ Measurements 74
4.3.2. $0\nu\beta\beta$ Limits 74

4.3.3. Future Measurement Prospects 77

I. $\beta\beta$-decay of ^{82}Se with NEMO-3 79

5. NEMO-3 Detector 80
5.1. Source Foils 81
5.1.1. ^{82}Se Source Foils 83
5.2. Tracker 86
5.3. Calorimeter 88
5.4. Electronics, DAQ and Trigger 89
5.4.1. Calorimeter Electronics 90
5.4.2. Tracker Electronics 90
5.4.3. Trigger System 91
5.5. Energy and Time Calibration 92
5.5.1. Radioactive Sources 92
5.5.2. Laser Survey 93
5.6. Magnetic Coil and Passive Shielding 94
5.6.1. Magnetic Coil 94
5.6.2. Mount Fréjus 94
5.6.3. Iron Shield 95
5.6.4. Neutron Shielding 95
5.7. Anti-radon facility 95

6. General Analysis Techniques 97
6.1. Monte Carlo Simulation 97
6.2. Reconstruction of Events 98
6.3. Particle Identification 98
6.3.1. Electron Identification 98
6.3.2. Gamma Identification 100
6.3.3. Alpha Identification 101
6.4. Time of Flight Information 102
6.4.1. Internal Probability 103
6.4.2. External Probability 105
6.5. Analysis Data Set 106

6.6. Statistical Analysis 107
    6.6.1. Fitting MC Distributions to Data 107
    6.6.2. Extracting Limits on Signal Strength 109
6.7. Half-life Calculation 111

7. Estimation of Backgrounds for the ^{82}Se Source Foils 112
7.1. Sources of NEMO-3 Background 113
7.2. NEMO-3 Background Classification 117
    7.2.1. Internal Backgrounds 117
    7.2.2. External Backgrounds 119
    7.2.3. Radon Backgrounds 122
7.3. Channels for Background Measurements 124
    7.3.1. General Quality Criteria 125
    7.3.2. Hot Spot Search 125
    7.3.3. 1e1α Channel 128
    7.3.4. 1e2γ Channel 129
    7.3.5. 1e1γ Channel 130
    7.3.6. 1e Channel 131
7.4. Results of Background Measurements 132
    7.4.1. Fitting Procedure 132
    7.4.2. Activity Estimations 135
    7.4.3. Control Distributions 144

8. Double Beta Decay Results for ^{82}Se 148
8.1. Optimisation of $2\nu\beta\beta$ Cuts 149
    8.1.1. Starting Point for Optimisation 149
    8.1.2. Optimisation Procedure 152
    8.1.3. Optimisation Results 154
8.2. $2\nu\beta\beta$ Results 159
    8.2.1. Re-measurement of Background Activities 159
    8.2.2. $2\nu\beta\beta$ Distributions 163
    8.2.3. $2\nu\beta\beta$ systematics 167
    8.2.4. $2\nu\beta\beta$ Half-life Measurement 170
8.3. Optimisation of $0\nu\beta\beta$ Cuts 171
8.4. $0\nu\beta\beta$ Results 176
    8.4.1. Mass Mechanism 176

8.4.2. Right-handed Current 178
8.4.3. Majoron Emission 181

II. Radon Research and Development for SuperNEMO 184

9. The SuperNEMO Experiment 185
9.1. SuperNEMO Baseline Design 185
9.2. Research and Development 187
9.3. Timescale and Sensitivity 189

10. Radon and SuperNEMO 192
10.1. Properties of Radon 192
10.2. Radon as a SuperNEMO Background 194
10.3. Radon Suppression with Gas Flow 194
10.4. ^{222}Rn Decay Chain to ^{214}Po 197
10.4.1. ^{222}Rn Activity 199
10.4.2. ^{218}Po Activity 200
10.4.3. ^{214}Pb Activity 200
10.4.4. ^{214}Bi Activity 202
10.4.5. ^{214}Po Activity 202
10.4.6. Decay chain activities 203

11. Electrostatic Detector and Radon Concentration Line 204
11.1. Electrostatic Detector 205
11.1.1. Detector Signal 207
11.1.2. Detector Efficiency Calibration 211
11.1.3. Detector Background Measurement 214
11.2. Radon Concentration Line (RnCL) 215
11.2.1. Design and Construction 216
11.2.2. Trapping Efficiency 218
11.2.3. Trap Background 223

12. Radon Concentration Line Sensitivity Estimates 225
12.1. Minimum Detectable Activity 225
12.1.1. Normal Approximation 227
12.2. Electrostatic Detector Sensitivity 228

12.3. Uniform Gas Measurement 231
12.4. C-Section Measurement 232

13. Low-level Radon Measurements **236**
13.1. Gas System 236
13.2. Gas Cylinders 238
    13.2.1. Modelling Cylinder Activity 238
    13.2.2. Measuring Full Cylinders 240
    13.2.3. Measuring Used Cylinders 242
13.3. C-section 244
    13.3.1. Measurement Starting Point 244
    13.3.2. Extracting C-section Activity 246
    13.3.3. Anti-Radon Tent 247
    13.3.4. C-section Results 247

14. Conclusion **251**

Bibliography **255**

List of Figures

2.1. Charged current and neutral current neutrino interactions 26

2.2. Combined LEP cross-section measurements for $e^+e^- \rightarrow hadrons$ around the Z^0 resonance 28

2.3. Feynman diagrams for Dirac and Majorana propagators 34

2.4. Sample spectrum for tritium decay 37

2.5. Normal and inverted mass hierarchies of absolute neutrino masses . . 41

3.1. Predictions of the SEMF for an even value of A 45

3.2. Feynman diagram for $2\nu\beta\beta$ 46

3.3. Majorana propagator resulting from any $0\nu\beta\beta$ process 47

3.4. Feynman diagram from $0\nu\beta\beta$ for the neutrino mass mechanism 48

3.5. Allowed regions of $\langle m_{\beta\beta} \rangle$ as a function of the lightest neutrino mass . 49

3.6. Distribution of the sum of electron energies for $2\nu\beta\beta$ and $0\nu\beta\beta$ . . . 50

3.7. Feynman diagram from $0\nu\beta\beta$ using a right handed weak current . . . 50

3.8. Angular and energy distributions for the mass mechanism and right-handed current decay modes 52

3.9. Energy spectra for $2\nu\beta\beta$, $0\nu\beta\beta$ and four Majoron modes 54

3.10. $0\nu\beta\beta$ NME for the neutrino mass mechanism, calculated with five different approaches 58

4.1. Energy spectrum from the Heidelberg-Moscow experiment 65

4.2. The energy spectrum from GERDA-I with pulse-shape discrimination applied 66

4.3. Energy spectrum showing the first results from KamLAND-Zen . . . 69

4.4. Energy spectrum for single site events in EXO-200 72

4.5. Comparison of limits on $T^{0\nu}_{1/2}$ from GERDA-I and EXO-200 and KamLAND-Zen, compared with the KK signal claim 76

5.1. Cut-away view of NEMO-3 81

5.2. Section across the diameter of NEMO-3 82

5.3. Distribution of source isotopes in NEMO-3 83

5.4. Location of selenium source in NEMO-3 84

5.5. Plan view of one sector of NEMO-3 87

5.6. Schematic of a NEMO-3 calorimeter module 88

6.1. An event from NEMO-3 data with two candidate electrons 99

6.2. Examples of calorimeter hits forming gamma clusters 100

6.3. Candidate BiPo event from NEMO-3 data 101

6.4. External background candidate events 103

6.5. Internal probability distributions for the $2\nu\beta\beta$ and 1e1γ channels . . 105

6.6. External probability distribution for the 1e1γ channel 106

6.7. Example distributions of the NLLR test statistic 110

7.1. ^{238}U decay chain 114

7.2. ^{232}Th decay chain 115

7.3. Decay scheme for the β-decay of ^{214}Bi 116

7.4. Decay scheme for the β-decay of ^{208}Tl 116

7.5. Feynman diagrams for internal backgrounds to the $2\nu\beta\beta$ channel . . . 118

7.6. Feynman diagrams for external backgrounds to the $2\nu\beta\beta$ channel . . 120

7.7. Radon level measured inside NEMO-3 123

7.8. BiPo event originating away from the source foil 123

7.9. Vertex position of electron tracks in the hot spot search 127

7.10. Electron energy vs. the sum of the two gamma energies for ^{214}Bi and ^{208}Tl MC samples 130

7.11. Alpha track length distributions 133

7.12. Alpha length distributions from the fit results 136

7.13. Electron energy distributions from the 1e2γ channel 137

7.14. Electron energy distributions from the 1e1γ channel 139

7.15. Electron energy distributions from the 1e channel 140

7.16. Distributions of variables from 1e1α channel 145

7.17. Distributions of variables from 1e1γ channel 146

8.1. Distribution of the electron energy sum for 2e events 151

8.2. Optimisation of binary cuts for $2\nu\beta\beta$ channel 154

8.3. Optimisation of energy and track length cuts for $2\nu\beta\beta$ channel 156

8.4. Optimisation of tracker layer, vertex separation and probability cuts for $2\nu\beta\beta$ channel 157

8.5. Efficiency for $2\nu\beta\beta$ as a function of vertex position 159

8.6. Distribution of electron energy sum in the $2\nu\beta\beta$ channel 164

8.7. Correlation matrix for the parameters of the signal and background fit 164

8.8. Distributions of single electron energies in the $2\nu\beta\beta$ channel 165

8.9. Cosine of the angle between the two electron tracks in the $2\nu\beta\beta$ channel 165

8.10. Distributions of vertex position in the $2\nu\beta\beta$ channel 166

8.11. Distribution of electron energy from special runs using well-calibrated ^{207}Bi sources 168

8.12. Distributions of energy asymmetry and maximum electron energy for the three main $0\nu\beta\beta$ decay modes and largest backgrounds 174

8.13. Optimisation of cuts for the mass mechanism decay mode 175

8.14. Optimisation of energy asymmetry cut for the right-handed current decay mode 176

8.15. Distribution of electron energy sum in the $0\nu\beta\beta$ mass mechanism channel 177

8.16. Distribution of electron energy sum in the $0\nu\beta\beta$ right-handed current 180

9.1. Exploded view of a SuperNEMO module 186

9.2. Schematic of the radon diffusion test bench 189

9.3. Photos of SuperNEMO construction 190

9.4. Projected sensitivity of SuperNEMO as a function of exposure 191

10.1. SuperNEMO sensitivity for different radon activities inside the tracker 195

10.2. Flow suppression factor for radon activity in the tracker 197

10.3. Activities of different isotopes in the ^{222}Rn decay chain 203

11.1. Electrostatic detector used for all radon measurements in this work . 206

11.2. Schematic diagram of the electrostatic detector 206

11.3. Response of the DAQ system for different input frequencies 208

11.4. Examples of the four types of event identified by the filtering stage of the event analysis 209

11.5. Example of a signal event with the fitting function superimposed . . . 211

11.6. Energy spectrum from a calibration run 212

11.7. ^{214}Po and ^{218}Po event rates for a spike-type calibration run 213

11.8. ^{214}Po and ^{218}Po event rates for a flow-through calibration run 214

11.9. Energy spectrum from a background measurement 215

11.10. ^{214}Po and ^{210}Po event rates for a typical background measurement run 216

11.11. Schematic diagram of the design of the RnCL 217

11.12. Photograph of the RnCL 218

11.13. Typical ^{214}Po and ^{218}Po rates measured in the detector during a trapping and transfer efficiency measurement 219

11.14. ^{214}Po activity in the detector during a flow-through trapping efficiency measurement 222

11.15. Radon activity in the carbon trap during a flow-through calibration run and the trapping and transfer efficiency as a function of flow time 223

11.16. Measurement of the intrinsic background of the carbon trap 224

12.1. Probability distributions for signal and signal-and-background hypotheses 227

12.2. Number of signal and background events expected in the electrostatic detector 230

12.3. MDA for the electrostatic detector as a function of the measurement time 230

12.4. MDA for a uniform supply of nitrgoen as a function of volume 233

12.5. MDA for different quantities of uniform gas supplied to the RnCL . . 233

12.6. Sensitivty of the RnCL for a C-section measurement 235

13.1. Measurements of the radon emanation from the SuperNEMO gas system 238

13.2. Specific activity at the output of four cylinders as a function of the volume remaining 240

13.3. Measurements of radon emanation from the MSSL gas supply line and a nitrogen cylinder 242

13.4. Activity inside the C-section whilst flushing prior to a radon measurement 245

13.5. Photograph of the anti-radon tent covering the C-section 247

13.6. Measurements of radon level and humidity inside the anti-radon tent 248

List of Tables

1.1. Results from a $0\nu\beta\beta$ search in ^{82}Se 20

2.1. Best current estimates for neutrino mixing parameters 32

2.2. Constraints on neutrino mass from different types of experiment . . . 39

2.3. Unknown neutrino properties that can be observed using different experimental techniques 40

3.1. Ten different Majoron models and their main properties 54

4.1. Details of isotopes commonly used in $0\nu\beta\beta$ experiments 61

4.2. Measurements of the $2\nu\beta\beta$ half-life for nine isotopes where a direct observation has been made 75

4.3. Half-life limits for different $0\nu\beta\beta$ isotopes 75

4.4. Summary of future $0\nu\beta\beta$ experiments 77

5.1. Summary of selenium source foils 84

5.2. HPGe measurements of selenium foil strips 85

6.1. NEMO-3 data set 107

7.1. Details of the external background model 121

7.2. Details of areas excluded as hot spots 128

7.3. Division of histograms used in the binned log-likelihood fit 134

7.4. Internal background activities from the fit 141

7.5. Internal background activites compared with HPGe results 142

7.6. Fit results for external backgrounds 142

7.7. Fit results for radon activities 143

8.1. Estimated number of internal, external and radon background events passing the $2\nu\beta\beta$ selection criteria 158

8.2. Background activities after fitting with $2\nu\beta\beta$ signal 161

8.3. Expected numbers of internal background events in the $2\nu\beta\beta$ channel 162

8.4. Expected numbers of external background events in the $2\nu\beta\beta$ channel 162

8.5. Expected numbers of radon background events in the $2\nu\beta\beta$ channel . 163

8.6. Comparison of analyses performed using phase 1, phase 2 and both phase 1 and phase 2 data 167

8.7. Summary of systematic errors contributing to the $2\nu\beta\beta$ half-life measurement 170

8.8. Predicted numbers of background events between $2.6-3.2$ MeV, using the $2\nu\beta\beta$ selection criteria 172

8.9. Results of a $0\nu\beta\beta$ search for the mass mechanism decay mode 178

8.10. Effective Majorana neutrino mass calculated using the half-life limit set in this work 179

8.11. Results of a $0\nu\beta\beta$ search for the two right-handed current decay modes 180

8.12. Half-life limits for Majoron emission decay modes 182

8.13. Majoron-neutrino coupling limits extracted from experimental results 182

9.1. Summary of experimental achievements of NEMO-3 and target levels for SuperNEMO 189

10.1. Details of isotopes in the radon decay chain 198

11.1. Typical results of calibration of the electrostatic detector for spike and flow-through calibration modes 214

11.2. Trapping and transfer efficiency measurement results 221

13.1. Measurements of gas cylinders of helium and nitrogen 244

13.2. Measurements of radon activity inside the first C-section 249

Chapter 1.

Introduction

Over many years, the Standard Model (SM) of particle physics has been tested with ever-greater precision. Up to now, it has proved incredibly successful and has been verified to a truly remarkable level of accuracy. However, in recent years, there has been a discovery in the neutrino sector that goes beyond the SM. Successive experiments have now confirmed the phenomenon of neutrino oscillations, where neutrinos change from one flavour to another. This flavour mixing and its associated non-zero mass cannot be unambiguously included in the SM, such that, uniquely amongst the known fundamental particles, neutrinos have measurable properties that are not accurately described by the SM.

Furthermore, it is not straight-forward to supplement the SM to agree with these observations of neutrino mixing and neutrino mass. Difficulties arise since the neutral nature of the neutrino allows the possibility of it being either a Dirac or Majorana fermion. Dirac neutrinos would have a distinct antineutrino partner, whereas Majorana neutrinos would be their own antiparticles. This ambiguity means that, given the current state of knowledge, it is not possible to unequivocally confirm or refute either possibility.

Neutrinoless double beta decay ($0\nu\beta\beta$) is a hypothesised, but as yet unobserved, nuclear process where two electrons are emitted from the same nucleus without accompanying neutrinos. The observation of $0\nu\beta\beta$ would confirm that the neutrino is a Majorana particle and the decay rate would allow (model-dependent) extraction of the absolute mass scale of the neutrino and may give insight into the mass hierarchy.

As well as $0\nu\beta\beta$, there is an allowed SM process of two neutrino double beta decay ($2\nu\beta\beta$) and, despite its rare nature, this process has been directly observed in nine isotopes. It is important to measure the $2\nu\beta\beta$ process precisely as this may be used to improve nuclear models which are used to extract information about $0\nu\beta\beta$. In addition, due to its similar event topology, $2\nu\beta\beta$ represents one of the major backgrounds to the $0\nu\beta\beta$ process.

The search for $0\nu\beta\beta$ is a highly active research area with many different experiments, using various technologies, studying the full range of viable $0\nu\beta\beta$ isotopes. The most important of these experiments are described in detail in Chapter 4. At present, there is a transition from a series of successful older experiments to a new generation of larger-scale detectors which hope to probe $0\nu\beta\beta$ further.

In the recent past, the strongest limits on $0\nu\beta\beta$ have come from semiconductor experiments using ^{76}Ge, such as Heidelberg-Moscow (H-M) and IGEX, with limits of $\langle m_{\beta\beta} \rangle < 0.25 - 0.50$ eV. In addition, there has been a controversial claim for discovery of $0\nu\beta\beta$ from a subset of the H-M collaboration.

In the last year, three of the new generation of experiments have produced results which supercede those of H-M and IGEX. No evidence for $0\nu\beta\beta$ has yet been found and the results strongly disfavour the previous discovery claim. These experiments all use different technologies: GERDA uses ^{76}Ge as a semiconductor in the same fashion as Heidelberg-Moscow; KamLAND-Zen uses ^{136}Xe-loaded liquid scintillator and EXO-200 uses ^{136}Xe in a scintillating time projection chamber. Many more experiments with similar expected sensitivities to these experiments, down to $\langle m_{\beta\beta} \rangle < 0.05 - 0.10$ eV, are either in advanced R&D stages or under construction.

The SuperNEMO experiment, which evolved from the NEMO-3 experiment, is one such experiment. Both SuperNEMO and NEMO-3 use a detector type known as tracker-calorimeter, and they perfectly encapsulate the transition between different generations of experiment.

1.1. NEMO-3

The NEMO-3 detector operated from 2003 to 2011 in the Laboratoire Souterrain de Modane (LSM), where it searched for $0\nu\beta\beta$ in seven different candidate isotopes

(^{100}Mo, ^{82}Se, ^{150}Nd, ^{116}Cd, ^{130}Te, ^{48}Ca and ^{96}Zr) with a total source mass of 10 kg. This source mass was contained in thin foils that were surrounded by a gas tracker and a calorimeter made from plastic scintillator. This configuration allowed for detailed event topology reconstruction. NEMO-3 has observed $2\nu\beta\beta$ in all seven isotopes, producing the most accurate $2\nu\beta\beta$ measurements for each isotope. The larger masses of ^{100}Mo (6.9 kg) and ^{82}Se (0.9 kg) mean that these isotopes can also provide results for $0\nu\beta\beta$ decay that are competitive with the current generation of experiments.

Part I of this thesis is dedicated to an analysis of ^{82}Se using NEMO-3 data. The full capabilities of the NEMO-3 detector are used to measure relevant backgrounds, the $2\nu\beta\beta$ half-life and finally to perform a search for the $0\nu\beta\beta$ process. Using 1918.5 days of data where 932 g of ^{82}Se was observed, the $2\nu\beta\beta$ half-life of ^{82}Se is measured to be $(9.93 \pm 0.14(\text{stat}) \pm 0.72(\text{syst})) \times 10^{19}$ yr. No evidence for $0\nu\beta\beta$ has been found, and limits have therefore been set for the $0\nu\beta\beta$ half-life for the neutrino mass mechanism, right-handed current and Majoron emission modes. These limits are summarised in Table 1.1. The $2\nu\beta\beta$ measurement and all of the $0\nu\beta\beta$ measurements are the world's best for this isotope.

$0\nu\beta\beta$ Decay Class	Mode	Half-life Limit (90% CL)	LNV Parameter
Mass Mechanism		$T^{0\nu}_{1/2} > 2.18 \times 10^{23}$ yr	$\langle m_{\beta\beta}\rangle < 1.0 - 2.8$ eV
RH Current	λ	$T^{0\nu\lambda}_{1/2} > 1.18 \times 10^{23}$ yr	$\langle\lambda\rangle < (2.8 - 3.0) \times 10^{-6}$
	η	$T^{0\nu\eta}_{1/2} > 1.90 \times 10^{23}$ yr	$\langle\eta\rangle < (2.1 - 2.2) \times 10^{-8}$
Majoron Emission	$n = 1$	$T^{0\nu\chi^0}_{1/2} > 4.89 \times 10^{22}$ yr	$\langle g_{\chi^0}\rangle < (3.7 - 7.8) \times 10^{-5}$
	$n = 2$	$T^{0\nu\chi^0}_{1/2} > 2.63 \times 10^{22}$ yr	–
	$n = 3$	$T^{0\nu\chi^0}_{1/2} > 1.42 \times 10^{22}$ yr	$\langle g_{\chi^0}\rangle < 1.62;\ 0.01 - 0.03$

Table 1.1.: Results for the $0\nu\beta\beta$ search in ^{82}Se, showing the half-life and lepton number violating (LNV) parameter for three different decay modes.

1.2. SuperNEMO

SuperNEMO is a next-generation $0\nu\beta\beta$ experiment that will build on the success of the NEMO-3 experiment, using the same tracker-calorimeter design and housing 100 kg of ^{82}Se. It is anticipated that a half-life sensitivity of 10^{26} years will be reached, corresponding to an effective Majorana neutrino mass of $\langle m_{\beta\beta}\rangle < 50 - 100$ meV.

Radon is a radioactive gas that is part of naturally occurring radioactive decay chains. If radon is present inside SuperNEMO, it can be a significant background to the search for $0\nu\beta\beta$. The most stable isotope of radon (^{222}Rn; $t_{1/2} = 3.82$ days), can enter the detector either through diffusion, contamination during detector construction or emanation from the detector materials themselves. Once inside the detector, this radon can move freely and deposit its progenies on the ^{82}Se foils. One of these progenies is ^{214}Bi which undergoes β-decay with a high Q_β value. This decay can mimic the rare $0\nu\beta\beta$ signal.

In order to achieve the target sensitivity for SuperNEMO, the radon level inside the detector must be less than 150 µBq/m^3. This is significantly lower than the 5 mBq/m^3 level that was achieved in the NEMO-3 detector. As a result, significant R&D effort has gone into reducing the level of radon inside the detector and measuring radon down to this low-level.

Part II of this thesis will discuss the R&D work that has been undertaken to measure radon levels at the sub mBq/m^3 level. State-of-the-art electrostatic detectors are only able to measure down to $\sim 1 - 2$ mBq/m^3, so a “Radon Concentration Line” (RnCL) has been developed that can first concentrate any radon present before making a measurement. The RnCL has a sensitivity of 40 µBq/m^3 for a uniform supply of gas and can measure the level inside a quarter-section of the SuperNEMO tracker down to a similar level. It has been used to measure gas bottles, gas supply lines and to make the first radon measurements of a SuperNEMO sub-module during the construction phase.

1.3. Author's Contributions

1.3.1. NEMO-3 Contributions

- Analysis of double beta decay in ^{82}Se:
  - Background measurements of the ^{82}Se foils
  - Optimisation of analysis cuts
  - Measurement of the $2\nu\beta\beta$ half-life
  - Search for $0\nu\beta\beta$ processes
- Development of core tools for a new analysis framework, so the user can:
  - Record exposure, including dead time corrections
  - Extract detector efficiencies correctly
  - Search for events with alpha candidates
  - Weight events for radon progenies based on previous radon measurements
  - Fit activities of isotopes in many different channels
  - Process multiple analysis jobs simultaneously on computing clusters
- Validation and verification of this new analysis framework:
  - Reconstruction of raw data and MC samples for calibration runs
  - Analysis of ^{207}Bi calibration runs to cross-check 2e & 1e1γ channels
  - Analysis of ^{232}U calibration runs to validate 1e2γ channel
  - Verification of implementation of data-quality cuts at reconstruction level
  - Comparison with another NEMO-3 software framework to ensure identical results
- Selection of runs to be included in a standardised run list
- Tuning of MC for gamma interactions to better replicate the energy and timing response of the NEMO-3 calorimeter

- Running of NEMO-3 data acquisition shifts
- Partial dis-assembly of NEMO-3 and recovery of electronics for use in commissioning of SuperNEMO

1.3.2. SuperNEMO Contributions

- Commissioning of an electrostatic radon detector:
  - Assembly of a data acquisition system to record signals
  - Application of styrene butadiene rubber (SBR) to stop diffusion through seals
  - Measurement of detector efficiency and background
- R&D for the RnCL:
  - Design, construction and further development of the system
  - Measurement of trapping and transfer efficiency
  - Measurement of radon emanation from cold trap
  - Calculation of the sensitivity of the RnCL to different experimental scenarios
- Radon measurements:
  - Quarter-section of the SuperNEMO tracker
  - He and N_2 gas bottles and gas delivery lines
  - SuperNEMO gas mixing and delivery system
  - Clean room where SuperNEMO is being built
  - Modelling of radon levels in connected volumes and extraction of separate emanation results
- Diffusion Studies:
  - Calculations of expected levels of radon diffusion into the SuperNEMO tracker

  - Calculations of the radon emanation expected from different materials
  - Participation in a cross-calibration of many institutions using radon emanation from glass beads
- Design and construction of a separate electrostatic radon detector
- Presentation of the collaboration's work at Neutrino2012 & LRT2013

Chapter 2.

Neutrino Phenomenology

2.1. Standard Model Neutrinos

2.1.1. Discovery of the Neutrino

As early as 1914, it had been observed that the electron emitted in beta decay has a continuous energy spectrum, however it was not until 1930 that Pauli hypothesised an additional particle as a "desperate remedy" to conserve energy, momentum and spin [1]. This particle was initially termed a neutron, but was re-named as a *neutrino* by Fermi in 1933 in order to distinguish it from Chadwick's recently discovered neutron [2]. Over the next few years, Bethe and Peierls elaborated on Pauli's theory and showed that this new particle must interact very weakly. It is this property that allowed the neutrino to remain elusive for a further quarter-century, until the advent of the atomic age when neutrinos were produced at high enough intensity to be detected. In 1956, at the Savannah River nuclear reactor, Reines and Cowan observed inverse beta decay, giving a unique signature of an anti-neutrino interaction [3].

2.1.2. Neutrino Interactions

Experimental observations have guided the addition of neutrinos to the SM. However, these experiments never directly observe neutrinos, instead studying the products of neutrino interactions. As such, it is worthwhile briefly noting how neutrinos interact. In the SM, neutrinos can only interact via the weak force, which can be broken down into two types of interactions: *charged current* (CC) interactions, which involve the exchange of a $W^{\pm}$ boson, and *neutral current* (NC) interactions, where a Z^0 boson is exchanged. Since neutrino cross-sections are very small, extremely large-scale detectors are needed to observe these interactions. In all detectors, neutrinos scatter off nucleons or atomic electrons and neutrinos are therefore detected via one of the four interactions shown in Figure 2.1. In the NC interactions, the neutrino is detected via the recoil (or disintegration) of the target, whereas in CC interactions, the outgoing lepton may also be observed, which provides the flavour of the incoming neutrino.

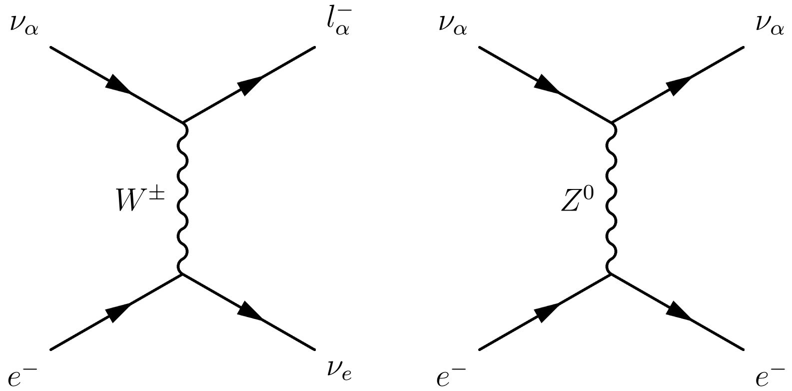

(a) CC ν-e^- Scattering **(b)** NC ν-e^- Scattering

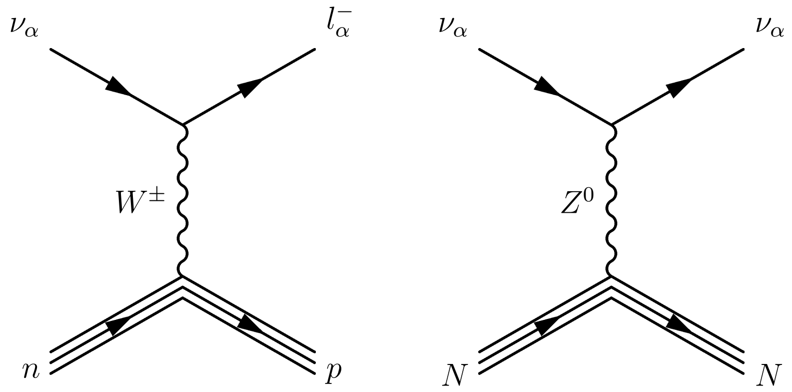

(c) CC ν-N Scattering **(d)** NC ν-N Scattering

Figure 2.1.: Two charged current and two neutral current neutrino interactions via which it is possible to detect neutrinos.

2.1.3. Neutrino Flavours

In 1962, a group of researchers at Brookhaven National Laboratory undertook the first experiment with an accelerator as a source of neutrinos. They observed a clear signature of a CC interaction with an outgoing muon, confirming that there were at least two different flavours of neutrino (ν_e and ν_μ) [4]. A third generation of leptons was found with the discovery of the tau particle in 1975 [5], but it would be 25 more years before direct evidence for the tau neutrino, ν_τ, was attained by the DONUT experiment in 2000 [6].

It is no coincidence that accelerator experiments were required to discover ν_μ and ν_τ. Indeed, a simple kinematic calculation shows that if the CC process shown in Figure 2.1c is to proceed, ν_μ and ν_τ must have energy greater than 110 MeV and 3.5 GeV respectively. Solar neutrinos have typical energies of ~ 1 MeV, and so only ν_e from the sun can interact via a CC interaction. Atmospheric neutrinos have similar energies to accelerator neutrinos at ~ 1 GeV, but have greatly reduced flux, such that accelerator neutrinos were a clear front-runner for the discovery. The NC interactions (Figures 2.1b and 2.1d) are elastic and therefore have no fundamental kinematic constraints.

Up to the present, three generations of neutrino have been directly observed (ν_e, ν_μ and ν_τ) which produce the three generations of charged leptons in CC interactions. There is strong evidence that there are only three active light neutrino generations, which comes from the four experiments that studied e^+e^- collisions at the LEP collider [7]. By measuring the width of the Z^0 resonance, as shown in Figure 2.2, the combined result from the four experiments measured the number of light active neutrinos, $N_\nu = 2.9840 \pm 0.0082$.

It should be noted that the Z^0 width provides a measure of the number of $Z^0 \to \nu_\alpha \overline{\nu_\alpha}$ decays. This means that it is not sensitive to neutrinos with a mass greater than $Z^0/2$ (45.6 GeV) nor neutrinos that do not couple to the Z^0, which are commonly termed *sterile neutrinos*. This may be pertinent since sterile neutrinos have been offered as a possible explanation for recent unexpected experimental results [8, 9].

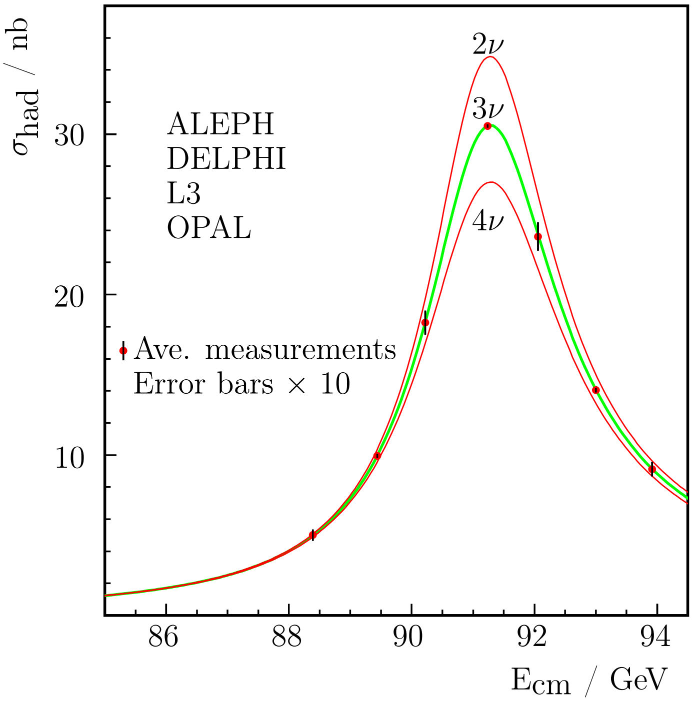

Figure 2.2.: Combined LEP cross-section measurements for $e^+e^- \rightarrow$ *hadrons* around the Z^0 resonance. $N_\nu = 3$ is clearly favoured. [7].

2.2. Neutrino Mixing and Oscillations

In 1968, the Homestake Experiment made the first measurements of neutrinos from the sun. The detector was only sensitive to the CC interaction (Figure 2.1c) and recorded only one third of the neutrino flux expected from solar models [10]. One possible solution to this problem was to resurrect a theory postulated by Pontecorvo, where if neutrinos have mass they are able to oscillate between different flavours [11, 12]. This was further extended by Maki, Nakagawa, Sakata in 1962 [13]. In this scenario, a ν_e ejected from the sun can oscillate to ν_μ or ν_τ, both of which would not be seen in the Homestake Experiment since they are below the requisite energy threshold to produce a muon or tau.

The "solar neutrino problem", as it became known, remained unresolved until 2001, when the Sudbury Neutrino Observatory (SNO) measured the solar neutrino flux in both the CC and NC channels [14]. They saw the familiar deficit in the CC channel, but found the NC channel, which was sensitive to ν_e, ν_μ and ν_τ, agreed well with predictions from solar models. This was certainly compelling evidence for the oscillation hypothesis.

2.2.1. Oscillation Phenomenology

The mixing between neutrino flavours and its associated oscillations can be described by the Pontecorvo-Maki-Nakagawa-Sakata (PMNS) matrix, U. This is a unitary matrix that defines the neutrino flavour states, $|\nu_\alpha\rangle$, in terms of the neutrino mass states, $|\nu_i\rangle$:

$$|\nu_\alpha\rangle = \sum_i U^*_{\alpha i} \, |\nu_i\rangle \tag{2.1}$$

The most common representation of U is shown below:

$$U = \overbrace{\begin{pmatrix} 1 & 0 & 0 \\ 0 & c_{23} & s_{23} \\ 0 & -s_{23} & c_{23} \end{pmatrix}}^{\text{Atmospheric}} \overbrace{\begin{pmatrix} c_{13} & 0 & s_{13}e^{-i\delta} \\ 0 & 1 & 0 \\ -s_{13}e^{i\delta} & 0 & c_{13} \end{pmatrix}}^{\text{Cross-mixing}} \overbrace{\begin{pmatrix} c_{12} & s_{12} & 0 \\ -s_{12} & c_{12} & 0 \\ 0 & 0 & 1 \end{pmatrix}}^{\text{Solar}} D_M \tag{2.2}$$

Here, $c_{ij} \equiv \cos\theta_{ij}$, $s_{ij} \equiv \sin\theta_{ij}$, θ_{ij} is a mixing angle which defines the degree of mixing between mass states i and j, and δ is a CP-violating phase that cannot be removed by re-phasing the fields. Furthermore, if the neutrino is a Majorana particle (Section 2.3.2) then there are additional CP-violating phases, α_1 and α_2, included in the diagonal matrix, D_M:

$$D_M = \begin{pmatrix} e^{\frac{i\alpha_1}{2}} & 0 & 0 \\ 0 & e^{\frac{i\alpha_2}{2}} & 0 \\ 0 & 0 & 1 \end{pmatrix} \tag{2.3}$$

It can be shown that, in vacuum, a neutrino of flavour α has probability to turn to flavour β given by [15]:

$$\begin{aligned} P\left(\nu_\alpha \rightarrow \nu_\beta\right) &= \left|\sum_i U^*_{\alpha i} e^{-im_i^2 \frac{L}{2E}} U_{\beta i}\right|^2 \\ &= \delta_{\alpha\beta} - 4\sum_{i>j} \Re\left(U^*_{\alpha i} U_{\beta i} U^*_{\alpha j} U_{\beta j}\right) \sin^2\left(\Delta m^2_{ij}\frac{L}{4E}\right) \\ &\quad + 2\sum_{i>j} \Im\left(U^*_{\alpha i} U_{\beta i} U^*_{\alpha j} U_{\beta j}\right) \sin^2\left(\Delta m^2_{ij}\frac{L}{2E}\right) \end{aligned} \tag{2.4}$$

where L is the distance travelled, E is the energy of the neutrino and m^2_{ij} is the mass splitting between the states i and j:

$$\Delta m^2_{ij} \equiv m_i^2 - m_j^2 \tag{2.5}$$

From Equation (2.4), it is clear that if a neutrino is produced in a weak interaction as a particular flavour with a given energy, it will mix between the different flavours as it travels. This mixing is governed by the parameters in the PMNS matrix and mass splittings.

2.2.2. Oscillations in Matter

If instead of propagating through vacuum, a neutrino propagates through matter with significant density, then coherent forward scattering from particles within the matter becomes important. The oscillatory behaviour of the neutrino will change, since there are now interactions that differ between the different flavour states. For example, a ν_e may interact with ambient electrons via both NC and CC interactions, exchanging either a $W^\pm$ or Z^0, whereas a ν_μ or μ_τ will interact via the NC interaction alone. This change in behaviour in matter is known as the Mikheyev-Smirnov-Wolfenstein (MSW) effect.

The MSW effect is particularly important when considering the passage of solar neutrinos from the centre of the sun to the earth. These neutrinos are created as electron neutrinos close to the centre of the sun where the electron energy density is large, such that matter effects dominate over vacuum oscillation. In this scenario, the electron neutrinos are approximately in the heavier of the two possible mass eigenstates, when taking into account a modified potential for the MSW interactions.

As the neutrinos move radially outwards from the sun, the electron density decreases slowly enough that the neutrinos propagate adiabatically. They thus remain in mass eigenstates of the modified vacuum potential as it slowly changes. When the neutrinos reach the edge of the sun and the electron density has become negligible, they are in a mass eigenstate of the vacuum potential, ν_2. Being an eigenstate of the vacuum Hamiltonian, this state will propagate all the way to earth without mixing and arrive in the same ν_2 state, which can be used to provide information on the sign of m^2_{21}.

2.2.3. Measurement of Oscillation Parameters

The early indication of neutrino oscillations from SNO has been corroborated in recent years by evidence from a series of dedicated neutrino oscillation experiments. There are two main types of experiment that contribute to these measurements: reactor and accelerator experiments.

Reactor experiments are usually detectors placed near one or more nuclear reactors which measure the flux of neutrinos as a function of energy and distance from the reactor core. Accelerator experiments typically involve a neutrino beam that is measured in a near detector and then propagated over a long baseline to a far detector. This allows the tuning of E and L to maximise the measurement sensitivity.

Neutrino oscillation experiments have enjoyed considerable success in measuring most of the mixing parameters which are summarised in Table 2.1. Despite this success, there are notable gaps in the current state of knowledge, including the sign of Δm^2_{32} and any information on the CP-violating parameters, δ, α_1 and α_2.

Irrespective of these unknowns, it is now beyond doubt that neutrino oscillation occurs and as a result of this mixing, it is known that neutrinos must have finite masses.

Parameter	Value
$\sin^2 2\theta_{12}$	$0.857^{+0.023}_{-0.025}$
$\sin^2 2\theta_{23}$	> 0.95
$\sin^2 2\theta_{13}$	0.095 ± 0.010
Δm^2_{21}	$7.50^{+0.19}_{-0.20} \times 10^{-5}$ eV^2
$\lvert\Delta m^2_{32}\rvert$	$2.32^{+0.12}_{-0.08} \times 10^{-3}$ eV^2

Table 2.1.: Best current estimates for neutrino mixing parameters from a global fit [16]

2.3. Neutrino Mass

There is now clear evidence that neutrinos have mass and as a result, many theorists have studied how to add this neutrino mass into the SM. Two methods arise naturally, where two distinct mass terms are added to the SM Lagrangian. These correspond to different types of neutrino - one is a *Dirac* particle, similar to the other SM fermions, and the other is a *Majorana* particle which is its own antiparticle. A combination of the two mass terms is theoretically preferable, as it may explain why the masses of the observed neutrinos are many orders of magnitude smaller than the other known fermions. This so-called *see-saw mechanism* (Section 2.3.3), also predicts high mass neutrinos which may play an important role in explaining the matter-antimatter asymmetry in the universe.

Throughout this section, for ease of understanding and simplicity of notation, only one flavour of neutrino will be considered. However, all results still hold for an arbitrary number of neutrinos. Sections 2.3.1–2.3.3 have been written with reference to [15, 17].

2.3.1. Dirac Mass

The SM, which omits neutrino masses, contains only chirally left-handed (LH) neutrinos, ν_L, which participate in the weak interaction, and no right-handed (RH) neutrinos, ν_R. Perhaps the most obvious method to add mass terms to the SM is to do so in the same way as for the charged leptons and quarks, which is done by coupling of LH and RH fields with the Higgs field. This type of mass term is called a *Dirac mass* term. To implement a Dirac mass term therefore requires the addition of a RH neutrino field, which will be contracted with the SM LH fields. Strictly-speaking, the minimal extension is to include only one RH field, but it is often considered more natural to include a RH field for each flavour of neutrino. For the simplified, single-flavour case, a Lagrangian is created as follows:

$$\mathcal{L}_D = -\frac{1}{2} m_D \left(\overline{\nu_L} \nu_R + \overline{\nu_R} \nu_L \right) + \text{h.c.} \tag{2.6}$$

where m_D is a constant mass term that represents the Yukawa coupling between the neutrino and Higgs fields, and h.c. is the Hermitian conjugate of the first two terms. It should be noted that the first coupling in Equation (2.6) turns a RH incoming neutrino into a LH outgoing one as shown in Figure 2.3a and vice versa for the second coupling. So it is clear that this Dirac mass term conserves lepton number as both incoming and outgoing particles are neutrinos.

This method requires only a small extension to the SM since it reproduces what is already in place for the other fermions. However, it is rather unsatisfactory as it requires the introduction of a sterile neutrino which cannot be directly experimentally observed and it offers no explanation for the extremely small Higgs-neutrino coupling.

2.3.2. Majorana Mass

To produce a non-zero mass term, a chirally RH fermion field must be contracted with a LH one. In general this is achieved with two distinct fields, as it is otherwise not possible to conserve quantities such as charge or weak-isospin. In the SM, LH fermion fields form weak-isospin doublets, whereas RH fields are weak-isospin singlets, which means that the RH neutrino proposed above for the Dirac mass carries no electric or colour charge and has no weak-isospin. It is therefore possible to form a non-zero mass term by charge-conjugating the RH field and contracting it with itself without violating any of the symmetries of the SM. This type of mass term was first put forward by Majorana in 1936 [18] and is known as a *Majorana mass* term. A charge conjugation operator can be defined up to an arbitrary phase as:

$$\nu_R^c = C \nu_R \equiv i \gamma^2 \nu_R \tag{2.7}$$

It is immediately clear that this will produce a field with LH chirality since γ^2 anti-commutes with γ^5 in the projection operator, $P_{L,R} = \left(1 \mp \gamma^5\right)/2$, such that:

$$\nu_R^c \equiv i\gamma^2 \frac{1}{2}\left(1+\gamma^5\right)\nu = \frac{1}{2}\left(1-\gamma^5\right) i\gamma^2 \nu = P_L \nu^c \tag{2.8}$$

The Majorana mass term to be included in the SM Lagrangian is therefore of the form:

$$\mathcal{L}_M = -\frac{1}{2} m_R \overline{\nu_R^c} \nu_R + \text{h.c.} \tag{2.9}$$

where m_R is a constant mass term. Equation (2.9) destroys an incoming neutrino and creates an outgoing anti-neutrino as shown in Figure 2.3b, so this mass term does not conserve lepton number and Majorana particles are their own anti-particles.

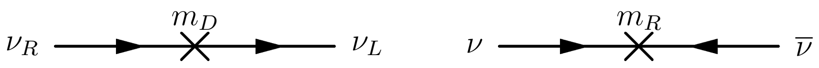

(a) Dirac Mass: $m_D \overline{\nu_L} \nu_R$ **(b)** Majorana Mass: $m_R \overline{\nu_R^c} \nu_R$

Figure 2.3.: Feynman diagrams showing the propagators for the Dirac and Majorana terms in Equations (2.6) and (2.9).

It is possible to level a similar criticism at the Majorana mass, regarding the addition of a sterile RH neutrino, as was raised with the Dirac mass, and this criticism would be justified. However, the great strength of the Majorana mass is that it offers a possible explanation of the disparity between neutrino masses and the masses of the charged leptons.

2.3.3. See-saw Mechanism

The see-saw mechanism is a class of model that predicts small masses for the known light neutrinos. The type 1 see-saw mechanism brings together the Dirac and

Majorana mass terms derived above into a single Lagrangian:

$$\begin{aligned}\mathcal{L}_{M+D} &= \mathcal{L}_D + \mathcal{L}_M \\ &= -\frac{1}{2}m_D\left(\overline{\nu_L}\nu_R + \overline{\nu_R}\nu_L\right) - \frac{1}{2}m_R\overline{\nu^c_R}\nu_R + \text{h.c.} \\ &= -\frac{1}{2}\begin{pmatrix}\overline{\nu_L} & \overline{\nu^c_R}\end{pmatrix}\mathcal{M}\begin{pmatrix}\nu^c_L \\ \nu_R\end{pmatrix} + \text{h.c.} \qquad (2.10)\end{aligned}$$

where $\mathcal{M}$ is given by:

$$\mathcal{M} = \begin{pmatrix} 0 & m_D \\ m_D & m_R \end{pmatrix} \qquad (2.11)$$

The neutrino states in Equation (2.10) are not mass eigenstates, but rather weak eigenstates in which the model is constructed. To find the the mass eigenstates, $\mathcal{M}$ must be diagonalised. From Equation (2.11), $\mathcal{M}$ has eigenvalues:

$$m_{1,2} = \frac{1}{2}m_R \pm \frac{1}{2}\sqrt{m_R^2 + 4m_D^2} \qquad (2.12)$$

In this model, it is assumed that m_D is of the same order of magnitude as the other known fermions and that m_R is at the Grand Unification Theory (GUT) scale ($\sim 10^{15}$ GeV). In this scenario, where $m_R \gg m_D$, the two eigenvalues reduce to:

$$m_1 \approx m_R \qquad (2.13)$$

$$m_2 \approx \frac{m_D^2}{m_R} \qquad (2.14)$$

Using these values, it is possible to find the mass states in terms of the new SM states used previously :

$$N \equiv \nu_2 \approx (\nu_R + \nu^c_R) + \frac{m_D}{m_R}(\nu_L + \nu^c_L) \qquad (2.15)$$

$$\nu \equiv \nu_1 \approx (\nu_L + \nu^c_L) - \frac{m_D}{m_R}(\nu_R + \nu^c_R) \qquad (2.16)$$

where the Hermitian conjugates have now been included. It has therefore been shown that the see-saw model can predict two very different mass regimes. The first is a heavy neutrino, N, close to the GUT scale which is made mostly of the ν_R and ν^c_R

fields. This neutrino forces the other state, ν, which is almost entirely composed of the ν_L and ν_L^c fields, to be very light as is observed in nature. The existence of a RH neutrino at the GUT scale is not only favourable for this reason, but may explain even more fundamental questions about the matter-antimatter asymmetry in the universe and why we exist at all (Section 2.5.3).

2.4. Experimental Constraints on Neutrino Mass

Experimental information on neutrino mass comes from four main sources. Tritium decay, $0\nu\beta\beta$ and cosmological models measure different combinations of masses and PMNS parameters, and all provide upper bounds on neutrino masses. This is in contrast to information from oscillation experiments which puts a lower bound on the heaviest mass state. A summary of the best results from each type of experiment is presented in Table 2.2.

2.4.1. Tritium Decay

Tritium (^{3}H) is an isotope of hydrogen that undergoes beta decay:

$$^3\mathrm{H} \to {}^3\mathrm{He} + \mathrm{e}^- + \overline{\nu_e} \tag{2.17}$$

where the energy of the electron obeys a beta decay spectrum. If the neutrino is massless, then the endpoint of the decay spectrum, Q_β, will be equal to the difference between the ^{3}H and $^3\mathrm{He} + e^-$ rest masses. However, in reality, Q_β will be reduced by the neutrino mass, which will cause the energy spectrum of the electron to deviate from the massless case as shown in Figure 2.4.

Theoretically, there are at least three separate Q_β values – one for each neutrino mass state. However, in reality, the energy resolution of any feasible experiment is not able to discern these different decays. Therefore an average deviation is measured, from which it is possible to infer the average of the neutrino mass states weighted by

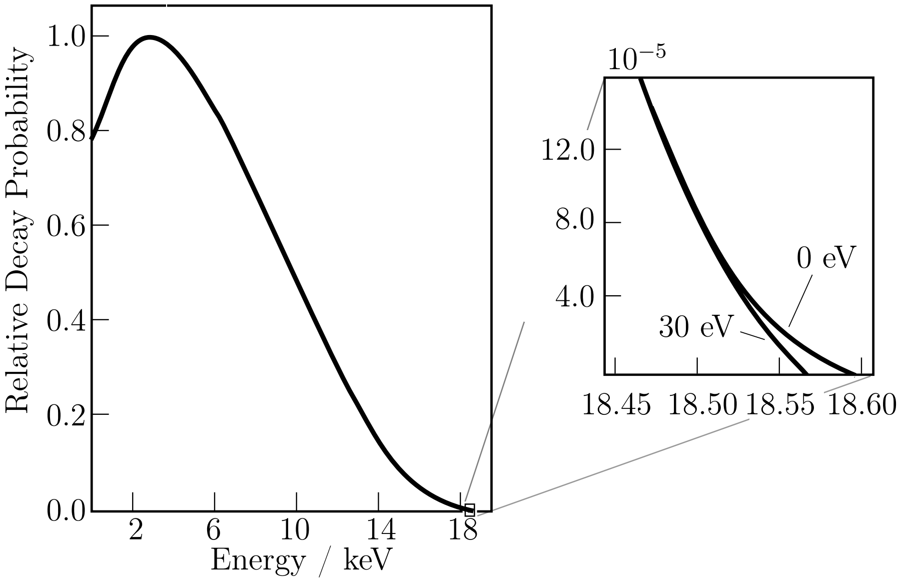

Figure 2.4.: Sample spectrum for tritium decay, showing exaggerated distortion in the high energy tail due to neutrino of mass 30 eV [19].

the coupling to the ν_e flavour state:

$$\langle m_\beta \rangle = \sqrt{\sum_i |U_{ei}|^2 m_i^2} \tag{2.18}$$

The best limit on $\langle m_\beta \rangle$ comes from a combination of independent measurements made by the Mainz and Troitsk experiments with a value of $\langle m_\beta \rangle < 2.0$ eV (95% CL) [16, 20, 21]. The KATRIN experiment, due to start taking data in 2015, will considerably improve this result with a predicted sensitivity of 0.2 eV (90% CL) [22].

The main advantage of tritium decay experiments is that they are essentially model independent, relying only on energy and momentum conservation to extract $\langle m_\beta \rangle$. However, to improve on the predicted KATRIN sensitivity would likely require a spectrometer of an unrealistically large scale. Therefore, 0.2 eV likely represents the best possible limit from tritium decay for the foreseeable future.

2.4.2. Cosmology

The standard hot big bang model predicts the existence of a sea of relic neutrinos and antineutrinos with a number density in the present epoch of ~ 340 cm^{-3}. This cosmic neutrino background (CNB) has not yet been directly observed, but its existence is well-established as a result of the accurate predictions of the primordial abundance of light elements alongside other cosmological observables [23].

Neutrinos play an important role in the evolution of the universe and by studying particular observables it is possible to glean information on the sum of neutrino masses, $\sum m_i$. To extract the strongest limits, many different observables are often combined. This means that the large amount of available data can be used, which affords very strong limits, but comes with the cost that these limits can be very model-dependent.

The most important probes for neutrino mass in cosmology are anisotropies in the cosmic microwave background (CMB) and large scale structure formation. The CMB is only sensitive to neutrino mass via secondary effects, but nonetheless, using the WMAP7 data alone, it is possible to extract an impressive limit of $\sum m_i < 1.3$ eV (95% CL) [24]. This result can be improved significantly, and in a relatively robust manner, by including independent measurements of baryon acoustic oscillations and a direct determination of the Hubble constant, giving $\sum m_i < 0.44$ eV (95% CL) [24].

Finally, it is possible to introduce information from galaxy power spectra, which can produce the most stringent limit of $\sum m_i < 0.28$ eV (95% CL) [25]. However, this result should be interpreted with care, since there are known difficulties in relating galaxy power spectra to the total matter power spectrum from which the limit is extracted [23].

2.4.3. Neutrinoless double beta decay ($0\nu\beta\beta$)

$0\nu\beta\beta$ (discussed in Chapter 3), if mediated by light neutrino exchange (Section 3.3.1), is sensitive to the effective Majorana neutrino mass, $\langle m_{\beta\beta} \rangle$:

$$\langle m_{\beta\beta} \rangle = \left| \sum_i U_{ei}^2 m_i \right| \tag{2.19}$$

The strongest limit currently comes from a combination of the Kamland-Zen and EXO experiments in ^{136}Xe, with a value of $\langle m_{\beta\beta} \rangle < 0.11 - 0.25$ eV (90% CL) where the range is a result of the chosen nuclear matrix element calculations (Section 3.4) [26].

$0\nu\beta\beta$ is expected to reach sensitivities of ~ 50 meV in the near future, although this limit only holds if the neutrino is a Majorana particle. If the neutrino is Dirac in nature, then $0\nu\beta\beta$ will not occur and can thus provide no information on neutrino mass.

2.4.4. Oscillations

The largest mass splitting, $|\Delta m^2_{23}|$, has been measured in neutrino oscillation experiments (Table 2.1). Since the lightest mass state cannot be less than 0, it is possible to place a lower bound on the heaviest active mass state as 0.05 eV ($\sqrt{|\Delta m^2_{23}|}$).

Parameter	Value	Source
$\langle m_\beta \rangle$	< 2 eV (95% CL)	Tritium Decay [20, 21]
$\sum m_i$	$< 0.28 - 0.44$ eV (95% CL)	Cosmology [24, 25]
$\langle m_{\beta\beta} \rangle$	$< 0.11 - 0.25$ eV (90% CL)	$0\nu\beta\beta$ [26]
m_1 or m_3	> 0.05 eV (68% CL)	Oscillations [16]

Table 2.2.: The most competitive constraints on neutrino mass for four different types of experiment.

2.5. Outstanding questions

There are good prospects for answering many of the outstanding questions of neutrino physics in the coming years and beyond. Oscillation, cosmology, tritium decay and $0\nu\beta\beta$ experiments all provide different and complementary information which will help to clarify the situation. The specific questions addressed by each type of experiment are summarised in Table 2.3.

2.5.1. Number of neutrinos

As discussed in Section 2.1.3, there are three light active flavours of neutrinos. However, the possibility of one or more sterile neutrinos in addition to the three

Property	Oscillation	Cosmology	β-decay	$0\nu\beta\beta$
Number of Neutrinos	✓	✓		
Absolute Mass		✓	✓	✓
Mass Hierarchy	✓			✓
Dirac or Majorana				✓
Dirac CP-violation	✓			
Majorana CP-violation				✓

Table 2.3.: Unknown properties of the neutrino that can be observed using the four main experimental techniques

known flavours has not yet been discounted. Indeed, some oscillation and cosmological results favour the existence of extra neutrinos, although none with enough statistical precision to draw firm conclusions [8, 9, 27]. The existence of sterile neutrinos that mix with the known neutrinos to such a large degree as these experiments suggest should be resolved with the next generation of reactor and accelerator experiments, but sterile neutrinos with small mixing angles may be much harder to detect or exclude.

2.5.2. Absolute Mass and Mass Hierarchy

Oscillation experiments have provided measurements of the mass splittings between the neutrino mass states, but do not allow the extraction of the absolute mass of each state. Therefore, there can be different scenarios depending on the mass of the lightest neutrino. If the lightest neutrino has low mass, then the splittings between the neutrinos are of significant size compared to their absolute masses. Whereas, if the lightest neutrino is more massive, there exists the possibility that the mass splittings are small compared to the absolute mass and the neutrinos are said to be degenerate. As discussed in Section 2.4, cosmology, tritium decay and $0\nu\beta\beta$ experiments can all provide information on the absolute masses of the neutrinos.

As well as absolute mass, oscillation experiments have not yet been able to measure the sign of Δm^2_{32}, so that the ν_1 and ν_2 pair may have higher or lower masses than ν_3. If ν_1 and ν_2 are lower than ν_3, the hierarchy is known as *normal* since ν_1 and ν_2 have larger fractions of ν_e and the electron is the lightest charged lepton. Conversely, if ν_1 and ν_2 are more massive, the hierarchy is said to be *inverted* as it is the reverse of what is observed in the charged leptons. Future oscillation experiments will be able to exploit differences between neutrino and antineutrino oscillations in matter to determine whether the mass hierarchy is normal or inverted. The current knowledge of neutrino masses can be represented pictorially as in Figure 2.5.

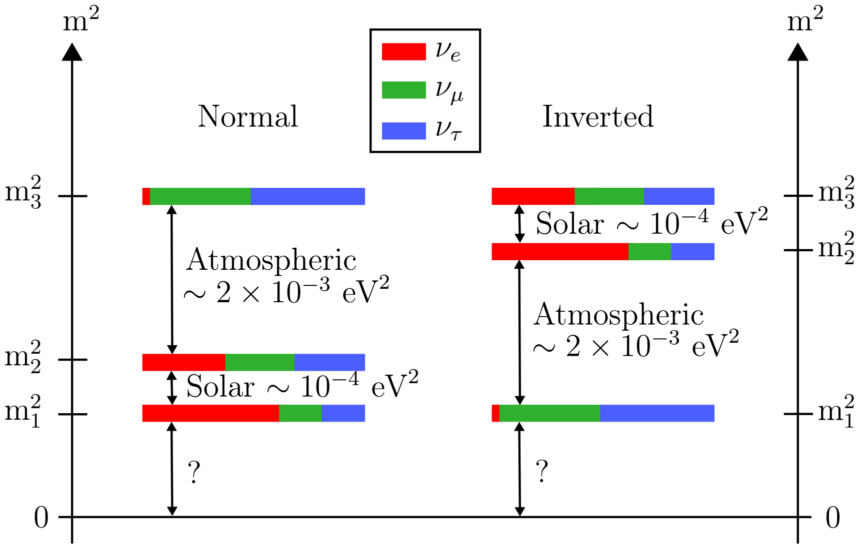

Figure 2.5.: A representation showing the "normal" and "inverted" mass hierarchies of absolute neutrino masses.

2.5.3. CP Violation

In the PMNS mixing matrix, there exists at least one CP-violating phase (and two more if neutrinos are Majorana fermions). CP-violation has been observed in the quark sector, and so the question arises of whether the leptonic sector also violates CP invariance. The answer to this question may have far-reaching implications.

Theoretical symmetries dictate that the Big Bang should have produced equal amounts of matter and antimatter. However, the universe we inhabit today is overwhelmingly composed of matter. In order to create this asymmetry, the following three conditions, known as *Sakharov conditions* [28], must be satisfied:

1. At least one baryon-number violating process must exist.
2. There must be a sufficient degree of C- and CP-violation.

3. Interactions outside of thermal equilibrium must occur.

The known CP-violation in the quark sector alone is not large enough to satisfy the second condition, so there is an intriguing possibility that CP-violation in the leptonic sector could be responsible. If CP-violation is observed in the known light neutrinos, it adds credibility to the “leptogenesis” argument where CP-violating heavy right-handed neutrinos transmit a matter-antimatter asymmetry to the baryons and as such are the progenitors of the universe as we know it.

The Dirac CP-violating phase, δ, may soon be accessible to current or near-future accelerator experiments or to precision measurements of atmospheric neutrinos [29]. A measurement of $0\nu\beta\beta$ will be required to determine the Majorana CP-violating phase, although this must also be coupled with another independent measurement from either oscillation or collider experiments as well as independent knowledge of the absolute mass scale to fully disentangle α_1 and α_2.

2.5.4. Nature of the neutrino

The preceding questions are very important, but perhaps the most fundamental question to be answered concerns the very nature of the neutrino itself - is it a Dirac or Majorana particle? Currently, the only feasible proposal to answer this question is through $0\nu\beta\beta$, which is discussed in detail in the next chapter.

Chapter 3.

Double Beta Decay

3.1. Beta Decay

Beta decay (β decay) is a type of radiocative decay that transmutes a nucleus to that of a different element. It is mediated by the weak force, and always results in the emission of a neutrino or antineutrino. The process can occur in three separate forms where the emission is either accompanied by an electron (β^- decay), a positron (β^+ decay) or, in the case of electron capture (EC), no other emissions.

In β^- decay, a neutron converts to a proton and an electron and antineutrino are emitted:

$$n \rightarrow p + e^- + \overline{\nu_e} \tag{3.1}$$

Whilst in β^+ decay, a proton converts to a neutron and a positron and neutrino are ejected:

$$p \rightarrow n + e^+ + \nu_e \tag{3.2}$$

Finally, EC occurs when an atomic electron exchanges a W boson with a quark inside the nucleus. It converts to a neutrino and a proton in the nucleus changes to a neutron.

$$p + e^- \rightarrow n + \nu_e \tag{3.3}$$

EC occurs in all isotopes where β^+ decay is energetically allowed. In some nuclei, where β^+ decay is not energetically possible, it can be the sole decay mode. The captured electron is usually in a low-lying orbital (most often in the K-Shell), which leaves a hole that the remaining orbital electrons can cascade into. EC is therefore usually accompanied by numereous low energy X-rays and/or Auger electrons.

3.1.1. Allowed and Forbidden Decays

All three β decay processes involve the emission of particles and loss of energy, so β decay can only occur if

$$M(A, Z_i) > M(A, Z_f) \tag{3.4}$$

where $M(A, Z)$ is the mass of the nucleus with A nucleons and Z protons, and the subscripts i and f denote the initial and final nuclear states.

The semi-empirical mass formula (SEMF) can be used to approximate the mass of an atomic nucleus for a given (A,Z) pairing [30] and can therefore be used to predict whether transititions between nuclear states are allowed or forbidden. The SEMF gives the mass of a nucleus, m, as:

$$m = Zm_p + (A - Z)m_n - a_V A + a_s A^{2/3} + a_c \frac{Z^2}{A^{1/3}} + a_A \frac{(A - 2Z)^2}{A} + \delta(A, Z) \tag{3.5}$$

where

$$\delta(A, Z) = \begin{cases} \frac{a_p}{A^{1/2}} & Z, N \text{ even } (A \text{ even}) \\ 0 & A \text{ odd} \\ \frac{-a_p}{A^{1/2}} & Z, N \text{ odd } (A \text{ even}) \end{cases} \tag{3.6}$$

The first two terms in this equation give an approximation of the mass of the nucleus by calculating the masses of individual nucleons. The remaining terms then provide corrections to this approximation in the form of a volume term, a surface term, a Coulomb term, an asymmetry term and a pairing term. For fixed A, parabolic curves are generated as a function of Z, which dictate which β decays are energetically allowed. If A is odd, only one curve will exist. However, if A is even, two curves will exist, split by the pairing term, $(\delta(A, Z))$, as shown in Figure 3.1.

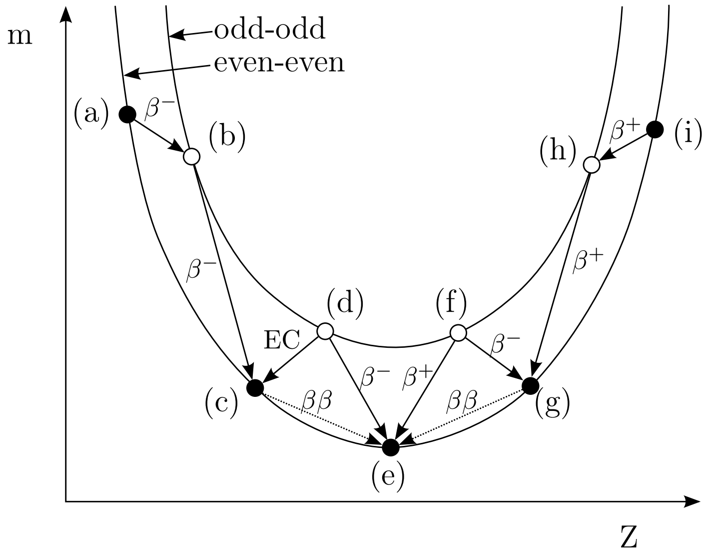

Figure 3.1.: Predictions of the SEMF for an even value of A. The arrows between the two parabolae show the energetically allowed β decays.

3.2. Two Neutrino Double Beta Decay

In Figure 3.1, it can be seen that the decay from isotope (c) → (d) or (c) → (b) is energetically forbidden and isotope (c) is therefore stable against β decay. However, isotopes such as (c) are not completely stable as there exists the possibility that they undergo two neutrino double beta decay ($2\nu\beta\beta$). This process, first hypothesised by Goeppert-Mayer in 1935 [31], is a rare nuclear process where two β^- decays happen simulataneously, so that two neutrons decay to two protons, resulting in the emission of two electrons and two antineutrinos:

$$(A, Z) \rightarrow (A, Z+2) + 2e^- + 2\overline{\nu_e} \tag{3.7}$$

$2\nu\beta\beta$ is a second order process that is allowed in the SM as can be seen from the sole use of SM vertices in Figure 3.2. It is clear from Figure 3.1 that $2\nu\beta\beta$ can only occur for even-even nuclei since odd-odd nuclei will predominantly decay via β decay to an even-even state.

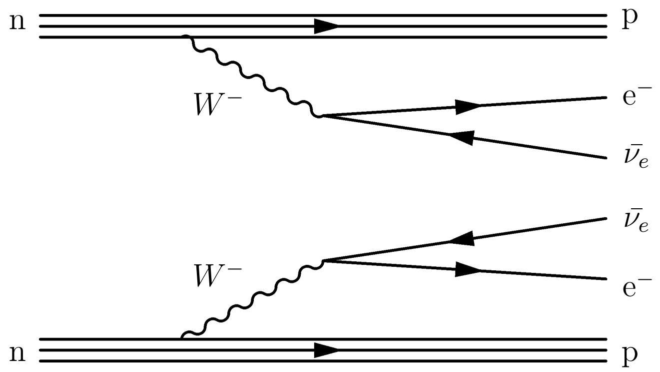

Figure 3.2.: Feynman diagram for $2\nu\beta\beta$, a second order SM process.

To measure $2\nu\beta\beta$, experiments usually study the spectrum of the total energy of the emitted electrons. Since the antineutrinos also carry away energy, this is a continuous spectrum with an end-point at the nuclear transition energy, $Q_{\beta\beta}$, defined as the total energy released in the decay:

$$Q_{\beta\beta} = M(A, Z) - M(A, Z + 2) \tag{3.8}$$

This shape of this spectrum can be seen in Figure 3.6. The half-life of the decay is parameterised as

$$\left(T^{2\nu}_{1/2}\right)^{-1} = G^{2\nu}\left(Q_{\beta\beta}, Z\right)\left|M^{2\nu}\right|^2 \tag{3.9}$$

where $G^{2\nu}$ is a four-body phase space factor that can be calculated analytically and goes as $Q^{11}_{\beta\beta}$. $M^{2\nu}$ is the $2\nu\beta\beta$ nuclear matrix element (NME) for the decay, which is effectively a nuclear structure calculation of the transition probability from the initial to final states. NME calculations are heavily model-dependent, so experimental information is vital to tune models appropriately (Section 3.4).

3.3. Neutrinoless Double Beta Decay

If an isotope is a candidate for $2\nu\beta\beta$, then it is also a candidate for neutrinoless double beta decay ($0\nu\beta\beta$). In this hypothesised decay, two β^- decays also occur simultaneously and two electrons are emitted, however, in contrast to $2\nu\beta\beta$, no antineutrinos are emitted:

$$(A, Z) \rightarrow (A, Z+2) + 2e^- \tag{3.10}$$

Clearly, $0\nu\beta\beta$ violates lepton number and it cannot occur in the SM. The significance of the process was recognised by Racah in 1937, when it was proposed as a method for testing for the Majorana nature of neutrinos [32].

There are many different hypothesised mechanisms via which $0\nu\beta\beta$ may be mediated, the most common of which are the neutrino mass mechanism, right-handed current and Majoron emission modes (Sections 3.3.1–3.3.3). There also exist a plethora of more exotic decay modes such as via R-parity violating super-symmetry, squark mixing or extra dimensions which are not presented herein.

For some mechanisms, such as the mass mechanism, it is readily apparent that $0\nu\beta\beta$ confirms that neutrinos are Majorana paricles. In constrast, for some of the more exotic decays where neutrinos are not involved at all, such as in R-parity violating SUSY [33], things are not so obvious. The situation was clarified by Schechter and Valle in 1980, who showed that any $0\nu\beta\beta$ process implies that neutrinos are Majorana particles [34]. This can be seen by replacing the $0\nu\beta\beta$ mechanism with a “Black Box” (Figure 3.3) and confirming that there exists a propagator that converts between neutrinos and antineutrinos as is required for a Majorana mass (Section 2.3.2).

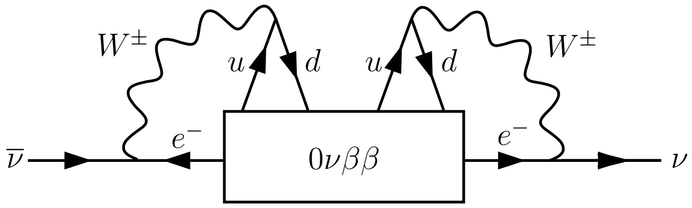

Figure 3.3.: Majorana propagator resulting from any $0\nu\beta\beta$ process [34].

The half-life of $0\nu\beta\beta$ is parameterised as:

$$\left(T^{0\nu}_{1/2}\right)^{-1} = G^{0\nu}\left(Q_{\beta\beta}, Z\right)\left|M^{0\nu}\right|^2 \eta^2_{LV} \tag{3.11}$$

where $G^{0\nu}$ is now a two-body phase space factor that goes as $Q^5_{\beta\beta}$, $M^{0\nu}$ is the $0\nu\beta\beta$ NME and η_{LV} is a lepton number violating parameter which encompasses all the physics behind the decay mechanism. Thus, η_{LV} takes on different forms depending on the mechanism via which $0\nu\beta\beta$ is mediated.

3.3.1. Neutrino Mass Mechanism

The neutrino mass mechanism, also called the light neutrino exchange mechanism, is the most commonly postulated $0\nu\beta\beta$ decay mode, since it involves the least deviation from the SM. In this mechanism, a scenario using only SM vertices is constructed where a RH (helicity) Majorana neutrino (simlar to a Dirac antineutrino) is emitted from one W boson and absorbed by another as a LH Majorana neutrino (Figure 3.4).

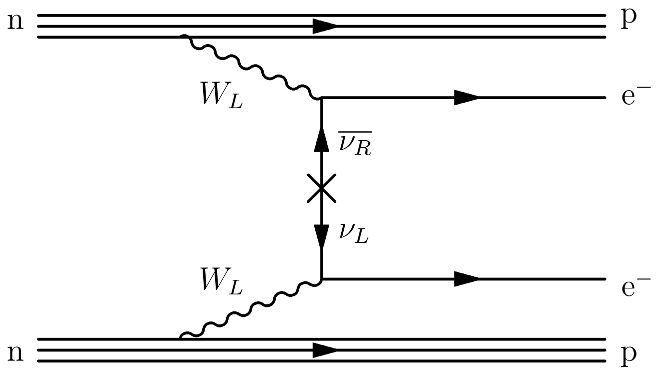

Figure 3.4.: Feynman diagram from $0\nu\beta\beta$ for the neutrino mass mechanism. The decay is facilited by the exhange of a Majorana neutrino.

In this mechanism, η_{LV} is given by the effective Majorana neutrino mass, $\langle m_{\beta\beta}\rangle$:

$$\left(T^{0\nu}_{1/2}\right)^{-1} = G^{0\nu}\left(Q_{\beta\beta}, Z\right)\left|M^{0\nu}\right|^2 \langle m_{\beta\beta}\rangle^2 \tag{3.12}$$

The form of $\langle m_{\beta\beta}\rangle$ can be explained intuitively. Since the RH helicity neutrino has mass, it must have a LH component proportional to m_i, and each vertex picks up a factor U_{ei}:

$$\begin{aligned}\langle m_{\beta\beta}\rangle &= \left|\sum_i U_{ei}^2 m_i\right| \\ &= \left|\cos^2\theta_{13}\left(m_1\cos^2\theta_{12} + m_2 e^{i\alpha_1}\sin^2\theta_{12}\right) + m_3 e^{i(\alpha_2-2\delta)}\sin^2\theta_{13}\right|\end{aligned} \tag{3.13}$$

It is instructive to use experimental information about the oscillation parameters to consider allowed values for $\langle m_{\beta\beta} \rangle$. Figure 3.5 shows the available phase space remaining for $\langle m_{\beta\beta} \rangle$ as a function of the lightest neutrino mass for the best fit values of oscillation parameters. The two distinct bands are formed for the normal and inverted hierarchies, with the width of each band governed by the uncertainty over the CP-violating phases. If nature has chosen the inverted hierarchy, then there are real prospects for either observing or excluding $0\nu\beta\beta$ mediated via the mass mechanism in the coming years.

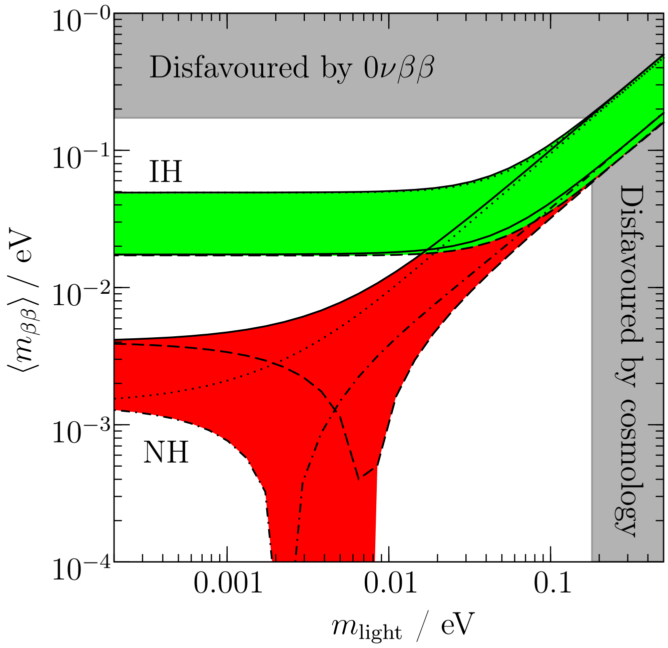

Figure 3.5.: Allowed regions of $\langle m_{\beta\beta} \rangle$ as a function of the lightest neutrino mass, with best fit values of the oscillation parameters, for normal hierarchy (red) and inverted hierarchy (green). Adapted from [35].

As there are no other particles emitted in light neutrino exchange, the experimental signature is given by two electrons whose energy sums to a monochromatic line at $Q_{\beta\beta}$, as shown in Figure 3.6.

3.3.2. Right-handed Current

In the SM, the weak interaction has couplings that have a $V - A$ nature, such that it is only propagated by a LH W boson, W_L. To resolve this apparent asymmetry,

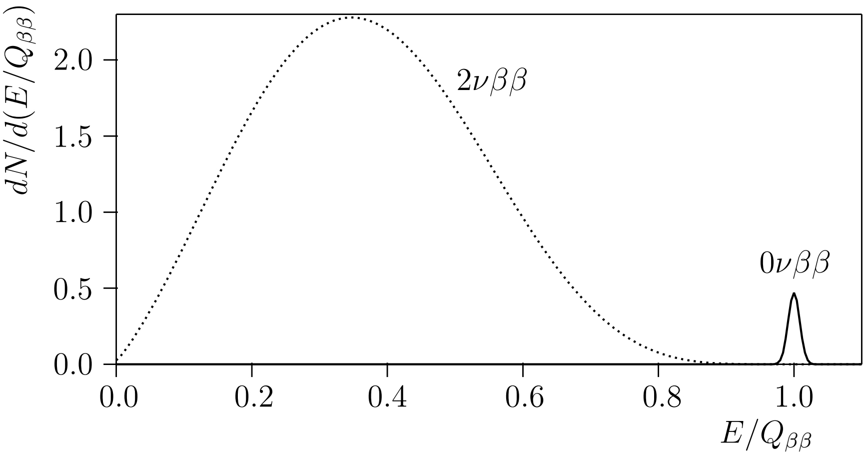

Figure 3.6.: Distribution of the sum of electron energies for $2\nu\beta\beta$ and $0\nu\beta\beta$. The curves assume that $T^{2\nu}_{1/2}$ is 1% of $T^{0\nu}_{1/2}$ and an energy resolution of 2% [17].

Left-Right Symmetric models have been proposed that introduce a coupling with a new RH gauge boson. This new boson may be completely new, such as a W' boson, or be an addition to the SM W boson such that W is an admixture of W_L and W_R. These new models have $V + A$ vertices can lead to $0\nu\beta\beta$ without a helicity flip, as can be seen from Figure 3.7 [36].

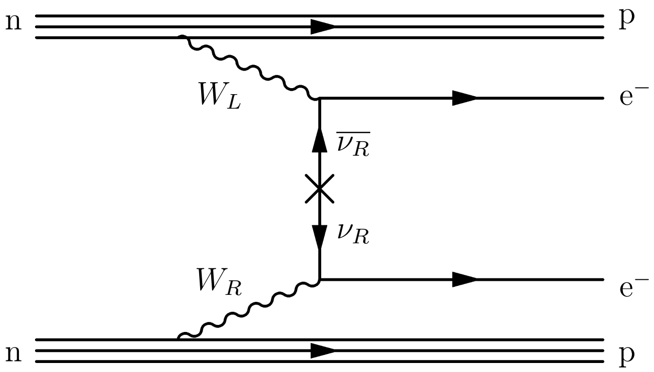

Figure 3.7.: Feynman diagram from $0\nu\beta\beta$ using a right handed weak current, described by the $\langle\lambda\rangle$ decay mode.

Two new physics parameters are commonly introduced to describe the physics behind the RH current mechanism. $\langle\lambda\rangle$ describes the coupling between RH quarks and RH leptons (as in Figure 3.7), which is given by the relative amplitudes of the contributions from W_R and W_L. $\langle\eta\rangle$ describes a coupling between LH quarks and RH leptons and so is related to the mixing angle between W_R and W_L. In this thesis, contributions from $\langle\lambda\rangle$ and $\langle\eta\rangle$ are presented separately, although in general the situation may be complicated by interference between them. These interfering admixtures are not implemented at Monte Carlo (MC) generator level so could not be studied here. The relevant lepton number violating parameters are related to the $0\nu\beta\beta$ half-life as:

$$T_{1/2}^{0\nu\lambda} = G^{0\nu\lambda}\left(Q_{\beta\beta}, Z\right)\left|M^{0\nu\lambda}\right|^2 \langle\lambda\rangle^2 \tag{3.14}$$

$$T_{1/2}^{0\nu\eta} = G^{0\nu\eta}\left(Q_{\beta\beta}, Z\right)\left|M^{0\nu\eta}\right|^2 \langle\eta\rangle^2 \tag{3.15}$$

The energy spectrum for the total electron energy is identical for the RH current mode as for the neutrino mass mechanism (Figure 3.6). However, there may be possibilities to tell the mechanisms apart by considering other variables such as the angle between the electrons, or the difference between the two electron energies as shown in Figure 3.8. It is therefore experimentally preferable to be able to independently measure each electron in $0\nu\beta\beta$, which may prove to be one of SuperNEMO's main strengths [37].

3.3.3. Majoron Emission

Some proposed extensions to the standard model violate a global symmetry in the difference between baryon and lepton number, $B - L$. This violation leads to the existence of a massless Goldstone boson, referred to as a Majoron, which could provide a mechanism for $0\nu\beta\beta$. Initially singlet, doublet and triplet models were developed [38–40]. The doublet and triplet models predict an additional coupling to the Z^0, increasing the Z^0 width by the equivalent of half or two extra neutrinos respectively. These models were excluded by the precise measurement of the width of the Z^0 boson at LEP (Section 2.1.3), but the singlet model is still viable. However, this singlet model is not without problems of its own as it predicts a coupling to the neutrino at tree level with a strength:

$$g \simeq \frac{m_{\nu_L}}{v_{BL}} \tag{3.16}$$

where m_{ν_L} is the light neutrino mass and v_{BL} is the scale at which the $B - L$ symmetry is broken. Therefore to preserve current constraints on neutrino mass but still predict a non-negligible rate of $0\nu\beta\beta$, a high degree of fine tuning is required.

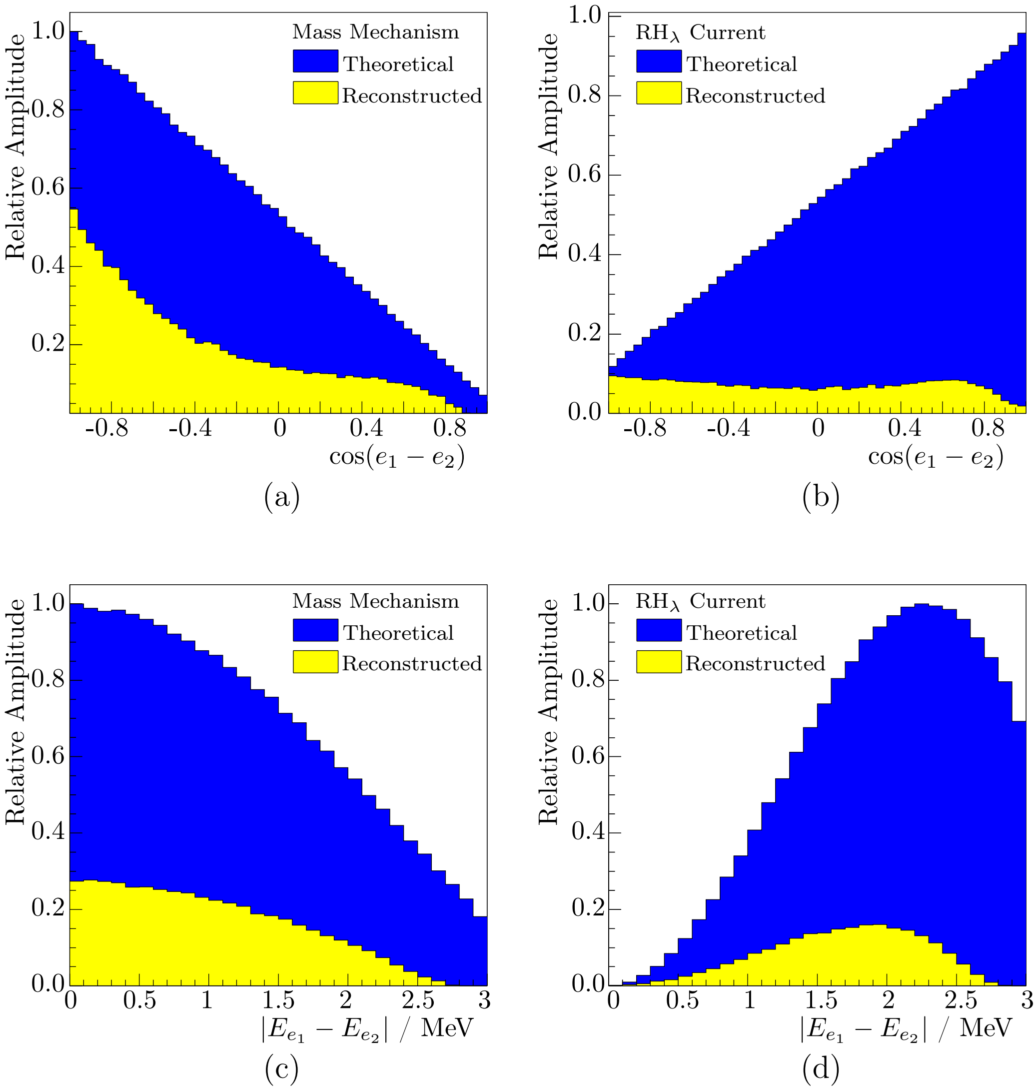

Figure 3.8.: Comparison of distributions of the angle between electrons and electron energy difference for the mass mechanism and right-handed current decay modes. Reconstructed distributions show the expected response of SuperNEMO and have the same normalisation as theoretical distributions [37].

To avoid such unnatural fine tuning, a range of new models have been developed, including decay modes where the Majoron can have lepton charge and need not be a Goldstone boson [41]. Furthermore, some of these new modes also predict the emission of two Majorons so that models now exist where $0\nu\beta\beta$ can proceed via either of the two processes:

$$(A, Z) \rightarrow (A, Z+2) + 2e^- + \chi^0 \tag{3.17}$$

$$(A, Z) \rightarrow (A, Z+2) + 2e^- + 2\chi^0 \tag{3.18}$$

The half-life of the process takes a similar form to previous decay modes, with an additional coupling factor for modes with more than one Majoron:

$$\left(T_{1/2}^{0\nu\chi^0}\right)^{-1} = G^{0\nu\chi^0}\left(Q_{\beta\beta}, Z\right)\left|M^{0\nu\chi^0}\right|^2 \langle g_{\chi^0}\rangle^2 \quad \text{for } 0\nu\beta\beta\chi_0 \tag{3.19}$$

$$\left(T_{1/2}^{0\nu\chi^0}\right)^{-1} = G^{0\nu\chi^0}\left(Q_{\beta\beta}, Z\right)\left|M^{0\nu\chi^0}\right|^2 \langle g_{\chi^0}\rangle^4 \quad \text{for } 0\nu\beta\beta\chi_0\chi_0 \tag{3.20}$$

where as before $G^{0\nu\chi^0}$ is a phase space factor, $M^{0\nu\chi^0}$ is a NME and $\langle g_{\chi^0}\rangle$ defines the coupling between the Majoron and the neutrino. As with the other $0\nu\beta\beta$ modes, the experimental signature for Majoron emission is identified by measuring the distribution of total electron energy. However, unlike the mass mechanism and RH current decay modes, there are now extra particles emitted in the decay, so that the energy spectrum is no longer a monochromatic line, but a continuous spectrum. The shape of the spectrum may be different for different Majoron models, and this is governed by a spectral index, n, which describes the dependence of the phase space factor on the energy of the Majoron(s):

$$G^{0\nu\chi^0} \propto \left(Q_{\beta\beta} - (E_{e_1} + E_{e_2})\right)^n \tag{3.21}$$

where E_e is the energy of an emitted electron. For the models presented herein, allowed values for n are 1, 2, 3 and 7, and these give four distinct energy spectra as shown in Figure 3.9.

The ten different Majoron models that are most commonly discussed are presented in Table 3.1. These are grouped into lepton number violating (I) and lepton number conserving (II) modes and are presented along with their most important properties. The names of the models follow the conventions dictated in [41].

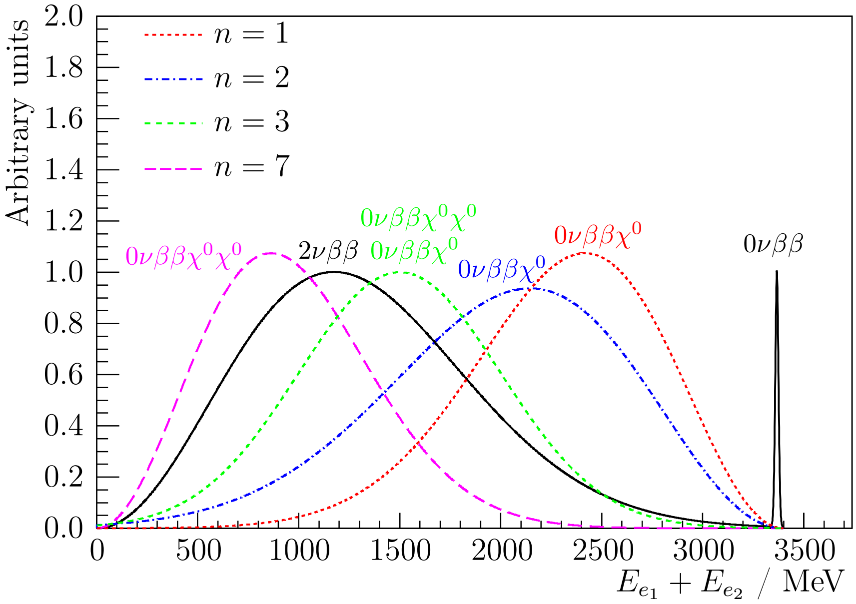

Figure 3.9.: Energy spectra for $2\nu\beta\beta$ and $0\nu\beta\beta$, along with four different Majoron decay modes with spectral indices 1, 2, 3 and 7 [42].

Model	Decay Mode	Goldstone	L	n	Matrix Element
IB	$0\nu\beta\beta\chi^0$	✗	0	1	$M_F - M_{GT}$
IC	$0\nu\beta\beta\chi^0$	✓	0	1	$M_F - M_{GT}$
ID	$0\nu\beta\beta\chi^0\chi^0$	✗	0	3	$M_{F\omega^2} - M_{GT\omega^2}$
IE	$0\nu\beta\beta\chi^0\chi^0$	✓	0	3	$M_{F\omega^2} - M_{GT\omega^2}$
IIB	$0\nu\beta\beta\chi^0$	✗	-2	1	$M_F - M_{GT}$
IIC	$0\nu\beta\beta\chi^0$	✓	-2	3	M_{CR}
IID	$0\nu\beta\beta\chi^0\chi^0$	✗	-1	3	$M_{F\omega^2} - M_{GT\omega^2}$
IIE	$0\nu\beta\beta\chi^0\chi^0$	✓	-1	7	$M_{F\omega^2} - M_{GT\omega^2}$
IIF	$0\nu\beta\beta\chi^0$	Gauge boson	-2	3	M_{CR}
Bulk	$0\nu\beta\beta\chi^0$	Bulk field	0	2	–

Table 3.1.: Ten different Majoron models and their main properties [43]. The model names follow [41], with IIF from [44] and the Bulk model from [45].

3.4. Nuclear Matrix Elements

Experiments searching for $0\nu\beta\beta$ produce a limit on the half-life of the decay, $T^{0\nu}_{1/2}$. To convert this to the physics parameter of interest (usually $\langle m_{\beta\beta}\rangle$), the appropriate nuclear matrix element (NME) must be used (Equation (3.11)). Therefore the accuracy with which NMEs can be calculated directly impacts the interpretation of any experimental result. NME calculations must be performed using the tools of nuclear structure theory and since there is no other observable that can be directly linked to the magnitude of $M^{0\nu}$, the results are necessarily model-dependent. The situtation is further complicated as the ground state and many different excited states of open-shell nuclei with complicated nuclear structures must be considered [46].

To date, five different techniques have been applied to the problem and in each of these frameworks, two different stages are followed. Firstly, a many-body Hamiltonian is created which describes the interactions between nucleons and encompasses known nuclear physics and the physics mechanism behind $0\nu\beta\beta$. Then, a mean field is introduced which supplies information about the nuclear structure and residual interactions. The complexity of the calculations mean that some approximation and/or truncation is always needed, and it is in these simplifying assumptions that the different techniques vary.

In this section, the five calculational techniques are briefly discussed and a comparison of the results from each technique is presented to give an overview of the remaining level of uncertainty (Section 3.4.6).

3.4.1. Interacting Shell Model

The interacting shell model (ISM) considers only a limited number of nuclear orbitals close to the Fermi level, but all possible correlations for these orbitals are included. This full treatment of the correlations tends to reduce the values of the NMEs, however the ISM may overestimate this effect due to the limited number of orbits in the valence space which causes a similar reduction. Despite being technically challenging, the ISM has been used to perform calculations for several nuclei. The results do not vary significantly between them (with the exception of doubly-magic ^{48}Ca). It is known that the ISM does not treat deformed nuclei, such as ^{150}Nd, correctly, and it is commonly accepted that the ISM produces more reliable results for smaller nuclei such as ^{48}Ca, ^{76}Ge and ^{82}Se.

3.4.2. Quasiparticle Random Phase Approximation

The quasiparticle random phase approximation (QRPA) takes a constrasting approach to the ISM. In this method, the number of different nuclear orbitals is greatly increased, but the complexity of the interactions between nucleons must be reduced accordingly. To calculate the NMEs, the initial and final nuclear states are connected via many virtual intermediate collective states. Recently, it has been shown that the uncertainties associated with QRPA calculations can be significantly reduced if the g_{pp} parameter, which parameterises proton-proton interactions, is tuned to reproduce $2\nu\beta\beta$ data. The QRPA is, to some degree, complementary to the ISM, and produces more reliable results for larger nuclei.

3.4.3. Interacting Boson Model

In the interacting boson model (IBM), the low-lying nuclear states are modelled as bosons. These bosons are restricted to angular momentum states of $L = 0$ (s boson) or $L = 2$ (d boson). Therefore only 0^+ and 2^+ neutron pairs can turn into two protons in $0\nu\beta\beta$. The IBM is similar in form to the ISM and therefore has the same advantages, but suffers from similar short-comings.

3.4.4. Projected Hartree-Fock-Bogoluibov Method

In the projected Hartree-Fock-Bogoluibov (PHFB) method, nuclear wave functions with good particle number and angular momentum are constructed by projection on the HFB wavefunctions. The nuclear Hamiltonian is simplified to include only quadrupole interactions and only neutron pairs with even momentum and positive parity (0^+, 2^+, 4^+ etc.) can participate in $0\nu\beta\beta$, although non-0^+ pairs are heavily suppressed compared to other calculations. The PHFB uses fewer model dependent parameters to calculate NMEs, although may suffer from a certain degree of over-simplification.

3.4.5. Energy Density Functional Method

The energy density functional (EDF) method is considered to be an improvement with respect to the PHFB. The inter-nucleon interaction is modified to reproduce the Gogny interaction and the single particle basis is enlarged.

3.4.6. Comparison of different NME calculations

As described above, each method of NME calculations makes differing assumptions in order to simplify the calculation. To understand the effect of each of these assumptions and the associated systematic error with the resulting NMEs, it is helpful to compare the NME results for each method.

In the conversion from an experimental half-life to $\langle m_{\beta\beta} \rangle$ (Equation (3.12)), the phase space factor, $G^{0\nu}$, enters into the calculation alongside the NME. This factor exhibits a proportionality given by

$$G^{0\nu} \sim \frac{g_A^4}{R_A^2} \tag{3.22}$$

where g_A is the ratio of the vector and axial-vector couplings and R_A is the atomic radius, commonly parameterised as $r_0 A^{1/3}$ [47]. Unfortunately, mostly for historical reasons, different NME calculations are performed with different values of g_A and r_0 so that the phase space factors, and therefore NME results, are not directly comparable. Common values for g_A are either 1.0 or 1.25 and for r_0 either 1.1 or 1.2 fm.

Therefore for a meaningful comparison, the NME results should be adjusted to use the same values of g_A and r_0. Results for 11 isotopes of experimental interest, with appropriate adjustments made, are shown graphically in Figure 3.10.

In general, there is disagreement across the range of methods for any given isotope up to a factor 2-3. For reasons discussed above (Section 3.4.1), the ISM produces results that are at the lower end of this range, but there does not seem to be a particular method producing high NMEs. It can also be seen that the ISM predicts similar values across all the different nuclei since only the outermost shells are considered.

For some isotopes, notably ^{130}Te and ^{128}Te, there is good agreement across all calculations (except for the ISM as previously explained). Additionally, the QRPA(T)

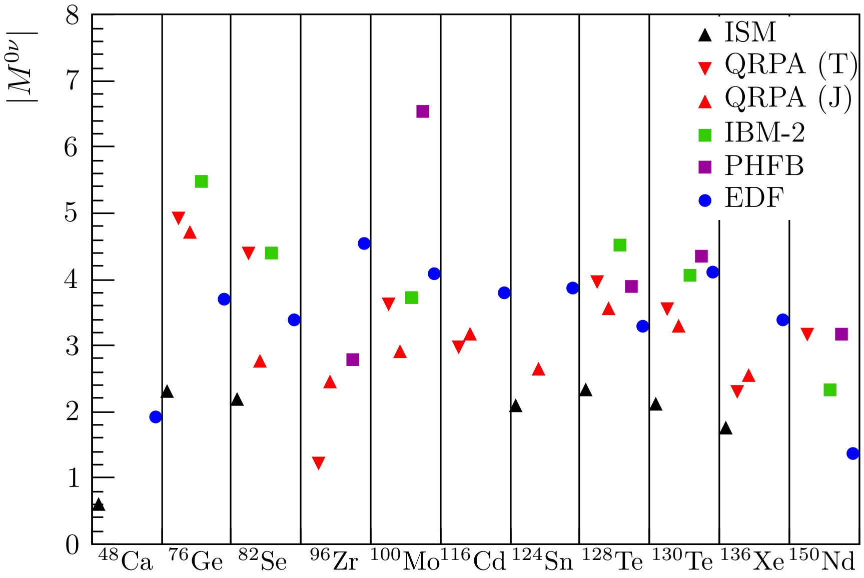

Figure 3.10.: $0\nu\beta\beta$ NME for the neutrino mass mechanism, calculated with five different approaches. QRPA(T) and QRPA(J) show the results of the Tübingen-Bratislava-Caltech and Jyväskylä groups. $\left|M^{0\nu}\right|$ values taken from [46]. Conversions for $g_A = 1.25$ and $r_0 = 1.2$ fm have been made where necessary.

and IBM methods agree well across all isotopes. These results are encouraging, however, there remain troublesome disparities between some calculations. There is disagreement between the two QRPA calculations, particularly for ^{82}Se, ^{96}Zr and ^{100}Mo, which must be explained. Furthermore, it is noted that the IBM is a truncation of the ISM to the S and D pair space and should produce similar results in the limit of spherical nuclei. As such, the large disagreement between these methods remains unexplained.

Chapter 4.

Double Beta Decay Experiments

4.1. Detector Design Considerations

Double beta decay experiments search for a small signal from $0\nu\beta\beta$ on top of backgrounds from natural radioactivity and $2\nu\beta\beta$. It is possible to approximately parametrise the expected half-life sensitivity of any given experiment using the following expression [17]:

$$T_{1/2}^{0\nu} > \frac{4.16 \times 10^{26}\ \text{yr}}{n_\sigma} \left(\frac{\epsilon a M t}{Z}\right) \sqrt{\frac{1}{N_B}} \tag{4.1}$$

where

- $T_{1/2}^{0\nu}$ is the half-life sensitivity to $0\nu\beta\beta$ in years
- n_σ is the number of standard deviations for a given confidence level (90% CL corresponds to $n_\sigma = 1.64$)
- ϵ is the event detection and identification efficiency
- a is the isotopic abundance of the $0\nu\beta\beta$ source isotope in the source mass
- Z is the molecular weight of the source isotope
- Mt is the total exposure of the experiment in kg yr
- N_B is the number of expected background events for the exposure

This equation is valid as long as the number of expected background events is large enough that its Poissonian error can be approximated as $\sqrt{N_B}$. Even if this criteria is not fulfilled, it is still helpful to study this equation as it contains all the necessary components to understand how experimental parameters affect the half-life sensitivity.

When $0\nu\beta\beta$ experiments are designed, the primary concept is to maximise the half-life sensitivity given by Equation (4.1). To maximise sensitivity in any experiment, the highest possible signal efficiency coupled with lowest error on a background level is desired, i.e. the maximal value of $S/\sqrt{B}$. As a result, the above equation can be broken down into two separate components corresponding to contributions from signal and background.

4.1.1. Maximising Signal

It should come as no surprise that to maximise an experiment's sensitivity, the largest possible number of atoms of isotope should be studied for the longest possible time. Additionally, if a decay does occur, then the best sensitivity will come with the maximum possible chance of detecting this event and thus the highest efficiency, ϵ. Indeed, a zero-background experiment will have a sensitivity directly proportional to

$$T^{0\nu}_{1/2} \propto \epsilon N_{\text{atoms}} t = \epsilon \frac{N_A a M}{Z} t \tag{4.2}$$

where N_A is Avogadro's constant. In a real world scenario, it is likely that an experiment will have dominant backgrounds that are also proportional to Mt, such that the dependency on exposure reduces to $\sqrt{Mt}$.

An experiment should therefore aim to contain as many atoms of the source isotope as is feasible. This is achieved by building large detectors that can hold a considerable source mass. However, it should be noted that both molar mass and abundance of source isotope in the source mass are also important when converting to the number of atoms. When selecting an isotope to study, the molar mass is generally a secondary consideration since there are more important factors that can counter-act any potential gain such as changes in the NME, M^{0v}, or the available phase space, $G^{0\nu}(Q_{\beta\beta}, Z)$. For example, the advantage from the molar mass of ^{76}Ge over ^{150}Nd is heavily outweighed by the difference in $0\nu\beta\beta$ phase space, as can be seen in Table 4.1.

In contrast, the ability to enrich an isotope to an acceptable abundance, a, cannot be disregarded so lightly. Table 4.1 shows the natural abundance and enrichment possibilities for the main isotopes studied in $0\nu\beta\beta$ experiments. For the majority of isotopes, centrifugation is possible, which allows for reasonably-priced enrichment up to large masses. However, for ^{48}Ca, ^{96}Zr and ^{150}Nd, only electromagnetic separation is currently available. Using this method, it is only possible to enrich small quantities of isotope, although R&D continues into new enrichment methods.

Isotope	$Q_{\beta\beta}$ keV	$G^{0\nu}$ 10^{-14} yr^{-1}	NA %	Enrichment Possibilities Current Method	 R&D Method(s)
^{48}Ca	4276	7.15	0.187	EMS	Laser Separation, Gaseous Diffusion
^{76}Ge	2039	0.71	7.8	Centrifugation	–
^{82}Se	2992	3.11	9.2	Centrifugation	–
^{96}Zr	3348	5.63	2.8	EMS	Laser Separation
^{100}Mo	3034	5.03	9.6	Centrifugation	–
^{116}Cd	2804	5.44	7.6	Centrifugation	–
^{130}Te	2529	4.89	34.5	Centrifugation	–
^{136}Xe	2467	5.13	8.9	Centrifugation	–
^{150}Nd	3368	23.2	5.6	EMS	Laser Separation, Centrifugation

Table 4.1.: Details of isotopes commonly used in $0\nu\beta\beta$ experiments, showing Q-value, phase space factor, natural abundance (NA) and possibilities for enrichment. EMS is electromagnetic separation. $G^{0\nu}$ is calculated with $g_A = 1.25$ and $R = 1.2\ A^{1/3}$ fm [35, 46].

For a typical experiment, a mass of $\sim$ 100 kg of source isotope that is studied for 5 years results in a sensitivity of $\sim$ 50 meV. To reduce this further to $\sim$ 10 meV, experiments containing $\sim$ 1000 kg will be required.

4.1.2. Minimising Background

As shown in Equation (4.1), the half-life sensitivity of an experiment goes as $1/\sqrt{N_B}$. Therefore, the best sensitivity will be achieved by minimising the number of background events, whilst keeping a high signal efficiency.

In the majority of current experiments, the main contributors to the background are the natural radioactive isotopes ^{214}Bi and ^{208}Tl, which are present in small amounts in all materials from the naturally occurring ^{238}U and ^{232}Th decay chains. These backgrounds are usually proportional to Mt, as is the signal term. However, the square-root in Equation (4.1) means that the signal term over-compensates for any increase in background with extra exposure. Therefore the exposure should still be as long as possible and the background rate should be reduced. To suppress these radioactive backgrounds, detector materials must be carefully chosen to be extremely radiopure. In order to reach the 10 meV level, it is expected that materials will require radiopurity below the µBq/kg level. To further reduce this contribution, it is also preferable to select an isotope with $Q_{\beta\beta} > 2.6$ MeV (as listed in Table 4.1) . This greatly reduces the background from ^{208}Tl which has the highest energy γ-line (at 2.6 MeV) in the ^{238}U and ^{232}Th decay chains.

There are other contributions to the background from external sources which can be reduced by use of shielding. Firstly, cosmic muons are reduced by placing detectors underground. Typically, $0\nu\beta\beta$ experiments have a substantial over-burden of rock of at least 2500 m water-equivalent. This muon background is often reduced further with the use of active shielding.

In addition to this, a range of active and passive shielding is used to reduce backgrounds from natural radioactivity in the surrounding rock. This background usually takes the form of gamma radiation from the natural decay chains and neutrons from spontaneous fission of uranium. These external backgrounds are dependent on the exposed surface of the experiment such that some experiments, particularly those using large volumes of liquid scintillator, are effectively self-shielded.

One external background source that cannot be shielded is ^{8}B solar neutrinos. This background is proportional to detector mass, so predominantly affect liquid scintillator detectors which normally have the largest masses. This background is not currently at a sensitivity-limiting level, but may become a significant problem for future experiments.

One of the most effective methods to reduce contributions to the background is the development of analysis techniques that distinguish between backgrounds and signal. These are applied in a number of different ways, ranging from full event reconstruction to simple algorithms to differentiate between electron and alpha particles.

As well as reducing backgrounds, it is important to design an experiment with good energy resolution so that the signal window can also be reduced. Since the signal is mono-energetic, the window can in principle be very narrow, but in practice is limited by the energy resolution of the detector. Since many of the background contributions are approximately constant in energy over a narrow range, a reduction in the signal window results in significant reduction of total background. Furthermore, it should be noted that even if contributions from natural radioactivity and external backgrounds can be reduced to negligible levels, there is an irreducible background from the tail of the $2\nu\beta\beta$ process which is only suppressed by improving energy resolution.

4.2. Detector Technologies

In general, signal or background contributions can be improved at the cost of reducing the other. For example, it is very difficult to build a tonne-scale detector whilst keeping very low backgrounds from natural radioactive contaminants. As a result of this trade-off, there are many different plausible experimental designs and numerous detector technologies, each of which has advantages and disadvantages. In this section, the five main technologies will be briefly described along with notable experiments and their main results. A comparative overview of $2\nu\beta\beta$ and $0\nu\beta\beta$ results is presented in Section 4.3.

4.2.1. Semiconductor Experiments

Semiconductor experiments use a $0\nu\beta\beta$ candidate that can be used as a semiconductor, such as ^{76}Ge, and place it between two electrodes to form a diode. Nuclear decays (or incident radiation) create electron-hole pairs in the material. Some of the electrons are transferred from the valence band to the conduction band and are migrated to the electrodes with an applied potential where they are measured.

Germanium can be readily enriched to produce large crystals which have a depletion layer of a few centimetres, allowing total absorption of gamma rays up to ~ 5 MeV. Germanium detectors of this size must necessarily be pure and are often referred to as high-purity germanium (HPGe) detectors. HPGe detectors must be operated at cryogenic temperatures to reduce electronic noise, but in this configuration they can achieve truly excellent energy resolution of $\sim 0.3\%$ (FWHM). For many years, HPGe detectors provided the strongest limits on $\langle m_{\beta\beta} \rangle$ with the results from the Heidelberg-Moscow (H-M) and IGEX experiments.

- **Heidelberg-Moscow (H-M)** ran from 1990 to 2003, with five HPGe detectors enriched to 86% in ^{76}Ge. For a total exposure of 35.5 kg yr, a limit of $T^{0\nu}_{1/2} > 1.9 \times 10^{25}$ yr was obtained [48], corresponding to $\langle m_{\beta\beta} \rangle < 250 - 500$ meV.

  In this result and those following, a range of values for $\langle m_{\beta\beta} \rangle$ is given. This range reflects the variation in $\langle m_{\beta\beta} \rangle$ as a result of uncertainties in NME calculations.

  In 2001, a subset of the H-M collaboration claimed a discovery of a $0\nu\beta\beta$ signal using the data from the spectrum shown in Figure 4.1 [49]. For an exposure of 71.7 kg yr, a half-life of $T^{0\nu}_{1/2} = 1.19^{+2.99}_{-0.50}(3\sigma) \times 10^{25}$ yr was claimed, corresponding to $\langle m_{\beta\beta} \rangle = 100 - 900$ meV. This so called Klapdor-Kleingrothaus (KK) claim has proved controversial due to the presence of an unidentified peak at 2030 keV, the wrong ratio of amplitudes of the nearby ^{214}Bi peaks, spurious peak identification and claims that the background and systematic uncertainty of the experiment are underestimated [50].

  Three experiments that have recently started collecting data are becoming sensitive to $\langle m_{\beta\beta} \rangle$ at the level of the KK claim and the initial results strongly disfavour the claim (Section 4.3).

- **IGEX** was a similar experiment to H-M, with six HPGe detectors enriched to 86% in ^{76}Ge containing 2.0 kg of source isotope. 8.9 kg yr of data produced a half-life limit of $T^{0\nu}_{1/2} > 1.57 \times 10^{25}$ yr [51], corresponding to $\langle m_{\beta\beta} \rangle < 280 - 550$ meV.

A new generation of HPGe experiments, namely GERDA and MAJORANA, are now building on the successes of the H-M and IGEX experiments:

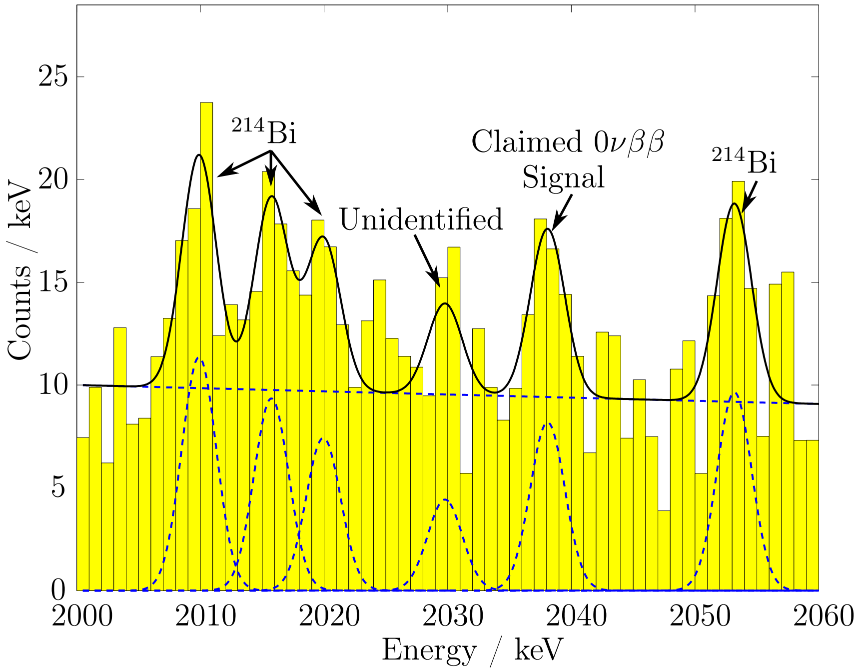

Figure 4.1.: Energy spectrum from the H-M experiment, from which a controversial claim of discovery of $0\nu\beta\beta$ has been made. Alongside the claimed $0\nu\beta\beta$ peak at 2309 keV, an unidentified peak at 2030 keV and four ^{214}Bi peaks can be seen [49].

- **GERDA** consists of a series of HPGe detectors immersed in a 64 m^3 cryostat filled with liquid argon (LAr). This LAr acts both as a coolant and as shielding from external backgrounds. This passive shielding is supplemented by 3 m of water shielding instrumented with PMTs to detect Cherenkov light from cosmic muons. The experiment is divided into two phases named GERDA-I and GERDA-II.

  GERDA-I used eight reprocessed HPGe detectors from H-M and IGEX, totalling 17.7 kg, along with 3.6 kg of new Broad Energy Ge (BEGe) detectors. Data-taking ran from Nov 2011 - May 2013, and no $0\nu\beta\beta$ signal has been observed (Figure 4.2). Despite the shorter running time, a much lower background means that a stronger limit can be set than that of H-M or IGEX. The resulting half-life of $T^{0\nu}_{1/2} > 2.1 \times 10^{25}$ yr corresponds to $\langle m_{\beta\beta}\rangle < 240 - 480$ meV [52].

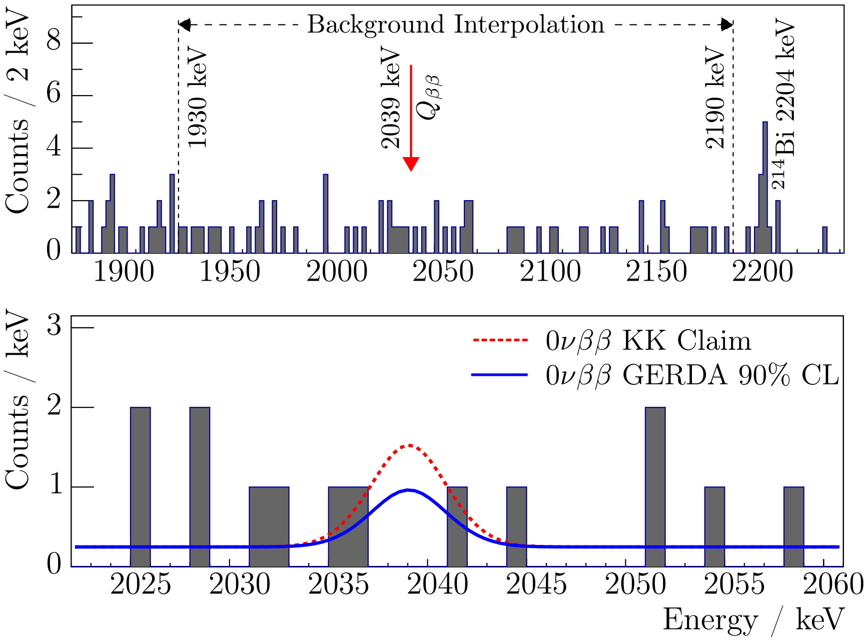

Figure 4.2.: The energy spectrum from GERDA-I with pulse-shape discrimination applied. The top panel shows the region used for background interpolation and the bottom shows the region around $Q_{\beta\beta}$. The $0\nu\beta\beta$ signals for the 90% CL from GERDA-I and the KK claim are also shown [52]

The next phase of the experiment, GERDA-II, involves the addition of a further 20 kg of enriched Germanium with an increase in sensitivity to reach the $50 - 100$ meV level [53].

- **MAJORANA** has kept a similar design to previous semiconductor experiments, but aims to surpass the sensitivity of IGEX and H-M by improving the radiopurity of detector materials, having more effective shielding and using pulse shape discrimination. Strings of enriched Ge with a total mass of 40 kg will be placed in electro-formed copper cryostats. If the desired background levels are achieved, a sensitivity of $80 - 160$ meV will be reached after 2.5 years of data-taking [54].

There are strong ties between the MAJORANA and GERDA collaborations, and depending on their findings, there is a possibility to merge the two projects to build an experiment in ^{76}Ge which could contain up to a tonne of isotope and have a sensitivity of $\langle m_{\beta\beta} \rangle \sim 10$ meV [55].

Whilst Germanium detectors are the most common detectors for spectroscopy and $0\nu\beta\beta$, other semiconductor technologies exist which can potentially provide competitive results.

- **COBRA** is an experiment that uses an array of CdZnTe (CZT) semiconductor crystals that have been enriched in ^{116}Cd. Its energy resolution is not as good as with HPGe experiments, but it possesses the advantage that it is operated at room temperature. Furthermore, by using a pixellated array, it is possible to track and identify particles which may greatly reduce the background level. The experiment is currently in an R&D phase and significant improvements must be made to the background level before the experiment is viable. If the background is sufficiently reduced, a 420 kg detector will be constructed with a target sensitivity of $50 - 70$ meV [56].

4.2.2. Scintillation Experiments

Scintillation experiments place the $0\nu\beta\beta$ candidate isotope inside a scintillating medium. When the isotope decays, the emitted particles excite the scintillator which then re-emits the absorbed energy as light. This light is usually detected by an array of photomultiplier tubes (PMTs). In general, scintillator is a good experimental material since is it relatively inexpensive and has a high degree of radiopurity.

Scintillation experiments can be divided into two main categories. One type of experiment is where the isotope is inherently part of the scintillator. The most successful experiments of this type, for example ELEGANT VI, have crystal scintillators containing ^{48}Ca.

- **ELEGANT VI** studied 23 CaF_2(Eu) crystal scintillators with a total mass of 6.6 kg and 7.6 g of ^{48}Ca. These crystals were completely surrounded by an active veto to reduce background. A total exposure of 0.015 kg yr produced a half-life limit of $T^{0\nu}_{1/2} > 5.8 \times 10^{22}$ yr or $\langle m_{\beta\beta} \rangle < 3.5 - 22$ eV [57].
- **CANDLES III** evolved from ELEGANT VI. 305 CaF_2 crystals are used that have a total mass of 305 kg and 300 g of ^{48}Ca. These crystals are surrounded by liquid scintillator which acts as active shielding and removes the need for doping of the crystals. The experiment is currently taking data and a sensitivity to $\langle m_{\beta\beta} \rangle$ of 0.5 eV is expected. If improvements in enrichment technology are realised, then the scale of the experiment will be increased by an order of magnitude to contain ~ 3 kg of ^{48}Ca and achieve a sensitivity of 50 meV [58].

An alternative technology is to use a large volume of liquid scintillator, into which a $0\nu\beta\beta$ isotope is dissolved. Experiments of this type commonly suffer from poor energy resolution. However, this is compensated by the ability to study relatively large masses of isotopes such as ^{136}Xe, ^{130}Te or ^{150}Nd without difficulty. Often, the large volume of scintillator comes with the added bonus that it provides a high level of self-shielding. The KamLAND-Zen experiment is studying liquid scintillator loaded with ^{136}Xe, whilst the SNO+ experiment has chosen ^{130}Te.

- **KamLAND-Zen** is an experiment that utilises the KamLAND detector, which was originally built to study neutrino oscillations. In KamLAND-Zen, 13 tonnes of xenon-loaded liquid scintillator is suspended in a nylon balloon at the centre of the KamLAND detector. This balloon is surrounded by 1000 tonnes of liquid scintillator which strongly suppresses backgrounds. The scintillation light is detected by 2000 PMTs and the whole assembly is surrounded by a 3200 tonne water-Cherenkov detector to veto cosmic-ray muons. The experiment contains 300 kg of ^{136}Xe and has achieved an exposure of 89.5 kg yr. From the resulting spectrum (Figure 4.3), it can be seen that there is a considerable background level in the region of $Q_{\beta\beta}$ (2.46 MeV). This background is thought to be caused by $^{110\mathrm{m}}$Ag either as a result of cosmogenic activation or the Fukushima nuclear disaster. Despite this unexpected background, KamLAND-Zen still provides the strongest single constraint on $\langle m_{\beta\beta} \rangle$, by measuring a half-life limit of $T^{0\nu}_{1/2} > 1.9 \times 10^{25}$ yr, corresponding to $\langle m_{\beta\beta} \rangle < 160 - 330$ meV [59]. Furthermore, due to its low background level, KamLAND-Zen can observe $2\nu\beta\beta$ across a wide energy range and provide strong constraints on Majoron emission decay modes [60].

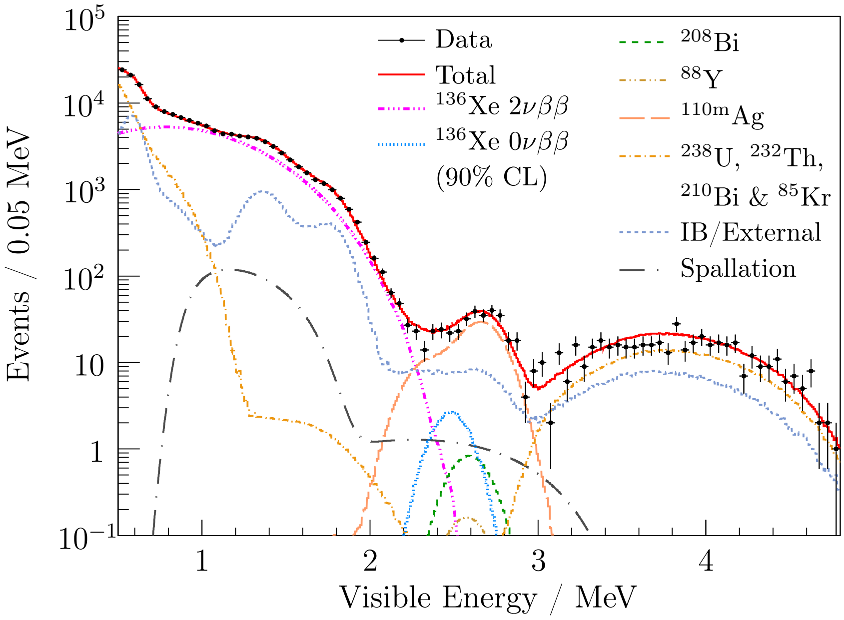

Figure 4.3.: Energy spectrum showing the first results from KamLAND-Zen. There is considerable background at $Q_{\beta\beta}$ (2.46 MeV) from ^{110m}Ag which has significantly reduced the sensitivity of the experiment [59].

Presently, a process of purification of the liquid scintillator is being undertaken to remove impurities such as ^{110m}Ag. In addition, a larger and more radiopure nylon balloon is being manufactured which will be able to hold 640 kg of ^{136}Xe. These improvements are expected to improve the sensitivity down to $\langle m_{\beta\beta} \rangle \sim 40$ meV.

In the near future, a new phase of the project, KamLAND2-Zen is anticipated. The KamLAND detector will be upgraded to improve light collection and the capacity will be enlarged to hold 1 tonne of ^{136}Xe. The final expected sensitivity is in the range of $\langle m_{\beta\beta} \rangle \sim 20$ meV [61].

- **SNO+** follows a similar principle to KamLAND-Zen, in that it will load $0\nu\beta\beta$ isotope into liquid scintillator and then use an existing neutrino detector, SNO. ^{130}Te will be dissolved in liquid scintillator contained in a 12 m diameter acrylic sphere. This acrylic sphere is shielded by a water bath and instrumented with 9500 PMTs. In an initial phase, tellurium will be loaded at 0.3%, giving 800 kg of ^{130}Te and a sensitivity of $\langle m_{\beta\beta}\rangle < 50 - 100$ meV. A second phase is then planned, with 3% loading and 8000 kg of ^{130}Te. This will allow SNO+ to reach the level of $\langle m_{\beta\beta}\rangle < 20 - 40$ meV [62].

4.2.3. Bolometer Experiments

Bolometer experiments measure small increases in temperature caused by the absorption of energy from radioactive decays. The increase in temperature of a material is inferred by changes in its electrical properties. At low temperatures, the heat capacity of material at temperature T is proportional to T^3. Therefore to measure a large temperature increase and improve the resolution of the bolometer, these detectors are typically operated at temperatures of 10 mK and below.

As a rule, bolometer experiments have good energy resolution. However, if only bolometry is used, as in the CUORICINO and CUORE experiments, particle identification is challenging. This can pose problems in reducing the background to the required levels.

- **CUORICINO** was a tower array of 62 TeO_2 crystals that operated between 2003 and 2008. The array was placed inside a dilution refrigerator to maintain cryogenic temperatures and surrounded by passive shielding. In total, 507 g of ^{130}Te was contained within the crystals and a total exposure of 19.75 kg yr was studied. A half-life limit of $T^{0\nu}_{1/2} > 2.8 \times 10^{24}$ yr was set, such that $\langle m_{\beta\beta}\rangle < 300 - 700$ meV [63].

- **CUORE** will build on the technology of CUORICINO, increasing the number of TeO_2 crystals to 988 and the mass of ^{130}Te to 204 kg. A prototype detector, CUORE-0, containing 52 crystals and 10.7 kg of ^{130}Te is currently taking data. This is re-using the cryostat from CUORICINO and consequently has a higher background than that anticipated for CUORE. The expected sensitivities for CUORE-0 and CUORE are $T^{0\nu}_{1/2} > 8 \times 10^{24}$ yr ($\langle m_{\beta\beta}\rangle < 180 - 420$ meV) and $T^{0\nu}_{1/2} > 2.1 \times 10^{26}$ yr ($\langle m_{\beta\beta}\rangle < 35 - 82$ meV) respectively [64].

In order to reduce the background level of bolometric experiments, it may be preferential to use a bolometric crystal that also acts as a scintillator. In this scenario, a small fraction of the energy deposited in the crystal is released as light which can be used to significantly reduce backgrounds from surface contamination.

- **LUCIFER** will use crystals of either ZnSe, $CdWO_4$ or $ZnMoO_4$ as scintillating bolometric crystals. The most sensitive proposed configuration is to use ZnSe crystals in an array of tens of bolometers contained within the same cryostat in a similar fashion to CUORE. In addition, an extra bolometer will act as a light detector for the scintillation light. The crystals will contain $\sim$ 18 kg of ^{82}Se and have a sensitivity of $\langle m_{\beta\beta} \rangle \sim 60$ meV [65].

4.2.4. Time Projection Chamber Experiments

Time projection chamber (TPC) experiments are able to track the path of an electron as it passes through a detector. This allows an experiment to search for two electrons from a common vertex, which greatly reduces background contributions. In a TPC, electrons ionise the detector medium and an electric field is applied to drift the ionisation electrons to a collection device. The level of ionisation is proportional to the energy deposited by an electron, so that the electron energy is also measured. As a result, the density of the detector medium is usually selected such that $0\nu\beta\beta$ events would be entirely contained.

Whilst it is possible to perform a $0\nu\beta\beta$ search using TPC technology alone, currently the most successful TPC experiments use a detector medium that is also a scintillator. These experiments therefore have a restricted choice of isotopes that may be used. The most promising scintillating-TPC experiments are EXO and NEXT which both search for $0\nu\beta\beta$ in ^{136}Xe, utilising the scintillating properties of xenon.

- **EXO-200** is a cylindrical homogeneous TPC that is filled with liquid xenon enriched to 80% in ^{136}Xe and observing a total mass of 80 kg. The TPC is symmetric about a cathode grid at its centre and at each end there are planes of wires and an array of avalanche photodiodes. The wires apply an electric field and read out ionisation signals and the photodiodes detect scintillation light. EXO-200 began taking data in 2011 and its initial results show that the target experimental parameters have been reached. No signal has been observed in an exposure of 32.5 kg yr (Figure 4.4), and a limit of $T^{0\nu}_{1/2} > 1.6 \times 10^{25}$ yr, corresponding to $\langle m_{\beta\beta} \rangle < 170 - 360$ meV, has been set [66].

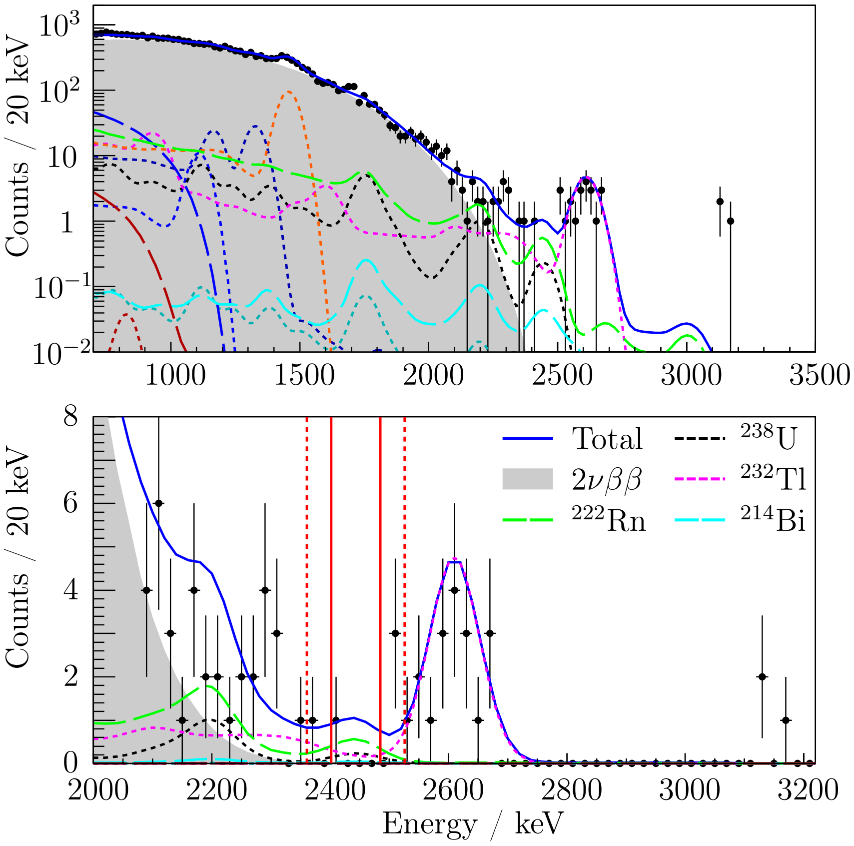

Figure 4.4.: Energy spectrum for single site events in EXO-200. The bottom panels shows the end-point region where the red solid (dotted) line shows the 1σ (2σ) region around $Q_{\beta\beta}$ [66].

EXO-200 will continue running and aims to achieve a final sensitivity of $T^{0\nu}_{1/2} > 6.4 \times 10^{25}$ yr ($\langle m_{\beta\beta} \rangle < 85 - 180$ meV), before being superseded by EXO [67]. The EXO experiment will attempt to scale similar technology to EXO-200 up to the tonne scale. In addition, a novel technique to tag the barium ions which are daughters of ^{136}Xe decay may significantly reduce the background level. The target sensitivity for EXO is $T^{0\nu}_{1/2} > 2 \times 10^{27}$ yr or $\langle m_{\beta\beta} \rangle < 15 - 32$ meV [67].

- **NEXT-100** follows similar ideas to EXO, using both scintillation and ionisation signals. However, it differs in the use of gaseous xenon at high pressure rather than liquid xenon. At one end of the TPC, an array of PMTs measures the energy resolution and at the other end the ionisation signal is converted into electroluminescent signals and read by silicon photomultipliers. This configuration allows energy resolution better than 1% whilst maintaining the ability to reconstruct electron tracks which greatly reduces background. The NEXT-100 detector is currently under construction and will contain 100 kg of gaseous xenon enriched to 91% in ^{136}Xe. After five years of running it has an anticipated sensitivity of $T^{0\nu}_{1/2} > 9 \times 10^{25}$ yr corresponding to $\langle m_{\beta\beta} \rangle < 70 - 150$ meV [68].

  One of the main strengths of the NEXT-100 concept is that it is readily scalable. If the experiment is successful, there is the possibility to enlarge it to contain a tonne of material and achieve sensitivities of $\langle m_{\beta\beta} \rangle < 15 - 32$ meV.

4.2.5. Tracker-Calorimeter Experiments

Tracker-calorimeter experiments combine tracking technology with an energy measurement by a separate calorimeter. Since the energy measurement is performed separately, the constraint of TPCs that require a high density tracking scintillator is removed and low density gases can be used. This minimises scattering of the emitted electrons which allows full reconstruction of the decay products and therefore greatly increases background rejection power. Tracker-calorimeter experiments therefore have amongst the lowest background rates of all $0\nu\beta\beta$ experiments across the entire energy spectrum, which makes them excellent detectors for both $2\nu\beta\beta$ and $0\nu\beta\beta$ measurements. The separation between source and detector also means that any $0\nu\beta\beta$ isotope can be studied. The most notable tracker-calorimeter experiments are the NEMO-3 and SuperNEMO experiments.

- **NEMO-3** operated from 2003 to 2011 and performed a $0\nu\beta\beta$ search in seven different $0\nu\beta\beta$ isotopes. The isotopes were housed in thin foils which were surrounded by a gas tracker containing a mix of helium, argon, alcohol and water. This was enclosed by a calorimeter made from plastic scintillator. NEMO-3 contained 6.9 kg of ^{100}Mo, which provides its strongest $0\nu\beta\beta$ limit of $\langle m_{\beta\beta} \rangle < 0.3 - 0.8$ eV for an exposure of 34.5 kg yr [69]. NEMO-3 is discussed at greater length in Chapter 5.
- **SuperNEMO** will build upon the successful NEMO-3 design, making improvements in radiopurity, calorimeter design and detection efficiency. 20 identical modules are envisaged that will contain up to 100 kg of ^{82}Se. The target sensitivity for SuperNEMO is $T^{0\nu}_{1/2} > 1.0 \times 10^{26}$ yr corresponding to $\langle m_{\beta\beta} \rangle < 50 - 100$ meV [70]. More information on SuperNEMO can be found in Chapter 9.

4.3. Double Beta Decay Measurements

4.3.1. $2\nu\beta\beta$ Measurements

Direct measurements of the $2\nu\beta\beta$ process have been made for nine isotopes. The most accurate values to date are presented in Table 4.2. $2\nu\beta\beta$ measurements are dominated by the NEMO-3 experiment, which has made the best measurement for seven of these nine isotopes. As described above, NEMO-3 has major advantages for measuring $2\nu\beta\beta$ since it has a very low background across the whole energy spectrum and can study any isotope. The remaining two isotopes of ^{76}Ge and ^{136}Xe have been recently remeasured by GERDA-I and EXO-200 respectively.

4.3.2. $0\nu\beta\beta$ Limits

In contrast to $2\nu\beta\beta$, a universally accepted observation of $0\nu\beta\beta$ has never been made. The most stringent present limits from individual experiments are listed in Table 4.3. The strongest bounds come from the measurements of ^{136}Xe by KamLAND-Zen and EXO-200 with the limits from ^{76}Ge experiments approaching the same level.

Isotope	Experiment	$T_{1/2}^{2\nu}$ / 10^{19} yr	Ref.
^{48}Ca	NEMO-3	$4.4\ ^{+0.5}_{-0.4} \pm 0.4$	[69]
^{76}Ge	GERDA-I	$184\ ^{+9}_{-8}\ ^{+11}_{-6}$	[71]
^{82}Se	NEMO-3	$9.93 \pm 0.14 \pm 0.72$	This Work
^{96}Zr	NEMO-3	$2.35 \pm 0.14 \pm 0.16$	[72]
^{100}Mo	NEMO-3	$0.711 \pm 0.002 \pm 0.054$	[73]
^{116}Cd	NEMO-3	$2.88 \pm 0.04 \pm 0.16$	[69]
^{130}Te	NEMO-3	$70 \pm 9 \pm 11$	[74]
^{136}Xe	EXO-200	$217.2 \pm 1.7 \pm 6.0$	[75]
^{150}Nd	NEMO-3	$0.911\ ^{+0.025}_{-0.022} \pm 0.063$	[76]

Table 4.2.: The most accurate measurements of the $2\nu\beta\beta$ half-life for nine isotopes where a direct observation has been made. The first error quoted is statistical and the second is systematic.

Isotope	Experiment	kg · yr	$T_{1/2}^{0\nu}$ Limit/yr	$\langle m_{\beta\beta}\rangle$/eV	Ref.
^{48}Ca	ELEGANT VI	0.015	5.8×10^{22}	$< 3.5 - 22$	[57]
^{76}Ge	H-M	35.5	1.9×10^{25}	$< 0.25 - 0.50$	[48]
^{76}Ge	IGEX	8.9	1.6×10^{25}	$< 0.28 - 0.55$	[51]
^{76}Ge	GERDA-I	16.4	2.1×10^{25}	$< 0.24 - 0.48$	[52]
^{82}Se	NEMO-3	4.90	2.2×10^{23}	$< 1.0 - 2.8$	This Work
^{96}Zr	NEMO-3	0.031	9.2×10^{21}	$< 7.2 - 19.5$	[72]
^{100}Mo	NEMO-3	34.5	1.0×10^{24}	$< 0.3 - 0.8$	[69]
^{116}Cd	Solotvina	0.14	1.7×10^{23}	$< 1.4 - 2.8$	[77]
^{130}Te	CUORICINO	19.75	2.8×10^{24}	$< 0.3 - 0.7$	[63]
^{136}Xe	EXO-200	32.5	1.6×10^{25}	$< 0.17 - 0.36$	[66]
^{136}Xe	KamLAND-Zen	89.5	1.9×10^{25}	$< 0.16 - 0.33$	[59]
^{150}Nd	NEMO-3	0.093	1.8×10^{22}	$< 4.0 - 6.3$	[76]

Table 4.3.: The best half-life limits from individual experiments for different $0\nu\beta\beta$ isotopes. The mass mechanism has been assumed to extract $\langle m_{\beta\beta}\rangle$. All limits are at the 90% CL.

It is common for independent experiments using the same isotope to combine results and produce a stronger half-life limit. This has been performed for ^{76}Ge by combining the latest energy spectrum from GERDA-I with those from H-M and IGEX, resulting in a limit of $T^{0\nu}_{1/2} > 3.0 \times 10^{25}$ yr or $\langle m_{\beta\beta} \rangle < 0.20 - 0.40$ eV [52]. A similar analysis using the data for ^{136}Xe from EXO-200 and KamLAND-Zen yields $T^{0\nu}_{1/2} > 3.4 \times 10^{25}$ yr or $\langle m_{\beta\beta} \rangle < 0.12 - 0.25$ eV [59].

As described in Section 4.2.1, the controversial KK claim is to have observed a $0\nu\beta\beta$ signal with $T^{0\nu}_{1/2} = 1.19^{+2.99}_{-0.50}(3\sigma) \times 10^{25}$ yr. This claim can be directly compared with the combined ^{76}Ge half-life limit shown above, irrespective of any NME uncertainties. It is clear that the combined result strongly disfavours the claim.

It is also possible to compare the KK claim with the ^{136}Xe results by considering different NME calculations. This comparison is shown graphically in Figure 4.5. The ^{136}Xe results also disfavour the claim and when these are combined with the ^{76}Ge results, the situation for the KK claim appears very grave indeed.

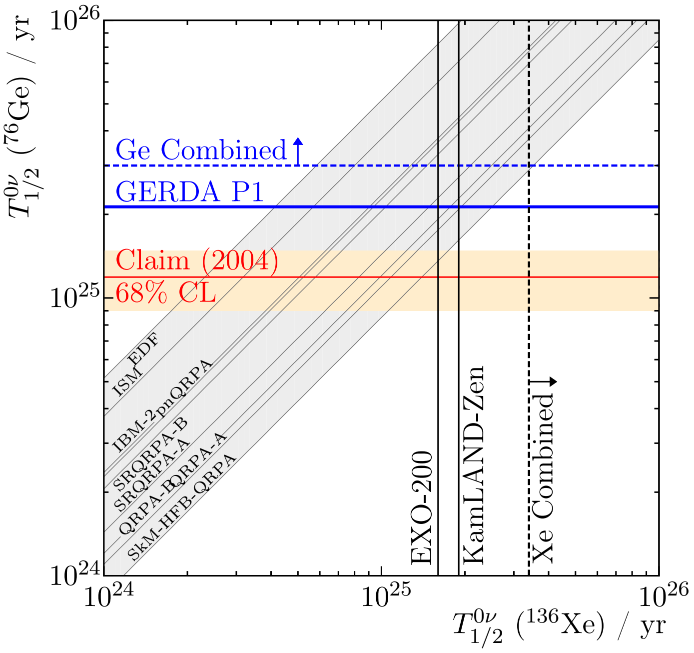

Figure 4.5.: Limits (90% CL) on $T^{0\nu}_{1/2}$ for ^{76}Ge from GERDA-I and ^{136}Xe from EXO-200 and KamLAND-Zen, compared with the KK signal claim. The grey shaded bands show the relations between ^{76}Ge and ^{136}Xe for a variety of different NME calculations [52].

4.3.3. Future Measurement Prospects

As the situation regarding the KK claim resolves, the outlook for $0\nu\beta\beta$ experiments moves from confirming or refuting this claim to further probing the $\langle m_{\beta\beta}\rangle$ parameter space. As discussed in the preceding sections, there are a wide variety of different types of experiments planned which are summarised in Table 4.4.

Experiment	Isotope	kg	Type	$\langle m_{\beta\beta}\rangle$/meV	Status	Ref.
GERDA-II	^{76}Ge	40	Semiconductor	50 – 100	Constr.	[53]
MAJORANA	^{76}Ge	40	Semiconductor	80 – 160	Constr.	[54]
CANDLES III	^{48}Ca	0.3	Scintillator	500	Running	[58]
KamLAND-Zen	^{136}Xe	640	Liquid Scint.	40 – 85	Constr.	[61]
SNO+ (0.3%)	^{130}Te	800	Liquid Scint.	50 – 100	Constr.	[62]
CUORE-0	^{130}Te	10.7	Bolometer	180 – 420	Running	[64]
EXO-200	^{136}Xe	80	Scint. TPC	85 – 180	Running	[67]
NEXT-100	^{136}Xe	90	Scint. TPC	70 – 150	Constr.	[68]
SuperNEMO	^{82}Se	100	Tracker-Calo	50 – 100	Constr.	[70]
1ton Ge	^{76}Ge	1000	Semiconductor	10	R&D	[55]
COBRA	^{116}Cd	420	Semiconductor	50 – 70	R&D	[56]
CANDLES	^{48}Ca	3	Scintillator	50	R&D	[58]
KamLAND2-Zen	^{136}Xe	1000	Liquid Scint.	20	R&D	[61]
SNO+ (3.0%)	^{130}Te	8000	Liquid Scint.	20 – 40	R&D	[62]
CUORE	^{130}Te	204	Bolometer	35 – 82	R&D	[64]
LUCIFER	^{82}Se	18	Scint. Bolom.	60	R&D	[65]
EXO	^{136}Xe	1000	Scint. TPC	15 – 32	R&D	[67]
NEXT	^{136}Xe	1000	Scint. TPC	15 – 32	R&D	[68]

Table 4.4.: Summary of future $0\nu\beta\beta$ experiments. The top panel shows experiments that are either running or under construction. The bottom panel contains experiments that have been proposed as successors to the current generation of experiments.

The experiments that are currently in construction or data-taking stages will be sensitive to $\langle m_{\beta\beta}\rangle \sim 75$ meV which approaches the top of the parameter space for the inverted hierarchy as shown in Figure 3.5. Many of these experiments are planning to scale to larger masses, where there are possibilities to reach the bottom of the inverted hierarchy parameter space at $\langle m_{\beta\beta} \rangle \sim 10$ meV. Therefore, if there is conclusive evidence from oscillation experiments that nature has chosen the inverted hierarchy, this generation of experiments will either discover or exclude the $0\nu\beta\beta$ process.

Part I.

$\beta\beta$-decay of ^{82}Se with NEMO-3

Chapter 5.

NEMO-3 Detector

NEMO-3 was a double beta decay experiment that searched for $0\nu\beta\beta$ in seven different isotopes. The experiment ran from February 2003 to January 2011, and in this time measured $2\nu\beta\beta$ in all seven isotopes. The strongest limit produced for $0\nu\beta\beta$ comes from ^{100}Mo, with a measurement of $T^{0\nu}_{1/2} > 1.0 \times 10^{24}$ yr corresponding to $\langle m_{\beta\beta} \rangle < 0.3 - 0.8$ eV [69].

The detector, shown in Figure 5.1, was cylindrical in design with a diameter of 5 m and a height of 3 m. It was composed of 20 identical segments, referred to as sectors, surrounding a hollow central column as depicted schematically in Figure 5.2. At the centre of each sector were thin vertical strips of either $0\nu\beta\beta$ isotope or copper, the latter of which were used for background measurements. These source foils, described in Section 5.1, contained a total mass of 10 kg.

The principle behind the experiment was the direct detection of two electrons from the source material. In order to facilitate this, the foils were surrounded by a gas tracker consisting of 6180 drift cells operating in Geiger mode (Section 5.2) onto which a magnetic field of 2.5 mT was applied (Section 5.6.1). The tracking volume was enclosed by the calorimeter walls which were composed of 1940 individual optical modules made of plastic scintillator blocks coupled to low-radioactivity PMTs (Section 5.3). The whole detector was then surrounded by passive shielding from iron, paraffin, borated water and wood.

The experiment was based in the Laboratoire Souterrain de Modane (LSM) on the French-Italian border. This underground laboratory is adjacent to a road tunnel travelling beneath Mount Fréjus. The mountain provides an overburden of 1200 m of rock (4800 m water-equivalent) which shielded the experiment from cosmic rays.

The main features of the detector are described in this chapter, which has been written with reference to the NEMO-3 technical design report [78].

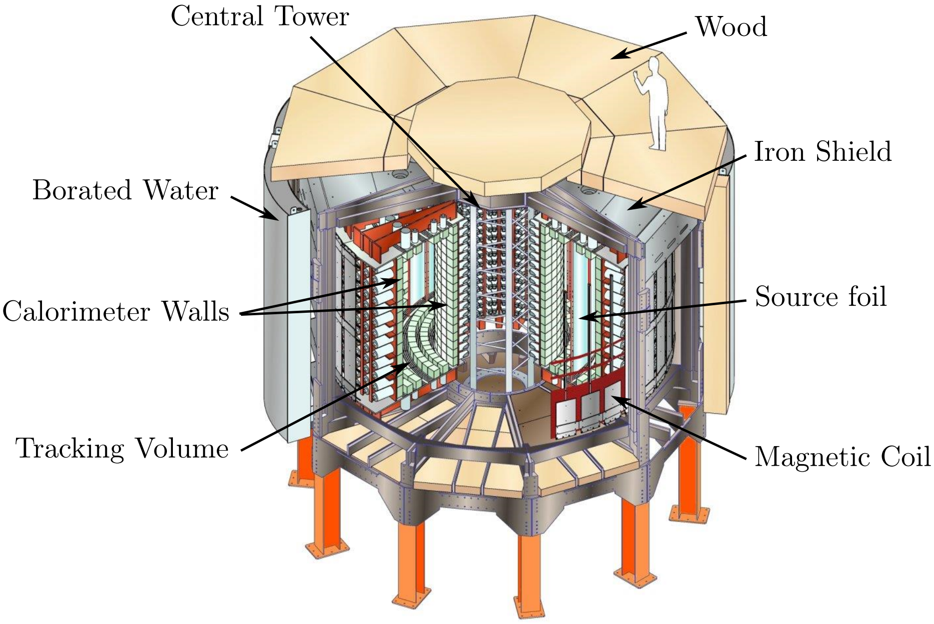

Figure 5.1.: Cut-away view of NEMO-3, showing the orientation of key aspects of the detector.

5.1. Source Foils

In the design of NEMO-3, the separation of source isotope and detector properties meant that any $0\nu\beta\beta$ isotope could be studied, subject to the selection criteria discussed in Section 4.1.1. There were 8.8 kg of enriched $0\nu\beta\beta$ isotopes in NEMO-3, with the majority of this mass composed of 6.91 kg of ^{100}Mo and 0.93 kg of ^{82}Se. The remaining source mass was made up of smaller quantities of isotopes that were included to study the $2\nu\beta\beta$ process, including ^{130}Te, ^{116}Cd, ^{150}Nd, ^{96}Zr and ^{48}Ca. Finally, alongside the enriched isotopes, there were 1.2 kg of source foils of high-levels of radiopurity, which were used to study detector backgrounds. These foils were made from ultra-pure copper and a separate sample of a very pure $^{\text{nat}}$Te compound. The

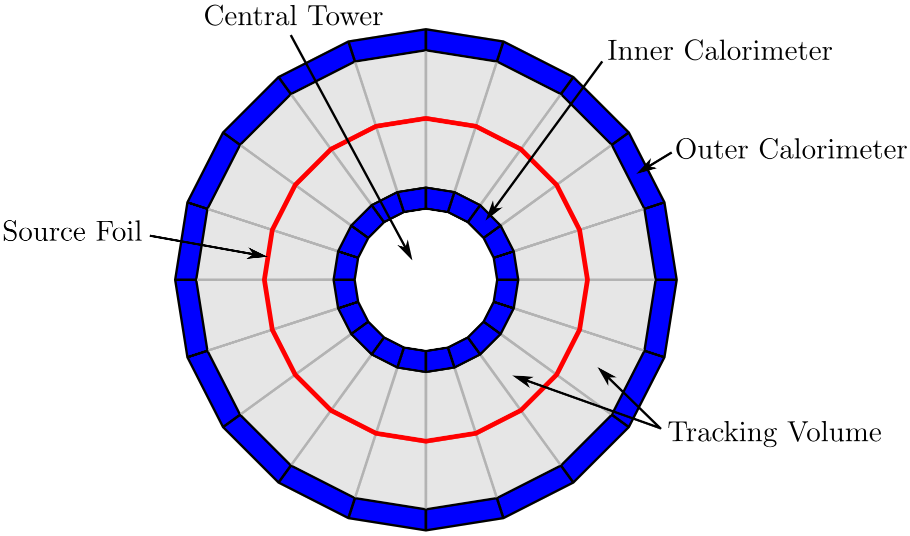

Figure 5.2.: Section across the diameter of NEMO-3, showing the decomposition into 20 identical sectors, each containing source foil, tracker and calorimeter.

${}^{\mathrm{nat}}$Te foils also allowed for a $2\nu\beta\beta$ measurement due to the high natural abundance of ^{130}Te.

Each sector contained a source frame that held seven strips of source material with a mean length of 2480 mm and widths of 65 mm for the five strips in the centre of the sector and 63 mm for the outer two strips. The distribution of the isotopes amongst the sectors is shown in Figure 5.3.

The thickness of the foil was a compromise between containing as much source isotope as possible and maintaining a good energy resolution, which is degraded by scattering in thicker foils. The optimal surface density of the foils was found to be in the range 30 – 60 mg/cm^2. There were two distinct types of foil in NEMO-3, metallic and composite foils. The cadmium, copper and 34% of the molybdenum foils were metallic and had a density of $\sim$ 10 g/cm^3 such that a thickness lower than 60 µm, or 0.5% of an interaction length, was required.

The remaining foils were all composite foils, consisting of a mixture of source powder and organic glue. Their lower density of $\sim$ 2 g/cm^3 allowed for a thickness up to 300 µm. To provide structural rigidity in the composite foils, the mixture of source powder and PVA glue was sandwiched between two thin layers of Mylar. These Mylar sheets were irradiated with a ^{84}Kr ion beam to create a large number of microscopic holes which ensured a good bond with the glue.

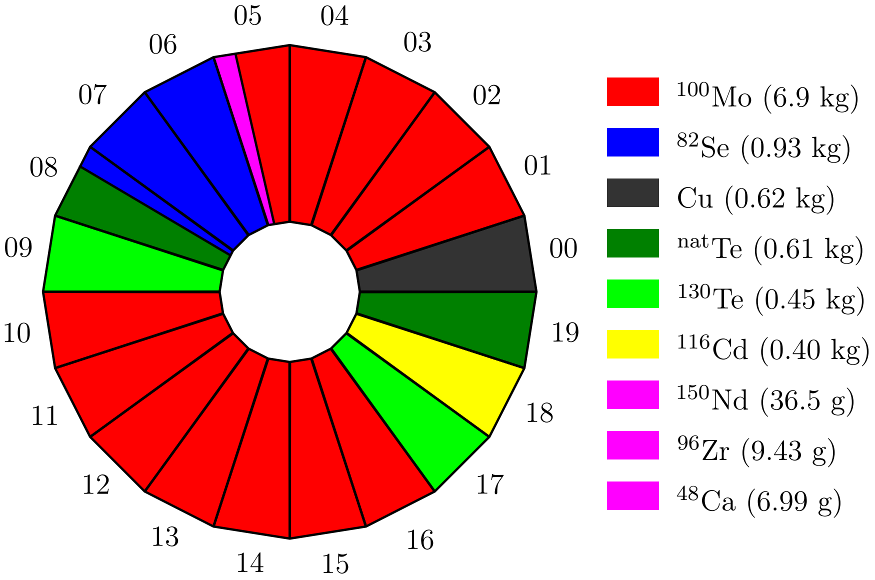

Figure 5.3.: Distribution of source isotopes across the 20 sectors of NEMO-3.

5.1.1. ^{82}Se Source Foils

The ^{82}Se foils, which are analysed in this thesis, are of the composite foil type. The natural abundance of ^{82}Se is 9.2%, so enrichment to higher fractions of ^{82}Se was desired. The enrichment process involved the production of SeF_6 gas from natural selenium. This gas was then centrifuged to isolate the heavier compound of $^{82}SeF_6$. Finally, an electrical discharge in the gas was used to dissociate the SeF_6 molecules and obtain the enriched powder. Due to time constraints, no further purification of the samples was undertaken.

Two different production runs were performed, attaining enrichment factors of $97.02 \pm 0.05\%$ for run 1 and $96.82 \pm 0.05\%$ for run 2. ^{82}Se from run 1 was used in the NEMO-2 prototype experiment, before being recovered to be used in NEMO-3. This sample is therefore known as SeOld, whilst that from run 2 which was produced specifically for NEMO-3 is known as SeNew. The SeOld foils were located in sector 6 of NEMO-3, and SeNew in sector 7. The first two strips of sector 8 mostly contain SeOld with a small strip of SeNew as shown in Figure 5.4.

The Mylar backing film for sectors 6 and 7 was 23 µm thick, whilst the strips in sector 8 were supported by a Mylar of thickness 18 µm. The total mass of both types

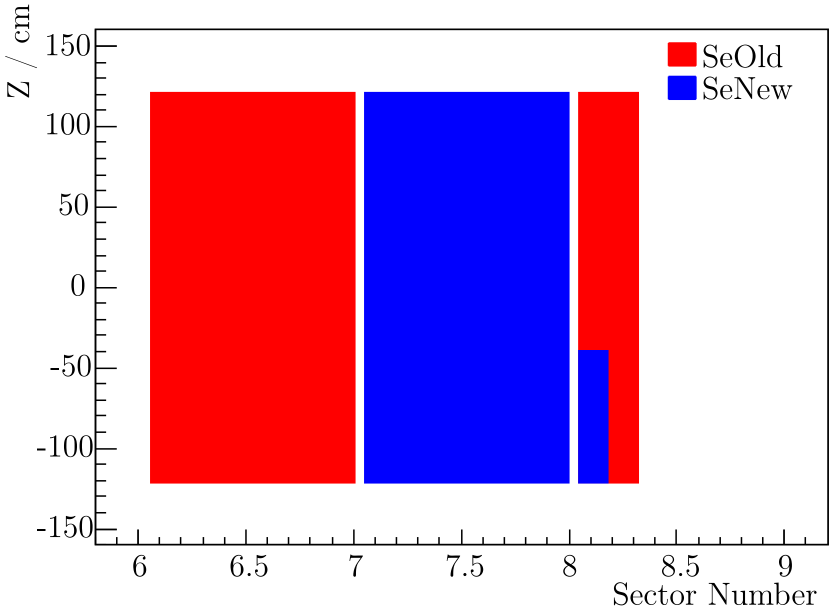

Figure 5.4.: Location of SeOld and SeNew source foils inside NEMO-3.

of source foil was 1127.1 g, which contained 932.4 ± 5.0 g of ^{82}Se. Further information on the masses of the foils for both selenium samples is presented in Table 5.1.

Sample	η / %	Foil / g	Se / g	^{82}Se / g
SeOld	97.02 ± 0.05	518.5	438.1	425.1
SeNew	96.82 ± 0.05	608.6	523.9	507.3
Total		1127.1	962.0	932.4

Table 5.1.: Summary of enrichment factors and masses contained in the selenium source foils of each sample type.

The design target for the NEMO-3 foils was that the dominant background to a $0\nu\beta\beta$ search should be from the $2\nu\beta\beta$ tail, which leads to constraints on the intrinsic radioactivity of these foils. The most important naturally occurring background isotopes to $0\nu\beta\beta$ are ^{214}Bi and ^{208}Tl due to their high Q_β values. The resulting activity targets for these isotopes in the selenium foils were:

$$A(^{214}\text{Bi}) < 0.7 \text{ mBq/kg} \tag{5.1}$$

$$A(^{208}\mathrm{Tl}) < 0.05\ \mathrm{mBq/kg} \tag{5.2}$$

Before being installed in the detector, the source foils were measured using a HPGe detector. Due to time constraints, only a mixture of the two samples was measured, with equal numbers of SeOld and SeNew strips. The results of this measurement are shown in Table 5.2.

The activities of ^{214}Bi and ^{208}Tl were found to be above the target levels. Despite this, it was decided that the foils should be included in the detector without purification. This was mainly due to time pressure since the ^{100}Mo foils, which were the largest part of the experiment, had achieved their target activities. At that time there was no proven purification technique available for ^{82}Se, so there would have been significant delays to the entire experiment if the selenium foils had been purified. In addition, the measured activities were close to the target levels and it was thought that the isotopes may have been concentrated in small areas of the foils that could be removed during analysis.

In addition to the small activities of ^{214}Bi and ^{208}Tl, there was significant contamination in the source foils from ^{40}K which can be a background to a $2\nu\beta\beta$ measurement, but should not adversely affect a $0\nu\beta\beta$ search. The measured value of ^{235}U was also relatively high, but no ^{227}Ac was observed so the decay chain was broken and ^{207}Tl and ^{211}Pb are not expected as backgrounds to a $2\nu\beta\beta$ measurement.

Mass / g	Exposure / hr	Sample Activity / mBq/kg					
				^{238}U chain		^{232}Th chain	
		^{40}K	^{235}U	^{234}Th	^{214}Bi	^{228}Ac	^{208}Tl
800	628	55 ± 5	20.0 ± 0.7	< 18	1.2 ± 0.5	< 1	0.4 ± 0.1

Table 5.2.: Radioactivity measurements of a mixture of equal numbers of SeOld and SeNew foil strips, made with HPGe before installation into NEMO-3. Error bars are statistical uncertainties at 1σ, whilst limits are at the 2σ level.

5.2. Tracker

The NEMO-3 tracker provided three-dimensional tracking of charged particles and was integral to the ability of the detector to fully reconstruct events. It consisted of 6180 vertical drift cells operating in Geiger mode. Each cell had an octagonal cross-section, with a central anode surrounded by eight cathode wires, as shown in the enlarged section of Figure 5.5. An elementary cell is 3 cm in diameter and 2.7 m long, with all wires made of stainless steel with a diameter of 50 µm. A copper cathode ring was positioned at either end of the cell to collect signals from plasma propagation. An extra ground wire was added between adjacent layers of the tracker to reduce electrostatic cross-talk. Cathode wires are shared between adjacent cells, which minimises the amount of material inside the tracking chamber. This has advantages from a radiopurity perspective and also reduces the amount of scattering inside the tracker.

The cells are divided into nine different layers which are configured in a group of four layers closest to the source foils, then two layers in the middle of the tracking volume and finally three layers closest to the calorimeter wall as shown in Figure 5.5. This 4-2-3 layout gave better the tracking resolution at the foil and scintillator walls, whilst allowing for calorimeter blocks in the spaces between the tracking layers. These extra calorimeter blocks significantly increased the coverage of the detector.

The drift cells were operated in a gas mixture consisting of 95% helium, 4% ethanol and 1% argon held at 10 mbar above atmospheric pressure. Helium was used as the basis of the tracking gas, since its low atomic number, Z, minimises multiple scattering of electrons. As a result, a typical electron only lost $\sim$ 30 keV when traversing the tracker. The ethanol was included in the mix to quench the photoionisation process by absorbing UV photons. This improved the performance of the detector by reducing the re-firing effect of one cell to another. The final component of the gas mixture was argon, which has a lower ionisation potential than helium and thus made the plasma propagation more stable. Additionally, in the final years of the detector, a small quantity of water vapour was introduced with the aim of rejuvenating some of the ageing cells.

As implied above, the tracker functioned via the principle of ionisation. As a charged particle passed through the gas mixture, an ionisation of $\sim$ 6 electrons/cm was produced. These electrons were accelerated towards an anode wire by an electric field, with an operating potential difference of ∼ 1600 V between anode and cathode wires. In Geiger mode, the cells had a rise time of ∼ 10 ns and could therefore provide accurate timing information. The time taken to produce an anode signal gave information on the radial distance of the track from the anode wire. As the ionisation electrons approached the anode, an avalanche was initiated which caused a Geiger plasma to propagate along the length of the wire at speeds of ∼ 6 − 7 cm/μs. This plasma propagation was detected by the cathode rings at the end of each cell and the timing information could be used to measure the vertical position of the cell firing.

In this operating mode, the average hit resolution of a cell was ∼ 0.5 mm in the transverse plane and ∼ 0.8 cm in the vertical direction.

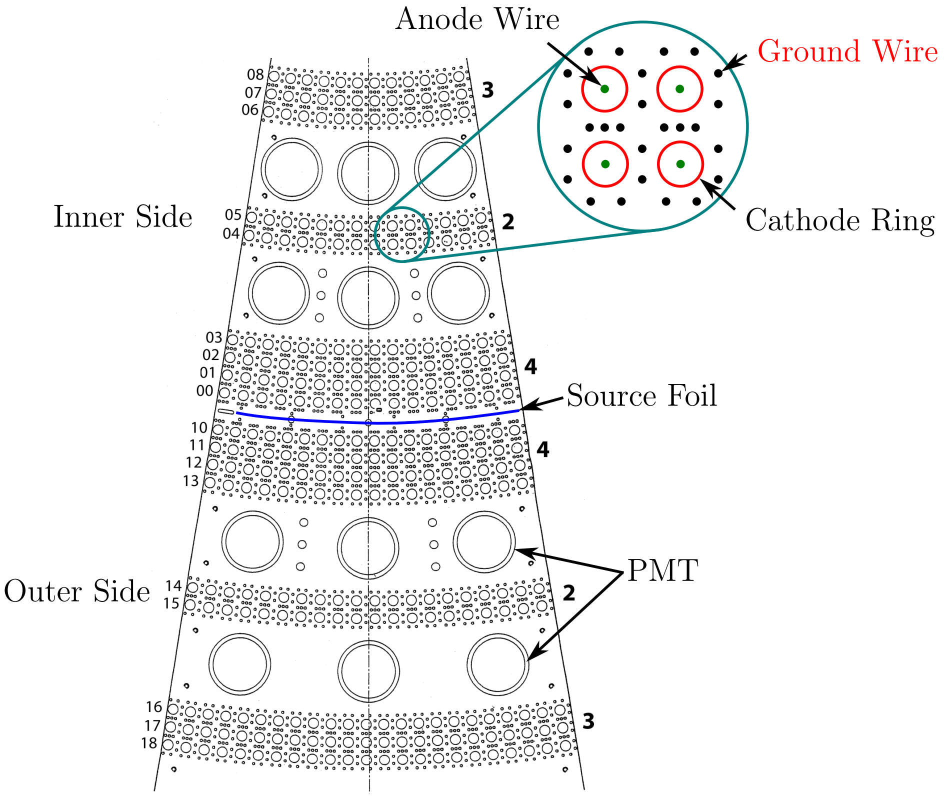

Figure 5.5.: Plan view of one sector of NEMO-3, showing the layout of tracker cells with an enlarged view of four individual drift cells.

5.3. Calorimeter

The NEMO-3 calorimeter's main function was to measure the energy of incident particles, but it also provided pivotal information on the arrival time of these particles and acted as a primary trigger. The calorimeter was modular in design, consisting of 1940 separate optical modules. Each module consisted of a scintillator block, two light guides and either a 3″ or 5″ PMT depending on its position in the detector (Figure 5.6).

The scintillator blocks were 10 cm thick, which was chosen to balance resolution against the photon detection efficiency, achieving a 50% probability of detecting a 0.5 MeV photon. 1460 optical modules covered the inner and outer walls of the detector, with the scintillator front faces approximately 15×15 cm^2 and 20×20 cm^2, respectively. The remaining 480 optical modules were positioned on the top and bottom sides of the detector, known as petals, and these modules are therefore referred to as petal scintillators.

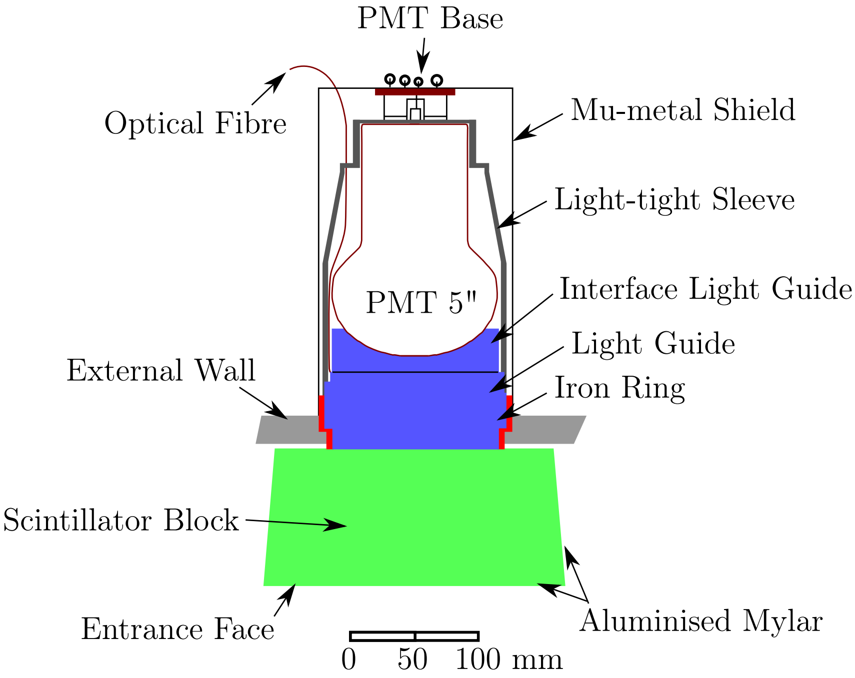

Figure 5.6.: Schematic of a NEMO-3 calorimeter module showing the configuration of scintillator block, light guides, 5″ PMT and mu-metal shield.

The scintillator blocks were made of polystyrene (PST) doped with a scintillation agent, p-Terphenyl (p-TP), and a wavelength shifter, 1,4-bis(5-phenyloxazol-2-yl) benzene (POPOP). The PST was chosen as the scintillator material due to its low Z value compared with mineral scintillators, which reduced back-scattering of low energy electrons, as well as for its improved radiopurity. Scintillators in the walls and petals varied slightly in their composition, with wall scintillators composed of 98.49% PST, 1.5% p-TP and 0.01% POPOP, whilst petal scintillators contained 98.75% PST, 1.2% p-TP and 0.05% POPOP. The four lateral sides of each scintillator block were wrapped with 350 µm of polytetrafluoroethylene (PTFE) which provided diffusive reflection of the scintillation light to increase overall collection. Finally, the blocks were covered with a 12 µm layer of aluminised Mylar which further increased light collection and protected the scintillators from UV photons produced in the tracker.

In order to separate the PMTs from the tracking volume where they would have been damaged by continued contact with helium, light guides made from poly(methyl methacrylate) (PMMA) were used. The PMTs employed in NEMO-3 were manufactured by Hamamatsu, supplied as 3″ (R6091) and 5″ (R6594) types. They were specially designed for the experiment, having low-radioactivity glass, fast rise-time and good linearity over a wide energy range. The 3″ PMTs, which were used on the inner wall and first three petal layers, had 12 dynodes and a flat photo-cathode. The 5″ PMTs, which were used for the remaining optical modules, had 10 dynodes and a hemispherical bulb which gave greater structural support. However, this shape required a secondary light-guide to couple to the scintillator block. All PMTs were then surrounded by a mu-metal shield that reduced the flux from the experiment's magnetic field.

Each of the optical modules was regularly characterised with respect to properties such as resolution, gain, dark noise, and linearity (Section 5.5). The optical modules began to exhibit non-linear behaviour above ~ 4 MeV, which is above $Q_{\beta\beta}$ for the sources used in NEMO-3. The energy resolution of the calorimeter modules ranged from $14 - 17\%$ (FWHM) at 1 MeV and their timing resolution was 250 ps (1σ) at 1 MeV.

5.4. Electronics, DAQ and Trigger

NEMO-3 had independent tracker and calorimeter electronics systems, which gave a high degree of flexibility for operating in different configurations. Individual or interdependent triggering and data readout systems were possible, which allowed for special triggering for calibration runs and specific studies of different elements of detector performance.

5.4.1. Calorimeter Electronics

The high voltage (HV) required to operate the 1940 PMTs of the calorimeter, typically 1800 V and 1350 V for 3″ and 5″ PMTs respectively, was supplied by three CAEN power supplies each of which was capable of supplying 240 HV channels. These 720 HV channels were transferred to the detector via 180 distribution boards (nine per sector). Each board had four HV inputs which were split into 12 outputs, such that each HV channel was shared by three PMTs. The outputs from the shared HV channel were then fine-tuned by selecting fixed resistors to act as a potential divider. The resistor values where chosen based on data from a ^{207}Bi source.

NEMO-3 had 97 optical modules per sector which were divided by the source foil into 46 modules on the inner side and 51 modules on the outer side. Each of these 40 half-sectors had a mother board supporting a daughter board for each PMT channel, which performed signal processing. Each daughter board had a low and high threshold leading edge discriminator. When the low threshold was exceeded, corresponding to 7 mV or 23 keV, a TDC (time-to-digital-converter) counter was started and a charge integration window of 80 ns was opened. If the high threshold of 48 mV or 150 keV was breached, the daughter board passed a signal to the mother board which, in turn, passed the number of fired PMTs to the trigger system.

If the desired multiplicity of PMT signals was reached, which for normal data acquisition was only one PMT, the integrated charge was digitised in preparation for storage of the data. The analog-to-digital conversions were performed with two 12-bit ADCs, allowing an energy resolution of 0.36 pC/channel ($\sim$ 3 keV/channel up to $\sim$ 12 MeV) and a timing resolution of 53 ps/channel.

5.4.2. Tracker Electronics

Two CAEN power supplies, each with 16 HV channels, were used to supply HV to the anode wires of the NEMO-3 tracker, usually at the level of $1620 - 1650$ V. There were

18 concentric layers of cells that made up the tracker and due to electrostatic effects, each layer required a slightly different voltage to those adjacent. For this reason, the inner-most nine layers were each supplied with a HV channel, and the outer-most nine each with two. Every sector was supplied with eight distribution boards which were used for fine control of the HV and contained a total of 15 daughter boards each with eight channels. These 15 daughter boards were assigned equally to anode, upper cathode and lower cathode signals.

In addition to the HV supply boards, eight data acquisition boards were provided per sector which contained 20 application specific integrated circuits (ASICs). These ASICs were programmed to first amplify and then discriminate signals above threshold before performing timing measurements for the anode and top and bottom cathode rings.

In a typical $2\nu\beta\beta$ event, a trigger from the calorimeter started the anode wire TDC counter. A signal from the anode wire stopped this timing measurement, allowing a radial measurement of the ionisation point. The anode signal also started the TDC counters for the top and bottom cathode rings, so that when a signal arrived at these rings, a measurement of the plasma propagation time was made. This measurement allowed the extraction of the vertical position of the ionisation point.

An important addition to the tracker was the ability to wait up to 710 µs after an initial trigger to search for delayed firings of the tracker cells. As previously discussed, ^{214}Bi from ^{222}Rn can be a problematic background to a $0\nu\beta\beta$ search. However, the immediate daughter isotope of ^{214}Bi, ^{214}Po, decays via α-decay with a half-life of 164.3 µs. This α particle may create a short, straight track in the tracker after the prompt electron track, leaving a distinct signature for these so-called BiPo events. Therefore, these delayed hits are very important in measuring the level of ^{214}Bi inside NEMO-3 and in vetoing such BiPo events. This technique is discussed in greater detail in Section 6.3.3.

5.4.3. Trigger System

The NEMO-3 trigger system has three separate levels known as T1, T2 and T3.

The first level trigger, T1, is based on information from the calorimeter. Specifically, it requires that a given number of PMTs have registered an energy above 150 keV.

For the normal acquisition mode, only one PMT is required, but for some calibration runs a higher number of PMTs may be required. For example, during ^{60}Co source runs, two PMTs above 150 keV are required (Section 5.5.1).

The second level trigger, T2, is applied based on information supplied by the tracker. To pass this trigger, there must be a hit in at least three out of the nine layers on one side of the foil, in the same or adjacent sectors. Further, at least two of these hits must be in the same group of layers in the $4-2-3$ configuration (i.e. layers 0 - 3, 4 - 5 or 6 - 8).

The third level trigger, T3, is only used during calibration runs. It combines information from T2 with information from the calorimeter to select events that are likely to have originated from radioactive sources placed in specific detector locations.

The trigger rate during normal data acquisition was 7.4 ± 0.1 Hz before the installation of the anti-radon facility (Section 5.7), reducing to 5.7 ± 0.1 Hz afterwards. This rate is dominated by events from radon and external radioactivity and has an associated detector dead time of $\sim 1\%$ of total running time. During calibration runs, where there are radioactive sources in the detector, the trigger rate increased to ~ 250 Hz with a dead time of $\sim 5\%$.

5.5. Energy and Time Calibration

In order to calibrate NEMO-3 with respect to absolute energy and time measurements, a procedure of dedicated calibration runs with radioactive sources was developed (Section 5.5.1). These calibration runs required ~ 24 hrs of data-taking and so only took place every ~ 40 days. To monitor the stability of the detector in between these runs, twice daily laser surveys were undertaken as described in Section 5.5.2.

5.5.1. Radioactive Sources

Every sector of NEMO-3 was equipped with a copper calibration tube, located at the same radius as the source foils, such that it ran vertically along the edge of a source strip. Each flattened tube had three pairs of kapton windows of thickness 25 µm and surface area ~ 500 mm^2, which faced towards the inner and outer calorimeter walls.

The size of the windows and their vertical positions ($z = 0, \pm 90$ cm) were chosen to maximise the illumination uniformity of the scintillator blocks when using three radioactive sources. Sources were introduced into the detector via a long delrin rod which could simultaneously contain three sources.

Absolute energy calibrations of the PMTs were carried out every ~ 40 days using ^{207}Bi sources, which provided 482 keV and 976 keV conversion electrons with branching ratios of 1.5% and 7.0%, respectively. In addition, a calibration run at the beginning of NEMO-3 was performed using a ^{90}Sr source, whereby the end-point of the β-decay spectrum of its daughter, ^{90}Y, provided a higher energy calibration point at 2.28 MeV.

Whilst every energy calibration provided important information on the stability of the detector, it was also possible to study the linearity of the NEMO-3 detector over its entire lifetime by using all ^{207}Bi calibrations from seven years of data-taking. This allowed the observation of the very rare 1682 keV conversion electron, with a branching ratio of 0.02%, and confirmed the energy linearity of the detector up to 1.7 MeV.

Furthermore, by combining multiple ^{207}Bi runs, it was also possible to correlate the impact point of 1 MeV electrons on the scintillator block with the energy response of the optical module. This effect was first observed with an electron spectrometer during assembly of the optical modules and may be as large as 10% for the 5″ PMTs. However, using these calibration measurements, it is possible to apply corrections to the energy response based on the impact point with the scintillator, which has been shown to improve detector response.

For timing calibration of the calorimeter, ^{60}Co sources were used. This isotope emits two coincident γ-rays with energies of 1173 keV and 1332 keV. The difference between arrival times at each of the 1940 channels can be used to calculate and calibrate the relative time shifts between each channel. Since tracking is not required for this calibration, relatively intense sources could be used.

5.5.2. Laser Survey

To provide a more frequent measure of the stability of the calorimeter, a twice-daily laser survey was undertaken. A N_2 laser with wavelength 337 ± 15 nm was passed through a series of attenuators and optical filters to allow control of its output. This light was then passed to a small sphere of scintillator wrapped in Teflon and aluminium to mimic an electron signal. This replica signal was transmitted via optical fibres to six reference PMTs fitted with ^{207}Bi sources and also to the PMTs of the calorimeter.

By interpolating from the results of two absolute energy comparisons and comparing with the output of the reference PMTs, it was possible to predict the expected response of the PMT to the incident laser survey. PMTs that were found to exhibit unexpected or unstable behaviour are excluded from analysis for the whole survey period. It has been found that there is no instability for 82% of the optical module exposure, with a further 7% showing only one deviation within a given period, which may be attributed to laser system instability.

5.6. Magnetic Coil and Passive Shielding

5.6.1. Magnetic Coil

To aid in particle identification inside the tracker, a solenoid coil was placed around the detector producing a magnetic field of 2.5 mT parallel to the drift cells. The coil has a diameter of 5.3 m, a height of 2.7 m and a mass of 5 tonnes. The field was generated by passing $\sim$ 30A of current through the coil and allows charge identification using the curvature of tracks. It was a very effective tool, allowing rejection of 95% of e^+e^- pairs at 1 MeV.

5.6.2. Mount Fréjus

As previously described, NEMO-3 was located in the LSM which has an overburden of 1200 m of rock or 4800 m water-equivalent, which greatly reduces the cosmic muon flux. Measurements inside the LSM have shown the cosmic muon flux to be 5×10^{-5} m^{-2}s^{-1} which is a reduction by a factor of one million from that at sea level.

5.6.3. Iron Shield

177 tonnes of iron, selected for its radiopurity, was used to provide 20 cm of shielding covering the whole detector. Its primary function was to suppress the γ-ray flux caused by radioactive decays in the surrounding rock and neutron capture. As a secondary advantage, it also acted as a flux return for the magnetic coil.

5.6.4. Neutron Shielding

Spontaneous fission of naturally-occurring uranium and thorium in the rock surrounding the experiment produced both fast and thermal neutrons, which could be captured by the detector materials, causing the emission of high energy photons. In order to reduce this background, a dedicated shield was constructed that suppressed the neutron flux inside the detector.

This shield was composed of three parts and placed outside the iron shield. The first was 20 cm of paraffin positioned below the central tower (not shown in Figure 5.1). Secondly, 35 cm of borated water was placed in tanks attached to the cylindrical exterior of the detector. Finally, 28 cm of wood was used between the borated water tanks and above and below the detector end caps.

Incident fast neutrons were moderated to lower energies by the paraffin, wood or water and then captured on boron or in the iron shield. Any photons emitted in the neutron capture reaction were shielded from the detector by the iron shield.

5.7. Anti-radon facility

After one year of data-taking, it was discovered that the radon level inside NEMO-3 was considerably higher than that expected from contamination of input gases or emanation from detector components. It was postulated that radon could be diffusing into the detector from the surrounding air. In order to suppress this process, a polyethylene tent was installed around NEMO-3 with the intention of filling this with radon-free air.

To create air with a low-level of radon, a radon trapping facility was installed at the LSM. This facility cools compressed air from the laboratory to −50°C where it is passed through two adsorption columns. Each of these columns has an internal diameter of 0.6 m and a height of 3 m and contains 500 kg of activated charcoal cooled to the same temperature. This vast amount of cooled charcoal has an enormous surface area and any radon passing through is adsorbed. Once trapped, this radon decays inside the columns before it has time to pass through. The anti-radon facility takes air from the LSM at a rate of 150 m^3/hr and an activity of 15 Bq/m^3 and produces an output with an activity of 18 mBq/m^3, achieving a reduction of three orders of magnitude.

After installation of the anti-radon facility, the level of radon inside NEMO-3 decreased from 37.7 ± 0.1 mBq/m^3 to 6.46 ± 0.05 mBq/m^3 [79]. This reduction factor was much lower than that from the anti-radon facility, which has not been fully explained. The two strongest hypotheses are that there is a higher radon level inside the anti-radon tent than at the facility output so the tent reduction factor is not as large as 1000, or a significant level of radon maybe be emanating from detector components.

There were clearly different detector conditions before and after the installation of the anti-radon facility in which there were different background levels. Accordingly, NEMO-3 data are split into two phases separated by the installation of the anti-radon facility. Phase 1 incorporates data from the beginning of the experiment in February 2003 to September 2004. Phase 2 encompasses data from October 2004 to January 2011.

Chapter 6.

General Analysis Techniques

The general principle behind a NEMO-3 analysis is the comparison of experimental data with those generated using a Monte Carlo simulation of physics processes and the detector response (Sections 6.1 and 6.2). The NEMO-3 detector provides a large amount of information for each individual event and this is fully utilised in the analysis process. The detector's ability to identify particle types and supply timing information are used to create a consistent background model (Sections 6.3 and 6.4). Once a background model has been built, a measurement of the $2\nu\beta\beta$ process and a search for the $0\nu\beta\beta$ process is undertaken (Section 6.6).

6.1. Monte Carlo Simulation

Monte Carlo simulation (MC) for NEMO-3 is performed using the DECAY0 event generator [80], which is capable of generating the initial particles in radioactive decays with the correct kinematics, timing and branching ratios. It provides all the necessary information on $2\nu\beta\beta$ and many $0\nu\beta\beta$ decay modes and is also used for all background isotopes.

Events generated with DECAY0 are propagated through a full detector description by GEANT-3.21 [81]. This simulates the interactions of the particles as they move through the detector according to their full and differential cross-sections. Events emerge from the simulation program in exactly the same format as raw data to allow for the same reconstruction process.

6.2. Reconstruction of Events

The reconstruction process takes raw output from the detector or MC and converts it into a useful form for a physics analysis. As a simple example, ADC and TDC content from a particular optical module is cross-referenced against information from calibration runs (Section 5.5) and accurate energy and timing information is created.

In general, the treatment of data and MC at reconstruction level is as similar as possible. To ensure that the simulation describes the data, an attempt to replicate real running conditions in the MC is performed. This encompasses such effects as the removal of hits generated for tracker cells that are not working, or the smearing of the energy response of individual optical modules based on calibration data.

In order to ensure that the conditions accurately reflect the state of the detector, MC events are distributed evenly across the entire detector lifetime, before applying appropriate running conditions.

6.3. Particle Identification

One of the main strengths of tracker-calorimeter detectors, such as NEMO-3, is their ability to distinguish between different types of particle. By using a combination of tracking and calorimetry, electrons, positrons, photons and alpha particles are identifiable in NEMO-3 data.

6.3.1. Electron Identification

Electrons and positrons are identified by tracks that can be extrapolated to an energy deposit in the calorimeter. An example of an event where two electrons have been identified in NEMO-3 data is shown in Figure 6.1. Electrons and positrons should be fully contained in a single scintillator block, so only calorimeter blocks that have no surrounding calorimeter hits are used to identify electrons. To distinguish between electrons and positrons, the curvature of the track as a result of the magnetic field can be used.

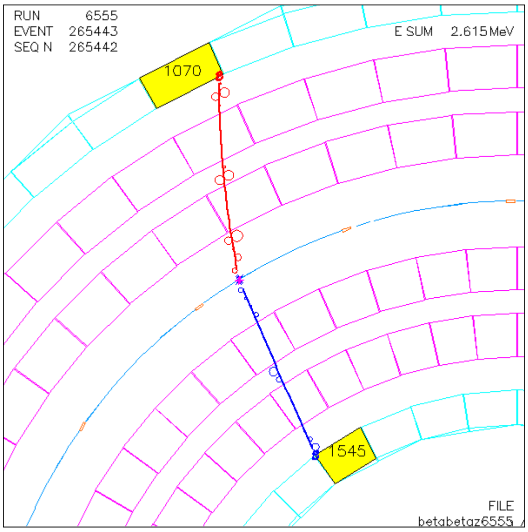

Figure 6.1.: An event from NEMO-3 data with two candidate electrons. The event display is viewed in projection on to the horizontal plane of the detector. The red and blue circles are Geiger hits. An anode wire is at the centre of each circle and the radius shows the possible ionisation points, given by the time of the anode signal after the initial trigger. The red and blue lines are reconstructed tracks which come from a common vertex, marked as the magenta cross on the foil. The cyan boxes are the inner and outer wall scintillator blocks showing two isolated energy deposits, whilst the magenta boxes are the petal scintillators.

6.3.2. Gamma Identification

Only charged particles produce ionisation in the tracker, so photons do not leave tracks. Gammas are therefore identified as an energy deposit in the calorimeter without an associated track. In contrast to electrons, a 0.5 MeV photon only has a 60% probability of interacting with a scintillator block. This efficiency is further reduced to 50% for the whole detector due to incomplete detector coverage.

As a result of this, there is no guarantee that the gamma is contained in a single block and the isolated calorimeter hit requirement used for electrons is no longer appropriate. Therefore, when identifying gammas, neighbouring calorimeter hits are clustered together and attributed to a single gamma with an energy equal to the sum of the individual hit energies. The time and position of the cluster are found with an energy-weighted mean of the constituent hits. Examples of neighbouring hits that would be clustered together are shown pictorially in Figure 6.2.

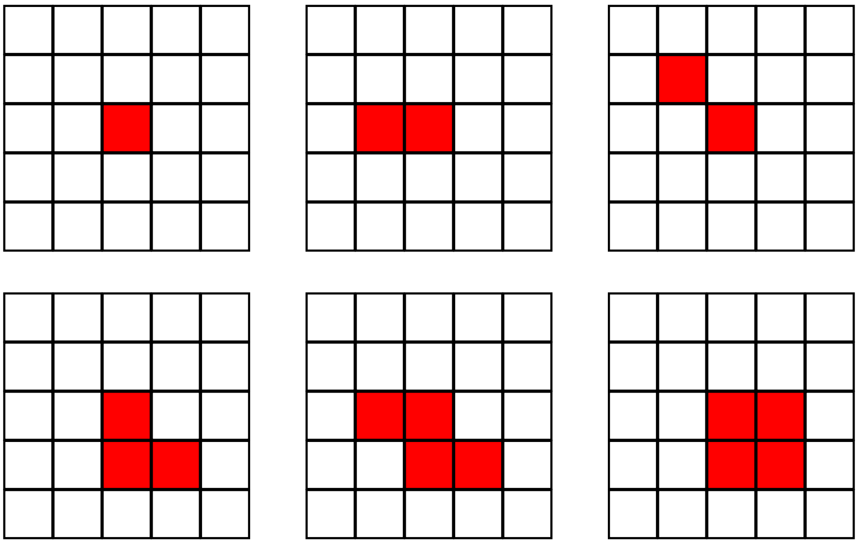

Figure 6.2.: Schematic showing examples of calorimeter hits (without associated tracks) that would be clustered together to form a gamma. The grid represents the array of scintillator blocks in the inner or outer walls and the red squares designate optical modules with energy deposits.

6.3.3. Alpha Identification

Alpha particles are charged and therefore trigger hits in the tracker. However, due to their increased mass in comparison to electrons, they interact more strongly in the tracking gas. For alpha particles from radioactive decays, the maximum distance travelled is ~ 35 cm, so they do not reach the calorimeter. Furthermore, the increased alpha mass means that there is very little deflection of the particle's trajectory by the magnetic field. Alpha particles can therefore be identified by short straight tracks.

For a double-beta decay analysis with NEMO-3, alpha particles from the vicinity of the foils do not, themselves, contribute to the background. However, they can be a useful tool for rejecting background events or measuring the background level in the detector. ^{214}Bi is a progeny of ^{222}Rn that can deposited on the source foils or on tracker cells close to the foil. ^{214}Bi decays to ^{214}Po via β-decay with a Q_β value of 3.27 MeV, which can be a problematic background for a $0\nu\beta\beta$ search. To identify events from ^{214}Bi, it is possible to use the short half-life of ^{214}Po, which decays via α-decay with $T_{1/2} = 164.3$ µs. NEMO-3 is therefore able to identify this type of bismuth-polonium (BiPo) event by searching for a prompt electron track followed by a delayed alpha track originating from the same location. An example of such an event from NEMO-3 data is shown in Figure 6.3.

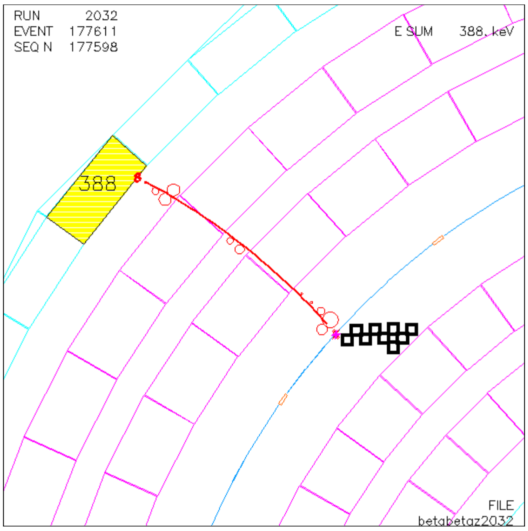

Figure 6.3.: Candidate BiPo event from NEMO-3 data. The red track is from a prompt electron, whilst the black squares are delayed Geiger hits that form a much shorter alpha track.

To suppress the background from ^{214}Bi in a $0\nu\beta\beta$ search or a $2\nu\beta\beta$ measurement, events where there are any number of delayed Geiger hits close to the electron vertex are usually removed. However, as well as this vetoing power, delayed hits may also be used to independently measure the level of ^{214}Bi and hence ^{222}Rn inside the tracker. In this case, a track is assigned to the candidate alpha particle in a BiPo event. The length of this track is a function of the alpha energy and therefore takes a different form depending on whether the particle originated from, for example, inside the source foil or at the surface of a tracker wire. An accurate description of the ^{222}Rn (and hence ^{214}Bi) distribution inside NEMO-3 can therefore be attained via events of this type.

6.4. Time of Flight Information

The central principle behind NEMO-3 is that any signal must originate from inside the foils in the centre of the detector. Therefore, when measuring either a signal or background inside these foils, it is imperative to reduce the influence of any events from an external source. Time of flight (ToF) information plays a pivotal role in establishing the origin of an event and therefore suppressing external backgrounds. There are two main channels where external sources can mimic internal events.

The most important case is the 2e channel, where external sources can be a significant background to a $2\nu\beta\beta$ measurement, as will be discussed in the next chapter. In this case, it is necessary to tell whether an electron crosses the foil, such as in Figure 6.4a, or whether there are two electrons that both originated within the foil. At low energies, a crossing electron can be easily rejected due to its incorrect curvature, but at higher energies, where the tracks are less curved, this identification is not 100% effective.

The second case is in the 1e1γ channel, where an external photon that interacts in the calorimeter and the source foil, as in Figure 6.4b, may mimic a nuclear decay inside the foil followed by photon emission. This type of event is important for measuring internal backgrounds from ^{214}Bi and ^{208}Tl.

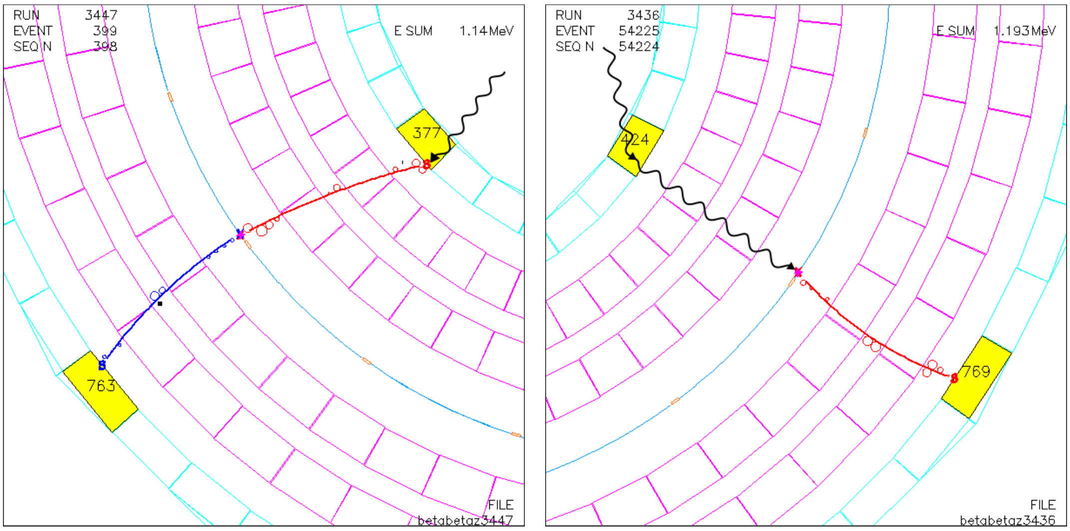

(a) Candidate crossing electron event **(b)** Candidate external 1e1γ event

Figure 6.4.: Events that are candidates to be of external origin as a result of ToF information. (a) shows a crossing electron event and (b) shows an external 1e1γ event.The black lines have been superimposed to show the presumed photon paths.

In both of these cases, it is possible to distinguish between the internal and external type events by using ToF information. In this section, the calculations required to assess the probability that an event is internal or external are presented.

6.4.1. Internal Probability

For the internal vertex hypothesis, it is assumed that the detected particles have a common origin inside the source foils. Provided that at least one particle leaves a track, it is possible to calculate the probability of this hypothesis given two different calorimeter hits with times t_i^{meas} $(i = 1, 2)$. This probability is referred to as the internal probability, since the origin of the event is internal to the foils.

The probability calculation proceeds as follows, using natural units throughout. The theoretical ToF, t_i^{tof}, for a particle to travel a distance l_i is

$$t_i^{\text{tof}} = \frac{l_i}{\beta_i} \tag{6.1}$$

where l_i is either the track length of an electron or the straight-line distance between the hypothesised vertex and the scintillator for a photon. For photons, $\beta_i = 1$, and for electrons, β_i is given by

$$\beta_i = \frac{\sqrt{E_i\left(E_i + 2m_e\right)}}{E_i + m_e} \tag{6.2}$$

where E_i is the calibrated energy recorded in the calorimeter and m_e is the electron rest mass. Assuming that the particles have an internal origin, the time of emission of each particle, t_i^{int}, can be written

$$t_i^{\text{int}} = t_i^{\text{meas}} - t_i^{\text{tof}} = t_i^{\text{meas}} - \frac{l_i}{\beta_i} \tag{6.3}$$

The timing distributions are approximately Gaussian and so a χ^2 test may be used with an appropriate χ^2 variable

$$\chi^2_{\text{int}} = \frac{\left(\left(t_1^{\text{meas}} - \frac{l_1}{\beta_1}\right) - \left(t_2^{\text{meas}} - \frac{l_2}{\beta_2}\right)\right)^2}{\sigma^2_{t_1^{\text{int}}} + \sigma^2_{t_2^{\text{int}}}} \tag{6.4}$$

$\sigma^2_{t_i^{\text{int}}}$ is the variance of the emission timing measurement, t_i^{int}, which is dominated by contributions from uncertainties on the measurement time, $\sigma_{t_i^{\text{meas}}}$, the particle speed σ_{β_i} and the distance travelled σ_{l_i}:

$$\sigma^2_{t_i^{\text{int}}} = \left(\frac{\partial t^{\text{int}}}{\partial t_i^{\text{meas}}}\right)^2 \sigma^2_{t_i^{\text{meas}}} + \left(\frac{\partial t^{\text{int}}}{\partial \beta_i}\right)^2 \sigma^2_{\beta_i} + \left(\frac{\partial t^{\text{int}}}{\partial l_i}\right)^2 \sigma^2_{l_i} \tag{6.5}$$

For electrons, the uncertainty on the path length can be neglected since their interaction point in the scintillator is well known from a combination of tracking information and their shallow interaction depth. Therefore to a good approximation, the variance of the measurement for electrons may be written

$$\sigma^2_{t_i^{\text{int}}} \simeq \sigma^2_{t_i^{\text{meas}}} + \left(\frac{t_i^{\text{tof}} m_e^2}{E_i\left(E_i + m_e\right)\left(E_i + 2m_e\right)}\right)^2 \sigma^2_{E_i} \tag{6.6}$$

In the case of photons, the uncertainty on particle speed is negligible, but there are significant unknown quantities relating to the uncertainty on the path length. This is due to a combination of no tracking information, so it is unknown where the photon intersected the face of the block, and the possibility of an interaction at any depth in the block. As a result, the variance for photons takes the form

$$\sigma^2_{t_i^{\mathrm{int}}} \simeq \sigma^2_{t_i^{\mathrm{meas}}} + \sigma^2_{l_i} \tag{6.7}$$

To convert the χ^2_{int} value into a probability, it should be noted that there is one degree of freedom, so that the probability is defined as

$$P\left(\chi^2_{\mathrm{int}}\right) = 1 - \frac{1}{\sqrt{2\pi}} \int_0^{\chi^2_{\mathrm{int}}} x^{-\frac{1}{2}} e^{-\frac{x}{2}} dx \tag{6.8}$$

The internal probabilities for the 2e channel (Section 8.2) and the 1e1γ channel (Section 7.3.5), constructed using this formulation are shown in Figure 6.5. Good agreement is seen between experimental data and simulation.

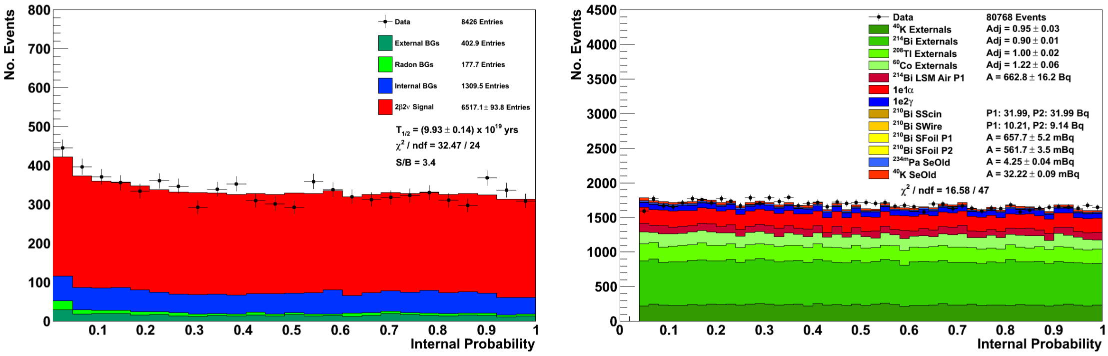

(a) 2e Channel

(b) 1e1γ Channel (SeOld)

Figure 6.5.: Internal probability distributions for the (a) $2\nu\beta\beta$ channel and (b) 1e1γ channel for the SeOld sample. Both distributions have been calculated using the above method. For more information on these channels, please refer to Sections 8.2 and 7.3.5.

6.4.2. External Probability

The external vertex hypothesis is that the two hits have a common origin that is external to the source foils. In this scenario, it is assumed that an incident photon interacts in the first PMT and causes either a crossing electron or an external 1e1γ event.

The probability calculation proceeds in a similar vein to that for the internal vertex hypothesis and the ToF of the particle(s) is now given by

$$t^{\text{tof}} = \frac{l_1}{\beta_1} + \frac{l_2}{\beta_2} \tag{6.9}$$

where l_i and β_i are defined as before. The χ^2 variable may therefore be constructed as

$$\chi^2_{\text{ext}} = \frac{\left(\left(t_2^{\text{meas}} - t_1^{\text{meas}} \right) - \left(\frac{l_1}{\beta_1} + \frac{l_2}{\beta_2} \right) \right)^2}{\sigma^2_{t_1^{\text{int}}} + \sigma^2_{t_2^{\text{int}}}} \tag{6.10}$$

where $\sigma^2_{t_i^{\text{int}}}$ is defined as for the internal probability hypothesis in Equations (6.5)–(6.7). The external probability, $P\left(\chi^2_{\text{ext}}\right)$, is calculated using Equation (6.8) as before.

The external probability for the 1e1γ channel for the SeOld sample is shown in Figure 6.6. As with the internal probability distributions shown in the previous section, good agreement is observed between data and MC.

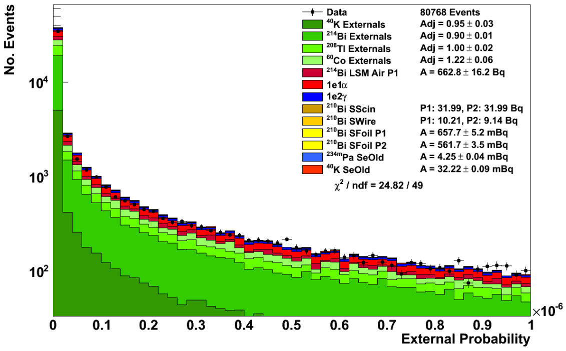

Figure 6.6.: External probability distribution for SeOld sample in the 1e1γ channel, showing good agreement between data and MC. Note that the x-axis scale is for very low probabilities only. For more information on this channel, please refer to Section 7.3.5.

6.5. Analysis Data Set

As described in Section 5.7, data from NEMO-3 are split into two phases due to different radon levels inside the detector. Phase 1 (P1) is the period before the installation of the anti-radon facility and therefore has a higher level of radon. This phase encompasses February 2003 - September 2004 (runs 1869 - 3395). Phase 2 (P2) covers the remainder of the experiment which has a lower radon level over the period October 2004 - January 2011 (runs 3396 - 9186).

The relevant exposures for P1 and P2 are presented in Table 6.1. This thesis analyses data from the standard analysis runs of the entire NEMO-3 data set, which, excluding detector dead time, gives a total time of 5.25 yr and an exposure to ^{82}Se of 4.90 kg yr.

Phase	Run Time / d	Dead Time / d	Exposure / d
P1	391.9	5.3	386.6
P2	1548.3	16.3	1531.9
P1+P2	1940.2	21.6	1918.5

Table 6.1.: Exposure of NEMO-3 using the standard analysis run set broken down into phase 1 and phase 2.

6.6. Statistical Analysis

All statistical analysis presented in this thesis is performed with C++ in the ROOT data analysis framework. Backgrounds, and signal where appropriate, are measured using a binned log-likelihood fit (Section 6.6.1). Where no statistically significant signal is observed, a limit on the signal strength is set using a negative log-likelihood ratio technique (Section 6.6.2).

6.6.1. Fitting MC Distributions to Data

In order to estimate the activities of different isotopes, a binned log-likelihood fit is used. This takes into account the shapes of different background and signal distributions to produce estimates of the most likely activity values. To form the likelihood function, it is assumed that the MC reliably produces the expected numbers of events in each bin of a number of histograms. Then, the number of expected events in the i^{th} bin of the n^{th} histogram is given by the addition of the signal events, $s_{i,n}$, and the sum of the j background contributions, $\sum_j b_{i,n,j}$. Poisson statistics apply to the number of observed events such that the probability, $p_{i,n}$, of observing $d_{i,n}$ events in data is

$$p_{i,n} = \frac{e^{-\left(s_{i,n}+\sum_j b_{i,n,j}\right)}\left(s_{i,n}+\sum_j b_{i,n,j}\right)^{d_{i,n}}}{d_{i,n}!} \tag{6.11}$$

The likelihood, L, is defined as the product of all the binned probabilities

$$L = \prod_{i,n} \frac{e^{-\left(s_{i,n}+\sum_j b_{i,n,j}\right)}\left(s_{i,n}+\sum_j b_{i,n,j}\right)^{d_{i,n}}}{d_{i,n}!} \tag{6.12}$$

It gives a measure of the overall likelihood of the particular set of data given the expectation from the MC and therefore the maximal value of L gives the best estimates for s and b_j. The maximum of L is unaffected by a monotonic function such as a logarithm, so that the maximum of L will correspond to the maximum of $\ln(L)$:

$$\ln(L) = \sum_{i,n}\left(-\left(s_{i,n}+\sum_j b_{i,n,j}\right) + d_{i,n}\ln\left(s_{i,n}+\sum_j b_{i,n,j}\right) - \ln(d_{i,n}!)\right) \tag{6.13}$$

The parameters s and b_j are proportional to the activities of these samples so that it is possible to numerically maximise Equation (6.13) by varying the activities of different samples. The errors on the activities are found by noting that L follows a χ^2 distribution such that a 1σ error reduces $\ln(L)$ by $\frac{1}{2}$.

It is also possible to include additional information into the binned log-likelihood fit, for example by adding a Gaussian constraint. This is typically used where there is very little distinguishing information in the data about the activity of a particular background as it is almost identical to another sample. In this scenario, a measurement from another source may be included in the log-likelihood fit.

For example, if an activity of $A = A_0 \pm \sigma_{A_0}$ has been measured elsewhere, then a term constraining MC activity, A_{MC}, such as the following may be included in $\ln(L)$:

$$\ln(L) \rightarrow \ln(L) - \ln\left(\sqrt{2\pi}\sigma_{A_0}\right) - \frac{1}{2}\left(\frac{A_{MC}-A_0}{\sigma_{A_0}}\right)^2 \tag{6.14}$$

6.6.2. Extracting Limits on Signal Strength

If no evidence of a signal above background is observed, it is useful to make a statistically meaningful statement about the maximum allowed signal strength. This procedure involves setting a limit to exclude the signal at a given confidence level (CL). A simple counting method can be used, such as in [82, 83], but by comparing data, signal and background distributions the same information utilised in Section 6.6.1 can be used to deliver an improved result.

A general principle behind setting limits on signal strength is to quantify how consistent the data are with a background-only (B-only) hypothesis and a signal and background ($S+B$) hypothesis. The most appropriate method for a search with small statistics utilises the likelihood ratio test statistic [84, 85]. This test statistic is defined as the ratio of likelihoods of the $S+B$ and B-only hypotheses:

$$\begin{aligned} Q(d) &= \frac{L\left(S+B\right)}{L\left(B\right)} && (6.15) \\ &= \prod_i \frac{e^{-(s_i+b_i)}(s_i+b_i)^{d_i}/d_i!}{e^{-b_i}b_i^{d_i}/d_i!} && (6.16) \\ &= \prod_i e^{-s_i}\left(\frac{s_i+b_i}{b_i}\right)^{d_i} && (6.17) \end{aligned}$$

where s_i and b_i are the expected number of signal and background events in the i^{th} bin of the distribution and d_i is the number of events observed in data in this bin. Usually, Q is transformed to a negative log-likelihood ratio (NLLR) defined as

$$\chi(d) = -2\ln\left(Q(d)\right) = 2\sum_i\left(s_i - d_i\ln\left(1+\frac{s_i}{b_i}\right)\right) \qquad (6.18)$$

According to Wilk's theorem, in the limit of a large data sample, $\chi(d)$ will be asymptotically distributed according to a χ^2 distribution with one degree of freedom [86]. In this scenario, confidence levels can be calculated directly. However, in reality, there is a limited sample of data and so a toy MC is used to generate the distributions of $\chi(d)$, which are then used to calculate appropriate confidence levels. Distributions of the NLLR are generated by replacing each value of d_i with pseudo-data, generated randomly as a Poisson variable with an expectation of s_i+b_i. The same procedure is followed for the B-only hypothesis to create distributions such as those shown in Figure 6.7.

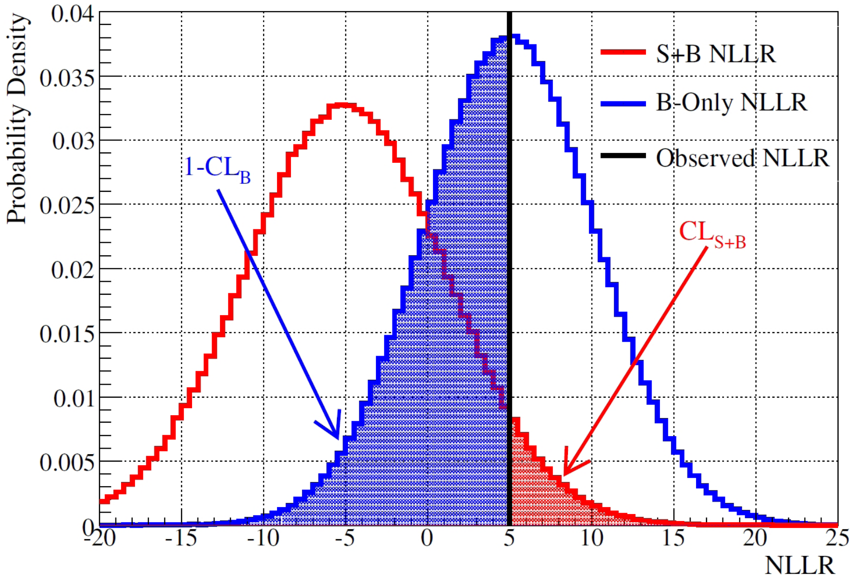

Figure 6.7.: Example distributions of the NLLR test statistic generated for the $S + B$ hypothesis (red) and B-only hypothesis (blue). Image sourced from [87].

From these distributions, it becomes clear that a confidence level can be constructed for outcomes where a result is less like the $S + B$ hypothesis than the observed value of $\chi(d)$. This confidence level is given by

$$\mathrm{CL}_{S+B} = P_{S+B}(\chi > \chi(d)) = \int_{\chi(d)}^{\infty} \frac{\partial P_{S+B}}{\partial \chi} d\chi \tag{6.19}$$

with a similar confidence level for the B-only hypothesis

$$\mathrm{CL}_{B} = P_{B}(\chi > \chi(d)) = \int_{\chi(d)}^{\infty} \frac{\partial P_{B}}{\partial \chi} d\chi \tag{6.20}$$

Finally, the confidence level for the signal is related to the $S + B$ and B-only hypotheses by

$$\mathrm{CL}_S = \frac{\mathrm{CL}_{S+B}}{\mathrm{CL}_B} \tag{6.21}$$

To find the appropriate limit, the signal strength is increased until $1 - \mathrm{CL}_S \geq 0.9$ so that the 90% CL is reached.

6.7. Half-life Calculation

If a signal is observed, then it is customary to report the resulting signal strength as a half-life of the source isotope. The appropriate calculation is detailed here.

As with all radioactive isotopes, those in NEMO-3 decay exponentially such that

$$N(t) = N(0)e^{-\lambda t} \tag{6.22}$$

where $N(t)$ is the number of atoms of the isotope remaining after time t, and λ is the decay constant for the isotope that is related to its lifetime, τ, and half-life, $T_{1/2}$ as

$$\lambda = \frac{1}{\tau} = \frac{\ln(2)}{T_{1/2}} \tag{6.23}$$

Since the half-lives involved in NEMO-3 are very large ($\mathcal{O}(10^{20}$ yr$)$) compared with the lifetime of the experiment, a Taylor expansion can be made in λt and to a very good approximation

$$e^{-\lambda t} \simeq (1 - \lambda t) \tag{6.24}$$

The number of decays that occur over t is given by $N(0) - N(t)$, so that if these are detected with efficiency ϵ, the number of observed events is given by

$$N_{\text{obs}} = \epsilon N(0)\left(1 - e^{-\lambda t}\right) \simeq \epsilon N(0)\lambda t = \epsilon N(0)\frac{\ln(2)}{T_{1/2}}t \tag{6.25}$$

The number of atoms at the start of the experiment, $N(0)$, can be written as

$$N(0) = \frac{N_A m}{A} \tag{6.26}$$

where N_A is Avogadro's constant, m is the mass of the source isotope and A is its atomic mass. Therefore Equation (6.25) can be re-arranged to find an expression for the half-life:

$$T_{1/2} = \frac{\epsilon}{N_{\text{obs}}}\frac{N_A m}{A}\ln(2)t \tag{6.27}$$

Chapter 7.

Estimation of Backgrounds for the ^{82}Se Source Foils

Double beta decay signals in NEMO-3 are characterised by the observation of two electrons originating from the same location inside a source foil. Therefore, any other process that can mimic this signal is a background for the experiment. To be a background to a $0\nu\beta\beta$ search, electrons must also have energies that sum to a high $Q_{\beta\beta}$. In contrast, the $2\nu\beta\beta$ process is observed across the entire energy spectrum and so all two electron-like backgrounds contribute.

The sensitivity of NEMO-3 is directly related to the background level (as discussed in Section 4.1), and so it is vitally important to be able to accurately measure this background level and to develop techniques that can remove background events.

This chapter is devoted to the determination of background levels for NEMO-3. It will discuss the main sources of background (Section 7.1), categorising them into three types based - internal backgrounds, which are caused by contamination of the source foils, external backgrounds that originate outside the source foils and radon-induced backgrounds (Section 7.2). Next, the selection channels that are used to measure the background levels are outlined (Section 7.3) before finally presenting the results of these measurements (Section 7.4).

7.1. Sources of NEMO-3 Background

The main source of background for NEMO-3 is the presence of small amounts of naturally occurring radioactive isotopes that are found in all materials. Of the isotopes that are inside the source foils, those that undergo β-decay are generally the most problematic, whereas γ-emitting sources contribute most to the background from external sources. Nearly all radioactive isotopes contribute to the background for $2\nu\beta\beta$, but only those with high Q_β values are of importance to a $0\nu\beta\beta$ search.

The two main isotopes of concern are the β-decaying isotopes ^{214}Bi and ^{208}Tl with Q_β values of 3.27 MeV and 4.99 MeV respectively. These are part of the ^{238}U and ^{232}Th decay chains which are presented in Figures 7.1 and 7.2. These decay chains are found in small amounts in all materials and despite the careful selection of all detector materials from a radiopurity perspective, there are small traces of these isotopes in NEMO-3.

The decay of ^{214}Bi is shown as a decay scheme in Figure 7.3. 19.9% of decays do so directly to the ground state of ^{214}Po, which thus emits an electron with a spectrum end-point of 3.27 MeV. The remaining 80% of β-decays proceed to one of the excited states of ^{214}Po which then loses energy via photon emission, with the strongest photon intensities at 1.76 MeV (15.3%), 1.12 MeV (14.9%) and 0.61 MeV (45.5%).

Similarly, the decay of ^{208}Tl (Figure 7.4) involves a β-decay to an excited state and the emission of photons. There is nearly always a 2.61 MeV photon and this is usually accompanied by one or more other photons with energies of 0.86 MeV (12.5%), 0.58 MeV (85.0%) and 0.51 MeV (22.6%). Pure β-decays and $\beta + \gamma$ decays can both mimic two electron events via processes which will be described in the next section.

Alongside the ^{214}Bi from ^{238}U inside the source foils, there can be an additional supply of ^{214}Bi from other sources of ^{222}Rn. This isotope of radon is also in the ^{238}U decay chain and is unique as it is the only gaseous isotope in the chain. As a result, ^{222}Rn from ^{238}U may emanate out of any material and move freely, which makes suppressing this background particularly troublesome. It can be introduced into NEMO-3 via a number of mechanisms, notably in emanation from detector materials, contamination of the tracker supply gas or of other detector surfaces, or via diffusion through the detector seals. Once inside the detector, this radon decays

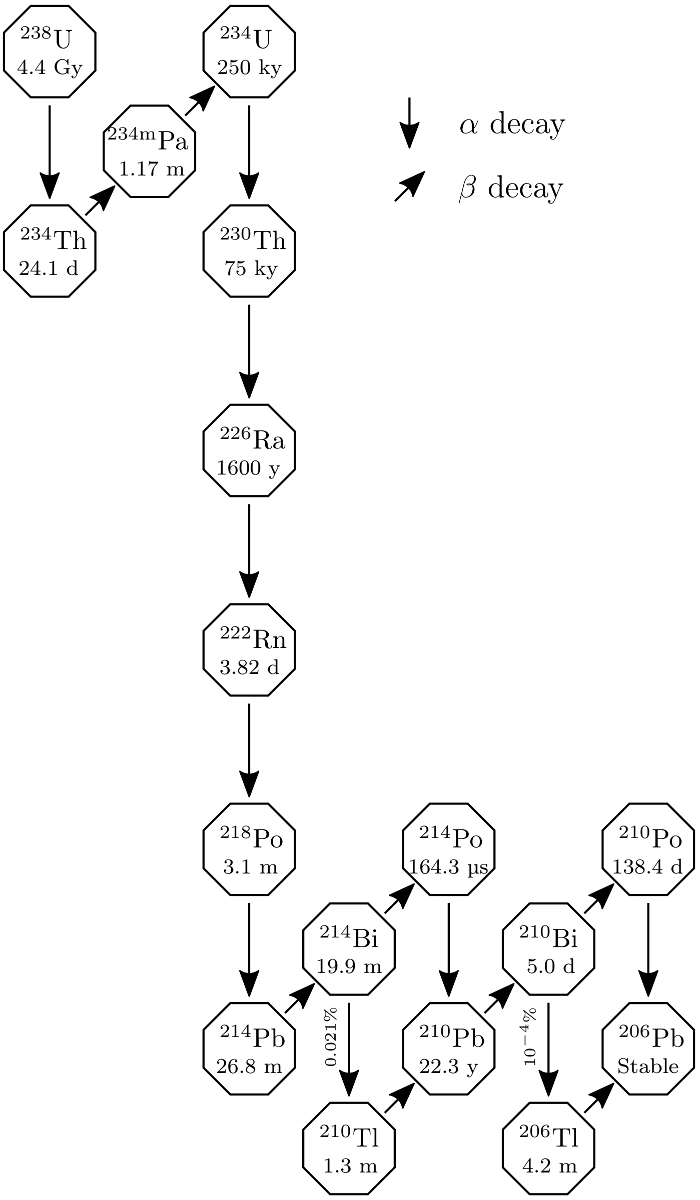

Figure 7.1.: ^{238}U decay chain, sometimes referred to as the radium series. α decays are shown as downwards arrows and β decays go upwards and to the right so that horizontal lines all show the same element. Where an isotope can decay in more than one mode, the branching fractions are marked on the α transition.

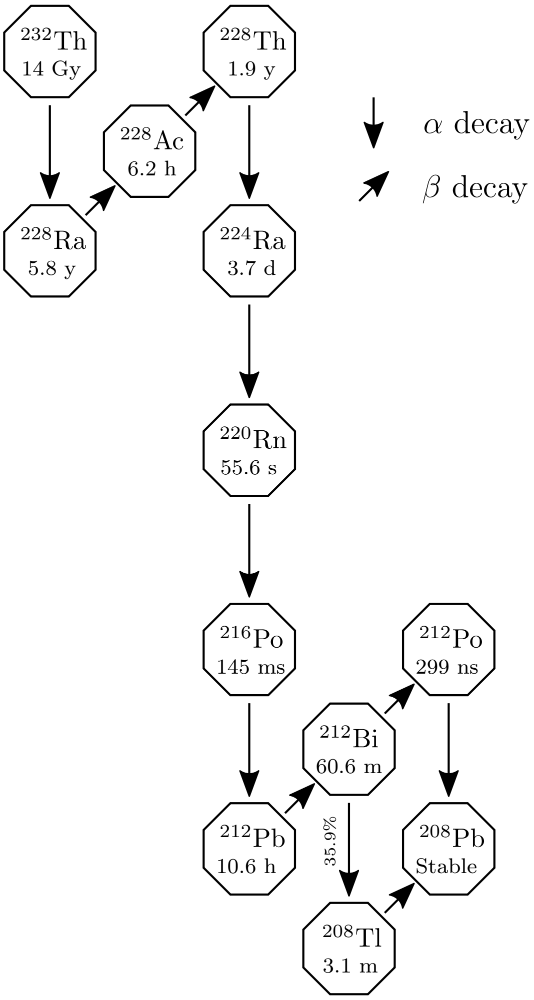

Figure 7.2.: ^{232}Th decay chain, also known as the thorium series. The notation used is the same as in Figure 7.1.

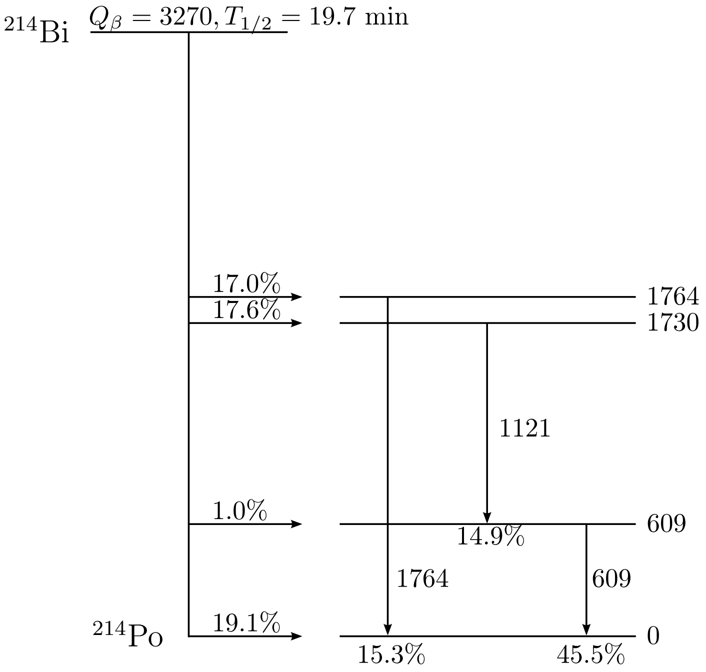

Figure 7.3.: Simplified decay scheme for the β-decay of ^{214}Bi to ^{214}Po, showing the three strongest gamma transitions. β-decays are shown as horizontal lines and γ transitions are shown vertically. All energies shown are in keV.

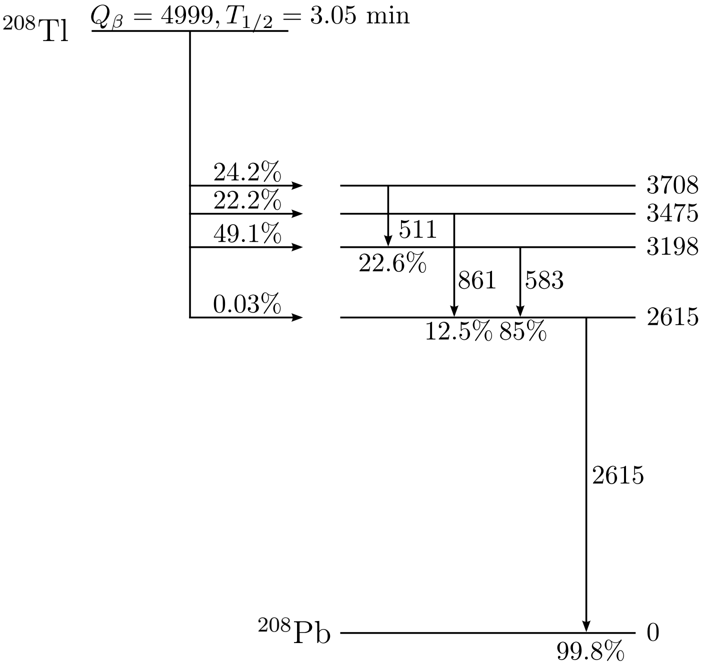

Figure 7.4.: Simplified decay scheme for the decay of ^{208}Tl to ^{208}Pb, showing the four strongest gamma transitions. All energies shown are in keV.

and in general, does so to predominantly positive ions. These charged progenies then drift towards the source foils or tracker wires where they settle, leaving deposits of ^{214}Bi near to the source material.

The ^{232}Th chain also contains a gaseous isotope of radon, ^{220}Rn, also known as thoron, which can decay to ^{208}Tl. However, this isotope does not cause such a problem for NEMO-3 since its very short half-life of 55.6 s means that very little thoron can emanate from detector materials before decaying. The resulting low level of ^{208}Tl on the surface of the tracking wires is measured separately using NEMO-3 data.

Finally, when considering a $0\nu\beta\beta$ process as the signal, the high energy tail of the $2\nu\beta\beta$ process can become a background rather than a signal. This can be particularly problematic for most decay mechanisms as it has an almost identical experimental signature to $0\nu\beta\beta$. The only practical way to suppress this background is with improved energy resolution. For isotopes such as ^{100}Mo, which have comparatively short $2\nu\beta\beta$ half-lives, this can produce a significant background but it is not expected to significantly affect the sensitivity of a $0\nu\beta\beta$ search in ^{82}Se with NEMO-3.

7.2. NEMO-3 Background Classification

7.2.1. Internal Backgrounds

Internal backgrounds are those which originate inside the source foils themselves and are dominated by the radioactive contaminants. The most harmful isotopes are those which undergo β-decay since they can mimic two electron events via the processes of β-decay with Møller scattering, β decay followed by internal conversion or β-decay to an excited state with Compton scattering of the de-excitation photon (Figure 7.5).

HPGe measurements of the selenium foils were made prior to their inclusion in the detector (Section 5.1.1), so that activity measurements made by NEMO-3 can be directly compared with these results. From these HPGe measurements and by considering commonly-found naturally occurring isotopes, the list of expected contaminants is comprised of ^{214}Bi, ^{214}Pb, ^{208}Tl, ^{212}Bi, ^{228}Ac, ^{234m}Pa and ^{40}K. All these isotopes are from the ^{238}U and ^{232}Th chains with the exception of ^{40}K.

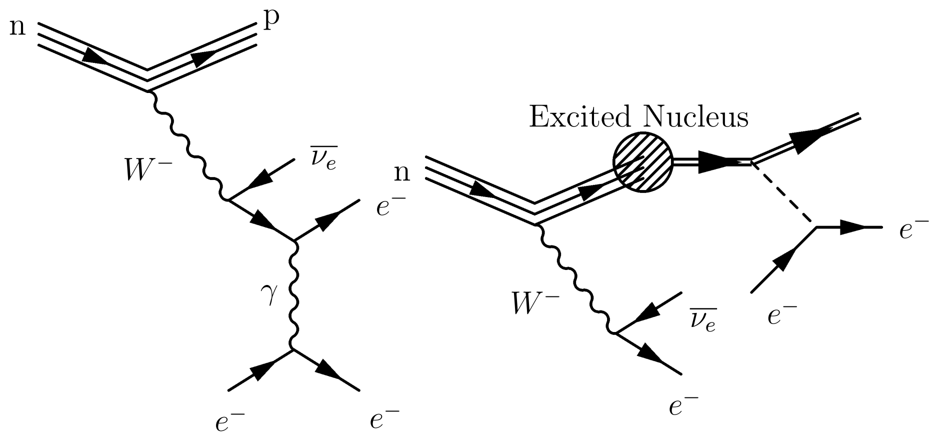

(a) β-decay and Møller Scattering **(b)** β-decay and Internal Conversion

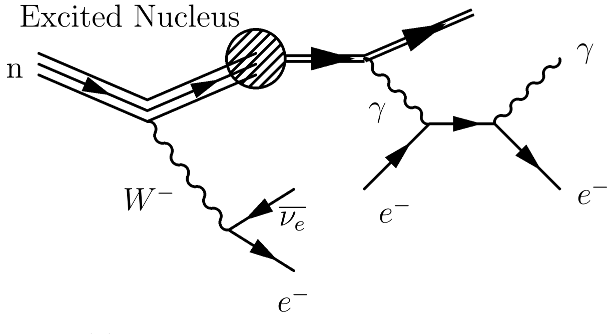

(c) β-decay and Compton Scattering

Figure 7.5.: Feynman diagrams showing the three dominant processes via which β-decay isotopes in the source foils can mimic two electron events.

Within these chains, certain isotopes have short half-lives and must therefore be in equilibrium with each other. For example, the activities of ^{214}Bi and ^{214}Pb must be equal and ^{212}Bi, ^{228}Ac and ^{208}Tl must also be in equilibrium, taking into account the branching fraction of 36% between ^{212}Bi and ^{208}Tl. However, due to long intermediate half-lives, equilibrium is not guaranteed between $^{234\text{m}}$Pa and ^{214}Bi.

The HPGe measurement also produced a non-zero result for contamination by ^{235}U, however, there was no evidence of ^{227}Ac so the equilibrium must be broken and no ^{207}Tl or ^{211}Pb is expected to contribute.

In this work, the internal backgrounds in the selenium foils of NEMO-3 are measured and verified by comparison with the results of the HPGe measurement.

7.2.2. External Backgrounds

External backgrounds are classed as those that originate anywhere in the detector other than the source foils and that are not radon-induced. In order to mimic two electron events, external backgrounds usually involve a photon that interacts with the source foil as shown in Figure 7.6. In the case of pair production, the outgoing positron must also be misidentified as an electron, which is unlikely given the magnetic field. Electrons that do not interact in the foil, but cross the detector as discussed in Section 6.4, can also be mistaken for two electron events. However, these crossing electrons are heavily suppressed by removing events based on their timing information.

Sources of external background are predominantly due to radioactive decay within the rock surrounding the laboratory, neutron capture and decay within the detector components themselves. The main types of event are external 1e1γ and crossing electron events as were shown in Figure 6.4. Analysis of these channels has allowed for the construction of an external background model that is capable of describing the γ flux incident on the detector.

External Background Model

The external background model is an *effective* model that is used to quantify the contribution of external background events to two electron measurements and is

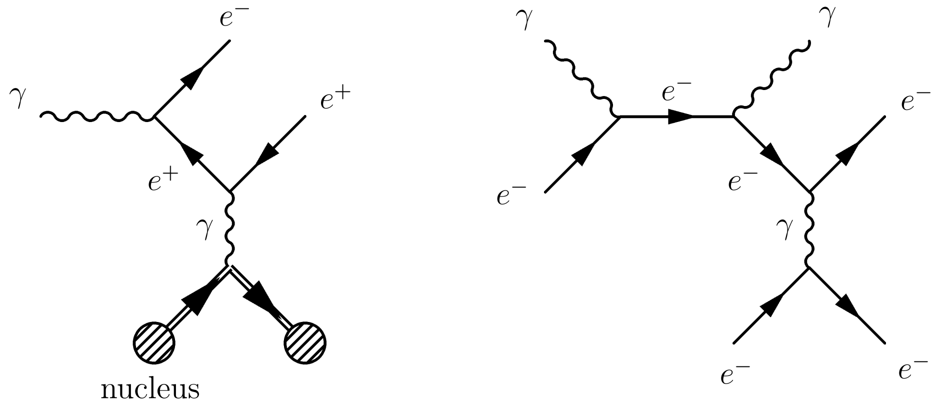

(a) Pair Production

(b) Compton + Møller Scattering

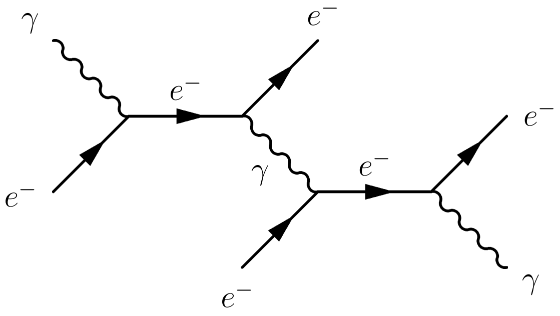

(c) Double Compton Scattering

Figure 7.6.: Feynman diagrams showing the three dominant processes via which external photons can interact in the source foils to produce two electron events.

described in [79]. In this model, the small contributions to the γ flux from the surrounding rock and from neutron capture are neglected and the components of the detector are the sole contributors.

The dominant source is the contamination of the PMTs with ^{226}Ra, ^{228}Ra and ^{40}K. This contribution is included with MC simulations of ^{214}Bi, ^{208}Tl, ^{228}Ac and ^{40}K inside the PMT glass. This is supplemented by additional activity from the other components of the detector and the parameters of the model are then found using the external 1e1γ and crossing electron channels. A summary of the activities that define the model is presented in Table 7.1.

NEMO-3	Activity / Bq			
Component	^{40}K	^{214}Bi	^{208}Tl	^{60}Co
PMTs	1078	324	27	-
Iron Petals	100	9.1	3.1	6.1
Iron Shield	-	7360	484	-
Internal Tower	-	-	-	18.4
Copper on Petals	-	-	-	47.6
Mu-Metal PMT Shields	-	-	-	14.6
Scintillators (Inner)	7.59	-	-	-
Scintillators (Outer)	12.53	-	-	-
Scintillators (Petals)	1.39	-	-	-

Table 7.1.: The activities given to each components of the external background model [79]. The activity of ^{228}Ac components is found by forcing equilibrium with ^{208}Tl.

The presence of ^{60}Co is from cosmogenic activation and this activity will therefore slowly decrease over the course of the experiment. The activity in the model is therefore an average activity over this time. This should not affect the result of this analysis as the data sets for both external background measurements and this analysis are similar.

Not all components of the detector were considered when making the external background model, so the numbers in Table 7.1 should not be taken as measurements of the activities of detector components. Rather, the intention is for the model to be capable of accurately reproducing the observed external γ flux.

The external model is used as a basis for the external backgrounds in this analysis and was constructed using measurements from all sectors. However, it is expected that small variations in the γ flux may be observed from sector-to-sector. As this analysis will only use sectors containing ^{82}Se, small variations in the activities of the model are expected in the final measurements.

7.2.3. Radon Backgrounds

The final background classification is radon-induced backgrounds. Although the origin of these backgrounds is external, they are given a separate classification as radon progenies can be deposited on the source foil surfaces, effectively becoming internal backgrounds, and as they should vary significantly between phases 1 and 2.

The radon level inside the detector can be measured with a fine granularity in time by studying BiPo type events as described in Section 6.3.3. The resulting radon activity over time is displayed in Figure 7.7, where a clear reduction can be seen between phases 1 and 2.

In addition to measuring the total activity of radon in the detector, it is possible to use BiPo events to measure the distribution of its progenies. In addition to BiPo events that originate from the source foils (Figure 6.3), it is also possible to locate BiPo events that start at tracking wires some distance away from the foil with events such as that shown in Figure 7.8. Using events of this type, an extensive radon model has been developed which distributes ^{214}Bi on the surface of the tracker wires, source foils and scintillators, denoted SWire, SFoil and SScin respectively. In addition, the SWire contribution is mapped by sector and tracker layer.

In the work described in this thesis, the SFoil contribution has been re-measured along with the contribution from the first layer of tracker wires in each sector. For the remaining wire activities, an overall normalisation is used, with relative activities taken from the previously measured radon map.

In addition to the ^{214}Bi and ^{214}Pb components that are measured with BiPo events, there are three further members of the set of radon backgrounds. The first is a product of thoron decay, ^{208}Tl, deposited on the surface of the wires, which was measured using 1e2γ and 1e3γ channels where the electron track starts away from

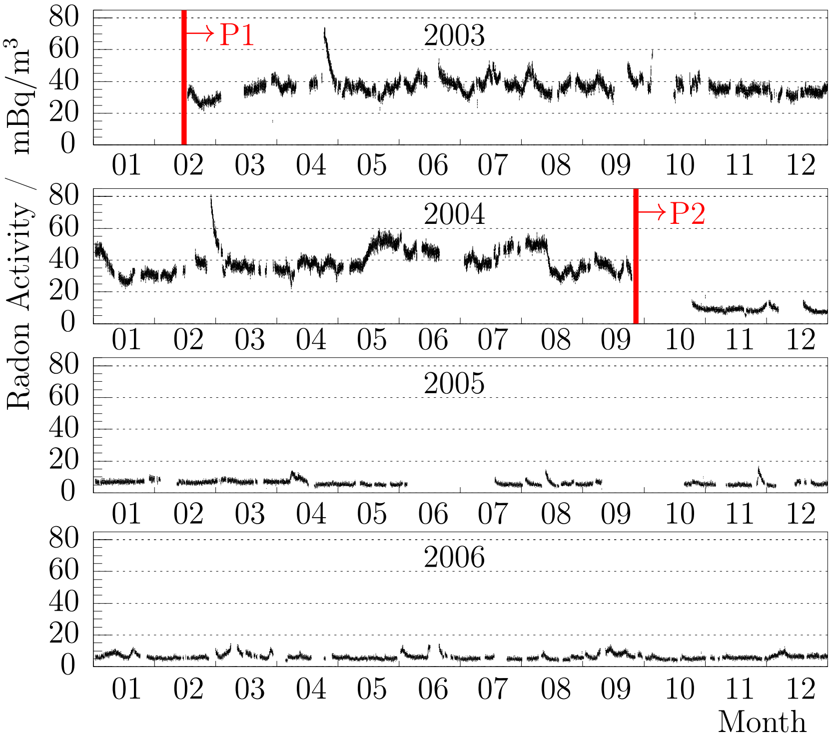

Figure 7.7.: Radon level measured inside NEMO-3 over time using BiPo events. There is a clear reduction in phase 2 after the installation of the anti-radon facility [79].

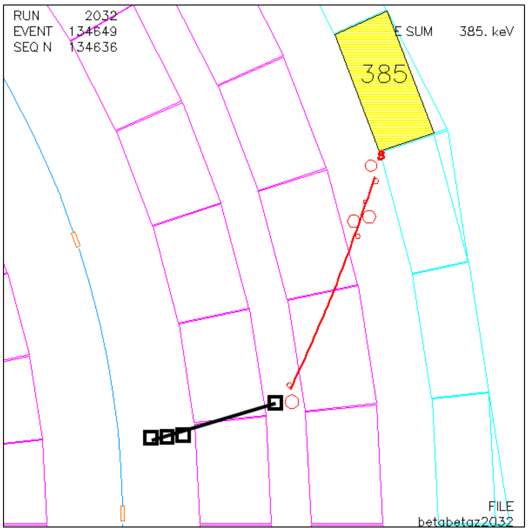

Figure 7.8.: Example of a BiPo event originating from a tracking wire away from the source foil. The prompt red track is from an electron and the short black track comes from a delayed alpha particle.

the foil. The levels inside the tracker were measured as 3.5 ± 0.4 mBq for phase 1 and 2.9 ± 0.4 mBq for phase 2, showing no significant decrease between the phases [79].

Another contribution to the radon background is given by ^{210}Bi SWire, SScin and SFoil components. The origin of this is from deposition of ^{210}Pb by ^{222}Rn during construction. This isotope has a half-life of 22.3 yr, so supplies ^{210}Bi over the lifetime of the experiment. From this half-life, it is expected that the reduction in ^{210}Bi activity between P1 and P2 should be $\sim 13\%$. In a similar manner to the ^{214}Bi SWire activities, a map of relative ^{210}Bi SWire activities divided by sector and tracker layer has been developed and this is used in this analysis. Furthermore, the ^{210}Bi SScin activity is also fixed from a previous analysis, but the SFoil component is re-measured.

The final source included in the radon backgrounds is ^{214}Bi, from radon in the air surrounding in the detector. This background could also be considered as an external background, but was included in the radon backgrounds since it is only present in phase 1, before the installation of the anti-radon tent. The level of radon inside the laboratory is mostly determined by emanation from the surrounding rock and has been measured at the level of ~ 15 Bq/m^3.

7.3. Channels for Background Measurements

Using the event topology reconstruction capabilities of NEMO-3, it is possible to infer the levels of backgrounds that may mimic two electron events in an independent manner by using different selection criteria. These different criteria are referred to as *channels* and are denoted by the set of particles that events will contain. Herein, a background model is produced by considering the 1e, $1e1\gamma$, $1e2\gamma$ and $1e1\alpha$ channels.

However, before measuring any backgrounds, agreement between data and MC must be achieved. In this section, general quality criteria and the removal of hot spots are discussed, which aids this agreement. Next, the background measurement channels are described before presenting the resulting activities that are measured using these channels.

7.3.1. General Quality Criteria

For any selection of NEMO-3 data, a number of quality cuts are applied that aim to remove events that involve unstable detector components. This means that events are removed from the data set if any of the following criteria are met:

- A non-calibrated PMT (in energy or time) is fired.
- An optical module with a known problem, such as a low counting rate or non-linearity, is present. These modules are identified during calibration runs with radioactive sources.
- There is a hit in an unstable optical module, as identified by the laser survey.
- The only calorimeter hit that passes other selection criteria has an out-of-time PMT hit, which means it is likely to be the result of noise from the PMT.

In addition, a misconfiguration of the latest reconstruction of data and MC accidentally removed electrons that were hitting the petal scintillators. As a result, these events are not present in this analysis.

7.3.2. Hot Spot Search

In simulation, signal and internal background events are distributed uniformly across the source foils. However, in reality, contaminants may be concentrated together in clusters to form so-called *hot spots*. The reasons for searching for and removing these hot spots are twofold: firstly, removing them will reduce the background level inside the detector with a minimal effect on signal efficiency; secondly, the detector acceptance varies as a function of the position of the event, so that in order to get good agreement between data and MC efficiencies, the distribution of background events should be as similar as possible in data and MC.

In order to search for these hot spots, the vertex distribution of single electron events in real data is used. An event is accepted if the following criteria are met:

- There was only one track in the event, which has negative curvature and intersects the source foil in a region given by $5.9 - 8.5$ in sector number and ± 120 cm in z.

- This track is associated to an isolated calorimeter hit, which was not in the petals and deposited an energy $>$ 400 keV.
- The track has a length of 50 cm, and Geiger hits in one of the two layers closest to the foil and one of the two layers before the scintillator. This improves track reconstruction efficiency and intersection resolution.
- There are no prompt unassociated hits within 15 cm of the electron intersection in the xy-plane. This aids in track reconstruction efficiency and suppresses backgrounds caused by emission from wires on the opposite side of the foil from the track.

After applying the hot spot search criteria, the intersection of the electron track with the foil, known as its vertex, can be plotted to search for areas with a non-uniform distribution of events. This can be seen in Figure 7.9a, where there are clear areas of higher activity. The strongest sources are based in the source foils of sector 5 on the left side of the plot, which have a relatively high level of internal contamination.

In addition, the windows of the calibration tubes (Section 5.5.1) can be seen at the start of sectors 6, 7 and 8. The calibration tubes are nominally located in the region from $S.00 - S.07$, where S is the sector, but it can be seen that the tracking vertex resolution misreconstructs some events into the source foil regions. Therefore, to remove events from the calibration tubes, exclusion zones are defined based on data from the hot spot search channel. These zones are elliptical to account for the different tracking resolutions in the transverse and vertical directions.

After removal of the calibration tubes, six hot spots are identified in the selenium foils. Two are in sector 6 and four are in sector 7, all of which are detailed in Table 7.2.

The location of the electron vertices after removing all calibration tube windows and hot spots and selecting events from the selenium foils are shown in Figure 7.9b. It is clear that there is extra contamination of the SeNew strip in sector 8, which will later be attributed to extra ^{210}Bi SFoil contamination. With the exception of this strip, the distribution of events is relatively uniform in each selenium sample, with a slightly higher level of contamination in SeNew than SeOld.

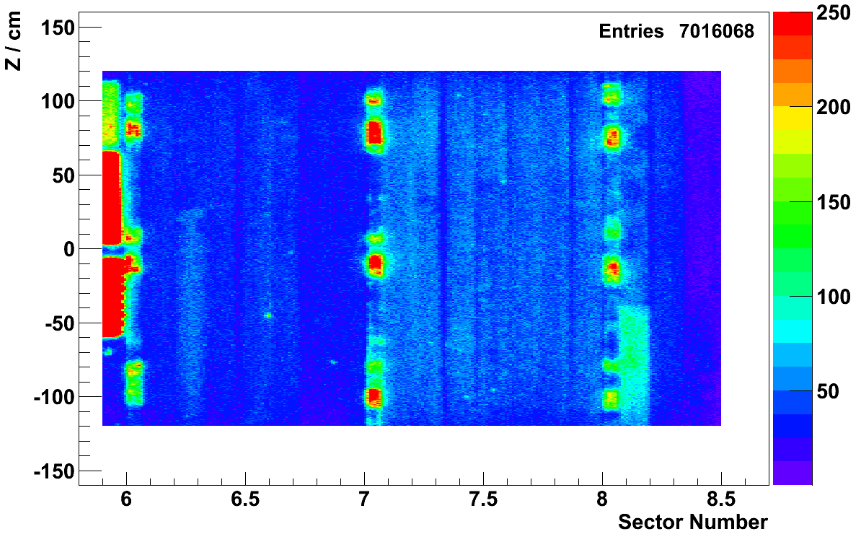

(a) Before Removal

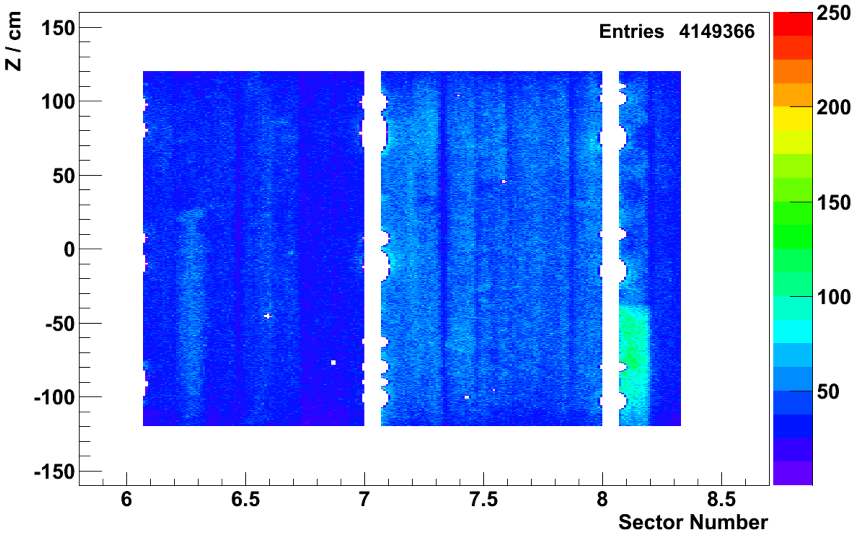

(b) After Removal

Figure 7.9.: Vertex position of the electron tracks in the hot spot search. 7.9a before and 7.9b after selecting events from the selenium foils and removing those originating in the identified hot spots.

Centre		Semi-axes		Area
Sector	Z / cm	XY / cm	Z /cm	cm^2
6.595	-45.5	1.75	0.73	4.01
6.870	-77.0	2.0	0.73	4.59
7.430	-100.5	1.5	0.73	3.44
7.585	45.5	1.5	0.73	3.44
7.545	-95.5	1.0	0.73	2.29
7.395	103.5	1.0	0.73	2.29

Table 7.2.: The location and size of ellipses used to remove hot spots in the selenium foils. The windows of calibration tubes are also excluded, but for the sake of brevity are not detailed here.

7.3.3. 1e1α Channel

The 1e1α channel uses BiPo events containing a prompt electron track and delayed alpha track to measure the levels of ^{214}Bi inside the detector. It is used to quantify the activities on the surface of the wires, the surface of the selenium foils, inside the Mylar backing film and, with a lower sensitivity, the internal contamination of the foils. The selection criteria for the 1e1α channel are as follows:

- There is only one prompt track in the event and this satisfies the selection criteria for the hot spot channel, with a lower energy cut of 200 keV.
- This electron track originates inside the selenium foils and is not in an area denoted as a calibration window or hot spot.
- The number of hits in the alpha track is > 4. This ensures good track reconstruction and suppresses random coincidences and re-firings of tracker cells.
- The alpha track occurs at least 4 µs after the prompt electron track, which removes the majority of events caused by re-firings.
- The alpha track has a hit within 5 cm in the xy-plane and 10 cm in z of the electron vertex. Further, it passes within 5 cm in the xy-plane and 10 cm in z of the electron vertex. These requirements remove tracks that do not originate from the same point as the electron.

Since no other isotope in NEMO-3 has a delayed alpha on the same timescale as ^{214}Bi, the 1e1α channel is a clean channel to measure this signal, with only a small fraction of contamination caused by re-firing of nearby tracker cells after the prompt track. This fraction, and that of random coincidences, can be assessed by studying the timing distribution of the delayed alpha tracks. The efficiencies for selection of ^{214}Bi with this channel are 0.49% and 0.41% for the SeOld and SeNew samples respectively, where the majority of the events are lost when requiring delayed hits in the designated time window.

Independent cross-checks between 1e1α and 1e1γ channels have shown agreement between measurements of ^{214}Bi to within 10%, providing an assessment of the systematic uncertainty of these measurements.

7.3.4. 1e2γ Channel

The 1e2γ channel exploits the decay scheme of ^{208}Tl (Figure 7.4) to obtain a high purity sample of ^{208}Tl events. In this channel, an electron is accompanied by two gamma candidates, one of which is required to be of high energy. This high energy requirement removes most other isotopes from this channel, with only a small contamination from ^{214}Bi, which has very little effect due to strong constraints from the 1e1α channel. The selection criteria for the 1e2γ channel are as follows:

- There is one electron candidate which passes the same selection criteria as the 1e1α electron.
- There are two gamma candidates with energy deposits greater than 200 keV, one of which must be above 1700 keV to remove events from ^{214}Bi whilst keeping those from ^{208}Tl.
- In addition, there may be no other gamma candidates with energies above 150 keV. This requirement selects events with two high energy gammas without being affected by the small amounts of noise from the PMTs.
- The internal probability of each gamma and electron pair is $> 4\%$ and the external probability is $< 1\%$. These values are the “usual” NEMO-3 values, which will be considered for re-optimisation for the two electron channels (Section 8.1).

- In order to suppress the contribution from ^{214}Bi, the electron energy is required to satisfy the requirement $E_e > 4.0$ MeV $- 1.5\,(E_{\gamma_1} + E_{\gamma_2})$. The effect of this cut can be understood by considering the distributions of ^{214}Bi and ^{208}Tl in these variables as shown in Figure 7.10.
- To further remove events from ^{214}Bi, no delayed hits are allowed within 25 cm in xy and 30 cm in z of the electron vertex. To reduce the impact from re-firings, single hits before 100 µs and multiple hits before 20 µs are exempt.

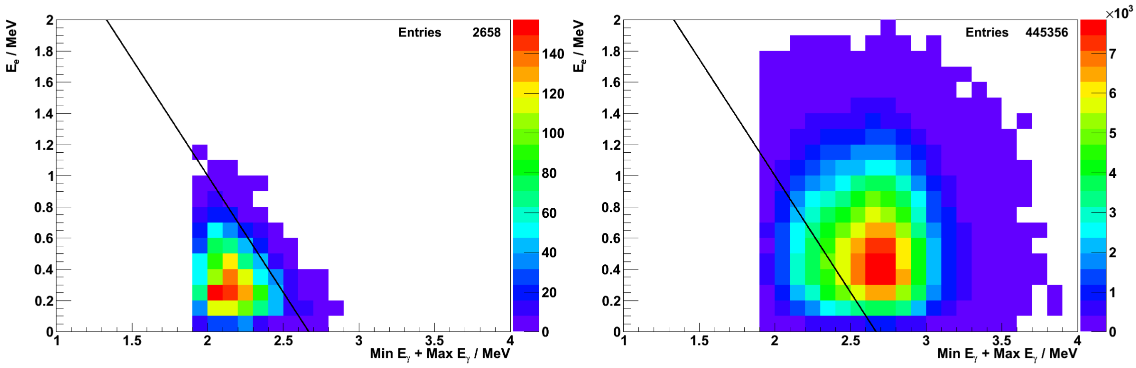

(a) ^{214}Bi MC (b) ^{208}Tl MC

Figure 7.10.: Electron energy plotted against the sum of the two gamma energies for ^{214}Bi and ^{208}Tl MC samples. The area to the left of the black line is removed by the cut implemented in the 1e2γ channel, which strongly suppresses ^{214}Bi whilst keeping ^{208}Tl.

These selection criteria lead to selection efficencies of 1.16% and 1.09% for ^{208}Tl in the SeOld and SeNew samples respectively. The majority of events are lost when requiring exactly two gamma candidates in the event and that the high energy gamma is above 1700 keV.

Measurements with a ^{232}U source, which decays via ^{208}Tl, were made with NEMO-3 to quantify the systematic uncertainty of this channel (which will be discussed in Section 8.2.3). Agreement was found between NEMO-3 and HPGe results at the level of 13%.

7.3.5. 1e1γ Channel

The 1e1γ channel is similar to the 1e2γ channel, except that only one gamma candidate is allowed. The channel can be used to assess the level of external backgrounds and the ^{214}Bi in the air of LSM in phase 1. In addition, there are contributions from the isotopes of the 1e1α and 1e2γ channel with smaller additions from internal contamination of ^{234m}Pa and ^{40}K. The selection criteria are as detailed below:

- There is one electron candidate in the event as described in the 1e1α and 1e2γ events, although this electron must have an energy > 400 keV to reduce copious low energy backgrounds.
- There is one gamma candidate with energy > 200 keV, internal probability $> 4\%$ and external probability $< 1\%$.
- The total energy of all other gamma candidates is < 150 keV, which allows for low energy decays and small amounts of noise, but ensures that only one high energy gamma is detected.
- The same delayed hit criteria as in the 1e2γ channel are required to reduce the impact of events from ^{214}Bi.

Unlike the 1e1α and 1e2γ channels, it is not possible to perform stand-alone measurements in the 1e1γ channel, due to cross contamination with the 1e channel. This means that results from the 1e1γ channel must be extracted simultaneously with the 1e channel.

7.3.6. 1e Channel

The 1e channel is the simplest channel available and is very sensitive to β-decay isotopes. This means that it is used to measure all the remaining backgrounds to which the other channels are not sensitive, which are predominantly ^{210}Bi, ^{234m}Pa and ^{40}K. The large number of data events in this channel, means that it is possible to disentangle the different background contributions by fitting them to the shape of the energy spectrum, when accompanied by information from the other background channels. The selection criteria for the 1e channel are understandably similar to those for the 1e1γ channel:

- There is one electron candidate in the event as set out in the 1e1γ channel.

- There may be any number of gamma candidates in the event, as long as their total energy is < 150 keV.
- The same delayed hit criteria as in the 1e1γ and 1e2γ channels are applied.

7.4. Results of Background Measurements

In order to extract the activities, the four channels described above (1e, 1e1γ, 1e2γ and 1e1α) are simultaneously fitted with a number of parameters that describe the activities of each MC sample. The data used was described in Section 6.5, totalling a dead-time corrected exposure of 1918.5 days. In this section, the procedure used for fitting is described (Section 7.4.1), followed by the presentation of the results of this process (Section 7.4.2). Finally, distributions that were not used to fit the background activities are shown as a cross-check of the validity of the background model (Section 7.4.3).

7.4.1. Fitting Procedure

The fitting procedure used to extract the different isotope activities is based on a binned log-likelihood fit as described in Section 6.6.1. All four channels are used to simultaneously extract the most likely activity parameters.

In the 1e, 1e1γ and 1e2γ channels, the electron energy distribution is used, since there are different isotopes present and each has a different spectral shape. However, in the 1e1α channel, only ^{214}Bi is present and so another variable is required to extract the relevant information. In this case, the length of the alpha track is used, which is suitable as it is a strong function of the energy of the alpha when released into the tracking gas. It is therefore sensitive to whether the particle originated, say, at the surface of the foil or inside the Mylar film.

In order to separate out the available information in each channel, different histograms are constructed with the aim of minimising the number of fit parameters to which each is sensitive. In particular, the 1e1α channel is separated out into 24 histograms of alpha track length, with different combinations of event geometry for each sector and each phase. The geometrical divisions relate to the sides of the detector of the alpha and electron tracks, giving four separate combinations as shown in Figure 7.11.

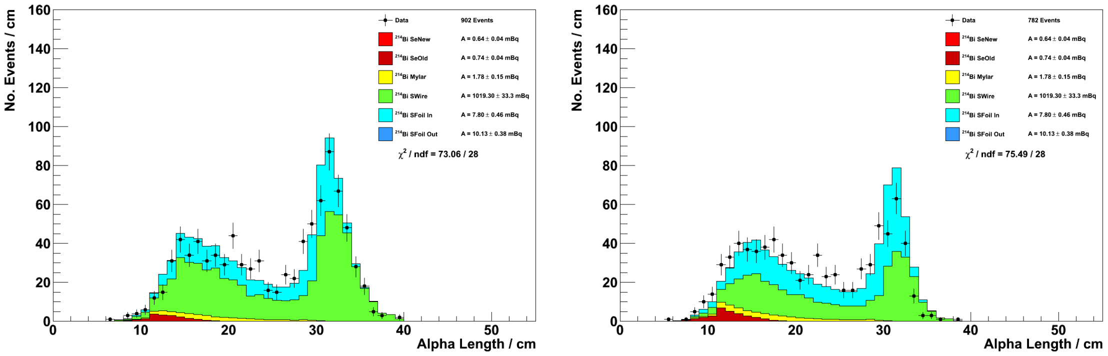

(a) Inner side, α & e^- same side **(b)** Inner side, α & e^- opposite side

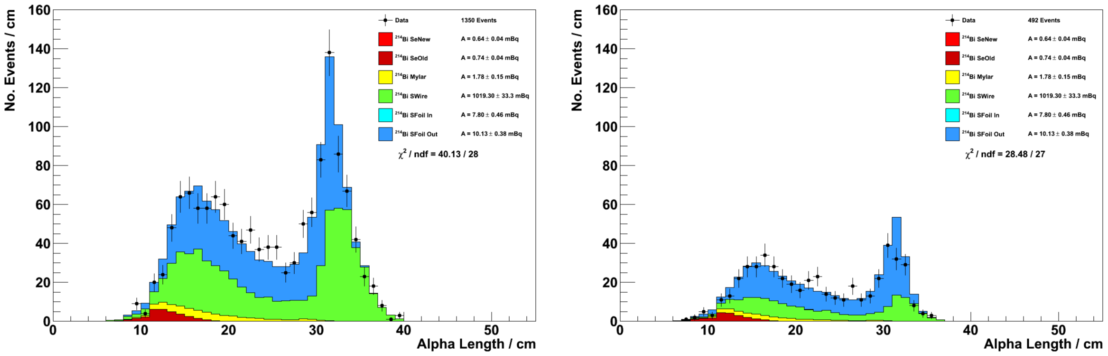

(c) Outer side, α & e^- same side **(d)** Outer side, α & e^- opposite side

Figure 7.11.: Distributions of the alpha track length in the 1e1α channel, which are those used in the fit. The distributions for sector 6 are shown with different combinations of alpha and electron side.

Where electron energy histograms are used (1e, 1e1γ and 1e2γ), the histograms are divided into different samples for SeOld and SeNew. In addition, for the 1e and 1e1γ channels, the SeNew sample is further subdivided into histograms for sector 7 and sector 8 to account for the higher activity observed in sector 8 during the hot spot search (Figure 7.9). Finally, these histograms are split between the two phases to give a total of 38 histograms for the binned log-likelihood fit as shown in Table 7.3.

These 38 histograms are fitted with 28 parameters that describe the background activities for the detector and are divided across the different background classifications as follows:

Channel	Histograms	Description
1e1α	24	4 × in/out combinations × 3 sectors × 2 phases
1e2γ	2	SeOld and SeNew
1e1γ	6	SeOld, SeNew (sect. 7) & SeNew (sect. 8) ×2 phases
1e	6	SeOld, SeNew (sect. 7) & SeNew (sect. 8) ×2 phases

Table 7.3.: Division of histograms used in the binned log-likelihood fit.

- **Internal Backgrounds:** 9 activities for the internal source contamination giving ^{214}Bi, ^{208}Tl, ^{234m}Pa, ^{40}K activities for samples of SeOld and SeNew and a final parameter to describe the contamination of the Mylar backing film with ^{214}Bi.

- **External Backgrounds:** 4 parameters that describe an "adjustment factor" for each isotope described in the external background model (^{40}K, ^{214}Bi, ^{60}Co and ^{208}Tl). For example, all ^{40}K activities in the external background model are scaled by the same adjustment factor.

- **Radon Backgrounds:** 15 activities divided into P1 and P2 contributions. These include 6 for ^{214}Bi encompassing SWire, SFoil (inner side), SFoil (outer side), 2 for ^{208}Tl SWire, 6 for ^{210}Bi SFoil split into SeOld, SeNew (sector 7) and SeNew (sector 8) and finally 1 activity for ^{214}Bi in the air of LSM which is only included in P1.

In all the channels, the ^{214}Pb activity is assumed to be in equilibrium with ^{214}Bi and likewise for ^{228}Ac, ^{212}Bi and ^{208}Tl. These sub-sets of decay chains are therefore only parametrised by one activity.

Finally, for certain parameters, there was not enough available information in these channels to perform a reliable measurement. As a result, Gaussian constraints (as described in Section 6.6.1) were used to constrain the activity of ^{214}Bi in the Mylar to 1.53 ± 0.46 mBq and the ^{208}Tl SWire to 3.5 ± 0.4 mBq for phase 1 and 2.9 ± 0.4 mBq for phase 2. These constraints were taken from a HPGe measurement and a separate NEMO-3 analysis, respectively. Finally, the contributions of ^{210}Bi SScin and SWire were fixed to activities from previous NEMO-3 analyses where a suitable constraining value could not be found.

7.4.2. Activity Estimations

The fitting procedure utilised to obtain the results is described in this section. First, the histograms that have been used to perform the fit are presented, showing good agreement between data and simulation. Then the best estimates for background activities are summarised and compared with other results where appropriate.

1e1α Channel Distributions

The alpha length distributions from the 1e1α channel, using the resulting ^{214}Bi activities, can be seen in Figure 7.12. The internal contribution (in red) has the shortest track lengths as these alpha particles must traverse the most material before entering the tracking gas. The mylar contribution (in yellow) has intermediate lengths between the internal and SFoil and SWire contributions (in blue and green respectively). The SWire sample has the longest tracks, out to 40 cm, since these alphas may originate from tracker cells away from the foil. Since the track length is calculated from the foil intersection, this artificially elongates the length. The peaks in the distribution are caused by the geometry of the tracker with the second peak at ~ 33 cm a result of the next layers of tracker cells.

The difference between phases 1 and 2 is immediately clear, with a significantly higher proportion of SWire and SFoil events during phase 1. In phase 2 there is a larger contribution from the internal and Mylar components which have common activities across both phases. There is also higher activity on the outer side of the foils than on the inner side, which is expected given the large volume on this side of the detector.

In general, there is fair agreement between data and simulation. There is more MC than data in the peak at 30 cm and the data appears systematically higher in the region of $20 - 30$ cm. This is likely to be as a result of poor replication of the composition of the tracking gas in the simulation as the length of the alpha track is sensitive to small changes in its alcohol content. This results in a transferral of activities from the SWire to SFoil samples which does not significantly affect the $2\nu\beta\beta$ or $0\nu\beta\beta$ channels, since these two samples have similar efficiencies when selecting 2e events.

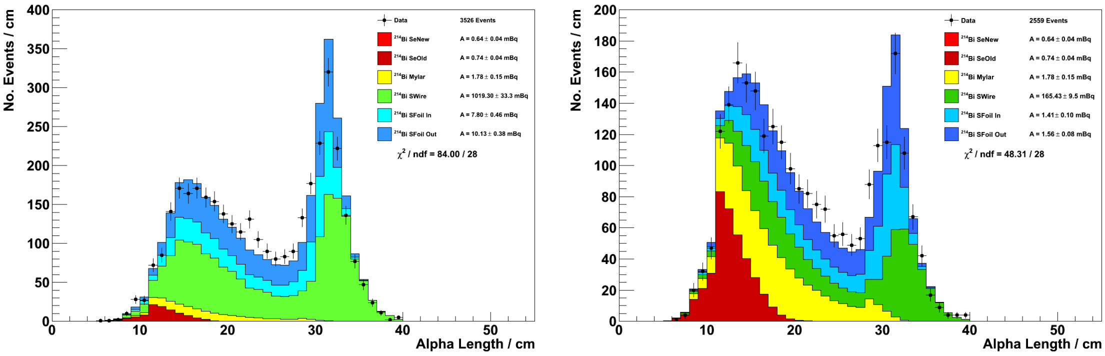

(a) Sector 6 Phase 1 **(b)** Sector 6 Phase 2

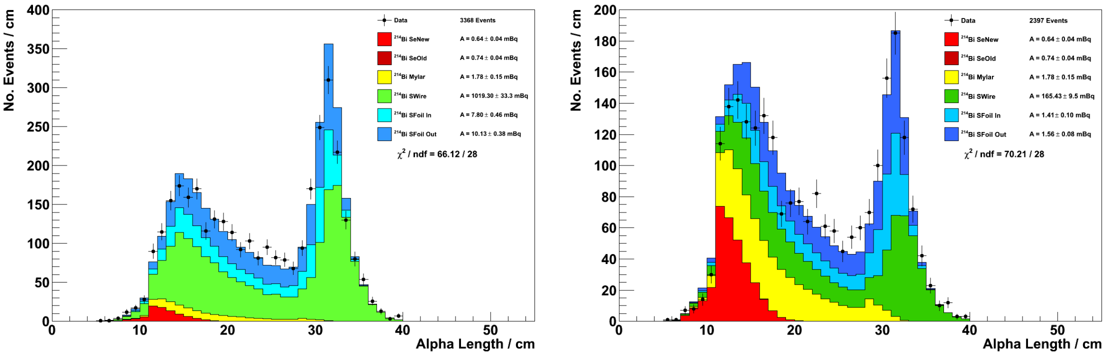

(c) Sector 7 Phase 1 **(d)** Sector 7 Phase 2

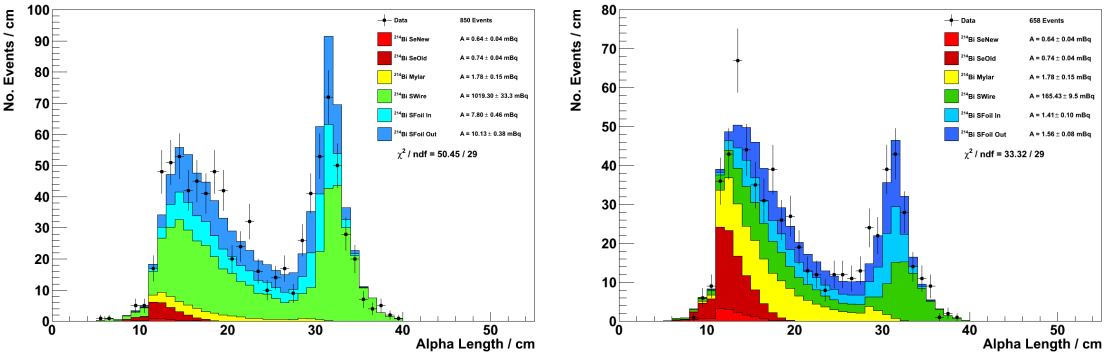

(e) Sector 8 Phase 1 **(f)** Sector 8 Phase 2

Figure 7.12.: Distributions of the length of alpha track from the 1e1α channel, after fitting for the activities. Plots are shown for each sector and phase, with each one the sum of four in/out combinations of fit histograms.

1e2γ Channel Distributions

The histograms used in the fit from the 1e2γ channel may be seen in Figure 7.13. As described in the 1e2γ selection, the contributions from ^{214}Bi are heavily suppressed such that channel is dominated by the internal contributions of ^{208}Tl, with a $\sim 10\%$ contribution from the ^{208}Tl SWire. It should be clear that there is no discriminating power between the internal and SWire ^{208}Tl samples in these histograms and as result, the Gaussian constraint is necessary. There is good agreement in the SeOld sample, but the SeNew component is overestimated. This disagreement appears as a result of inclusion of the histograms from the 1e channel. The difference between this result and the SeNew ^{208}Tl activity from the 1e2γ channel alone is within the systematic uncertainty for measurements of the internal backgrounds.

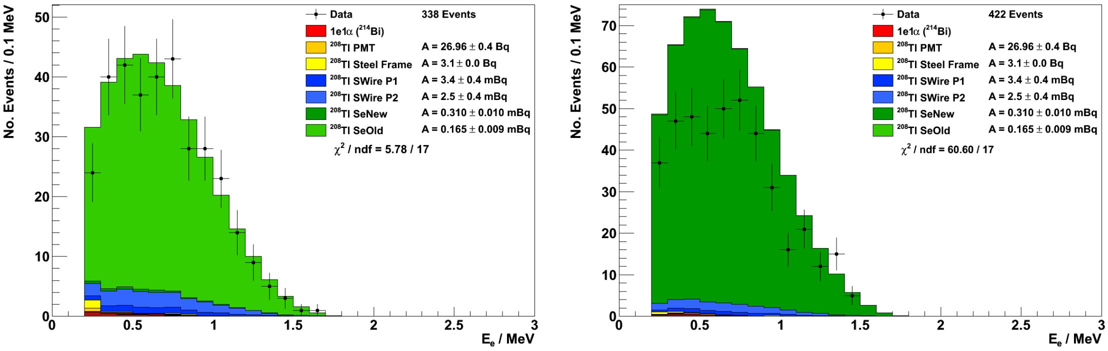

(a) SeOld (b) SeNew

Figure 7.13.: Electron energy distributions from the 1e2γ channel, with activities extracted via the fitting procedure. The SeNew and SeOld samples are shown separately.

1e1γ Channel Distributions

The resulting distributions for the 1e1γ channel are shown in Figure 7.14. There is very little difference between the SeOld and SeNew samples – both are dominated by external backgrounds with small additions from samples which are in the 1e1α and 1e2γ channels. The difference between phases 1 and 2 provides the activity of the ^{214}Bi in the LSM air.

The agreement between data and simulation is good, although there appears to be a small deficit of MC at low energies and there are some high energy outliers in data that are not reproduced in MC. The low energy deficit is a result of the copious number of gamma-emitting isotopes with low Q values that are not fully replicated in the external background model. This situation can be improved by the addition of a small 1 MeV gamma flux, but this small deficit does not have a significant impact on the 2e channels. The few high energy events in data are likely to be caused by neutrons where the events have not been rejected based on timing. Again, these have minimal effect in the 2e channels.

1e Channel Distributions

The electron energy distributions for the 1e channel for phase 2 data are displayed in Figure 7.15. The equivalent distributions from phase 1, which are not shown, are very similar. In general, there are broad similarities between the different samples and phases. In all, the distributions are dominated by contributions from ^{210}Bi, ^{40}K and $^{234\text{m}}$Pa. The ^{210}Bi end-point is at 1.0 MeV, the ^{40}K at 1.3 MeV and the $^{234\text{m}}$Pa at 2.4 MeV. In the higher energy region, the contributions from the external ^{208}Tl and ^{214}Bi backgrounds become significant and at energies above 2.7 MeV, the internal and SWire ^{214}Bi samples are the only remaining contributions.

In the SeOld and SeNew (sector 7) distributions there is excellent agreement, and there is clear evidence of the uneven distribution of $^{234\text{m}}$Pa between the two samples. It is apparent that the greater activity that was seen in SeNew in sector 8 in the hot spot search can be explained by an extra addition of ^{210}Bi. The resulting ^{210}Bi SFoil activity is nearly an order of magnitude larger than the level in the remainder of the SeNew sample. ^{210}Bi is a result of deposition of ^{210}Pb by radon during manufacture of the foils, so if this strip of SeNew was exposed to radon in the air for a longer time, then a higher level of ^{210}Bi would be expected.

However, even with the addition of extra ^{210}Bi, the agreement in SeNew (sector 8) at energies below 1 MeV is not perfect, which is likely due to small variations in the ^{40}K and $^{234\text{m}}$Pa234m activities in this sector compared to SeNew (sector 7). It is not anticipated that this small, low energy discrepancy in one small strip will cause significant problems for the background model in a $2\nu\beta\beta$ analysis or $0\nu\beta\beta$ search.

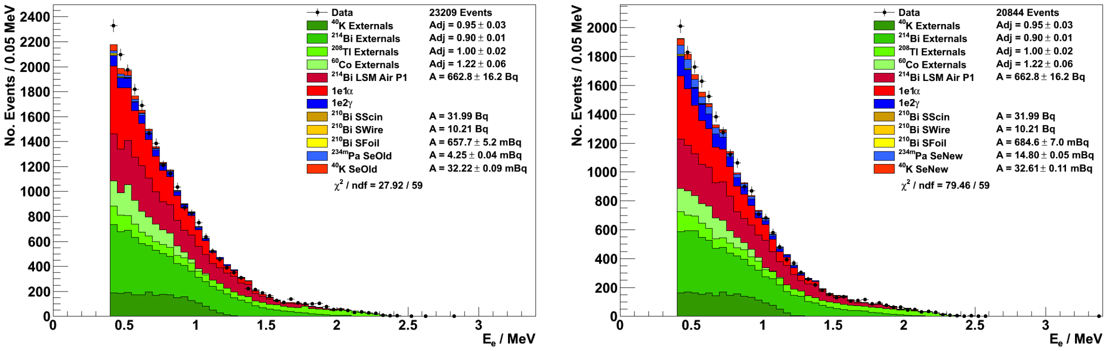

(a) SeOld Phase 1 **(b)** SeNew Phase 1

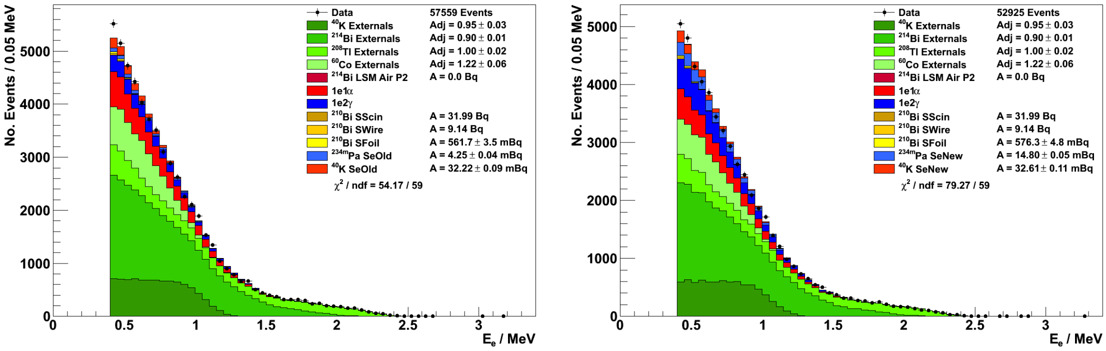

(c) SeOld Phase 2 **(d)** SeNew Phase 2

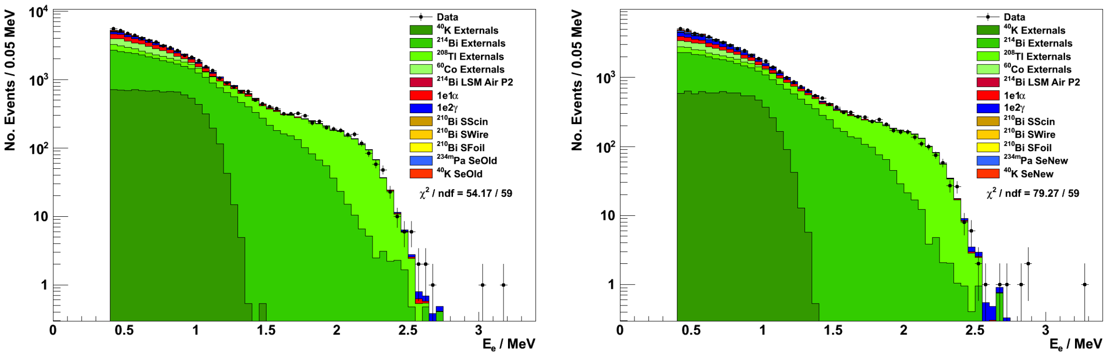

(e) SeOld Phase 2 (log scale) **(f)** SeNew Phase 2 (log scale)

Figure 7.14.: Electron energy distributions for the 1e1γ channel for the SeOld and SeNew sample. The phase 1 and phase 2 histograms are displayed, with the phase 2 plots also shown on a logarithmic scale.

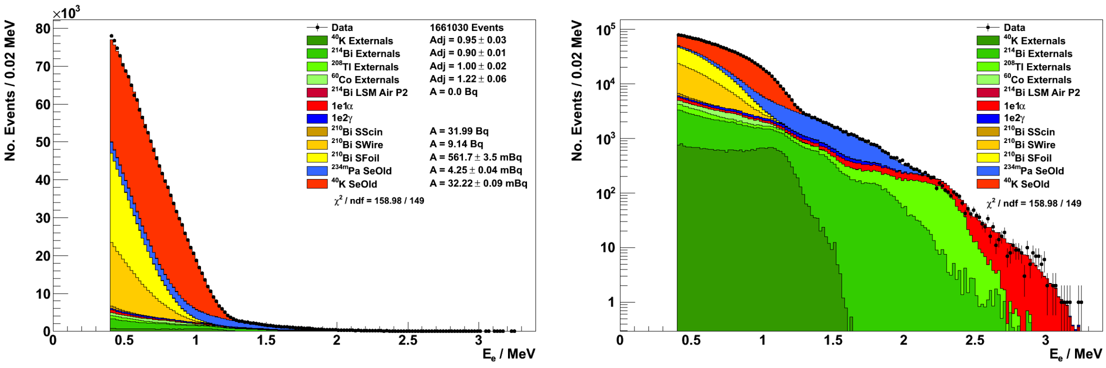

(a) SeOld **(b)** SeOld (log scale)

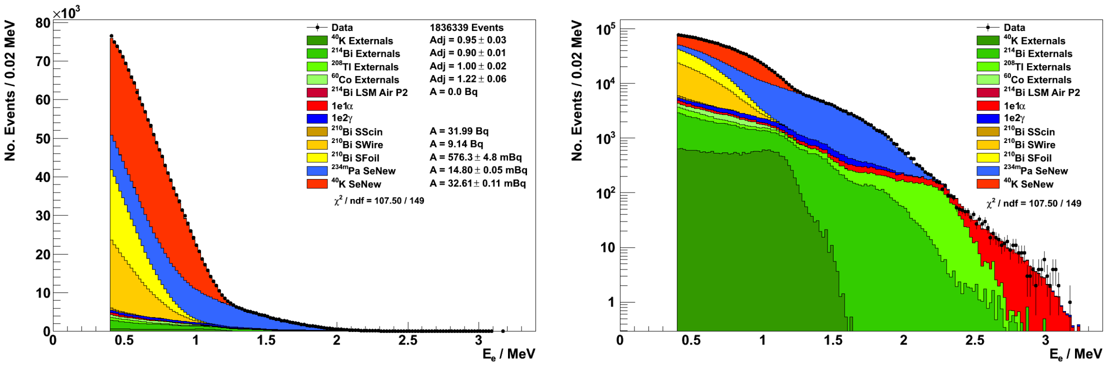

(c) SeNew Sector 7 **(d)** SeNew Sector 7 (log scale)

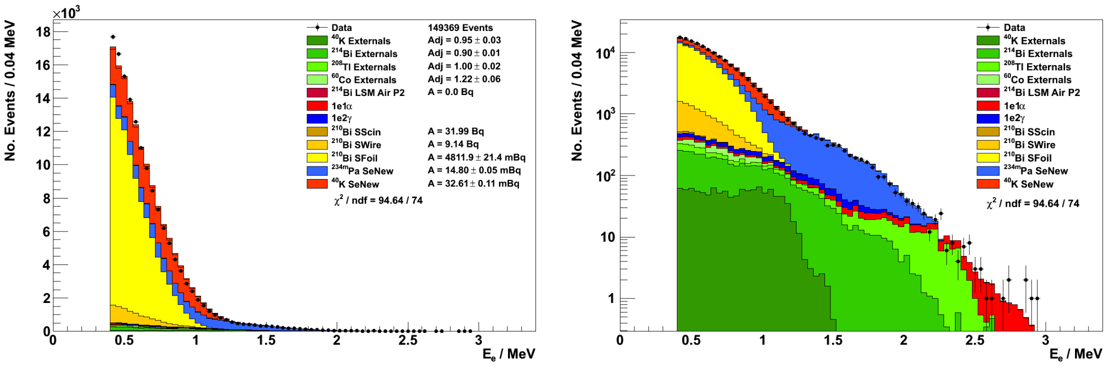

(e) SeNew Sector 8 **(f)** SeNew Sector 8 (log scale)

Figure 7.15.: Electron energy distributions for the 1e channel from phase 2 data. The SeOld sample is displayed along with the SeNew sample broken down into components from sector 7 and sector 8.

Internal Background Results

The internal background activities that emerge as a result of the fit are shown in Table 7.4. The contributions from ^{208}Tl and ^{214}Bi are small, which is essential for a sensitive $0\nu\beta\beta$ search. The dominant contaminants inside the foils are ^{234m}Pa and ^{40}K. The level of ^{40}K is similar in both foil samples at $\sim 50 - 60$ mBq/kg, but there is a large difference in the ^{234m}Pa contamination with SeNew almost three times as dirty as SeOld.

Isotope	Location	Activity / mBq	Activity / mBq/kg
^{214}Bi	SeOld	0.74 ± 0.04	1.73 ± 0.09
^{214}Bi	SeNew	0.64 ± 0.04	1.21 ± 0.07
^{214}Bi	Mylar	1.78 ± 0.15	2.01 ± 0.17
^{208}Tl	SeOld	0.16 ± 0.01	0.32 ± 0.02
^{208}Tl	SeNew	0.31 ± 0.01	0.51 ± 0.02
^{234m}Pa	SeOld	4.25 ± 0.04	8.19 ± 0.07
^{234m}Pa	SeNew	14.80 ± 0.05	24.32 ± 0.08
^{40}K	SeOld	32.22 ± 0.09	62.14 ± 0.18
^{40}K	SeNew	32.61 ± 0.11	53.59 ± 0.18

Table 7.4.: Resulting internal background activities from the global background fit. All errors are statistical only and are shown at the 1σ level.

As described in Section 5.1.1, before inclusion in the detector, a HPGe measurement was made of the selenium foils. Due to time constraints, only one measurement could be made, which was a single measurement of equal numbers of SeOld and SeNew strips with roughly equal masses of both samples. The results of the measurements with NEMO-3 (Table 7.4) can be compared with the results of the HPGe measurement and this is shown in Table 7.5. There is remarkably good agreement between NEMO-3 and HPGe across all the isotopes.

Isotope	NEMO-3/ mBq/kg	HPGe / mBq/kg
^{214}Bi	1.54 ± 0.05	1.2 ± 0.5
^{208}Tl	0.41 ± 0.01	0.4 ± 0.13
^{234m}Pa	16.26 ± 0.06	< 18
^{40}K	57.86 ± 0.13	55 ± 5

Table 7.5.: A comparison of the measurements of internal backgrounds made by NEMO-3 and independently with a HPGe detector. The NEMO-3 activities have been calculated assuming equal masses of SeOld and SeNew and 15% mylar for ^{214}Bi. All error bars are statistical only and are at the 1σ level. The limit shown is at the 2σ level. The HPGe measurements are taken from [78].

External Background Results

The contributions from the external background model were measured with a single parameter for each isotope, which is an adjustment factor from the external background model. These values are shown in Table 7.6. Any deviation from unity expresses disagreement with the external background model, so it can be seen that there is reasonable agreement between the values for ^{214}Bi, ^{208}Tl and ^{40}K. There is a larger discrepancy observed between this work and the external background model for ^{60}Co, but this may be expected since the external background model is measured over all sectors and this analysis has only concentrated on a small fraction of the detector. The effective background model is expected to show variation at the level of $10 - 20\%$ from sector-to-sector and so these discrepancies are perfectly plausible.

Isotope	Adjustment
^{214}Bi	0.90 ± 0.01
^{208}Tl	1.00 ± 0.02
^{40}K	0.95 ± 0.03
^{60}Co	1.22 ± 0.06

Table 7.6.: The resulting adjustment factors for the external background activities from the fitted samples. The external background activities may be found by multiplying the values in the external background model (Table 7.1) by the appropriate adjustment factor for that isotope. The errors shown are 1σ statistical errors.

Radon Background Results

The final results from the background measurement are for the radon backgrounds, which are presented in Table 7.7. The ^{214}Bi SWire and SFoil results are sensitive to the radon level inside the detector and these results confirm that there is a reduction of a factor ~ 6 between P1 and P2. The measured ^{214}Bi activity in the LSM air in P1 corresponds to ~ 13 Bq/m^3, which is in good agreement with the measured value of ~ 15 Bq/m^3.

Recalling that the expected reduction in ^{210}Bi between phases 1 and 2 is $\sim 13\%$, it is apparent that the measured values are in reasonable agreement with this number. The larger reduction values of $17-19\%$ measured for the SeOld and SeNew (S7) foil surfaces can be explained by an overestimation of the value of ^{210}Bi SWire in P2 which was fixed in this analysis. The ^{210}Bi SWire activities were measured for a shorter period of data than this analysis, so the activity for P2 is slightly overestimated. Accordingly, the values measured for ^{210}Bi SFoil in this work are underestimated in phase 2. This hypothesis is further strengthened by noting that in the SeNew (S8) distribution, where the effect of the ^{210}Bi SWire is much smaller, agrees much better with the expected reduction.

Isotope	Location	P1 / mBq	P2 / mBq	P1:P2
^{214}Bi	SWire	1019.3 ± 33.3	165.4 ± 9.5	6.2 ± 0.4
^{214}Bi	SFoil (In)	7.80 ± 0.46	1.41 ± 0.10	5.5 ± 0.5
^{214}Bi	SFoil (Out)	10.13 ± 0.38	1.56 ± 0.08	6.5 ± 0.4
^{214}Bi	LSM Air	$(662.8 \pm 16.2) \times 10^3$	-	-
^{208}Tl	SWire	3.42 ± 0.40	2.45 ± 0.40	1.40 ± 0.28
^{210}Bi	SeOld	657.7 ± 5.2	561.7 ± 3.5	1.17 ± 0.01
^{210}Bi	SeNew (S7)	684.7 ± 7.0	576.3 ± 4.8	1.19 ± 0.02
^{210}Bi	SeNew (S8)	5439.9 ± 43.5	4811.9 ± 21.3	1.13 ± 0.01
^{210}Bi	SWire	10.21×10^3	9.14×10^3	1.12
^{210}Bi	SScin	31.99×10^3	31.99×10^3	1.00

Table 7.7.: Resulting activities for the radon backgrounds, showing the measured values for P1, P2 and their ratio. Errors are statistical only and at the 1σ level.

7.4.3. Control Distributions

As a further check of the validity of the background model, it useful to study control distributions which have not been used in the fitting procedure. These can highlight inconsistencies in the background model or degeneracies in the electron energy distributions where the wrong combination has been found.

Regular calibrations are made with electron sources inside NEMO-3 and as a result, the response of the detector to electrons is well-understood. However, alpha calibration sources are necessarily open and were therefore never used. As a result, it is particularly important to study well calibrated distributions for the 1e1α channel, rather than relying solely on the length of the alpha track. Some of these other distributions for the 1e1α channel can be seen in Figure 7.16.

In order to confirm the 1e1α channel is indeed studying BiPo type events, it is possible to use the time of the delayed alpha track to measure the ^{214}Po half-life. This distribution is shown in Figure 7.16b. In addition to true BiPo events, there is also a small contamination from re-firing of tracker cells at early times. Once this has been taken into account, a half-life of 162.1 ± 4.0 µs is measured, in good agreement with the expected value of 164.3 µs. The remaining distributions of electron and gamma energies confirm that there is good agreement between data and MC and the overall normalisation of ^{214}Bi is correct. Finally, the distribution of events across different runs also shows that both phase 1 and phase 2 data are well reproduced.

Another set of control plots can be observed from the 1e1γ channel, shown in Figure 7.17. In these plots, the cosine of the angle between the electron and gamma is shown, along with the energy of the gamma.

The cosine of the angle between the electrons shows reasonable agreement, although there may be a small deficit of back-to-back particles and those at acute angles. However, the Bremsstrahlung electrons produced by ^{40}K, ^{234m}Pa and ^{210}Bi at very narrow angles appears to be replicated accurately in simulation. The energy of the gamma appears well reproduced over the whole energy range in both the SeOld and SeNew samples, although there may be a hint of the same overestimation of ^{208}Tl in the SeNew sample as seen in the 1e2γ channel.

In general, there is good agreement between the NEMO-3 measurements and all other available information, so it is reasonable to have a high degree of confidence in this

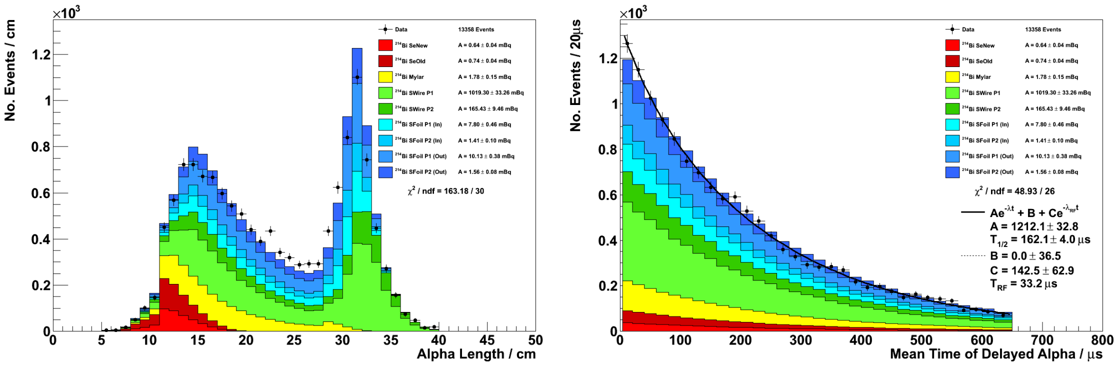

(a) α track length **(b)** α trigger time

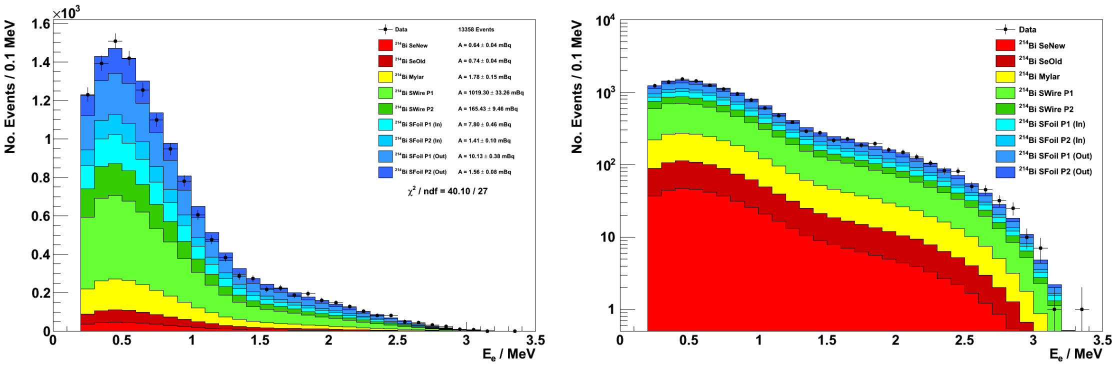

(c) e^- energy **(d)** e^- energy (log scale)

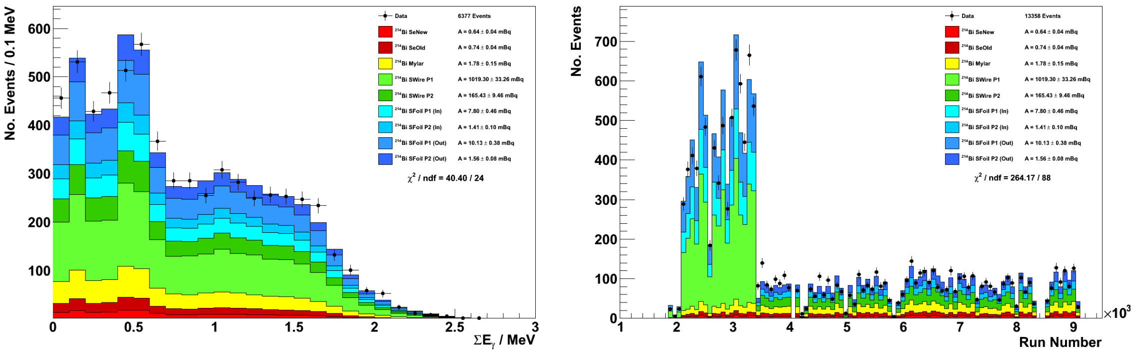

(e) Total γ energy **(f)** Run number

Figure 7.16.: Distributions from the 1e1α channel, showing good agreement between data and simulation across a wide range of variables.

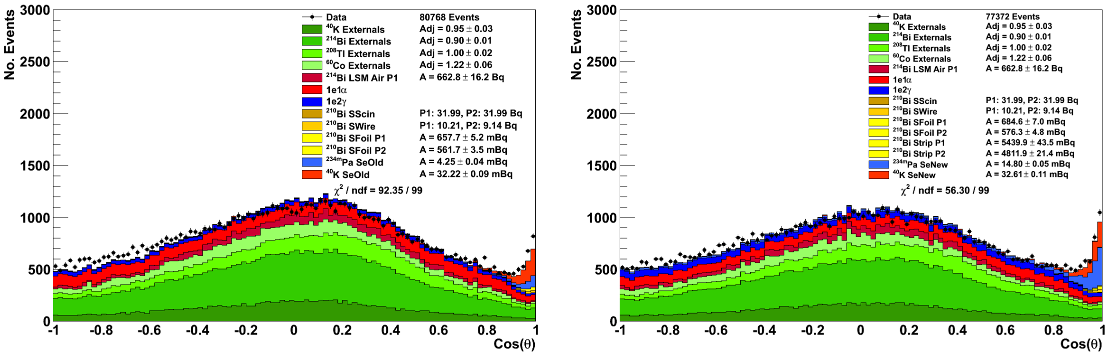

(a) $e^- - \gamma$ cosine SeOld **(b)** $e^- - \gamma$ cosine SeNew

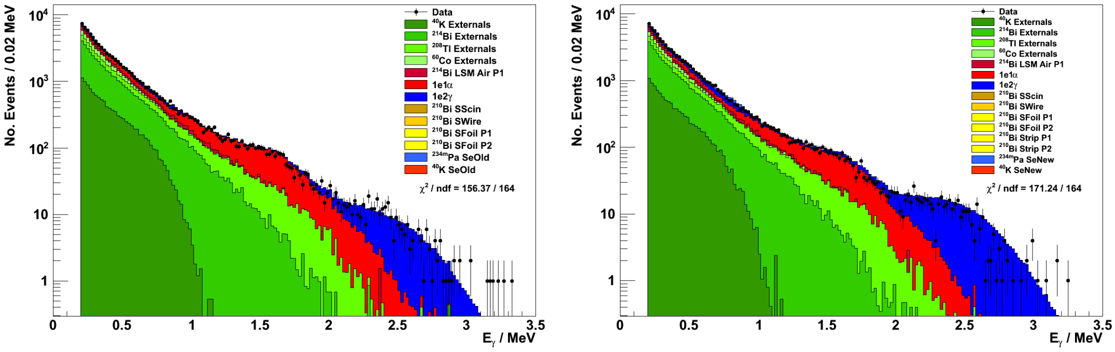

(c) γ Energy SeOld **(d)** γ Energy SeNew

Figure 7.17.: Distributions from the 1e1γ channel. The cosine of the angle between the γ and e^- emissions and the energy of the γ are displayed.

background description. Further, as will be shown in Section 8.2.3, the systematic uncertainties associated with these background measurements have a small effect on any $2\nu\beta\beta$ measurement compared to other systematic uncertainties. The background levels detailed here are ultimately re-measured along with any observed signal, but this model is used to optimise the appropriate cuts for a $2\nu\beta\beta$ measurement, which will be described in the next chapter.

Chapter 8.

Double Beta Decay Results for ^{82}Se

The main aims of the NEMO-3 analysis described in this thesis are the measurement of the $2\nu\beta\beta$ half-life of ^{82}Se and a search for $0\nu\beta\beta$ with the same isotope. The extraction of these results is the focus of this chapter. The double beta decay analyses follow the procedure outlined in Chapter 6, where simulated $2\nu\beta\beta$, $0\nu\beta\beta$ and background events are propagated through a description of the NEMO-3 detector and then compared with experimental data.

The measurement of the $2\nu\beta\beta$ half-life is performed first, as it is required for the $0\nu\beta\beta$ search. In order to achieve the best measurement of $2\nu\beta\beta$, the background model that was defined in the previous chapter is used to optimise a set of selection criteria to create a $2\nu\beta\beta$ channel (Section 8.1). This optimised channel is then used to produce a measurement of the $2\nu\beta\beta$ half-life (Section 8.2).

Having measured the $2\nu\beta\beta$ process, it is possible to perform a similar optimisation to ensure the best sensitivity for the various different $0\nu\beta\beta$ mechanisms (Section 8.3). Finally, the results of measurements with these $0\nu\beta\beta$ channels are outlined (Section 8.4).

8.1. Optimisation of $2\nu\beta\beta$ Cuts

8.1.1. Starting Point for Optimisation

In order to make a measurement of the $2\nu\beta\beta$ half-life with NEMO-3, a new channel is introduced alongside the four background channels described in Section 7.3. This $2\nu\beta\beta$ channel should aim to allow the best possible measurement of the $2\nu\beta\beta$ half-life, which here is taken to mean the measurement with the lowest possible statistical and systematic errors. In this section, the optimisation of the channel is detailed.

It is important not to introduce any bias by using experimental data to perform the optimisation and so MC simulations will be used for the process. However, before moving to the sole use of MC, a suitable starting point must be found where data and MC are in good agreement. The key principle behind this starting point is to find a very loose set of analysis cuts, which leave plenty of room for optimisation, whilst ensuring that un-simulated detector behaviour or backgrounds do not affect the result.

The optimisation is performed on MC distributed over the same set of runs as the background measurements, which gives an exposure of 1918.5 days (Section 6.5). The sum of the electron energy will be used to extract the $2\nu\beta\beta$ half-life, so it is imperative that there is good agreement between data and MC in this distribution. To assess the level of agreement, the background model described in the previous chapter is used, along with a signal with half-life of 10^{20} yr which is similar to the previously measured phase 1 value of $(9.6 \pm 0.3(\text{stat}) \pm 1.0(\text{syst})) \times 10^{19}$ yr [73].

To find the starting point for the optimisation, the minimal set of cuts that form a two electron channel is applied, as set out below:

- There are two tracks in the event, both of which intersect the foil and are associated with isolated (and different) calorimeter hits.
- These calorimeter hits pass the quality criteria set out in Section 7.3.1.
- The vertex of the event, defined as the midpoint of the two track intersections, must be within the selenium foils, ± 120 cm in z and not in a hot spot.

- There is a maximum of one prompt, unassociated Geiger hit within 15 cm of the vertex in the xy-plane, which acts as a safe-guard against poor track reconstruction.
- If the tracks are on the same side of the foil, no prompt, unassociated Geiger hits are allowed within 15 cm of the vertex in the xy-plane and there are a maximum of two anywhere in the detector.
- If the tracks are on the same side of the foil, at least one of the track hits is in the first tracker layer.

After the application of these cuts, the distribution of total electron energy appears as in Figures 8.1a and 8.1b, where it can be seen that although the overall normalisation is impressively similar, there are significant disagreements at low and high energies. To improve this agreement, a further set of very loose cuts is applied according to the following selection criteria:

- The two electrons have an internal probability $> 0.0001\%$ and an external probability $< 10\%$. These values remove a large proportion of background events from external sources.
- The energy of each electron is > 400 keV. This value is chosen as this was the minimum energy of electrons when building the background model.
- The distance between the two electron intersections is < 30 cm in the xy-plane and < 50 cm in z.
- There are enough Geiger cathode signals to locate the vertex in z.
- The total γ energy in the event is < 250 keV.

The total electron energy distribution, after applying these extra cuts, can be seen in Figures 8.1c and 8.1d. There is clearly much better agreement between data and simulation and the optimisation can proceed from this point using only simulated data.

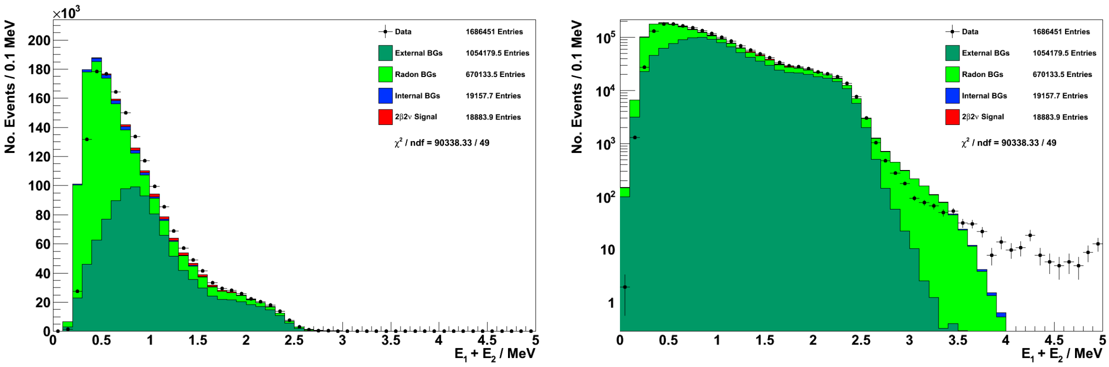

(a) Minimal 2e Cuts **(b)** Minimal 2e Cuts (log scale)

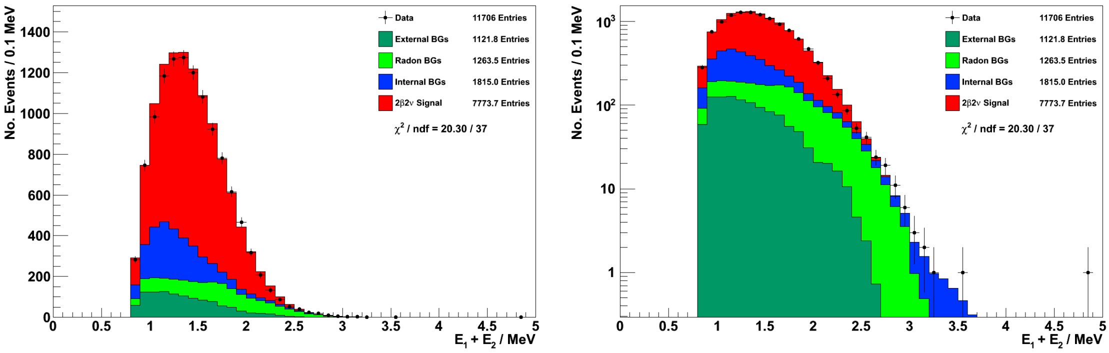

(c) Starting Point Cuts **(d)** Starting Point Cuts (log scale)

Figure 8.1.: Distribution of the electron energy sum for the events. (a) and (b) show the distribution after a minimal set of cuts. (c) and (d) show the distribution after applying very loose cuts to form the starting point for the optimisation.

8.1.2. Optimisation Procedure

In this optimisation procedure, two different types of cuts are considered. The first type are “binary” cuts, which are those cuts that may either be on or off and may or may not improve the $2\nu\beta\beta$ result. The second type are “optimisable” cuts which can take a range of values and which may improve the $2\nu\beta\beta$ result if an appropriate value is chosen.

Five different cuts of the binary type were considered for optimisation:

- **Phase 1:** There is a higher level of background in phase 1, with roughly equal numbers of radon events in phases 1 and 2, despite having only 20% of the exposure. Therefore, it may be beneficial to remove this period from the analysis.
- **Run status:** There is a sub-set of data runs in the NEMO-3 standard analysis data set where the detector is performing at its very best. An improved result may be achieved by using only these runs, obtaining higher quality data with a reduction of exposure of $\sim 10\%$.
- **Negative tracks:** Requiring negative tracks suppresses backgrounds from positrons and crossing electrons, but it also removes true signal events due to identification inefficiencies.
- **SeNew (sector 8):** The strip of SeNew in sector 8 has a much higher level of ^{210}Bi and a comparatively small amount of ^{82}Se. The measurement may be more accurate without this strip.
- **Delayed alphas:** Requiring no delayed alpha candidate near to the vertex removes ^{214}Bi events, which should remove background without affecting signal. The proximity to the vertex is defined as in Section 7.3.4.

At the same time as optimising these binary cuts, the following continuous variables were considered for an optimisable cut:

- **Electron energy:** As detailed above, the minimum requirement for agreement between data and MC is that electrons must have an energy deposit > 400 keV. There may be further improvement by putting further requirements on any of the minimum electron energy (E_{min}), maximum electron energy (E_{max}) or sum of electron energies ($E_{min} + E_{max}$).

- **Track length:** The length of an electron track directly impacts on the ability to distinguish between external and internal events since longer track lengths will have greater temporal separation. Similarly to the electron energy, can a better result be achieved by cutting on L_{min}, L_{max} or $L_{min} + L_{max}$?
- **Track hit layers:** Track reconstruction and vertex location is improved by requiring that the track has hits near to the foil or scintillator. Additionally, requirements on track hits may also remove backgrounds originating on the tracker wires. The two ends of the track are put forward for optimisation in the form of how many tracker layers are missed from the foil and to the scintillator hit.
- **Vertex separation:** The track vertex resolution means that the electron vertices may be a certain distance apart, however, background contributions may have an even larger spatial separation between their two electrons. This cut removes events based on the electron vertex separation in the xy-plane and in z independently.
- **Event probabilities:** It is clear that signal and external backgrounds will have different internal and external probability distributions. However, the same may also be true for internal backgrounds if a decay is to an excited state with a significant lifetime. Therefore, the internal and external probability cut values are considered for optimisation.

In order to find the optimal set of cuts, each combination of binary cuts is considered separately. For each of these 32 cases, different values of the optimisable cuts were scanned to find the best combination. This was defined as the combination that provided the lowest expected statistical error on a measurement of the $2\nu\beta\beta$ half-life, found using a toy MC simulation. Finally, the best statistical error values for each of the 32 combinations were compared to find the best combination of binary cuts. The results of this procedure are presented in the next section.

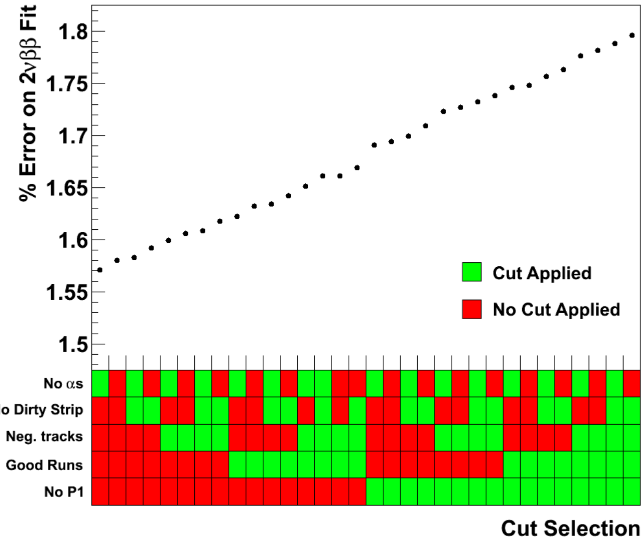

Figure 8.2.: The lowest statistical error, achieved by varying the optimisable cuts, for each combination of binary cuts.

8.1.3. Optimisation Results

The best statistical error value found for each combination of binary cuts is shown graphically in Figure 8.2. In this plot, the upper pane shows the expected error for the set of cuts given in the bottom pane. At a glance, it can be seen that there is a general trend of improved performance for the application of fewer cuts, with the best combination using only the alpha-proximity cut. The effects of the binary cuts are of increasing importance moving down those listed in the plot, with the strongest effect from the phase 1 cut and weakest from the alpha proximity cut.

Once the best collection of binary cuts has been found, it is possible to set the values used by the optimisable cuts. When choosing these values, it should be noted that as well as minimising statistical error, the level of systematic uncertainty must also be reduced. Therefore as a general principle, when there is little improvement in statistical accuracy, conservative cut values are chosen.

The results of scanning over the optimisable cut parameters, using the best combination of binary cuts (no α candidates only), are presented in Figures 8.3 and 8.4. In the plots shown, when scanning across one parameter, all others are fixed to their chosen values indicated by the red lines on each plot.

The results of moving the electron energy cut values are shown Figures 8.3a–8.3c. From these plots, there is no advantage in increasing any of the cut values from their minimum values. Indeed, for the minimum electron energy in particular, the response is a strong function of energy and there may be considerable improvement by lowering this value. However, this would require re-building the background model with a lower cut threshold which may prove challenging.

The track length parameters (Figures 8.3d–8.3f) are chosen to have the longest possible tracks without losing accuracy in the measurement. This increases the separation between the time of calorimeter hits and mitigates systematic uncertainty associated with this timing. The values chosen are $L_{min} > 20$ cm, $L_{max} > 50$ cm and $L_{min} + L_{max} > 80$ cm.

The parameters controlling the cuts based on the tracker layers that have been hit are shown in Figures 8.4a and 8.4b. There is no significant advantage from increasing the threshold to allow more than one missed layer and this could amplify the effect of noisy tracker cells in experimental data. As such, the first tracker hit is required to be in one of the first two layers, and the last tracker hit must be in one of the last two layers.

Similar reasoning is employed when considering the choice of the vertex separation cut values (Figures 8.4c and 8.4d). There is minimal improvement for a large vertex separation which would increase the possibilities of spurious tracks from noisy tracker cells, so conservative cut values of $\Delta XY < 2$ cm and $\Delta Z < 4$ cm are chosen.

The final optimisation parameters relate to the internal and external probabilities (Section 6.4) and are shown in Figures 8.4e and 8.4f. The internal probability variable has a stronger influence than the external probability value with the result improving down to very low probabilities. The “usual” NEMO-3 cut values are 4% and 1% for internal and external probability respectively. There is no variation in the accuracy of the measurement with external probability, so this value is kept at 1%. However, this analysis suggests that a slightly improved result can be achieved by lowering the minimum internal probability from 4%. It should be noted that the “usual” NEMO-3 values refer to $0\nu\beta\beta$ events so it is may be expected that a lower requirement is set for $2\nu\beta\beta$. A minimum internal probability value of 1% is chosen to improve the result whilst minimising any effects from systematic uncertainty associated with timing of calorimeter hits.

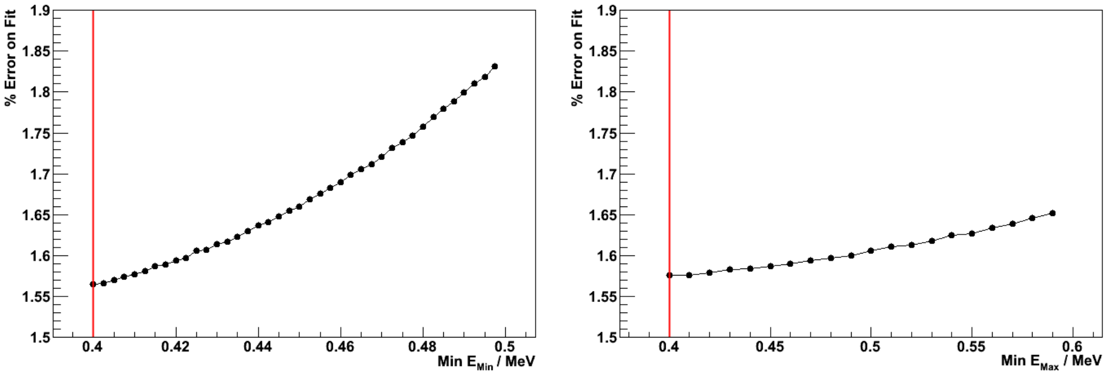

(a) Minimum e^- Energy **(b)** Maximum e^- Energy

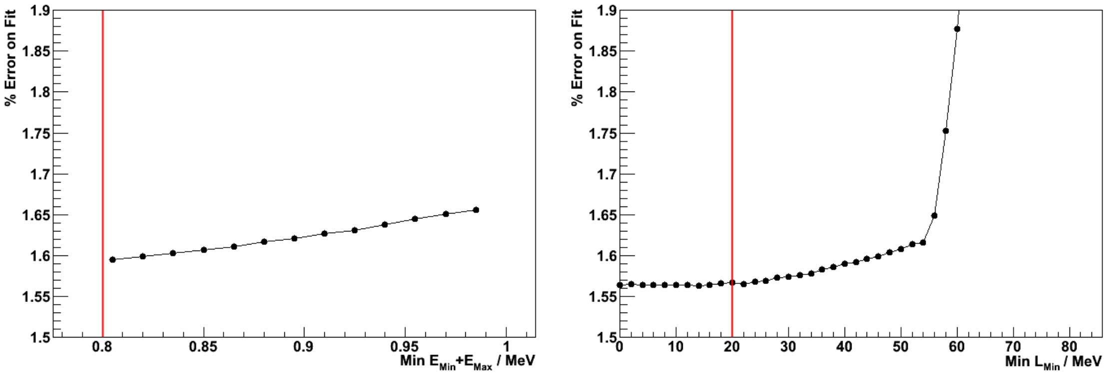

(c) Sum of e^- Energies **(d)** Minimum Track Length

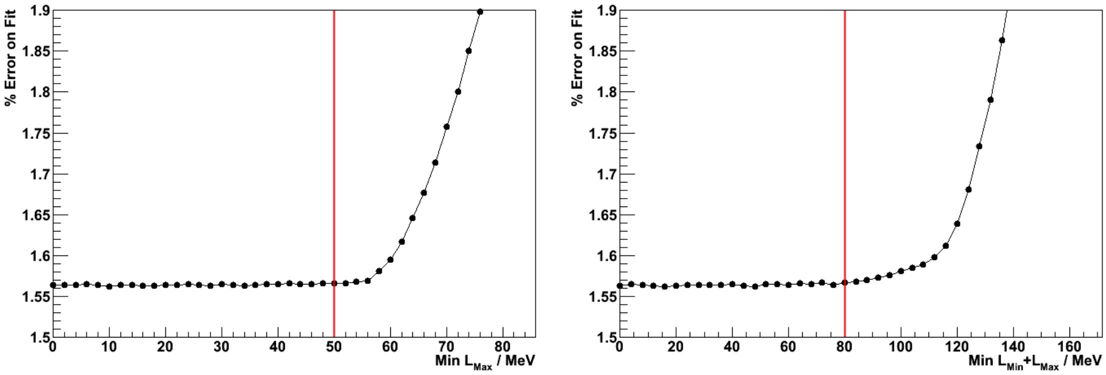

(e) Maximum Track Length **(f)** Sum of Track Lengths

Figure 8.3.: The expected statistical error on a $2\nu\beta\beta$ half-life of 10^{20} yr for different values of energy and track length cuts. The α candidate cut is the only binary cut that has been applied. The red lines show the chosen cut value for the $2\nu\beta\beta$ analysis.

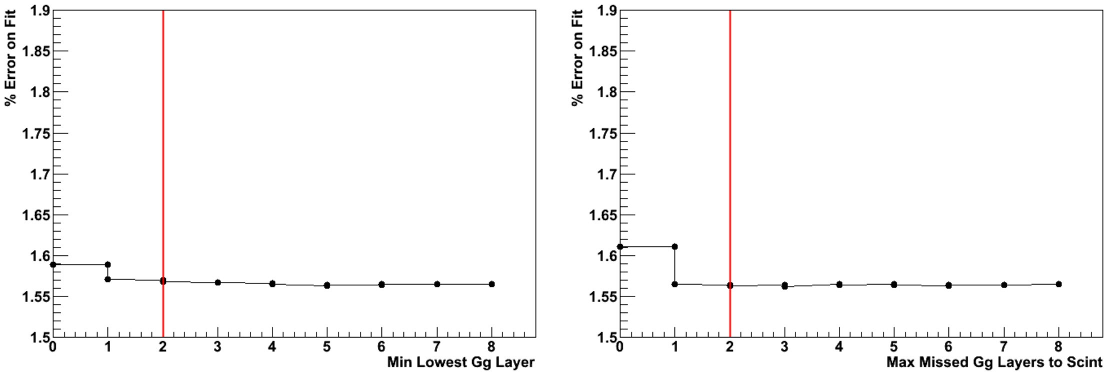

(a) Lowest Tracker Layer **(b)** Missed Layers to Calorimeter

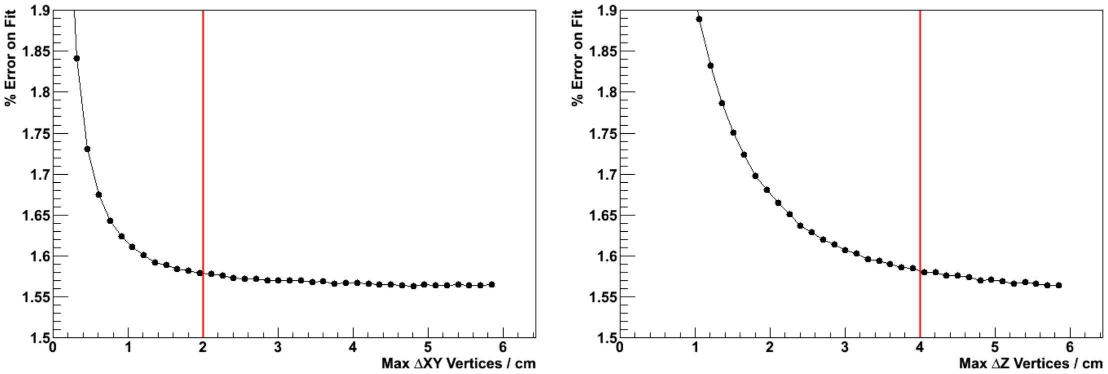

(c) Vertex Separation - xy **(d)** Vertex Separation - z

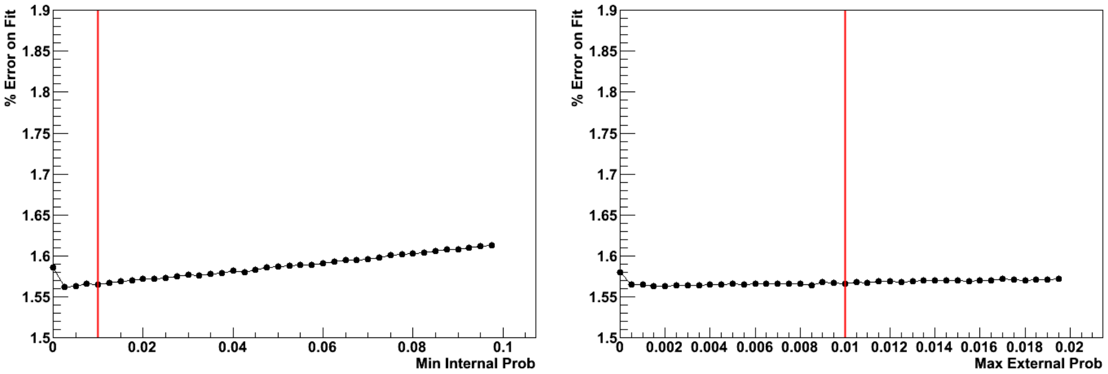

(e) Minimum Internal Probability **(f)** Maximum External Probability

Figure 8.4.: The expected statistical error on a $2\nu\beta\beta$ half-life of 10^{20} yr for different values of tracker layer, vertex separation and probability cuts. The α candidate cut is the only binary cut that has been applied. The red lines show the chosen cut value for the $2\nu\beta\beta$ analysis.

The incremental effect of the optimised cuts on the expected number of background events and $2\nu\beta\beta$ signal efficiency is shown in Table 8.1. The most significant cut for removing external and radon backgrounds is the internal probability cut. As expected, a large proportion of internal background events survive this cut and it also does not adversely affect the signal efficiency. One of the most damaging cuts for signal efficiency is the minimum energy requirement on electron energy. However, this also removes most of the internal background and radon background contributions, as well as a large proportion of the external backgrounds.

The final selection efficiency for the $2\nu\beta\beta$ signal is $(2.596 \pm 0.002(\text{stat}))\%$ and 1919.0 background events are expected. This selection efficiency is fairly uniform over most of the source foil area. However there are significant reductions towards the top and bottom of the detector as shown in Figure 8.5. This main cause of this reduction is the accidental removal of electrons hitting the petals scintillators as mentioned in Section 7.3.1.

	Expected Events			$2\nu\beta\beta$ Eff. /
Selection Cut	Internal	External	Radon	%
Minimum 2e cuts*	17382.3	1044918.0	651479.7	7.509
Both energies > 400 keV	2240.0	232258.3	54540.3	3.204
Total gamma energy < 250 keV	2066.4	219717.9	44793.6	3.195
Internal prob. > 0.01	1869.8	1000.4	1296.0	3.131
External prob. < 0.01	1869.8	1000.4	1296.0	3.131
Vertex not at $z = 0$	1869.8	985.6	1288.7	3.131
$\Delta XY < 2$ cm	1513.0	474.2	462.4	2.812
$\Delta Z < 4$ cm	1415.7	432.8	358.6	2.667
Track length cuts	1415.7	432.8	358.6	2.667
Gg hit in layer 0 or 1	1355.9	404.7	286.5	2.602
Gg hit in layer 7 or 8	1353.0	403.9	285.6	2.596
No α near vertex	1336.8	403.9	178.3	2.596

Table 8.1.: Expected number of internal, external and radon background events passing each stage of the optimised selection criteria sequentially. Also displayed is the $2\nu\beta\beta$ signal selection efficiency. *Minimum 2e cuts refers to those described in Section 8.1.1.

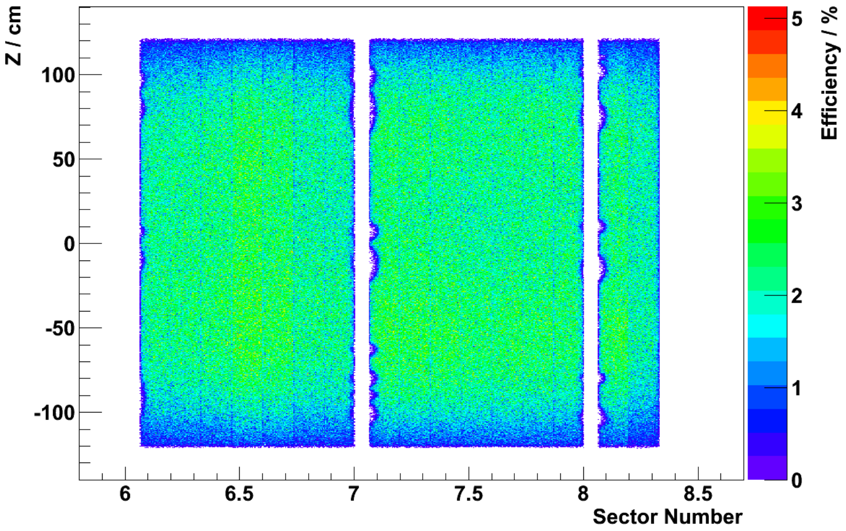

Figure 8.5.: Signal selection efficiency for the $2\nu\beta\beta$ channel as a function of the generated vertex position.

8.2. $2\nu\beta\beta$ Results

The procedure to find the strength of the $2\nu\beta\beta$ signal follows a binned log-likelihood method as described in Section 6.6.1 and as implemented to create the background model. In order to ensure that statistical correlations between signal and backgrounds are correctly treated, the method used to measure the background activities (Section 7.4.1) is simply extended to include a measurement of the signal.

Therefore, the $2\nu\beta\beta$ signal component is added to the four channels already used in the background measurement (1e, 1e1γ, 1e2γ, 1e1α) and the new $2\nu\beta\beta$ channel is added to the log-likelihood fit. The $2\nu\beta\beta$ signal is not expected to contribute to the 1e1γ, 1e1α or 1e2γ channels, but may have a small effect on the 1e channel where its low activity is compensated by a high selection efficiency of 10.83%. To include the $2\nu\beta\beta$ channel, the electron energy sum distribution is added to the background activity fit to take the total number of histograms to 39.

8.2.1. Re-measurement of Background Activities

The resulting background activities for the new fit can be seen in Table 8.2, which shows the new signal-and-background fit result alongside the ratio of the new value to that attained with the background-only fit. There is no significant change to any of the background activities, with the exception of the internal $^{234\mathrm{m}}$Pa contributions which have been slightly reduced. This is to be expected as the $2\nu\beta\beta$ signal has a more similar spectral shape to this isotope than any other. Further confirmation of $2\nu\beta\beta$ as the cause of this reduction comes by noting that the absolute reduction in activities of the $^{234\mathrm{m}}$Pa in SeOld and SeNew is similar.

In the $2\nu\beta\beta$ channel, a total of 8426 data events were selected from the 1918.5 days of data. The measurement predicts a total of 1890.1 background events, with 1309.5 from internal backgrounds, 402.9 from external backgrounds and 177.7 from radon backgrounds.

The sub-division of the internal background events can be seen in Table 8.3, where it can be seen that by far the largest proportion comes from contamination by $^{234\mathrm{m}}$Pa, which accounts for nearly half of the total expected background. The only other large contributor is ^{214}Bi which will become important for the $0\nu\beta\beta$ search. Between the two samples, there are more than twice as many expected background events from SeNew as SeOld and this is mainly due to its much higher level of $^{234\mathrm{m}}$Pa.

The breakdown of the external backgrounds is equally asymmetric as can be seen from Table 8.4. In this case, the majority of events come from sources of ^{208}Tl and ^{214}Bi. As discussed in Section 7.2.2, the origin of these backgrounds is from photons penetrating the detector and the strong gamma transitions of ^{208}Tl and ^{214}Bi are the cause of these dominating external backgrounds.

In the events from radon backgrounds (Table 8.5), again ^{214}Bi is dominant. The majority of these events come from the surface of the tracker wires with smaller contributions from the surface of the foil and from the air of the LSM. There are more than twice as many expected events in phase 1 compared to phase 2, but the overall contribution of the radon events is still sufficiently small that it is beneficial to include this period in the analysis.

Isotope	Location	Activity / mBq	Act.:BG-only Act.
^{214}Bi	SeOld	0.74 ± 0.03	0.998
^{214}Bi	SeNew	0.64 ± 0.03	0.996
^{214}Bi	Mylar	1.79 ± 0.12	1.002
^{208}Tl	SeOld	0.16 ± 0.01	1.000
^{208}Tl	SeNew	0.31 ± 0.01	1.001
^{234m}Pa	SeOld	4.01 ± 0.04	0.945
^{234m}Pa	SeNew	14.54 ± 0.05	0.983
^{40}K	SeOld	32.14 ± 0.09	0.997
^{40}K	SeNew	32.52 ± 0.10	0.997
^{214}Bi	Ext. BG Model	$0.90 \pm 0.01^{\dagger}$	1.003
^{208}Tl	Ext. BG Model	$1.00 \pm 0.02^{\dagger}$	0.994
^{40}K	Ext. BG Model	$0.94 \pm 0.03^{\dagger}$	0.989
^{60}Co	Ext. BG Model	$1.23 \pm 0.06^{\dagger}$	1.008
^{214}Bi	SWire P1	1018.4 ± 19.0	0.999
^{214}Bi	SWire P2	165.3 ± 7.8	0.999
^{214}Bi	SFoil (In) P1	7.81 ± 0.33	1.001
^{214}Bi	SFoil (In) P2	1.41 ± 0.07	1.000
^{214}Bi	SFoil (Out) P1	10.14 ± 0.30	1.001
^{214}Bi	SFoil (Out) P2	1.56 ± 0.07	1.000
^{214}Bi	LSM Air P1	$(663.0 \pm 13.7) \times 10^3$	1.000
^{208}Tl	SWire P1	3.42 ± 0.39	1.000
^{208}Tl	SWire P2	2.45 ± 0.36	1.000
^{210}Bi	SeOld P1	657.0 ± 5.1	0.999
^{210}Bi	SeOld P2	561.1 ± 3.4	0.999
^{210}Bi	SeNew (S7) P1	683.7 ± 6.6	0.999
^{210}Bi	SeNew (S7) P2	575.4 ± 4.3	0.998
^{210}Bi	SeNew (S8) P1	5438.4 ± 42.5	1.000
^{210}Bi	SeNew (S8) P2	4810.2 ± 20.8	1.000

Table 8.2.: Internal, external and radon background activities after including $2\nu\beta\beta$ in the background fit. The fourth column displays the ratio of the new activity to that measured using the background-only method. ^{210}Bi SWire and SScin values are still fixed and are therefore not included here. †Adjustment values rather than activities.

	Expected Events			
Isotope	SeOld	SeNew	Mylar	Total
^{214}Bi	91.3 ± 3.9	72.3 ± 3.6	15.4 ± 1.1	179.0
^{208}Tl	13.1 ± 0.7	21.7 ± 0.7	-	34.8
^{212}Bi	7.5 ± 0.4	13.0 ± 0.4	-	20.5
^{228}Ac	20.1 ± 1.1	33.2 ± 1.1	-	53.3
$^{234\text{m}}$Pa	219.5 ± 2.1	727.0 ± 2.3	-	946.5
^{40}K	45.0 ± 0.1	30.5 ± 0.1	-	75.5
Total	396.5	897.7	15.4	1309.5

Table 8.3.: Expected numbers of events in the $2\nu\beta\beta$ channel from the internal backgrounds, divided by isotope and broken down into SeOld and SeNew samples. ^{214}Pb has no expected events and is therefore not included.

Isotope	Expected Events
^{214}Bi	144.6 ± 2.2
^{208}Tl	229.3 ± 3.3
^{228}Ac	3.7 ± 0.1
^{40}K	16.4 ± 0.6
^{60}Co	8.9 ± 0.4
Total	402.9

Table 8.4.: Predicted background events for the external backgrounds in the $2\nu\beta\beta$ channel, by isotope. ^{214}Bi and ^{208}Tl are located in the PMT glass, steel frame and iron shielding. ^{40}K is in the PMT glass, steel frame and scintillator blocks. ^{60}Co is in the steel frame, mu-metal shielding, copper on petals and internal tower.

		Expected Events		
Isotope	Location	P1	P2	Total
^{214}Bi	SWire	70.8 ± 1.3	32.6 ± 1.5	103.5
^{214}Bi	SFoil (In)	9.6 ± 0.4	6.4 ± 0.3	16.0
^{214}Bi	SFoil (Out)	15.4 ± 0.5	9.1 ± 0.4	24.6
^{214}Bi	LSM Air	27.9 ± 0.6	-	27.9
^{214}Bi	SScin	0.4 ± 0.1	1.2 ± 0.1	1.6
^{208}Tl	SWire	0.5 ± 0.1	1.3 ± 0.2	1.8
^{210}Bi	SeOld	0.4 ± 0.1	0.6 ± 0.1	1.0
^{210}Bi	SeNew (S7)	0	0.2 ± 0.05	0.2
^{210}Bi	SeNew (S8)	0	1.0 ± 0.05	1.0
^{210}Bi	SWire	0	0.1 ± 0.05	0.1
Total		125.0	52.5	177.7

Table 8.5.: Expected background events in the $2\nu\beta\beta$ channel from the radon backgrounds for different isotopes and locations, showing values for phase 1 and phase 2. There are no expected events from any ^{214}Pb samples or ^{210}Bi SScin so they are not included here.

8.2.2. $2\nu\beta\beta$ Distributions

After the addition of the $2\nu\beta\beta$ signal, the binned log-likelihood fit measures 6517.1 ± 93.8 signal events, with a signal-to-background ratio of 3.4. The resulting distribution of the sum of the two electron energies, which was used in the fit, is shown in Figure 8.6. There is good agreement between data and simulation across the entire energy range.

The correlation matrix from the fit, which assesses how each parameter is correlated with the others, is displayed in Figure 8.7. The $2\nu\beta\beta$ signal strength has very little correlation with the other parameters which is unsurprising given the small contributions from all the backgrounds in the $2\nu\beta\beta$ channel.

As has been stressed throughout this thesis, one of the main strengths of the NEMO-3 detector is its ability to reconstruct the whole topology of an event. By studying many variables, added confidence can be gained in the understanding of the signal and detector. In this spirit, the energies of the lower and higher energy electrons can be seen in Figure 8.8.

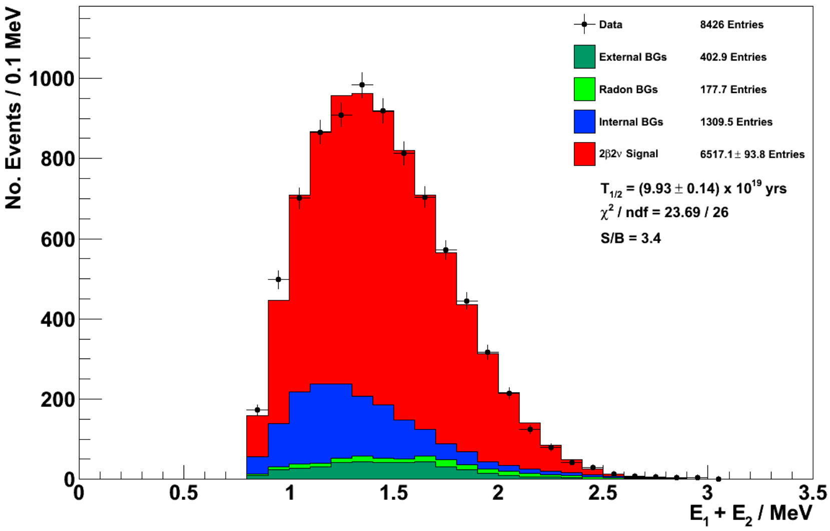

Figure 8.6.: Distribution showing the sum of the energy of the two electrons in the $2\nu\beta\beta$ channel.

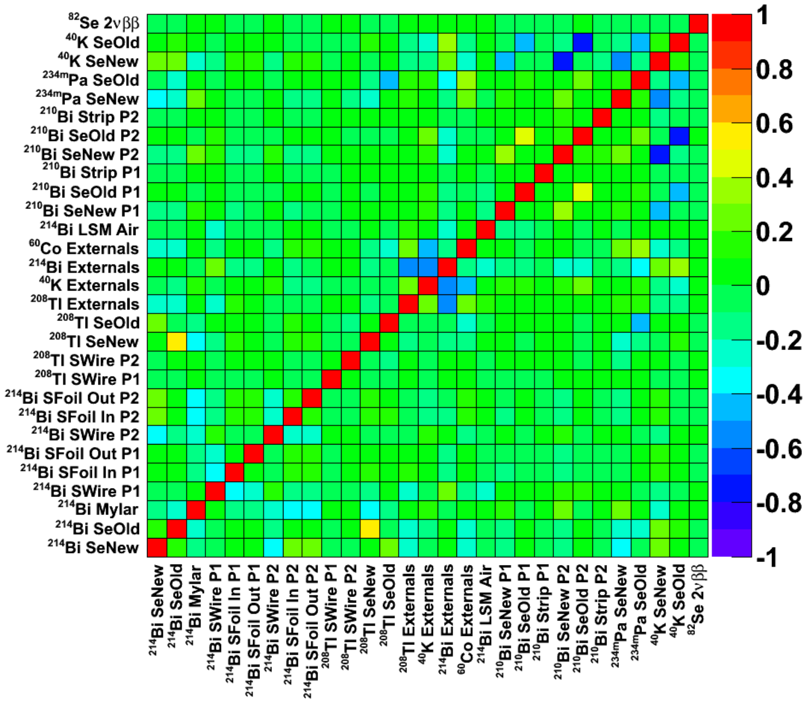

Figure 8.7.: Correlation matrix for the parameters of the signal and background fit, showing the level of correlation between them. A value of +1 shows 100% correlation and −1 shows 100% anti-correlation.

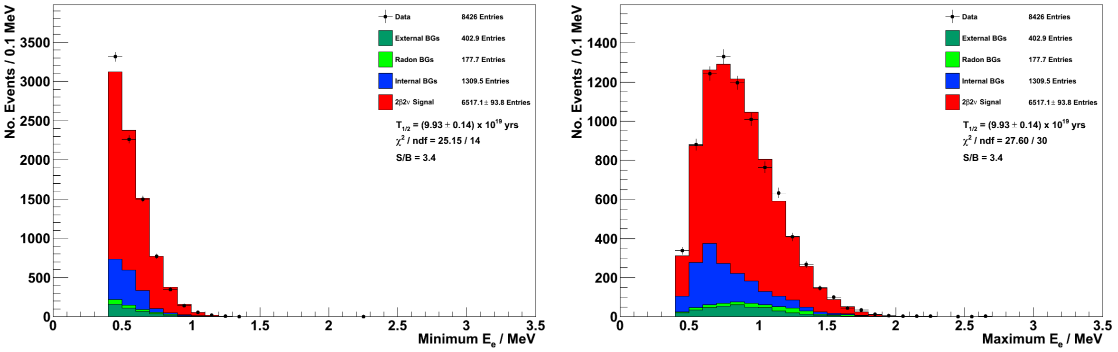

(a) Minimum Electron Energy **(b)** Maximum Electron Energy

Figure 8.8.: Distributions of single electron energies in the $2\nu\beta\beta$ channel, divided into the more and less-energetic electron in the event.

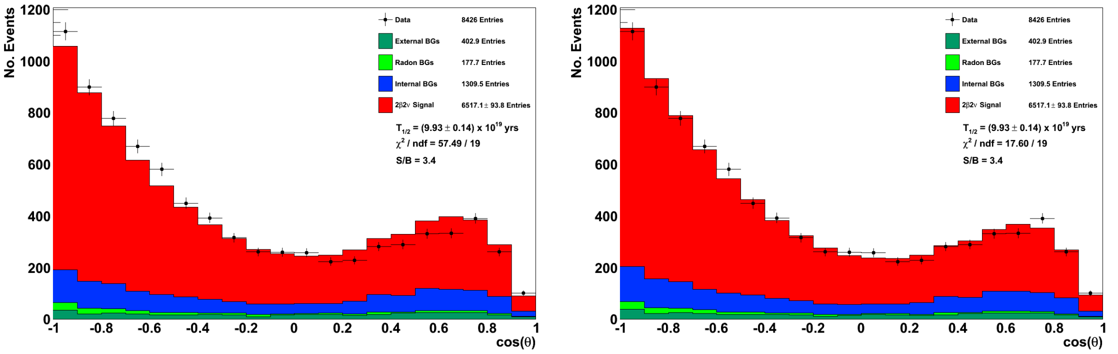

(a) Unweighted MC **(b)** Re-weighted MC

Figure 8.9.: Cosine of the angle between the two electron tracks at the point of emission in the $2\nu\beta\beta$ channel. (a) shows the raw MC samples and (b) shows MC that has been re-weighted using ^{207}Bi calibration data.

The angular distribution of the electrons is an important variable as it not only verifies the background model, but may provide a method to distinguish between different mechanisms of $0\nu\beta\beta$. The cosine of the angle between the electron tracks can be seen in Figure 8.9. In general, there is a discrepancy between data and simulation with an excess of data below -0.3 and a deficit between $0.2 - 0.8$. This disagreement is attributed to detector effects, since it is also present in the angular distributions for the ^{207}Bi calibration runs. To improve the agreement, the simulation may be re-weighted based on this calibration data, the result of which is shown in Figure 8.9b where there is considerable improvement.

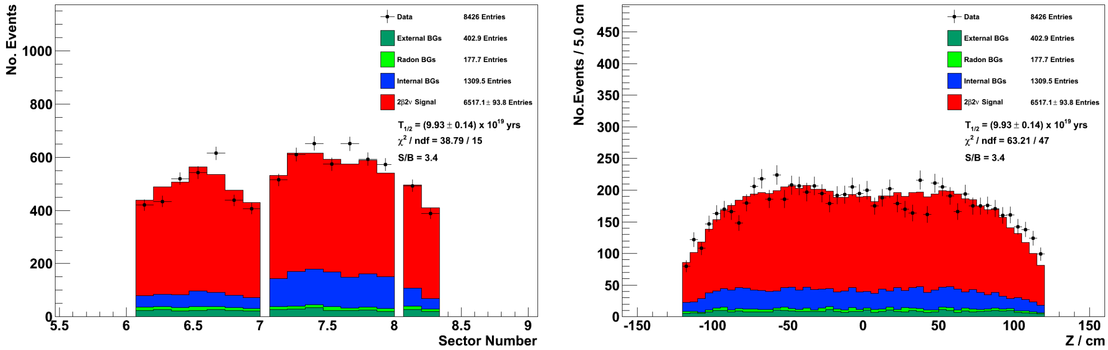

(a) Vertex Sector (b) Vertex Z

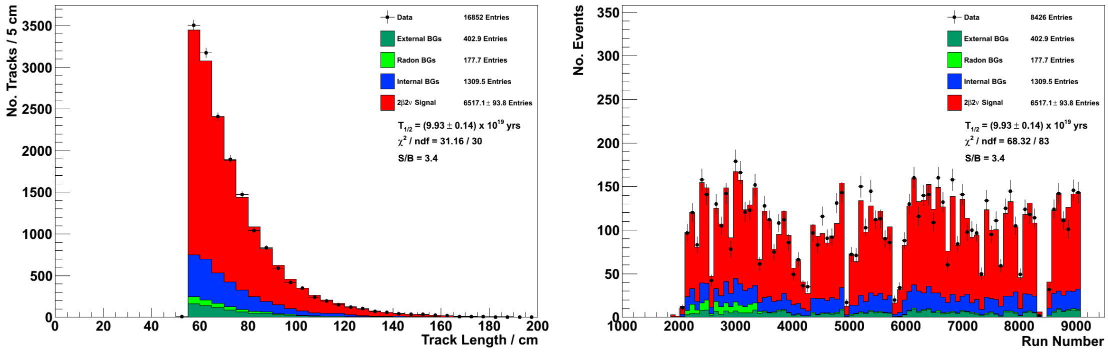

(c) Track Length (d) Run Number

Figure 8.10.: Distributions of vertex position, described by sector and z position. Track length and run number distributions are also shown.

The final distributions for the $2\nu\beta\beta$ channel are included in Figure 8.10. The position of the event vertex (Figures 8.10a and 8.10b) shows that there is a good description in the z direction but some small variation in the sector variable. This is likely to be a cause of non-uniform background contamination levels across the samples which modelled as the same in each strip but may vary slightly from one strip to the next. The run length distribution shows that the detector running conditions are well replicated and that the $2\nu\beta\beta$ signal is constant in time as expected. In addition, it should be recalled that good agreement was seen in the internal probability distribution shown in Figure 6.5.

One of the final cross-checks of the validity of the analysis procedure can be to verify that the result is unchanged when data from phase 1 and phase 2 are analysed separately. Since there are different background levels in these periods, this should be a consistency check of the analysis techniques used. The result of re-performing the analysis using P1 and P2 data separately can be seen in Table 8.6. The entire analysis is performed separately, so there are different background models for each phase compared with that presented herein. The bottom line shows that the same $2\nu\beta\beta$ half-life is measured in both phases, within statistical precision.

Data Set	P1	P2	P1 & P2
Exposure / days	391.9	1548.3	1918.5
Data Events	1867	6559	8426
Internal BG Events	294.3	1031.4	1309.5
External BG Events	99.0	318.1	402.9
Radon BG Events	97.9	54.1	177.7
Signal Events	1381.3 ± 43.6	5132.9 ± 80.0	6517.1 ± 93.8
Efficiency / %	2.756	2.556	2.596
Half-life / 10^{19} yr	10.05 ± 0.32	9.91 ± 0.15	9.93 ± 0.14

Table 8.6.: Comparison of analyses performed using phase 1, phase 2 and both phase 1 and phase 2 data. The complete analysis is re-performed so that background models differ between the three columns, but the resulting signal strength is consistent.

8.2.3. $2\nu\beta\beta$ systematics

Whilst every effort has been made to understand and account for detector effects and other experimental uncertainties, there some outstanding factors that may provide additional error in the measurement of the $2\nu\beta\beta$ half-life. The main sources of these systematic uncertainties will be quantified in this section.

By far the most important source of systematic error is the uncertainty on the detector acceptance and reconstruction and selection efficiency. To quantify this, data-taking runs were performed with four precisely-measured ^{207}Bi sources in the detector. The activity of these sources was measured using a very similar two electron channel to that presented here. The resulting electron energy distributions are shown in Figure 8.11. Since backgrounds are negligible in this scenario, the difference between the measurement by NEMO-3 and that by a HPGe detector may be taken as a measure of the uncertainty in the efficiency of the detector. The values

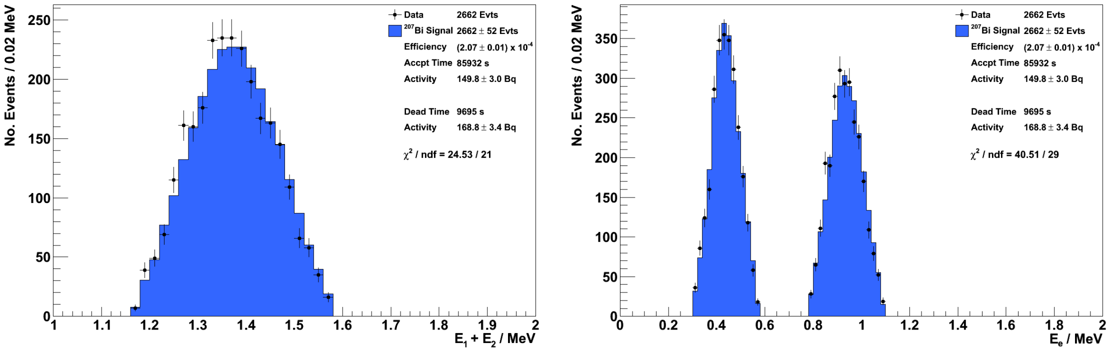

(a) Total Electron Energy **(b)** Individual Electron Energies

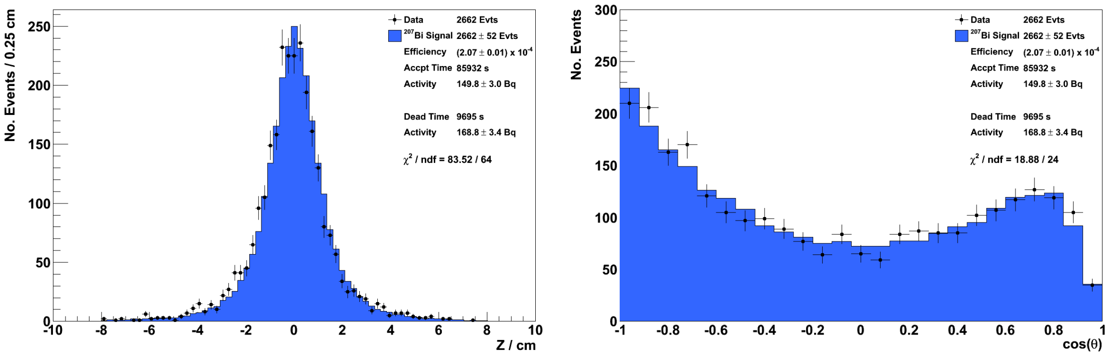

(c) Vertical Vertex Position **(d)** Cosine of Electron Opening Angle

Figure 8.11.: Distribution of electron energy from special runs using well-calibrated ^{207}Bi sources. Total energy and individual electron distributions are displayed. Also displayed are the reconstructed vertex position in the vertical direction and the cosine of the angle between the electrons.

differed by 7% and the systematic uncertainty on the HPGe measurement was 5%. A conservative approach was taken and a ±7% systematic uncertainty was transposed on to the $2\nu\beta\beta$ half-life.

Alongside the electron energy distributions are those for the vertex position in the vertical direction and the cosine of the angle between the two electrons. These distributions confirm that the tracking capabilities of the detector are well reproduced in addition to the good understanding of the energy response of the calorimeter.

The precision of the energy calibration of the calorimeter is 1% and inaccuracies in the derived energies affect the spectral shapes of all samples. This therefore can alter the results of background and signal measurements and impact a half-life measurement. To determine the size of this effect, all energies are altered by ±1%

and the background model and signal strength re-evaluated. The resulting half-lives were in the range $(9.83 - 10.07) \times 10^{19}$ yr, so a systematic error of ±1.25% is included.

To maximise the sensitivity of the half-life measurement, the entire range of energy values in the total energy distribution of the $2\nu\beta\beta$ channel is used. If everything is modelled correctly and all backgrounds are measured correctly, the signal strength should not vary if the fit is performed across any range of energy values. To assess the effect of this particular choice, various fitting windows were investigated. The resulting half-life did not vary more than ±1%.

The effect of mis-measurement of the background components in general has very little effect on a $2\nu\beta\beta$ measurement since there is a relatively large signal-to-background ratio. The most important background contributions come from the internal backgrounds which in turn are dominated by $^{234\mathrm{m}}$Pa. This isotope is effectively measured in the 1e channel, although as was seen above, it is sensitive to the inclusion of the $2\nu\beta\beta$ signal. To estimate the possible variation between the 1e and $2\nu\beta\beta$ channels, again the ^{207}Bi source runs are used. The variation in activity measurement between 1e and 2e channels is at the level of 4% which is therefore used as the uncertainty on the $^{234\mathrm{m}}$Pa measurement. This corresponds to an uncertainty of 0.8% on the half-life.

The measurements of internal ^{208}Tl activities is validated by using a 1e2γ channel on runs with a ^{232}U source in the detector. The uncertainty level here is found to be ±15% compared to a HPGe measurment. This produces a negligible effect on the $2\nu\beta\beta$ half-life.

The most important external backgrounds are from ^{208}Tl and ^{214}Bi. The re-evaluation of these backgrounds in this analysis have shown agreement to the level of 10% with the external background model, which is roughly the level of accuracy to which the model is thought to be determined. This ±10% variation translates to ±0.6% in the half-life measurement.

The dominant radon backgrounds to the $2\nu\beta\beta$ channel, composed of the ^{214}Bi SWire and SFoil contributions, have mostly been determined using information from the 1e1α channel. A separate study that measured the level of ^{214}Bi using a 1e1γ channel agreed with the 1e1α channel within 10% [79]. This uncertainty leads to the inclusion of an error of 0.25% on half-life.

The final systematic on the $2\nu\beta\beta$ measurement simply comes from the measurement of the mass of ^{82}Se of 932.4 ± 5.0 g. This error of $\pm0.5\%$ is transferred directly on to the half-life [78].

The contributions to the systematic error are summarised in Table 8.7. To combine the individual systematics, they are assumed to be uncorrelated so that the total systematic error is found to 7.3% by adding the contributions in quadrature.

Systematic Cause	Uncertainty on Systematic	$2\nu\beta\beta$ Half-life Uncertainty / %
$2\nu\beta\beta$ efficiency	$\pm7.0\%$	±7.0
Energy calibration	$\pm1.0\%$	±1.25
Fitting window	$\sum E_e > (0.8 - 2.0)$ MeV	±1.0
Internal BG activities	$\pm4.0\%$	±0.8
External BG activities	$\pm10.0\%$	±0.6
Radon BG activities	$\pm10.0\%$	±0.25
^{82}Se mass	$\pm0.5\%$	±0.5
Total Systematic Error	-	±7.3

Table 8.7.: Summary of systematic errors contributing to the $2\nu\beta\beta$ half-life measurement.

8.2.4. $2\nu\beta\beta$ Half-life Measurement

In the $2\nu\beta\beta$ channel, 6517.1±93.8(stat) signal events were measured from 932.4±5.0 g of ^{82}Se with a signal efficiency of 2.596%. This can be converted into a half-life measurement, following Section 6.7, to give the final result of

$$T^{2\nu}_{1/2} = (9.93 \pm 0.14(\text{stat}) \pm 0.72(\text{syst})) \times 10^{19} \text{ yr} \tag{8.1}$$

By way of comparison, this result is twice as precise as the previous NEMO-3 measurement of $(9.6 \pm 0.3(\text{stat}) \pm 1.0(\text{syst})) \times 10^{19}$ yr [73]. It is also in agreement with the NEMO-2 value of $(8.3 \pm 1.0(\text{stat}) \pm 0.7(\text{syst})) \times 10^{19}$ yr [88], the best value from non-NEMO direct detection experiments of $(10.8\ ^{+2.6}_{-0.6}) \times 10^{19}$ yr [89] and the best estimate from a combination of geochemical experiments of 10×10^{19} yr [90].

The $2\nu\beta\beta$ matrix element, $M^{2\nu}$, which is of importance when tuning NME models for $0\nu\beta\beta$, can be deduced from this measurement using Equation (3.9), which is re-iterated below.

$$\left(T^{2\nu}_{1/2}\right)^{-1} = G^{2\nu}\left(Q_{\beta\beta}, Z\right)\left|M^{2\nu}\right|^{2}$$

where $G^{2\nu}\left(2995.5\text{ keV}, 82\right) = 4.3 \times 10^{-18}\text{ yr}^{-1}$ is the analytically calculated phase space factor, evaluated for $g_A = 1.254$ [91]. The resulting matrix element is then extracted as

$$\left|M^{2\nu}\right| = 0.0484 \pm 0.0018 \qquad (8.2)$$

where the quoted error includes both statistical and systematic errors. This value can be compared with a value calculated in the shell model, 0.084 [92], and a value found using the QRPA technique, 0.046 [93]. Care should be taken when interpreting the latter result as there is considerable tuning of the QRPA model based on experimental data, so the comparison becomes rather circular. However, this does highlight that this more precise value of $M^{2\nu}$ may be used to tune NME calculations for $M^{0\nu}$ in ^{82}Se.

8.3. Optimisation of $0\nu\beta\beta$ Cuts

Now that all backgrounds and the $2\nu\beta\beta$ half-life have been measured, it is possible to conduct a search for $0\nu\beta\beta$. In order to maximise the sensitivity, an optimisation programme is undertaken similar to that for the $2\nu\beta\beta$ channel.

The starting point for the optimisation is the $2\nu\beta\beta$ channel and additional analysis cuts are investigated to see whether improvements in the $0\nu\beta\beta$ sensitivity can be made. Each $0\nu\beta\beta$ decay mode is treated separately with an individual optimisation.

Before selecting the cuts that may be suitable for optimisation, it is instructive to consider the different backgrounds that are expected for a $0\nu\beta\beta$ search. The most common decay modes of the mass mechanism (Section 3.3.1), right-handed current (Section 3.3.2) and Majoron with $n = 1$ (Section 3.3.3) all have an experimental signature at energies around $Q_{\beta\beta}$. The main backgrounds in the region $2.6 - 3.2$ MeV are shown in Table 8.8.

Sample	^{214}Bi	^{208}Tl	$2\nu\beta\beta$	Total
SeOld	2.75 ± 0.11	1.40 ± 0.08	-	4.15
SeNew	2.02 ± 0.10	2.65 ± 0.09	-	4.67
Mylar	0.50 ± 0.03	-	-	0.50
External BG	-	0.07 ± 0.01	-	0.07
SWire P1	1.88 ± 0.04	0.05 ± 0.01	-	1.93
SWire P2	1.05 ± 0.05	0.14 ± 0.02	-	1.19
SFoil P1	0.94 ± 0.16	-	-	0.94
SFoil P2	0.53 ± 0.12	-	-	0.53
SScin P2	0.07 ± 0.01	-	-	0.07
^{82}Se $2\nu\beta\beta$	-	-	2.07 ± 0.37	2.07
Total	9.74	4.31	2.07	16.14

Table 8.8.: Predicted numbers of background events in the energy window $2.6 - 3.2$ MeV, using the $2\nu\beta\beta$ selection criteria. An exposure of 1918.5 days is assumed, for an exposure of 4.9 kg yr of ^{82}Se.

The dominant contributors to the $0\nu\beta\beta$ background are sources of ^{214}Bi and ^{208}Tl as well as the tail from $2\nu\beta\beta$. The largest contributions come from internal contamination of the foils, accounting for 9.3 out of the 16.1 expected background events. Backgrounds from radon and thoron contribute 4.7 events, separated into 2.9 from phase 1 and 1.8 from phase 2. Finally, 2.1 events are expected from the $2\nu\beta\beta$ tail of ^{82}Se. It should be noted that spectral information will be used in the search for $0\nu\beta\beta$ and the background distributions are far from flat. Therefore, these numbers are a useful guide, but may not accurately represent the effect each background has on the measurement.

When choosing cuts that may enhance the $0\nu\beta\beta$ sensitivity of the experiment, a general principle should be to look for those which suppress the backgrounds whilst keeping the $0\nu\beta\beta$ signal. The metric which is used as a measure of success when optimising the selection is the expected half-life sensitivity for the particular $0\nu\beta\beta$ decay mode under investigation. This is found by generating pseudo-data based on a background-only hypothesis and evaluating a limit as described in Section 6.6.2.

Binary cuts are defined in the same way as in Section 8.1.2, and the only ones considered are the exclusion of phase 1 data and a requirement for negative tracks.

As was the case with the $2\nu\beta\beta$ channel, it transpires that neither of these cuts is beneficial and so are not applied.

Similar parameters are considered for the optimisable cuts as were with the $2\nu\beta\beta$ channel. One idea is to exploit the differences in spectral shapes of the backgrounds and signals by cutting on electron energies individually and the sum of both energies. Additionally, the internal probability is re-evaluated as at the high energies concerned timing of electrons is more accurate and external backgrounds are less significant.

The third category of optimisable cut aims to exploit the different division of total energy between the two electrons for different samples. The parameter that is considered for optimisation is a measure of the asymmetry between the electron energies defined as:

$$A = \frac{E_{\text{max}} - E_{\text{min}}}{E_{\text{max}} + E_{\text{min}}} \tag{8.3}$$

By looking at the distribution of this variable, shown in Figure 8.12a, it is clear that there may be significant gains made in the right-handed current mode using this parameter, but other decay modes are not expected to benefit greatly.

The final optimisable cut is intended to suppress the background from ^{208}Tl by targeting electrons caused by the 2.6 MeV nuclear transition (Figure 7.4). Events resulting from this ^{208}Tl transition have conversion electrons that deposit energy at $\sim$ 2.4 MeV as shown in Figure 8.12b. This proposed cut is implemented by excluding events in the region given by n_σ around 2.42 MeV, where the n_σ is the number of energy resolutions found from calibration data.

The results of scanning over the optimisable parameters using the mass mechanism decay mode are shown in Figure 8.13. Figures 8.13a–8.13c make it immediately clear that there is no advantage gained by removing events based on their constituent energies.

The sensitivity for different internal probability cuts are relatively flat across the entire range shown (Figure 8.13d), which is a result of the small contribution from the external backgrounds. The advantage that was present for a 1% cut in the $2\nu\beta\beta$ channel is no longer present, and so a cut is implemented at the more conservative value of 4%. This is the extremity of the the flat region before the sensitivity begins

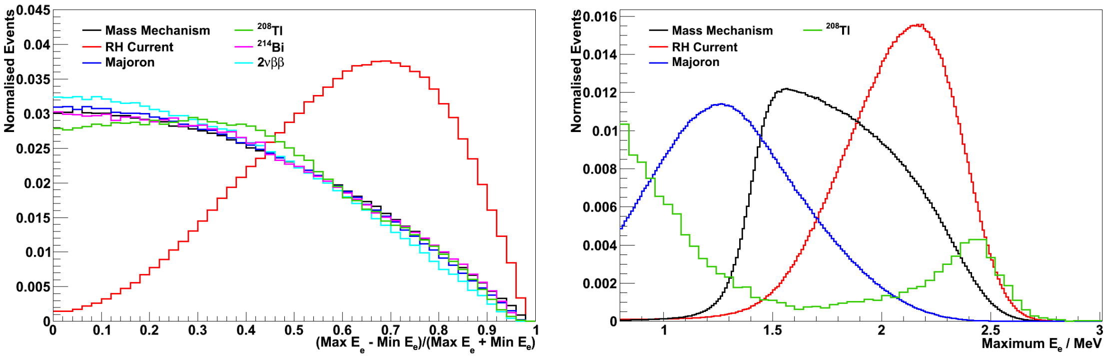

(a) Energy Asymmetry **(b)** Maximum Electron Energy

Figure 8.12.: Distributions of energy asymmetry and maximum electron energy for the three main $0\nu\beta\beta$ decay modes and the largest backgrounds. Energy asymmetry is defined by Equation (8.3).

to slowly decrease and is in good agreement with other studies of optimal values for the internal probability cut.

As expected, in Figure 8.13e there is no advantage for the energy asymmetry cut in this mass mechanism decay mode, with a rapid decrease in sensitivity as the cut value is increased. The same plot, using the right-handed current λ decay mode is shown in Figure 8.14. In this case, there is a clear improvement in sensitivity by cutting at $A = 0.26$.

The final optimisable cut for removing ^{208}Tl events (Figure 8.13f) shows less conclusive results. There may be a slight advantage in a cut with $n_\sigma \sim 1$, but the improvement is small, so in order to be conservative the cut is not applied.

The same distributions for the remaining decay modes show similar behaviour to the mass mechanism and are thus not shown. Out of the proposed cuts, the energy asymmetry cut has a positive impact on the $0\nu\beta\beta$ sensitivity for the right-handed current λ mode. It is therefore applied before performing this $0\nu\beta\beta$ search, whilst all other decay mode searches use the same selection criteria as the $2\nu\beta\beta$ channel with a modified internal probability cut of 4%. The results of these searches are presented in the next section.

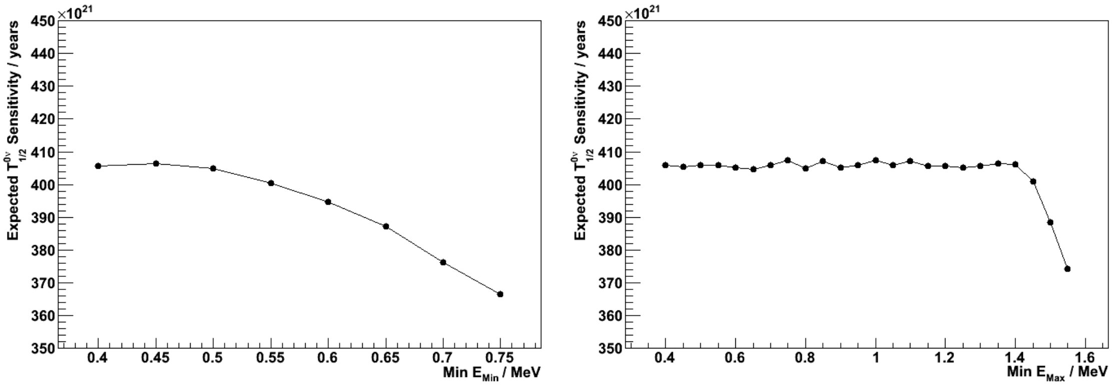

(a) Minimum e^- Energy **(b)** Maximum e^- Energy

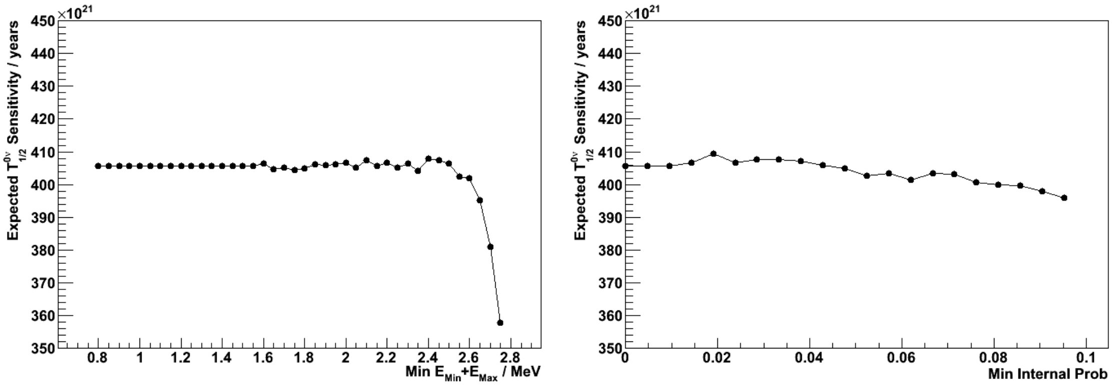

(c) Sum of e^- Energies **(d)** Internal Probability

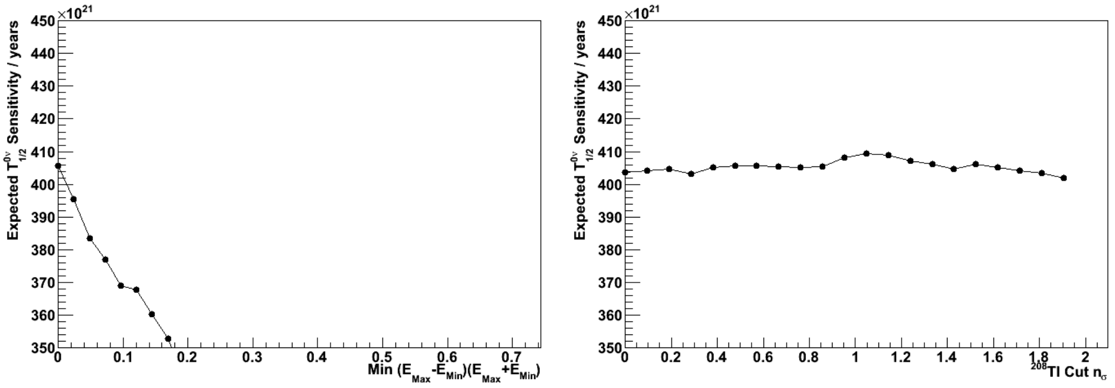

(e) Energy Asymmetry **(f)** ^{208}Tl Cut n_σ

Figure 8.13.: Expected half-life sensitivity for the mass mechanism $0\nu\beta\beta$ mode as a function of different optimisable cut parameters.

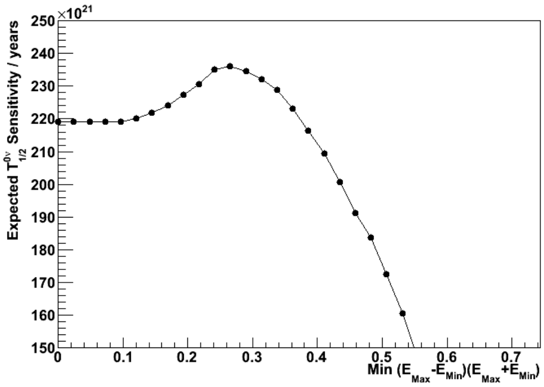

Figure 8.14.: Expected half-life sensitivity for the right-handed current (λ) decay mode as a function of energy asymmetry defined by Equation (8.3).

8.4. $0\nu\beta\beta$ Results

Using the selection criteria described in the previous section, $0\nu\beta\beta$ searches are performed for the most common mechanisms. No evidence for $0\nu\beta\beta$ has been found for any decay mode, so limits on the signal strength are set using the procedure described in Section 6.6.2.

In this section, the results and interpretation for the different decay modes are presented. The mass mechanism is presented in Section 8.4.1, followed by the right-handed current and Majoron emission modes in Sections 8.4.2 and 8.4.3 respectively.

8.4.1. Mass Mechanism

The mass mechanism decay mode, presented in Section 3.3.1, is the most commonly discussed $0\nu\beta\beta$ decay mode. It has an experimental signature characterised by a peak in the distribution of the electron energy sum at the $Q_{\beta\beta}$ value. No evidence is seen for $0\nu\beta\beta$ decay using a binned log-likelihood fit with this distribution, so it is used to extract a limit on the signal strength.

Before working with the observed data, it is important to consider the expected result of the experiment, which is not sensitive to fluctuations in the small number of data events concerned. Using the background model and the result for the $2\nu\beta\beta$ half-life, 7.5 events are expected to be excluded at the 90% CL, corresponding to an expected half-life limit of 3.91×10^{23} yr.

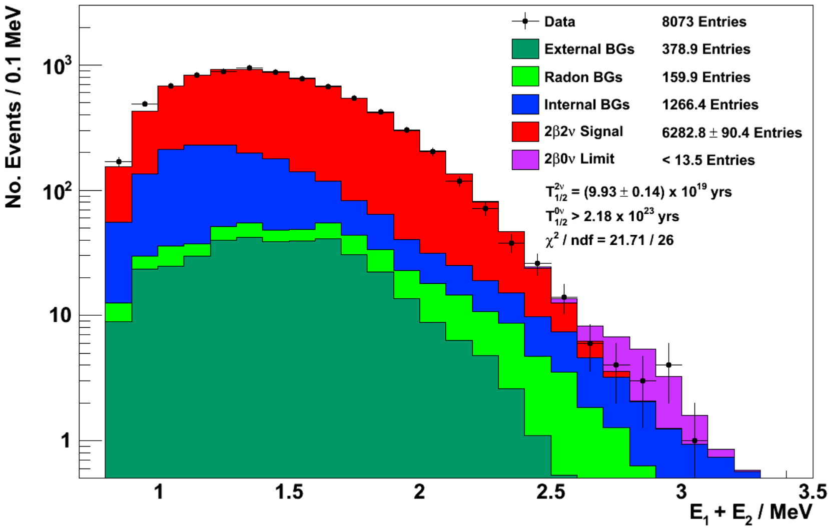

Figure 8.15.: Distribution of electron energy sum in the $0\nu\beta\beta$ mass mechanism channel. The limit on the signal at 90% CL is shown in violet.

In the observed data, there is a slight excess of data over MC around the $Q_{\beta\beta}$ value, consistent with a statistical fluction, as shown in Figure 8.15. As a result, the limit that can be placed on the signal strength is weaker than in the expected case. At 90% CL, 13.5 events are excluded and using the detection efficiency of 11.83%, results in a limit of

$$T^{0\nu}_{1/2} > 2.18 \times 10^{23} \text{ yr (90\% CL)} \tag{8.4}$$

This result from the full spectrum may be cross-checked using an energy window method, commonly called the Helene method [82]. This method is effectively a simplification of the full spectrum technique used above, where the spectrum has been replaced by a single histogram bin. In the energy window of $2.6 - 3.2$ MeV, 14.7 events are expected from background and the $0\nu\beta\beta$ efficiency is 9.96%. This leads to an expected limit of 7.2 events or 3.46×10^{23} yr at 90% CL, thus confirming that including more information in the full spectrum case improves the expected result. In the observed data, the upward fluctuation raises the number of excluded events to 10.5 and the half-life limit becomes 2.36×10^{23} yr (90% CL), which is comparable with the result from the full spectrum method.

The results from both techniques are shown in Table 8.9. The data show the unusual scenario where the full spectrum sets a weaker limit, which in this case is the result of the upward fluctuations being concentrated in the higher energy bins. Statistically speaking, the weaker limit from the full spectrum technique is the more accurate limit as it is using more of the available information. The value from Equation (8.4) is therefore used when setting limits for $\langle m_{\beta\beta} \rangle$.

Limit-Setting Technique	Eff. %	Exp. Limit $N_{0\nu}$	Exp. Limit $T^{0\nu}_{1/2}$ / yr	Obs. Limit $N_{0\nu}$	Obs. Limit $T^{0\nu}_{1/2}$ / yr
Full Spectrum	11.83	7.54	3.91×10^{23}	13.50	2.18×10^{23}
2.6 – 3.2 MeV	9.96	7.17	3.46×10^{23}	10.51	2.36×10^{23}

Table 8.9.: Results of a $0\nu\beta\beta$ search for the mass mechanism decay mode using full spectrum and energy window limit-setting methods. A total exposure of 4.9 kg yr of ^{82}Se has been used. The quoted results are statistical only and at the 90% CL.

The effective Majorana neutrino mass, $\langle m_{\beta\beta} \rangle$, is extracted from the half-life limit using Equation (3.12). As was explained in Section 3.4, the resulting values of $\langle m_{\beta\beta} \rangle$ are heavily dependent on the calculation used for the nuclear matrix element. The values for a range of different models are shown in Table 8.10. These can be summarised to present a single result reflecting this range as:

$$\langle m_{\beta\beta} \rangle < 1.0 - 2.8 \text{ eV (90\% CL)} \tag{8.5}$$

Despite the upward fluctuation in data, this result is still an improvement on the best limit for ^{82}Se which comes from the value previously published by the NEMO-3 collaboration of $T^{0\nu}_{1/2} > 1.0 \times 10^{23}$ yr corresponding to $\langle m_{\beta\beta} \rangle < 1.7 - 4.9$ eV [73].

8.4.2. Right-handed Current

The right-handed current decay mode is an alternative to the mass mechanism as was discussed in Section 3.3.2. The distribution of the sum of electron energies is identical to that of the mass mechanism, but the distribution of each electron energy and their angular separation differs.

Model	$\langle m_{\beta\beta} \rangle$/ eV	Ref.
ISM	< 2.8	[94]
QRPA	$< 1.0 - 1.3$	[95]
QRPA	$< 1.3 - 1.7$	[96]
IBM-2	< 1.4	[97]
EDF	< 1.5	[98]

Table 8.10.: Effective Majorana neutrino mass calculated using the half-life limit set in this work and the matrix elements for different NME calculations. Values of $g_A = 1.25$ and $G^{0\nu} = 3.11 \times 10^{-14}$ yr^{-1} have been used [46].

The difference between electron energies is particularly striking for the λ decay mode (Figure 8.12a). As a result, the selection criteria for this decay mode also require a cut on the energy asymmetry (Equation (8.3)) and the events are a sub-set of those used in the mass mechanism case.

A calculation of the expected limit on the number of events for this decay mode leads to an expected signal exclusion at 5.5 events or 2.28×10^{23} yr at 90% CL. The situation with observed data, presented in Figure 8.16, is similar to that of the mass mechanism case, again showing an excess of data events. This weakens the limit to an exclusion of 10.6 events, which using the detection efficiency of 5.02% leads to a half-life of

$$T^{0\nu\lambda}_{1/2} > 1.18 \times 10^{23} \text{ yr (90\% CL)} \tag{8.6}$$

The alternative to the λ mode is known as the η mode and has an experimental signature that is very similar to that of the mass mechanism. As such, the results for these decay modes are very similar. The limit for the η mode is again weaker than expected with a half-life of:

$$T^{0\nu\eta}_{1/2} > 1.90 \times 10^{23} \text{ yr (90\% CL)} \tag{8.7}$$

The results for both right-handed current decay modes are summarised in Table 8.11.

For the right-handed decay modes, the decomposition of phase space factors and matrix elements is non-trivial. As a result, in order to extract a limit on the associated

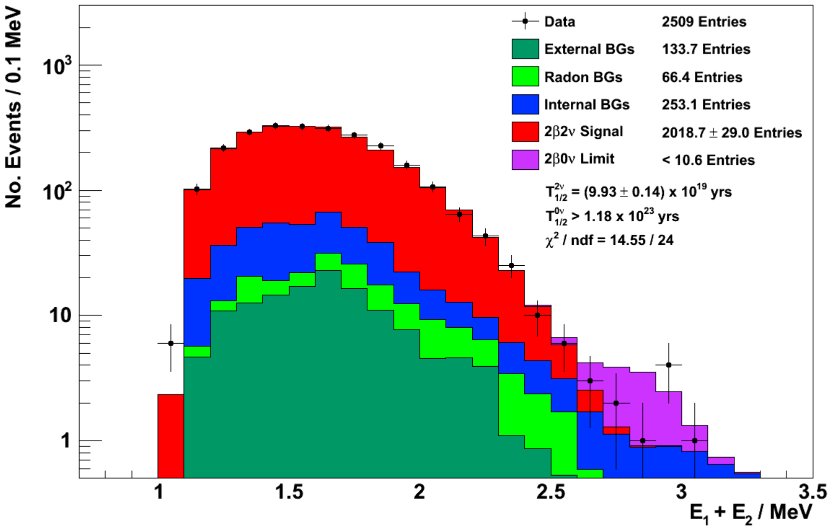

Figure 8.16.: Distribution of sum of the energies of the two electrons in the $0\nu\beta\beta$ right-handed current (λ mode) channel. The limit on the signal at 90% CL is shown in violet.

RH	Eff.	Exp. Limit		Obs. Limit	
Mode	%	$N_{0\nu}$	$T^{0\nu}_{1/2}$ / yr	$N_{0\nu}$	$T^{0\nu}_{1/2}$ / yr
λ	5.02	5.50	2.28×10^{23}	10.56	1.18×10^{23}
η	10.42	7.73	3.36×10^{23}	13.71	1.90×10^{23}

Table 8.11.: Results of a $0\nu\beta\beta$ search for the two right-handed current decay modes. The quoted results are statistical only and at the 90% CL.

lepton number violating parameters, C factors are defined such that

$$\left(T^{0\nu}_{1/2}\right)^{-1} = C\eta^2_{LV} \tag{8.8}$$

$C^0_{\lambda\lambda}$ describes the coupling for the λ decay mode and has been calculated in the range $(0.90 - 1.05) \times 10^{-12}$ yr^{-1} [99]. This leads to a limit on the coupling parameter, $\langle\lambda\rangle$, as

$$\langle\lambda\rangle < (2.8 - 3.0) \times 10^{-6} \tag{8.9}$$

This limit is the best in ^{82}Se and only a factor $2 - 3$ weaker than the best results from the Heidelberg-Moscow experiment of $\langle\lambda\rangle < 1.1 \times 10^{-6}$ [100] and the NEMO-3 ^{100}Mo result of $\langle\lambda\rangle < 1.4 \times 10^{-6}$.

The equivalent C factor for the η decay mode, $C^0_{\eta\eta}$ is calculated to be $(1.08 - 1.21) \times 10^{-8}$ yr^{-1} [99], leading to a limit of

$$\langle\eta\rangle < (2.1 - 2.2) \times 10^{-8} \tag{8.10}$$

Whilst this limit is the strongest found in ^{82}Se, it is not particularly competitive with Heidelberg-Moscow, which produced a value of $\langle\eta\rangle < 0.64 \times 10^{-8}$ [100].

8.4.3. Majoron Emission

The Majoron emission mode, which was described in Section 3.3.3, is considered more exotic than the mass mechanism or right-handed current modes. The mode differs significantly from the previous mechanisms as hypothetical Majorons are also emitted with the electrons. This means that the sum of the two electrons is no longer a single peak at the $Q_{\beta\beta}$ value, but rather a continuous spectrum.

The shape of the spectrum is described by the spectral index of the model, denoted n. As n increases, the peak of the spectrum shifts to lower energies, so that the $n = 7$ distribution is much more similar to that of $2\nu\beta\beta$ than the $n = 1$ case as illustrated in Figure 3.9. There is no evidence for the $n = 1, 2, 3$ modes and limits for these signal strengths are presented in Table 8.12. However, there is not enough statistical power in the ^{82}Se data samples to discern between the $n = 7$ distribution and the background from $2\nu\beta\beta$ and internal contamination.

Majoron Mode	Eff. %	Exp. Limit $N_{0\nu}$	Exp. Limit $T^{0\nu}_{1/2}$ / yr	Obs. Limit $N_{0\nu}$	Obs. Limit $T^{0\nu}_{1/2}$ / yr
$n = 1$	7.92	47.6	4.15×10^{22}	40.4	4.89×10^{22}
$n = 2$	6.14	85.8	1.78×10^{22}	58.2	2.63×10^{22}
$n = 3$	4.63	120.5	0.96×10^{22}	81.2	1.42×10^{22}

Table 8.12.: Half-life limits for the Majoron emission $0\nu\beta\beta$ decay modes, listed by spectral index, n. All results are statistical only and at the 90% CL.

The half-life limits from Table 8.12 can be converted to a limit on the coupling between the Majoron and neutrino using Equation (3.20). The results from this procedure can be seen in Table 8.13.

Model	χ^0	n	$M^{0\nu\chi^0}$	$G^{0\nu}$ yr^{-1}	$T^{0\nu\chi^0}_{1/2}$ Limit 10^{22} yr	$\langle g_{\chi^0}\rangle$
IB	1	1	$2.63 - 5.60$	4.84×10^{-16}	> 4.89	$< (3.7 - 7.8) \times 10^{-5}$
IC	1	1	$2.63 - 5.60$	4.84×10^{-16}	> 4.89	$< (3.7 - 7.8) \times 10^{-5}$
ID	2	3	10^{-3}	1.01×10^{-17}	> 1.42	< 1.62
IE	2	3	10^{-3}	1.01×10^{-17}	> 1.42	< 1.62
IIB	1	1	$2.63 - 5.60$	4.84×10^{-16}	> 4.89	$< (3.7 - 7.8) \times 10^{-5}$
IIC	1	3	$0.14 - 0.44$	3.49×10^{-18}	> 1.42	$< 0.01 - 0.03$
IID	2	3	10^{-3}	1.01×10^{-17}	> 1.42	< 1.62
IIF	1	3	$0.14 - 0.44$	3.49×10^{-18}	> 1.42	$< 0.01 - 0.03$
Bulk	1	2	–	–	> 2.63	–

Table 8.13.: Results from a search for Majoron for 9 different decay models which were detailed in Table 3.1. Matrix elements for $n = 1$ are from [101–103], and $n = 3$ are from [104, 105]. Phase space factors are from [91] and [106] for $n = 1$ and $n = 3$, respectively.

Interestingly, the NEMO-3 limits for ^{82}Se are equivalent to those from ^{100}Mo, despite having considerably less source mass. This is a result of the disparity between the $2\nu\beta\beta$ half-lives of the two isotopes, with ^{100}Mo almost an order of magnitude shorter.

These results are the strongest limits using ^{82}Se, however they have been superseded by recent results from KamLAND-Zen with an improvement of a factor ~ 3 [60].

Part II.

Radon Research and Development for SuperNEMO

Chapter 9.

The SuperNEMO Experiment

The SuperNEMO experiment is a next-generation double beta decay experiment that builds on the successes of NEMO-3, using the same tracker-calorimeter technology. Its aims are to search for $0\nu\beta\beta$ of ^{82}Se with a half-life sensitivity of 10^{26} yr, corresponding to an effective neutrino mass of $50 - 100$ meV.

The baseline design of SuperNEMO consists of 20 identical modules, each housing $5 - 7$ kg of source isotope. The general layout of each module is similar to NEMO-3, with thin source foils surrounded by a gas tracker which in turn is enclosed by a calorimeter. These modules are discussed in greater detail in Section 9.1.

SuperNEMO is not simply a scaled-up version of NEMO-3. A considerable amount of research and development (R&D) has been undertaken to improve many aspects of the design. This R&D programme concentrated on the key areas of source foil production, tracker development, calorimeter development and ensuring that ultra-low levels of background are achieved. The successes of each area of research will be briefly outlined in Section 9.2.

The remainder of this chapter (Section 9.3) is dedicated to the expected timescale and sensitivity of the experiment.

9.1. SuperNEMO Baseline Design

In its baseline design, the SuperNEMO experiment will contain 100 kg of ^{82}Se, although ^{150}Nd and ^{48}Ca may also be considered if improved enrichment possibilities arise. This source mass allows a target sensitivity of 10^{26} yr which translates to an effective neutrino mass of $50 - 100$ meV.

The source isotope is divided between 20 identical modules, which unlike NEMO-3, are planar in geometry, as shown in Figure 9.1. These modules are $4 \times 6 \times 2$ m^3 in size and are independent detectors which are fully operational, stand-alone devices. At the centre of every module are thin source foils of density ~ 40 mg cm^{-2} and length 2.7 m, containing $5 - 7$ kg of source isotope. Outside these foils is a tracking chamber that will hold 2000 drift cells that are operated in Geiger mode in similar conditions to those of NEMO-3. The tracking volume is closed by the calorimeter walls, which are composed of 550 optical modules consisting of PMTs and scintillator blocks. Each module is completed with its own magnetic field and passive shielding.

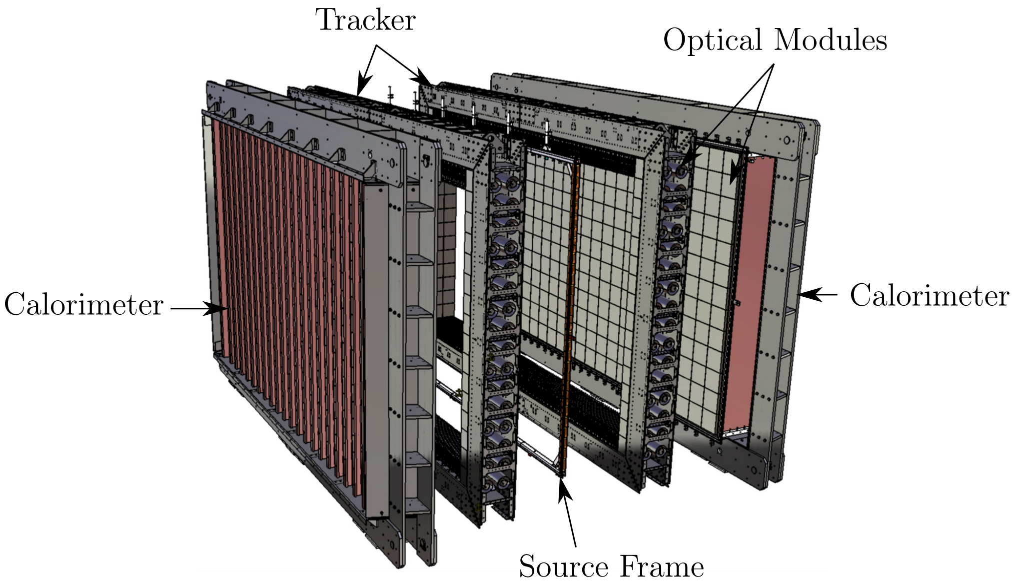

Figure 9.1.: Exploded view of a SuperNEMO module, showing the locations of the source foils, tracker and calorimeter walls.

The modular design has been chosen as it provides some major advantages. Primarily, it is directly scalable such that if one module is shown to function correctly, the mass can be increased in a straight-forward manner. It also provides flexibility in the location of the detector as the modules can be arranged to maximise available space in underground laboratories. Finally, it reduces the lead time between construction and the start of data-taking as each module will become live as soon as it is built. However, the main drawback of this type of design comes from a cost perspective.

9.2. Research and Development

By using design concepts similar to those of NEMO-3, the valuable experience of running this detector may be exploited for SuperNEMO. The areas where improvements could be made on the NEMO-3 design were the focus of an extensive and varied programme of R&D, outlined in this section.

As was seen in the measurement of $0\nu\beta\beta$ with NEMO-3 in the previous chapter, backgrounds inside the source foils can severely hamper the physics reach of an experiment such as SuperNEMO. There has therefore been concerted effort into reducing the contamination of the source material using chemical and distillation purification techniques. Furthermore, a new large-scale detector has been developed which is capable of measuring very low levels of ^{214}Bi and ^{208}Tl contamination inside the foils using BiPo type events [107]. This detector will ensure that the required level of radiopurity of the foils has been reached before they are installed into the modules of the detector.

Due to the larger height of the SuperNEMO modules compared to NEMO-3, the tracker cells must be 10% longer in the new design. This prompted a re-evaluation of all properties of the drift cells and an optimisation of the cell dimensions looking at properties such as plasma propagation, efficiency and ageing. Prototypes were built, including a large tank that could house 90 cells which showed that resolutions of 0.7 mm in the transverse plane and 1.3 cm in the longitudinal direction could be achieved.

An additional step forward in tracker production has been the design and construction of a wiring robot, which has automated the manufacturing process. This greatly reduces the risk of contamination of the 260,000 wires required for the 20 modules. This contamination can prove problematic for the radiopurity of the detector and for achieving good plasma propagation along the drift cells.

As was seen in Section 4.1, the sensitivity of a $0\nu\beta\beta$ experiment is heavily dependent on its energy resolution. Therefore, a key target for SuperNEMO is to improve this resolution by a factor of ~ 2. One improvement has been replacing the polystyrene scintillator used in NEMO-3 with poly-vinyl toluene (PVT), but the biggest effect has been as a result of removing the need for a light guide. This was achieved by creating a hemispherical indentation in each scintillator block which can couple to the PMT directly.

Improvements have also been made in the calibration system, with the removal of the calibration tubes and windows that were less radiopure than the source foils in NEMO-3 (Figure 7.9a). The new system will use free-hanging weights to guide the calibration sources into position so that no material will remain in the detector outside of calibration runs. This will have the added benefit of allowing calibration with open sources if desired.

As was discussed in Section 7.1, most backgrounds for NEMO-3 were as a result of natural radioactivity. The situation with SuperNEMO is no different, and so all detector components are tested for radiopurity in HPGe detectors prior to inclusion. Where materials do not reach the required levels, new materials have generally been found that can act as a substitute. Components that are in contact with the tracking gas are also measured for radon emanation, which has motivated the construction of a new 0.7 m^3 emanation tank capable of measuring large samples to enhance sensitivity [108].

A more fundamental solution to reduce the level of radon emanation in to the tracker has been put forward in the form of a barrier that will separate the tracker and calorimeter. This material must necessarily be thin to maintain the energy resolution of the calorimeter but must also act as an effective radon barrier. To find a suitable material, a dedicated test-bench has been used to test various thin films [109]. The setup consists of two chambers separated by the test material as shown in Figure 9.2. A high level of radon is maintained in one chamber and the radon level in the other is monitored, which gives a measure of the diffusion coefficient of the material.

Additionally, this diffusion setup has been used to test various adhesives for radon permeability with one candidate, sytrene butadiene rubber (SBR), being incorporated into the detector seals to reduce diffusion from outside. The remaining focus of radon R&D involves the development of a dedicated system to measure low-levels of radon in gases, which is the subject of Chapter 11.

An overview of the progress from NEMO-3 to SuperNEMO made as a result of this R&D programme is shown in Table 9.1. In this table, the $0\nu\beta\beta$ selection efficiency is higher than in Section 8.4 as a lower energy threshold for each electron has been

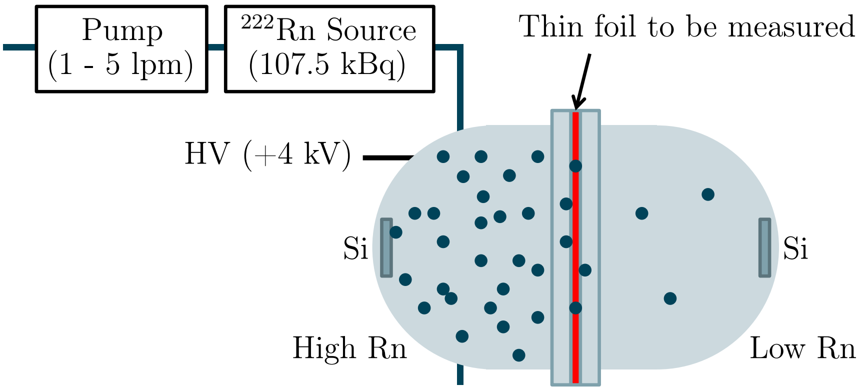

Figure 9.2.: Schematic of the radon diffusion test bench showing two chambers with high and low radon content, separated by a thin barrier material.

used. This is in order to make a fair comparison between NEMO-3 and SuperNEMO as it is expected a lower energy threshold will be possible in SuperNEMO.

Detector Property	NEMO-3	SuperNEMO
Isotope	^{100}Mo	^{82}Se
Source Mass	7 kg	100 kg
$0\nu\beta\beta$ Efficiency	18%	30%
Energy Resolution	8% @ 3 MeV	4% @ 3 MeV
^{214}Bi in foils	300 µBq/kg	10 µBq/kg
^{208}Tl in foils	20 µBq/kg	2 µBq/kg
^{222}Rn in tracker	5 mBq/m^3	0.15 mBq/m^3
$T^{0\nu}_{1/2}$ Sensitivity	10^{24} yr	10^{26} yr
$\langle m_{\beta\beta}\rangle$ Sensitivity	0.3 – 0.7 eV	40 – 100 meV

Table 9.1.: Summary of the key experimental achievements of NEMO-3 and the target levels for SuperNEMO.

9.3. Timescale and Sensitivity

The first module of SuperNEMO is referred to as the demonstrator module as it is intended to demonstrate all aspects of detector performance and that the target background levels can be achieved. It will contain 7 kg of ^{82}Se and has a target sensitivity of 6.5×10^{24} yr, which means it will also provide useful physics results in its own right.

Construction of the demonstrator has begun, with many different components already manufactured. Assembly of the tracker is taking place under clean room conditions in a dedicated assembly hall at the Mullard Space Science Laboratory (MSSL) in Surrey, UK. The tracker is built in four separation sections, known as C-sections due to their C-shape. Optical modules and supports for the tracker cells have been installed into the first C-section frame as shown in Figure 9.3. Radon tests have now been completed for this empty C-section (Section 13.3), and so assembly may continue with the installation of tracker cells from the wiring robot.


(a) (b)

Figure 9.3.: Photos of SuperNEMO construction, showing the installation of optical modules into the first C-section. (a) shows two rows of 16 wrapped scintillator blocks attached to the frame and (b) shows the tracker cell support structure in front of another row of larger optical modules.

Upon completion of the tracker, calorimeter and source foils for the module, scheduled for late 2014, assembly of the detector will take place in the LSM in the space vacated by NEMO-3. Commissioning of the detector will be finished by 2015, when data-taking will begin and the target sensitivity will be reached by 2016.

If the demonstrator is successful, successive SuperNEMO modules will be deployed from 2016 in the extension to the LSM laboratory which is currently under construction. The projected sensitivity of 10^{26} yr ($50 - 100$ meV) will be reached with an exposure of 500 kg yr as shown in Figure 9.4.

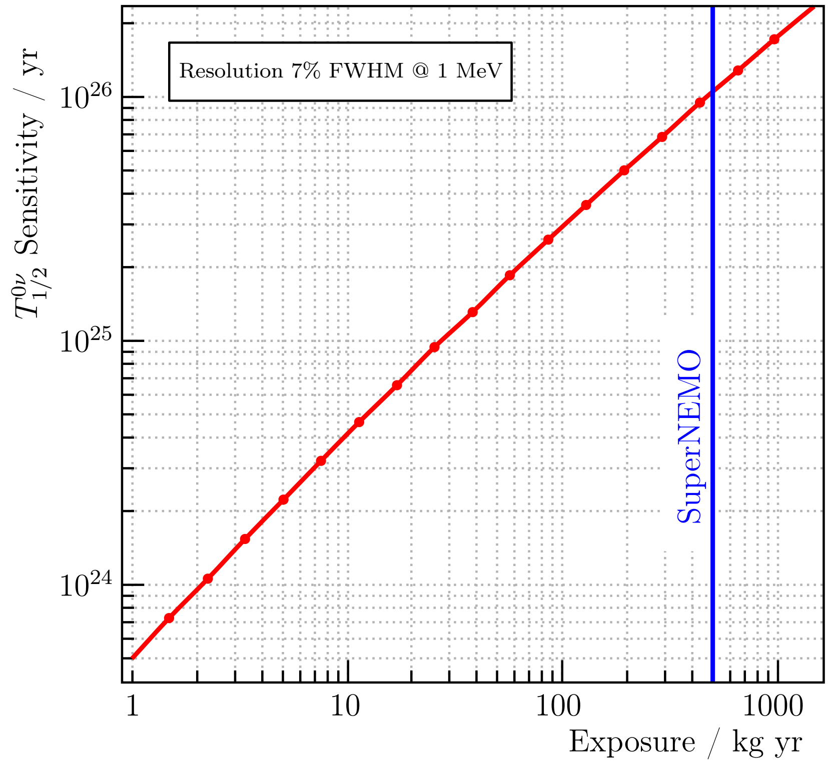

Figure 9.4.: Projected sensitivity of SuperNEMO as a function of exposure for the baseline design and target experimental parameters from Table 9.1. A sensitivity of 10^{26} yr will be reached after 500 kg yr.

Chapter 10.

Radon and SuperNEMO

10.1. Properties of Radon

Radon is a chemical element with atomic number 86. It is found as monatomic gas with the unusual property that it is the only gas that has solely radioactive isotopes.

In 1900, Friedrich Ernst Dorn reported experiments that showed emanation of a radioactive gas from radium compounds [110]. This is commonly attributed as the discovery of radon, although there are claims that the discovery should be attributed to Ernest Rutherford for his discovery of similar emanation from thorium oxide in 1899 [111]. These gases were simply named radium emanation and thorium emanation, as little else about their properties was known.

The situation improved between 1904 and 1910, when William Ramsay studied the properties of these gases at University College London. From similarities between their spectra and those of argon, krypton and xenon and their low level of chemical interaction, Ramsay correctly postulated that the emanations may be a new element in the group of noble gases [112]. Furthermore, he successfully isolated radon and determined that it was the densest known gas at that time. After a series of suggestions, finally, in 1920, the new names of radon and thoron were accepted for the emanated gases.

All isotopes of radon are radioactive, and only four are found in nature. Radon (^{222}Rn) comes from the ^{238}U decay chain (Figure 7.1), which also causes a very small amount of the ^{218}Rn isotope. In addition, the ^{232}Th decay series (Figure 7.2) provides thoron (^{220}Rn) and the ^{228}Ac series supplies actinon (^{219}Rn). ^{222}Rn is the most stable of all radon isotopes with a half-life of 3.8235 days. As far as $0\nu\beta\beta$ experiments are concerned, the only radon isotopes of interest are radon and thoron due to their progenies of ^{214}Bi and ^{208}Tl (Section 7.1).

Under standard temperature and pressure (STP) conditions, radon is a colourless and odourless gas. Its melting and boiling points are comparatively high for a noble gas, at -71 °C and -61.7 °C, respectively. With a density of 9.7 kg/m^3, it is the densest of the noble gases, and one of the most dense of all known gases. Although it is colourless at STP, radon emits a brilliant radioluminescence when cooled below its freezing point and a hazy glow upon condensation.

As a noble gas, radon is inert to most chemical reactions due to its full outer valence shell. This means that it cannot easily be filtered via chemical means and removal must be achieved using physical methods. It is only slightly soluble in water, but is considerably easier to dissolve in organic liquids, such as liquid scintillator. A further result of this chemical inactivity is that radon often exhibits a long diffusion length in solids which makes forming large scale seals difficult.

Typical radon activities from natural sources are $30 - 50$ Bq/m^3 indoors, however, these values can vary significantly. For example, clean rooms, usually with high rates of ventilation and lack of exposed brickwork, normally have levels < 5 Bq/m^3. Atmospheric radon activities are nominally ~ 10 Bq/m^3, but may be as low as 0.1 Bq/m^3 above oceans or in Antarctica. Underground laboratories, where low background experiments reside, display a similar level of variation dependent on the content of the surrounding rock. Salt mines are amongst the lowest at ~ 2 Bq/m^3, rising up to uranium mines which unsurprisingly have very high levels of up to 10 kBq/m^3.

There is a high degree of general interest in measurement of radon activities as it is hazardous to health in high quantities. Indeed, it is responsible for the majority of public exposure to ionising radiation and is the second greatest cause of lung cancer, after smoking [113]. Activity levels that are considered dangerous to health for long term exposure vary, but are normally above $200 - 400$ Bq/m^3. As a result, there are a wide range of commercial devices available for measuring radon activity in the 0.5 Bq/m^3 $-$ 1 MBq/m^3 range. However, the activity requirements for low background experiments are far below these sensitivities and so custom-made detectors are normally required.

10.2. Radon as a SuperNEMO Background

As was the case with NEMO-3, radon can present a significant source of background to SuperNEMO. The mechanism is identical with radon inside the tracker depositing ^{214}Bi on the source foils or tracker wires. The sources of radon background can come from emanation, contamination or diffusion, all of which have been addressed in the SuperNEMO R&D programme to improve on the performance of NEMO-3.

In order to quantify an acceptable level of radon contamination of the tracker, simulations were undertaken for varying radon activities. The resulting sensitivity curves are shown in Figure 10.1. In this study, the contributions of radon from the tracker and from internal ^{214}Bi contamination were treated separately, so that the sensitivity of 10^{26} yr that is achieved for 280 µBq/m^3 is only possible with no ^{214}Bi inside the foils. Therefore, when setting a target level for radon activity inside the tracker, the activity of ^{214}Bi is divided between internal contamination and radon in the tracking chamber, leading to a requirement that the tracker activity must be $<$ 150 µBq/m^3.

10.3. Radon Suppression with Gas Flow

In addition to the raft of improvements for the radon level from the R&D programme, an additional defence against radon in SuperNEMO is gained by the flow of gas through the modules. Provided that the supply gas has a lower level of radon contamination than that in the tracking chamber, the replacement of the dirtier gas produces a suppression of the radon level in the tracker.

As one might expect, the suppression that can be achieved is a function of the activity of the supply gas and the flow rate. The latter is limited by the tracker, which has decreased performance if gas volumes are exchanged too quickly. This nominal flow rate is $\sim$ 0.5 m^3/hr into the tracking volume of 15.2 m^3, but flow rates up to 1.0 m^3/hr are expected to be possible.

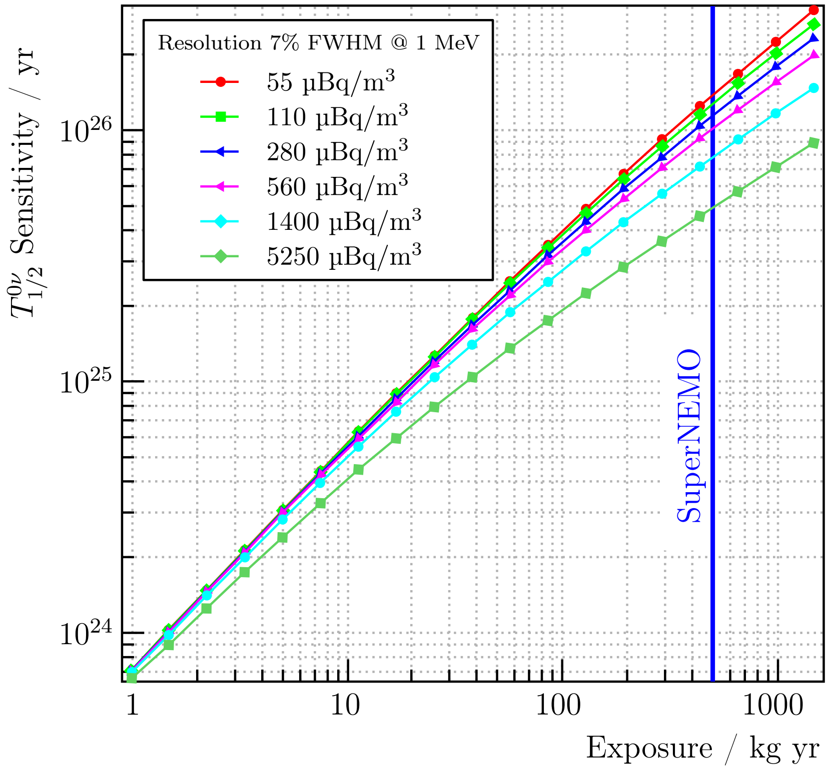

Figure 10.1.: SuperNEMO sensitivity as a function of exposure for different radon activities inside the tracker. Internal contamination of ^{214}Bi is neglected [114].

Naively, it might be assumed that gas can be supplied to the tracker at an arbitrarily low radon concentration. However, a gas-mixing system must be used to create the appropriate tracking mixture that, despite being carefully designed, will emanate a small activity of radon. Therefore, whilst clean gas can be supplied to the gas system via a series of radon traps, the output to the detector will be contaminated.

In order to calculate a flow suppression factor, a model is created where radon activity emanates uniformly within the gas system and is passed into the tracker as a result. The number of radon atoms inside the gas system, N_G, is given by the relationship between emanation from the gas system, atoms decaying within the gas system and those that are extracted by the gas flow:

$$\frac{dN_G}{dt} = A_G - \lambda N_G - \frac{f N_G}{V_G} \tag{10.1}$$

Here, A_G is the intrinsic ^{222}Rn activity of the gas system, λ is the radon decay constant, f is the gas flow rate and V_G is the total volume of the gas system. In general running conditions, the gas system will be in equilibrium, so that N_G is given by

$$N_G = \frac{A_G}{\lambda + \frac{f}{V_G}} = \frac{A_G V_G}{\lambda V_G + f} \approx \frac{A_G V_G}{f} \tag{10.2}$$

where the final approximation is very good since it is expected that $\lambda V_G \sim O(10^{-3})$ m^3/hr and $f \sim O(1)$ m^3/hr.

A similar equation gives the number of radon atoms inside the tracker, N_T, with an extra term for the radon supplied by the gas system:

$$\frac{dN_T}{dt} = A_T + \frac{f N_G}{V_G} - \frac{f N_T}{V_T} - \lambda N_T = A_T + A_G - \lambda'_T N_T \tag{10.3}$$

where V_T is the volume of the tracker and the calculated form of N_G (Equation (10.2)) has been used to illustrate that any emanation from the gas system has the same effect as if it were in the tracker itself. Further, the effect of the flow is shown to be equivalent to increasing the natural ^{222}Rn decay constant to become an effective decay constant λ'_T:

$$\lambda'_T = \lambda + \frac{f}{V_T} \tag{10.4}$$

Under static conditions, with no gas flow in the tracker, the number of radon atoms is simply given by $N_T^0 = A_T/\lambda$. Therefore a flow suppression factor, F_S, can be found by considering Equation (10.3) in the case of equilibrium:

$$F_S = \frac{N_T}{N_T^0} = \frac{A_T + A_G}{\lambda'_T}\frac{\lambda}{A_T} = \frac{1 + A_G/A_T}{1 + f/V_T\lambda} \tag{10.5}$$

This relationship is shown graphically in Figure 10.2 for three different values of A_G. For the anticipated gas flow rate of 0.5 m^3/hr (8.3 lpm) there is a reduction in radon activity by a factor of ~ 5.

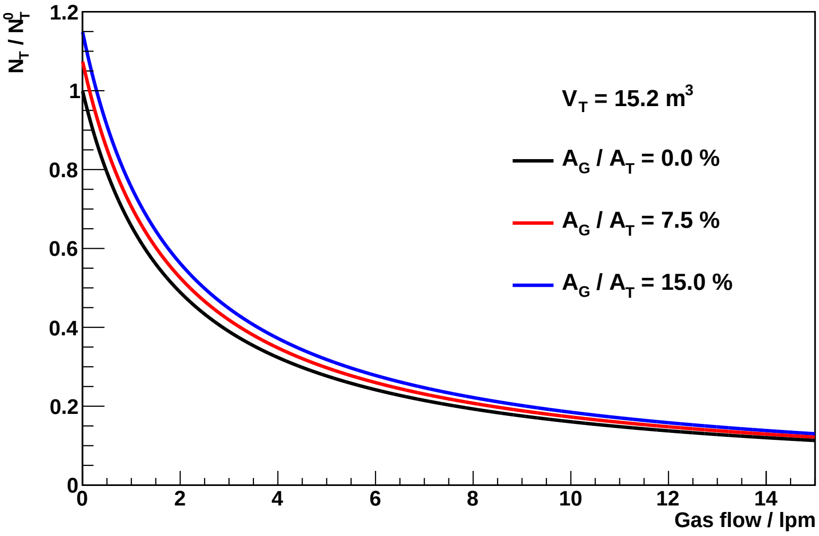

Figure 10.2.: Flow suppression factor for radon activity in the tracker. The three different curves are for three different activities of the gas system at 0%, 7.5% and 15% of the tracker activity.

10.4. ^{222}Rn Decay Chain to ^{214}Po

Up to now, only radon itself has been considered. However, electrostatic detectors which are commonly used to detect radon (Section 11.1) measure the levels of radon progenies ^{214}Po and ^{218}Po. It is therefore important to understand how the activity of these isotopes is related to that of their parent isotope ^{222}Rn. The details of the decay of each isotope are summarised in Table 10.1. The relationships between the activities in this decay chain are derived in this section.

Isotope	Decay	Half-life	Q Value / MeV	Daughter
^{226}Ra	α	1602 yr	4.871	^{222}Rn
^{222}Rn	α	3.8235 d	5.590	^{218}Po
^{218}Po	α	3.10 min	6.115	^{214}Pb
^{214}Pb	β	26.8 min	1.024	^{214}Bi
^{214}Bi	β	19.9 min	3.272	^{214}Po
^{214}Po	α	164.3 µs	7.883	^{210}Pb

Table 10.1.: Details of isotopes in the radon decay chain, starting from ^{226}Ra and continuing down the ^{214}Po.

When considering the radon decay chain, it is helpful to introduce the following notation to identify the number of atoms and decay constant for each isotope:

$$\begin{array}{ccccccccc} ^{222}\text{Rn} & \rightarrow & ^{218}\text{Po} & \rightarrow & ^{214}\text{Pb} & \rightarrow & ^{214}\text{Bi} & \rightarrow & ^{214}\text{Po} \\ N_0, \lambda_0 & & N_1, \lambda_1 & & N_2, \lambda_2 & & N_3, \lambda_3 & & N_4, \lambda_4 \end{array}$$

In a radioactive decay chain, the number of atoms of a given isotope is dictated by the balance between the number of atoms that decay to a new isotope and new atoms supplied by the decay of a parent isotope. This can be expressed as

$$\frac{dN_i}{dt} = \lambda_{i-1}N_{i-1} - \lambda_i N_i \tag{10.6}$$

The recipe to find the numbers of atoms of isotopes further down the decay chain is simply to iteratively solve these differential equations starting at $i = 0$, or ^{222}Rn, and using appropriate starting conditions to find any constants of integration.

In addition to this isotope labelling notation, another new definition will become algebraically useful during the following calculations. Thus, the following series of constants are defined as:

$$k^j_{i,N} = \prod_{m=N-j}^{N} [1 + (1 - \delta_{im})(\lambda_m - \lambda_i - 1)] \tag{10.7}$$

where δ_{im} is a Kronecker delta. These constants are the product of j terms containing λ_i subtracted from other λ. They can be found by starting at $(\lambda_N - \lambda_i)$, multiplying by $(\lambda_{N-1} - \lambda_i)$ and ending after $(\lambda_{N-j} - \lambda_i)$ where the Kronecker delta ensures the self-term $(\lambda_i - \lambda_i)$ is omitted from the product. This is best illustrated by expanding out a few example terms:

$$\begin{aligned}
k^4_{0,4} &= (\lambda_4 - \lambda_0)(\lambda_3 - \lambda_0)(\lambda_2 - \lambda_0)(\lambda_1 - \lambda_0)\\
k^4_{1,4} &= (\lambda_4 - \lambda_1)(\lambda_3 - \lambda_1)(\lambda_2 - \lambda_1)(\lambda_0 - \lambda_1)\\
k^3_{1,4} &= (\lambda_4 - \lambda_1)(\lambda_3 - \lambda_1)(\lambda_2 - \lambda_1)\\
k^3_{2,3} &= (\lambda_3 - \lambda_2)(\lambda_1 - \lambda_2)(\lambda_0 - \lambda_2)\\
k^2_{0,2} &= (\lambda_2 - \lambda_0)(\lambda_1 - \lambda_0)
\end{aligned}$$

With this new notation, the machinery is now in place to move through the decay chain, calculating the numbers of atoms of each isotope.

10.4.1. ^{222}Rn Activity

In the scenario of interest, a signal activity, A_S, corresponding to A_S/λ radon atoms, is introduced into a detector. The detector itself is assumed to have an intrinsic background activity, A_D, caused by emanation of radon from ^{226}Ra decay, which is assumed constant due to its long half-life. The number of radon atoms in the detector after a given time can be found by solving the differential equation

$$\frac{dN_0}{dt} = -\lambda_0 N_0 + A_D \tag{10.8}$$

This can be solved by noting that

$$\frac{d}{dt}(e^{\lambda_0 t} N_0) = e^{\lambda_0 t}(\frac{dN_0}{dt} + \lambda_0 N_0) = e^{\lambda_0 t} A_D \tag{10.9}$$

so that

$$e^{\lambda_0 t} N_0 = \int e^{\lambda_0 t} A_D dt = \frac{A_D}{\lambda_0} e^{\lambda_0 t} + C \tag{10.10}$$

Assuming that the detector has been cleared of all radon before the start of the measurement leads to the boundary condition that $N = A_S/\lambda_0$ at $t = 0$. Therefore

$C = A_S/\lambda_0 - A_D/\lambda_0$ and

$$N_0 = \frac{A_D}{\lambda_0}(1 - e^{-\lambda_0 t}) + \frac{A_S}{\lambda_0} e^{-\lambda_0 t} \tag{10.11}$$

which can be seen as the characteristic sum of the increasing background term and the exponentially decaying signal term.

10.4.2. ^{218}Po Activity

For ^{218}Po the equation to be solved is

$$\frac{dN_1}{dt} = \lambda_0 N_0 - \lambda_1 N_1 \tag{10.12}$$

which following the same process as for equation (Equation (10.9)) yields

$$\begin{aligned} e^{\lambda_1 t} N_1 = \int e^{\lambda_1 t} \lambda_0 N_0 dt = \int A_D e^{\lambda_1 t} + (A_S - A_D) e^{(\lambda_1 - \lambda_0) t} dt \\ = A_D \frac{e^{\lambda_1 t}}{\lambda_1} + (A_S - A_D) \frac{e^{(\lambda_1 - \lambda_0) t}}{\lambda_1 - \lambda_0} + C \end{aligned} \tag{10.13}$$

where C is again a constant of integration. Applying the same boundary condition that $N_1 = 0$ at $t = 0$, the form of N_1 is

$$N_1 = \frac{A_D}{\lambda_1}(1 - e^{-\lambda_1 t}) + (A_S - A_D) \left(\frac{e^{-\lambda_0 t}}{\lambda_1 - \lambda_0} + \frac{e^{-\lambda_1 t}}{\lambda_0 - \lambda_1} \right) \tag{10.14}$$

which using the $k^j_{i,N}$ notation can be written

$$N_1 = \frac{A_D}{\lambda_1}(1 - e^{-\lambda_1 t}) + (A_S - A_D) \left(\frac{e^{-\lambda_0 t}}{k^1_{0,1}} + \frac{e^{-\lambda_1 t}}{k^1_{1,1}} \right) \tag{10.15}$$

10.4.3. ^{214}Pb Activity

Continuing down the decay chain to ^{214}Pb, the differential equation to be solved is

$$\frac{dN_2}{dt} + \lambda_2 N_2 = \lambda_1 N_1 \tag{10.16}$$

As before

$$\begin{aligned} e^{\lambda_2 t} N_2 &= \int e^{\lambda_2 t} \lambda_1 N_1 dt \\ &= \int A_D \left(e^{\lambda_2 t} - e^{(\lambda_2-\lambda_1)t}\right) \\ &\qquad + (A_S - A_D)\lambda_1 \left(\frac{e^{(\lambda_2-\lambda_0)t}}{k^1_{0,1}} + \frac{e^{(\lambda_2-\lambda_1)t}}{k^1_{1,1}}\right) dt \end{aligned} \tag{10.17}$$

So that

$$N_2 = \frac{A_D}{\lambda_2} - \frac{A_D e^{-\lambda_1 t}}{\lambda_2 - \lambda_1} + (A_S - A_D)\lambda_1 \left(\frac{e^{-\lambda_0 t}}{k^2_{0,2}} + \frac{e^{-\lambda_1 t}}{k^2_{1,2}}\right) + Ce^{-\lambda_2 t} \tag{10.18}$$

And assuming $N_2 = 0$ at $t = 0$ it is found that

$$C = -\frac{A_D}{\lambda_2} - \frac{A_D}{\lambda_1 - \lambda_2} - (A_S - A_D)\lambda_1 \left(\frac{1}{k^2_{0,2}} + \frac{1}{k^2_{1,2}}\right) \tag{10.19}$$

This can be further simplified by noting that

$$\begin{aligned} \frac{1}{k^2_{0,2}} + \frac{1}{k^2_{1,2}} &= \frac{1}{(\lambda_2-\lambda_0)(\lambda_1-\lambda_0)} + \frac{1}{(\lambda_2-\lambda_1)(\lambda_0-\lambda_1)} \\ &= \frac{-(\lambda_1-\lambda_0)}{(\lambda_2-\lambda_0)(\lambda_1-\lambda_0)(\lambda_2-\lambda_1)} = -\frac{1}{k^2_{2,2}} \end{aligned} \tag{10.20}$$

So that performing the substitution leads to the final form for N_2, where the benefit of the $k^j_{i,N}$ notation is becoming apparent:

$$\begin{aligned} N_2 = \frac{A_D}{\lambda_2}(1 - e^{-\lambda_2 t}) - A_D \left(\frac{e^{-\lambda_1 t}}{k^1_{1,2}} + \frac{e^{-\lambda_2 t}}{k^1_{2,2}}\right) \\ + (A_S - A_D)\lambda_1 \left(\frac{e^{-\lambda_0 t}}{k^2_{0,2}} + \frac{e^{-\lambda_1 t}}{k^2_{1,2}} + \frac{e^{-\lambda_2 t}}{k^2_{2,2}}\right) \end{aligned} \tag{10.21}$$

10.4.4. ^{214}Bi Activity

Following the same procedure for ^{214}Bi, it is found that N_3 has a similar solution to N_2 although with additional terms:

$$\begin{aligned} N_3 = \frac{A_D}{\lambda_3} - \frac{A_D e^{-\lambda_2 t}}{\lambda_3 - \lambda_2} - A_D\lambda_2 \left(\frac{e^{-\lambda_1 t}}{k^2_{1,3}} + \frac{e^{-\lambda_2 t}}{k^2_{2,3}} \right) \\ + (A_S - A_D)\lambda_1\lambda_2 \left(\frac{e^{-\lambda_0 t}}{k^3_{0,3}} + \frac{e^{-\lambda_1 t}}{k^3_{1,3}} + \frac{e^{-\lambda_2 t}}{k^3_{2,3}} \right) + Ce^{-\lambda_3 t} \end{aligned} \tag{10.22}$$

Using the same boundary condition that $N_3 = 0$ at $t = 0$ leads to

$$\begin{aligned} N_3 = \frac{A_D}{\lambda_3} \Bigg[1 - e^{-\lambda_3 t} - \lambda_3 \left(\frac{e^{-\lambda_2 t}}{k^1_{2,3}} + \frac{e^{-\lambda_3 t}}{k^1_{3,3}} \right) \\ - \lambda_2\lambda_3 \left(\frac{e^{-\lambda_1 t}}{k^2_{1,3}} + \frac{e^{-\lambda_2 t}}{k^2_{2,3}} + \frac{e^{-\lambda_3 t}}{k^2_{3,3}} \right) \\ - \lambda_1\lambda_2\lambda_3 \left(\frac{e^{-\lambda_0 t}}{k^3_{0,3}} + \frac{e^{-\lambda_1 t}}{k^3_{1,3}} + \frac{e^{-\lambda_2 t}}{k^3_{2,3}} + \frac{e^{-\lambda_3 t}}{k^3_{3,3}} \right) \Bigg] \\ + A_S\lambda_1\lambda_2 \left(\frac{e^{-\lambda_0 t}}{k^3_{0,3}} + \frac{e^{-\lambda_1 t}}{k^3_{1,3}} + \frac{e^{-\lambda_2 t}}{k^3_{2,3}} + \frac{e^{-\lambda_3 t}}{k^3_{3,3}} \right) \end{aligned} \tag{10.23}$$

This can be written more concisely using sum and product notation, with the final form for N_3 as

$$N_3 = \frac{A_D}{\lambda_3} \left\{ 1 - \sum_{i=0}^{3} \left[\left(\prod_{j=i+1}^{3} \lambda_j \right) \sum_{k=i}^{3} \frac{e^{-\lambda_k t}}{k^{3-i}_{k,3}} \right] \right\} + A_S\lambda_1\lambda_2 \sum_{i=0}^{3} \frac{e^{-\lambda_i t}}{k^3_{i,3}} \tag{10.24}$$

10.4.5. ^{214}Po Activity

The final isotope in the decay chain that is of interest is ^{214}Po. As was apparent from the previous solutions, the algebra becomes rather arduous at this point and so only the result shall be quoted here, which is a straight-forward extension of the N_3 case:

$$N_4 = \frac{A_D}{\lambda_4} \left\{ 1 - \sum_{i=0}^{4} \left[\left(\prod_{j=i+1}^{4} \lambda_j \right) \sum_{k=i}^{4} \frac{e^{-\lambda_k t}}{k^{4-i}_{k,4}} \right] \right\} + A_S\lambda_1\lambda_2\lambda_3 \sum_{i=0}^{4} \frac{e^{-\lambda_i t}}{k^4_{i,4}} \tag{10.25}$$

10.4.6. Decay chain activities

Now that the expected numbers of atoms of each isotope in this decay chain have been calculated, the resulting activities inside the detector can be plotted to more readily understand the properties of the decay chain. This plot is shown in Figure 10.3. It should be noted that the ^{218}Po reaches equilibrium with the ^{222}Rn rather quickly whilst the decay chain delays the ^{214}Po for some time so it is only in equilibrium after 4.5 hrs.

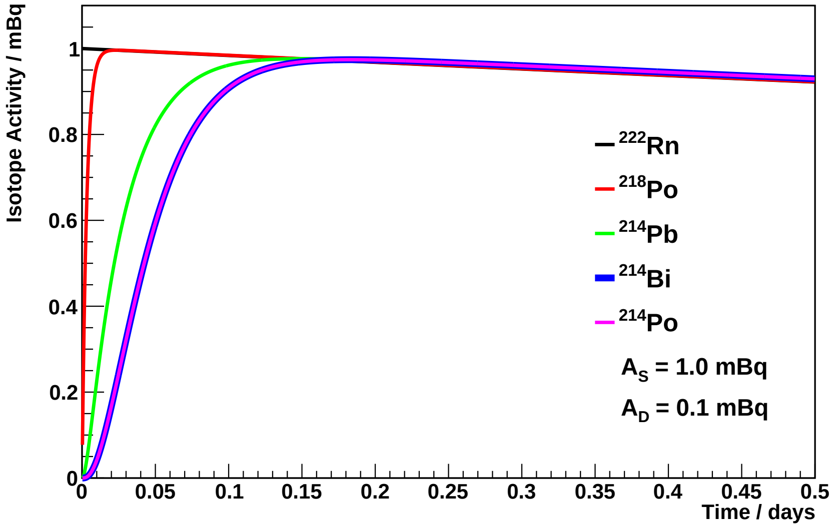

Figure 10.3.: Activities of different isotopes in the ^{222}Rn decay chain with respect to time after introduction of 1 mBq of ^{222}Rn into a detector with 0.1 mBq background.

Chapter 11.

Electrostatic Detector and Radon Concentration Line

The SuperNEMO requirement of radon activity inside the tracker at a level less than 150 µBq/m^3 poses significant technical challenges in the design and construction of the detector. Furthermore, the level is so low that even confirming that the target has been reached is not straight-forward. A considerable amount of effort has gone into the design and construction of a system capable of measuring below this level of radon in gases, which is the subject of this chapter.

As mentioned in the previous chapter, commercial radon detectors are available with sensitivities down to ~ 0.5 Bq/m^3, which is some four orders of magnitude away from the sensitivity required for a reliable measurement of the radon activity in the tracker. Therefore, a custom-made electrostatic detector, developed for use in many low background experiments is used in this work. The commissioning of this radon detector is discussed in Section 11.1.

Even this state-of-the-art detector is only capable of measuring down to the level of $\sim 1 - 2$ mBq/m^3, as will be shown in Section 12.2. Therefore, in order to reach the target sensitivity, a "radon concentration line" (RnCL) has been developed, which uses a cooled carbon trap to store radon from gases that are passed through it. This concentrated sample of radon is then passed to the electrostatic detector to be measured. The design and operation of the RnCL will be outlined in the second half of this chapter (Section 11.2).

The combination of RnCL and electrostatic detector easily reaches the desired sensitivity for the SuperNEMO tracker and is amongst the world's most sensitive pieces of apparatus for measuring low levels of radon in gases as will be shown in Chapter 12.

11.1. Electrostatic Detector

Electrostatic detectors operate by using an electric field to move the progenies of radon decay to a region of the detector where their subsequent decay is measured. The technique exploits a particular property of alpha decay that the daughter atom is likely to be be found as a charged atom or part of a charged compound. The charge can either be negative or positive and in some cases progenies become multiply positively charged. The fraction of positive ions and compounds from radon decay in air was measured to be 88% as long ago as 1913 [115], in surprisingly good agreement with more modern measurements of $87.3 \pm 1.6\%$ [116].

The electrostatic detector used in this work was developed to measure low-levels of radon for the ELEGANT V and Super-Kamiokande experiments [117, 118], and is shown in Figure 11.1.

The detector is relatively simple, consisting of an electro-polished stainless steel chamber with a volume of 70 litres, which has a silicon PIN diode placed at one end, as shown schematically in Figure 11.2. The associated electronics are separated from the measurement chamber by a sheet of perspex with a feedthrough for the PIN diode. There is an inlet and outlet for gas flow and all valves are either metallic or have been coated in styrene butadiene rubber (SBR) to reduce diffusion. An electric field is generated inside the chamber by applying a negative high voltage (typically -1500 V) onto the PIN diode.

In standard operation, a measurement sample is introduced into the detector, where any radon subsequently decays to predominantly positive ions. These ions are collected onto the PIN diode as a result of the applied electric field. Once on the diode, their decays are detected, particularly the alpha decays of ^{218}Po and ^{214}Po, and are identified by the amount of energy deposited.


(a) Normal operation **(b)** With lid removed

Figure 11.1.: Electrostatic detector used for all radon measurements in this work. (a) shows the detector in normal operation, and (b) shows the lid removed where the feedthrough for the PIN diode can be seen.

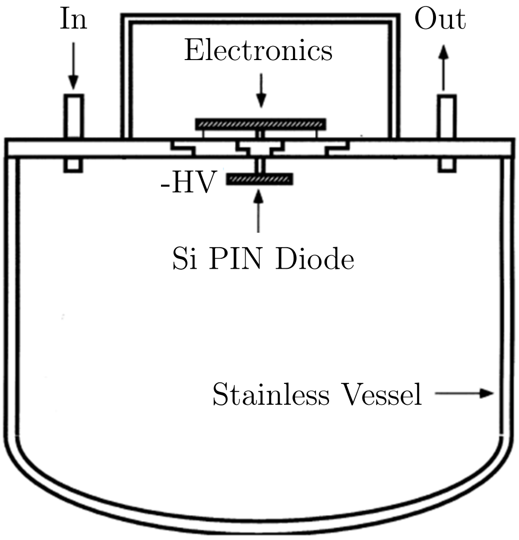

Figure 11.2.: Schematic diagram of the electrostatic detector shown in Figure 11.1.

^{214}Po is most commonly used as a measure of the radon level, as it generally has a higher detection efficiency. Naively one might expect that the efficiencies for ^{214}Po and ^{218}Po should be identical, but in reality the collection efficiency for ^{218}Po is not 100%. The intermediate isotopes of ^{214}Pb and ^{214}Bi may also be collected onto the PIN diode so that the level of ^{214}Po is higher than that of ^{218}Po. In addition, these isotopes, and ^{214}Po itself, are not as susceptible to neutralisation as ^{218}Po such that the collection efficiency for ^{214}Po is more stable in the presence of trace amounts of impurities.

11.1.1. Detector Signal

The detector has a self-contained set of electronics, which filters the HV supply, supplies a bias voltage and provides the required voltage rails for the multi-stage amplification of the signal. These electronics are housed within the lid of the detector which minimises the distance of signal cable before pre-amplification and provides shielding from external noise.

The detector signal is passed to a NEMbox DAQ system (Wiener NEMbox SU706), which is a programmable FPGA intended to perform the functions of a NIM crate in a small, stand-alone, bench-top unit. The NEMbox is used to trigger and digitise the pulse for storage along with preventing re-triggering from after pulses. The full pulses are stored for offline analysis which causes a dead time of ~ 17 ms whilst the signals are written to disk. This dead time was quantified by supplying signals of known frequency and measuring the response of the system as shown in Figure 11.3. It has a negligible effect in normal data-taking modes, but must be taken into account in some calibration runs where there is a high activity in the detector.

The analysis of signal events from the detector proceeds in two stages. The first stage is a preliminary filter and the second stage involves the extraction of relevant parameters with a fitting function.

Event Filtering

The filtering stage of the analysis is present to reduce the possibility of mis-identification of an event and to deal with cases that may be pathological for

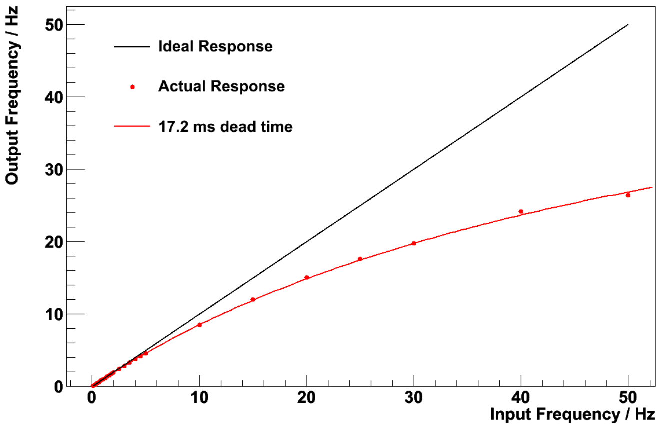

Figure 11.3.: Response of the DAQ system for different input frequencies, where the red points show measured values and the red line shows the expected results for a dead time of 17.2 ms between each pulse.

the fitting function. A peak-finding algorithm is used to identify the number of peaks in an event along with their times and magnitudes. This information is then used to identify four different types of event. The majority of these are of the normal signal type as shown in Figure 11.4a. These events contain only one peak and are passed straight to the fitting stage.

The next two event types are rare scenarios where there are two peaks in an event, which is not handled by the fitting function. The first are BiPo events, where the decay of the electron from ^{214}Bi is detected along with the alpha from ^{214}Po as in Figure 11.4b. These events are rare as only $\sim$ 10% of ^{214}Po atoms decay in the 15 µs pre-trigger window and both particles must deposit energy in the PIN diode. However, they form a constant proportion ($\sim$ 1%) of ^{214}Po events in both normal data-taking and in calibration runs. The other two-peak scenario is pile-up events where there is more than one decay in the signal window, as shown in Figure 11.4c. These events are only observed in calibration runs where the activity is high, but can adversely affect an efficiency measurement if not properly treated.

The final type of events are those caused by electrical noise. These events have a large number of peaks in quick succession with similar magnitudes as shown in Figure 11.4d. Most of these events have low amplitudes, but very occasionally one may be large enough to be mistaken for a signal event.

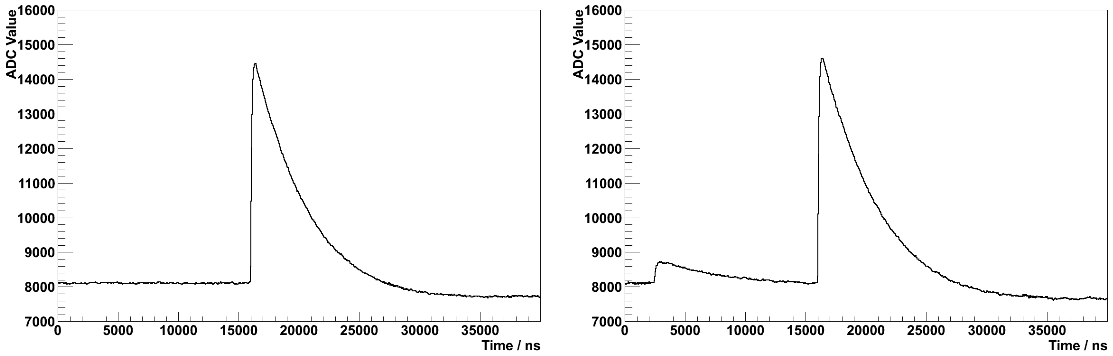

(a) Normal Signal

(b) BiPo Signal

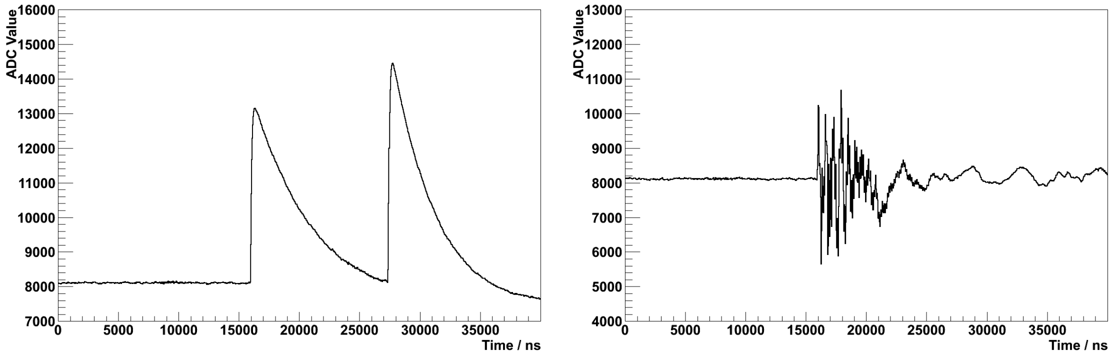

(c) Pile-up Event

(d) Noise Event

Figure 11.4.: Examples of the four types of event identified by the filtering stage of the event analysis, described in the text.

Pulse shape function

To extract the best possible value of signal amplitude, each pulse is fitted with the function described in this section. The main advantage of such a treatment is that any events that have passed the pre-filter but are not of the normal signal type are rejected. The fitting function is found by taking the expected signal from the PIN diode and propagating this through a theoretical description of a pre-amplifier to calculate the expected form of the output.

To find the form of the PIN diode signal, a fast LED was shone onto the photodiode and the output observed directly. This showed a signal that could be modelled as a linear rise, followed by an exponential decay:

$$V_{in}(t) = \begin{cases} \dfrac{-V_0 t}{T} & 0 \leq t \leq T \\ -V_0 e^{-\lambda(t-T)} & t \geq T \end{cases} \tag{11.1}$$

To calculate the response of the detector's inverting amplifier to such a signal, it was assumed to have an ideal response such that the output voltage, V, is described by

$$\frac{dV}{dt} + \frac{V}{\tau} = \begin{cases} \dfrac{V_0 t}{T\tau} & 0 \leq t \leq T \\ \dfrac{V_0 e^{-\lambda(t-T)}}{\tau} & t \geq T \end{cases} \tag{11.2}$$

where $\tau = RC$ is the characteristic time constant of the pre-amplifier. This can be solved to find the form of the fitting function:

$$V(t) = \begin{cases} \dfrac{V_0 t}{T} - \dfrac{V_0 \tau}{T}\left(1 - e^{-\frac{t}{\tau}}\right) & 0 \leq t \leq T \\ \dfrac{V_0}{1-\lambda\tau}\left(e^{-\lambda(t-T)} - \lambda\tau e^{-\frac{t-T}{\tau}}\right) - \dfrac{V_0\tau}{T}\left(1 - e^{-\frac{T}{\tau}}\right)e^{-\frac{t-T}{\tau}} & t \geq T \end{cases} \tag{11.3}$$

In this function, the values of λ and τ are fixed to measured values for this experimental setup, so that even single peaked events that do not originate from the PIN diode may be rejected.

An example of an event with a superimposed fit is shown in Figure 11.5, showing that the agreement between the actual and theoretical response is excellent.

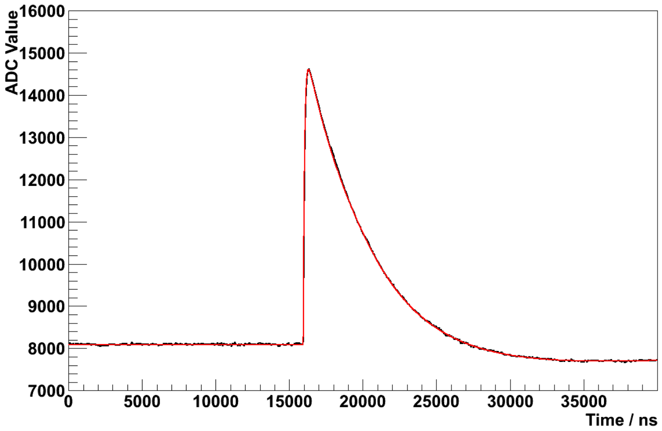

Figure 11.5.: Example of a signal event (black) with the fitting function (Equation (11.3)) superimposed (red).

11.1.2. Detector Efficiency Calibration

In order to investigate the response of the detector to a known activity of radon, a calibrated source was procured. This source is a 1.32 kBq "flow-through" ^{226}Ra source (Pylon Electronics, RN-1025), the design of which allows the flow of gas through the source material. This ensures that all the emanated radon is exhausted and provides considerable flexibility in the possible measurements that can be made.

Radon progenies are identified by the energy they deposit in the PIN diode, which is proportional to the amplitude of the signal. Three isotopes of polonium, all of which decay via alpha decay, are clearly visible in an energy spectrum after introducing radon from the source into the detector as displayed in Figure 11.6. The ^{214}Po peak, which is used to measure the radon level is the highest energy peak (7.9 MeV). The ^{218}Po peak (6.1 MeV) has a slightly lower height as its collection efficiency is lower for reasons discussed above. Finally, a much smaller peak from ^{210}Po is visible (5.4 MeV), the height of which is unrelated to the current level of radon in the detector as it is caused by residual activity from previous calibration runs. The resolution of the detector is excellent with clear separation between the peaks. Even so, there is overlap between the tail of the ^{218}Po peak and the ^{210}Po which is further reason to base radon measurements on the ^{214}Po activity.

In order to calibrate the efficiency of the detector, two different methods are used. The first is a "spike" method, where a known amount of radon is introduced into the

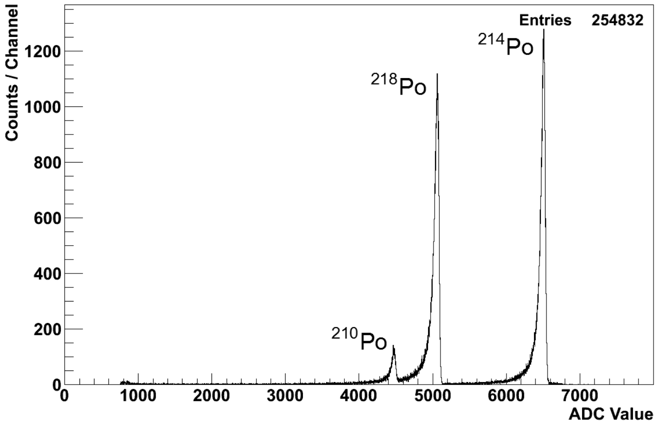

Figure 11.6.: Energy spectrum from a calibration run with a high activity of radon in the detector. Peaks from ^{214}Po, ^{218}Po and ^{210}Po are labelled.

detector and measured as it decays. To achieve this, the radon source is first cleared by flushing thoroughly, then is sealed to allow radon to build up. When the desired amount of radon has been emanated, the radon is purged from the source into the detector.

This scenario is the same as that envisaged in the derivation in Section 10.4 and so the activities of ^{218}Po and ^{214}Po are given by Equations (10.15) and (10.25), respectively. In a typical calibration, helium is used as a carrier gas to move 2.5 Bq of radon into the detector. A typical result of this type of calibration is shown in Figure 11.7, showing good agreement with the expected behaviour of the activities.

The resulting efficiency measurements are $31.5 \pm 1.3\%$ and $28.4 \pm 1.1\%$ for ^{214}Po and ^{218}Po respectively, where the error is dominated by uncertainty on the source activity. At this stage, it should be noted that the maximum efficiency for a detector of this type is 50% as this is the probability that the alpha from the decay will be emitted into the PIN diode, rather than away from it.

Using helium as the measurement gas is expected to show improved efficiency over nitrogen due to impurities in the form of nitrous oxides in the latter. This is indeed what is observed, with reduced efficiencies of $28.1 \pm 1.1\%$ for ^{214}Po and $22.3 \pm 0.9\%$ for ^{218}Po in nitrogen. The reduction is more severe for ^{218}Po which is more sensitive to the impurities.

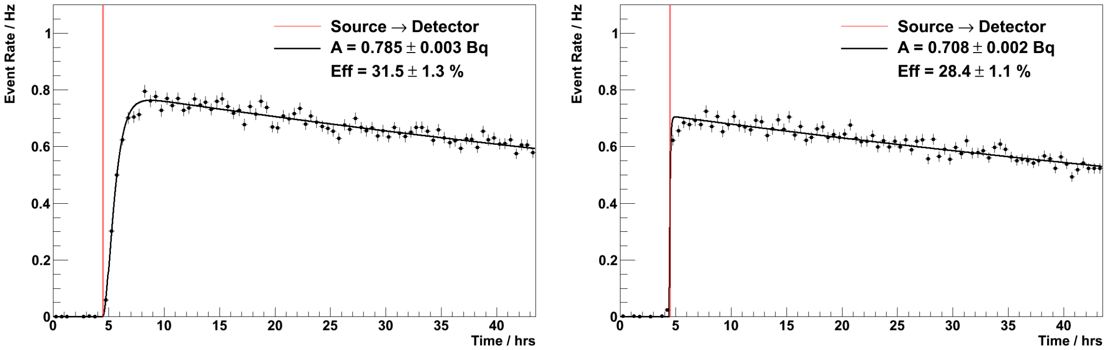

(a) ^{214}Po Event Rate

(b) ^{218}Po Event Rate

Figure 11.7.: ^{214}Po and ^{218}Po event rates for a spike-type calibration run with 2.5 Bq of radon introduced into the detector filled with helium. The black lines show the expected response from Equations (10.25) and (10.15), fitted for an overall normalisation with all half-lives fixed to their known values.

This calibration method is identical to the method used in real measurements and provides the most accurate result. However, added confidence can be gained by calibrating with a second method. One possibility is a “flow-through” method, where gas is continuously moved through the source and detector. This method reduces uncertainties associated with the level of radon extracted from the source, but good knowledge of the flow rate and volume of the detector is required which makes this method less accurate overall.

The resulting ^{214}Po and ^{218}Po activities from a typical flow-through calibration may be seen in Figure 11.8. In this calibration, nitrogen flows at 4.2 lpm, resulting in efficiencies of 29.4 ± 2.0 and 23.2 ± 1.6 for ^{214}Po and ^{218}Po, respectively. These results are comparable to those found using the spike method and can easily be accounted for in the uncertainty in flow rate. Again, ^{218}Po is lower than the ^{214}Po and the ratio between them is strikingly similar to that found for nitrogen in the spike method.

The detector is regularly calibrated to ensure stable performance. Some typical results from calibration runs, which were included in the above text, are displayed in Table 11.1.

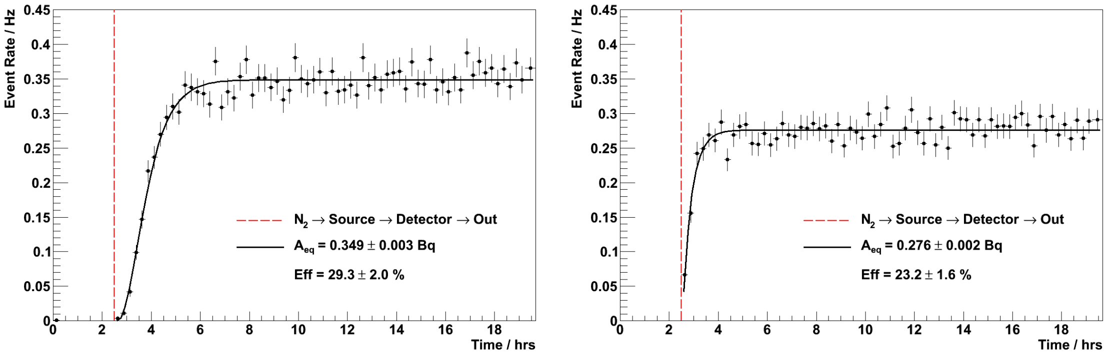

(a) ^{214}Po Event Rate **(b)** ^{218}Po Event Rate

Figure 11.8.: ^{214}Po and ^{218}Po event rates for a flow-through calibration run with a flow rate of 4.2 lpm of nitrogen. The black lines show the expected response from a similar calculation to that shown in Section 10.4, fitted for an effective radon half-life and overall normalisation.

Calibration Mode	Measurement Gas	Efficiency / %	
		^{214}Po	^{218}Po
Spike	He	31.5 ± 1.3	28.4 ± 1.1
Spike	N_2	28.1 ± 1.1	22.3 ± 0.9
Flow-through	N_2	29.3 ± 2.0	23.2 ± 1.6

Table 11.1.: Typical results of calibration of the electrostatic detector for spike and flow-through calibration modes in helium and nitrogen.

11.1.3. Detector Background Measurement

As shown above, the electrostatic detector has an efficiency of over 30%. However, a sensitive detector must also have a low background counting rate, which is the subject of this section.

In general, before performing every measurement, the background level of the detector is measured to ensure that the best estimate of the activity of introduced radon is made. Additionally, on occasion there have been some extended runs which were solely dedicated to a background measurement of the detector. In order to perform these measurements, the detector is sealed for $20 - 25$ days whilst the radon activity inside is measured. The energy spectrum from this type of run is different to that of a calibration run as can be seen in Figure 11.9.

This spectrum is much more similar to that observed in real measurements where there is very little radon in the detector and the ^{210}Po peak from previous calibration runs dominates. On a logarithmic scale, the ^{214}Po and ^{218}Po peaks become visible along with a smaller peak from ^{212}Po at 8.9 MeV, which is a thoron progeny.

A typical measurement of the detector background is shown in Figure 11.10. The ^{214}Po rate (Figure 11.10a), which is the main quantity of interest for a radon measurement shows a level of 7.27 ± 0.53 counts-per-day (cpd). In this measurement, the detector is filled with helium and so, using an efficiency of 31.5%, the intrinsic activity of the detector is 0.27 ± 0.02 mBq or 3.82 ± 0.28 mBq/m^3. This background value is combined with the detector efficiency to estimate the sensitivity of the detector in Section 12.2.

As well as the ^{214}Po rate, the ^{210}Po activity is measured as shown in Figure 11.10b. Although this provides no information on the radon activity in the chamber, it should be relatively constant over time which provides a good handle for checking the stability of the detector and DAQ system.

11.2. Radon Concentration Line (RnCL)

The performance of the electrostatic detector is amongst the best compact radon detectors in the world. Even so, it is not sufficiently sensitive to measure the

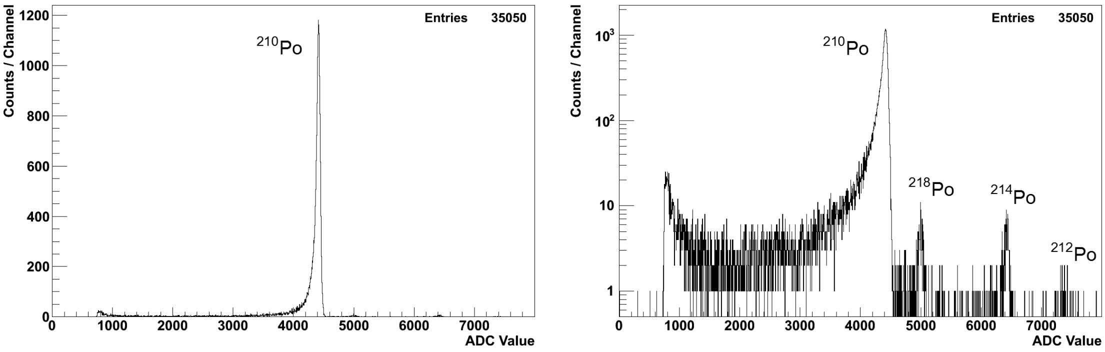

(a) Energy Spectrum

(b) Energy Spectrum (log scale)

Figure 11.9.: Energy spectrum from a background measurement showing peaks from ^{210}Po, ^{214}Po, ^{218}Po and an additional peak assumed to be from ^{212}Po.

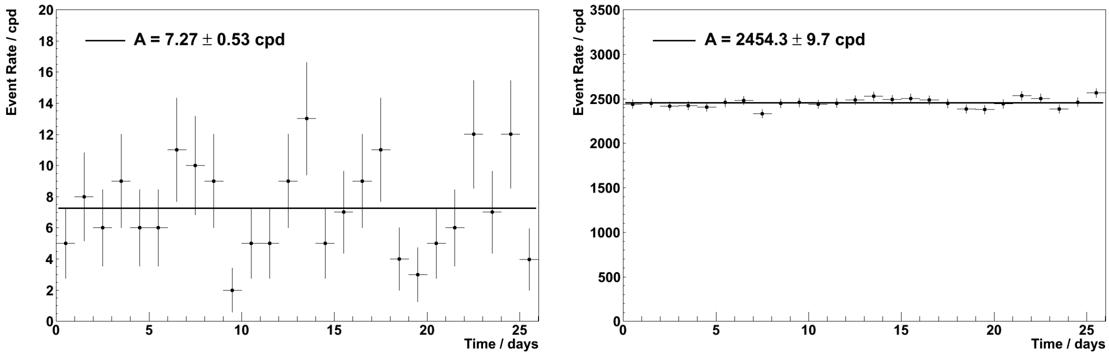

(a) ^{214}Po Activity **(b)** ^{210}Po Activity

Figure 11.10.: ^{214}Po and ^{210}Po event rates for a typical background measurement run. The ^{214}Po rate shows a low background level and the ^{210}Po rate is stable across the measurement.

SuperNEMO radon requirement of 150 µBq/m^3. Ultimately, SuperNEMO will use BiPo type events to measure the radon content inside the tracker. However, it is important to measure the radon level as the detector is built so that an unexpectedly high level can be addressed before the detector is fully assembled.

In order to measure radon concentrations below 150 µBq/m^3 in the construction phase of the experiment, a new piece of apparatus has been developed. This system processes large volumes of gas from which the radon content is stored, before transferring the concentrated sample into the electrostatic detector, where it can be measured. It is therefore called the "Radon Concentration Line" (RnCL).

The concept is based on previous work for the Borexino experiment, where a similar concentration line, MoREx, was developed [119]. The RnCL described in this work is designed to be portable and so is a stream-lined version of MoREx, yet is still capable of very sensitive measurements.

11.2.1. Design and Construction

The concept behind the RnCL is simple: a sample gas is passed through an activated carbon trap and the radon content is adsorbed onto the surface of the carbon whilst the carrier gas passes through. Throughout this trapping stage, the carbon trap is cooled to improve its adsorption power. After collection is complete, the trap is heated to release the radon, which is then passed into the electrostatic detector.

In order to facilitate a high degree of flexibility in operation of the RnCL, the design shown in Figure 11.11 was chosen. In this schematic, the gas enters from the left-hand side and moves to the right. All gas is passed though a 3 nm particle filter before meeting a series of valves to allow the opportunity to choose a path through the system. During a measurement, the typical path is through the carbon trap and one of the flow meters, by-passing the detector and out to exhaust through the buffer volume.

This buffer volume is an addition to the core design, which is coupled with a diaphragm pump to allow a lower pressure on the RnCL output. This means that samples at atmospheric pressure can also be collected, which is important for the C-section measurement described in Section 13.3, as this cannot mechanically accommodate a large over-pressure.

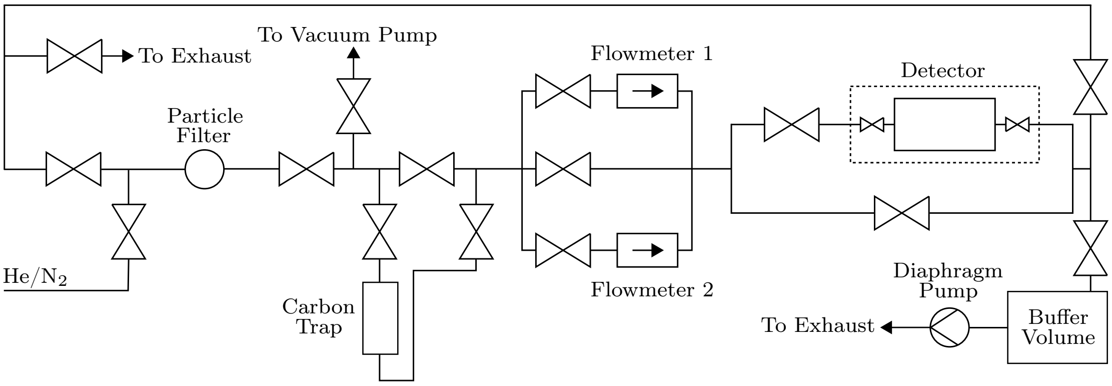

Figure 11.11.: Schematic diagram of the design of the RnCL.

The main challenge in the design and construction of the RnCL is maintaining the required degree of radiopurity. To this end, only essential components are placed in the critical region upstream of the carbon trap. All pipework is made from stainless steel and all valves are fully metallic, which reduces radon emanation. The only non-metal component before the carbon trap is the particle filter, which is made from a PTFE membrane (Pall Emflon series) in a stainless steel housing.

The carbon trap itself is made entirely from stainless steel with the smallest possible amount of welding. This welding was undertaken with zirconiated, rather than thoriated, welding rods. This is important as the latter contain 1 – 2% thorium and invariably also contain high levels of uranium, which leads to radon emanation. A mass of 57 g of activated carbon (a synthetic charcoal from Carbo-Act international) was placed inside the carbon trap. This particular carbon was chosen due to its high adsorption coefficient and very low level of radon emanation, with a previous measurement of 0.3 ± 0.1 mBq/kg [119].

In order to keep the RnCL as portable as possible, it is self-contained and mounted on a trolley frame such that it can be moved freely. The real life incarnation of the design can be seen in Figure 11.12, where key components are marked to aid comparison with the above schematic.

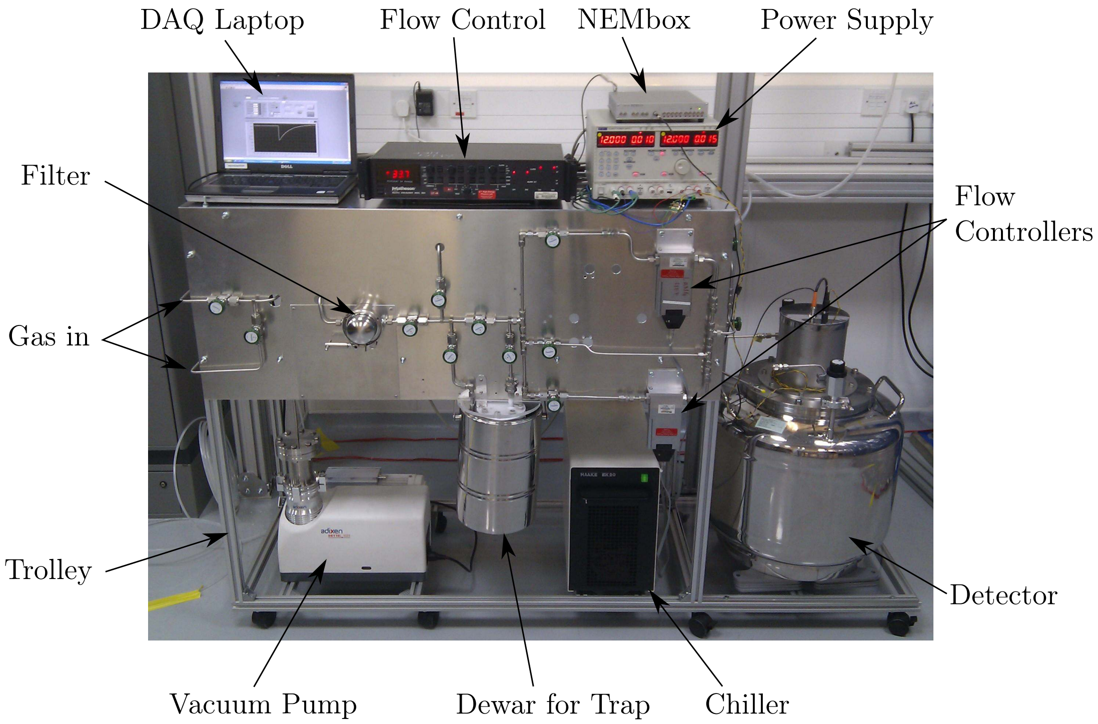

Figure 11.12.: Photograph of the RnCL in operation, with important components marked.

11.2.2. Trapping Efficiency

To provide meaningful measurements of a sample of gas, the efficiency for trapping radon and transferring this to the detector must be known. There are two methods used to make this measurement, which are described in this section.

The first method starts in the same manner as the spike-type detector calibration procedure, where radon is transferred to the detector from the source and measured. After ~ 48 hr, the trapping procedure is initiated. First, the carbon trap is heated to 220 °C and helium is flushed through it to remove any residual radon, before cooling back to room temperature. If the trap is to be cooled for the measurement, it is immersed in a dewar filled with isopropyl alcohol and cooled with an immersion chiller to −25 °C.

At this stage, gas is flowed through the detector and into the trap, which extracts the measured sample of radon. When the trapping run is complete, the trap is re-heated and the radon sample is returned to the detector. A typical calibration run is shown in Figure 11.13, where radon can be seen in the detector, then is moved to the trap, before being re-introduced into the detector.

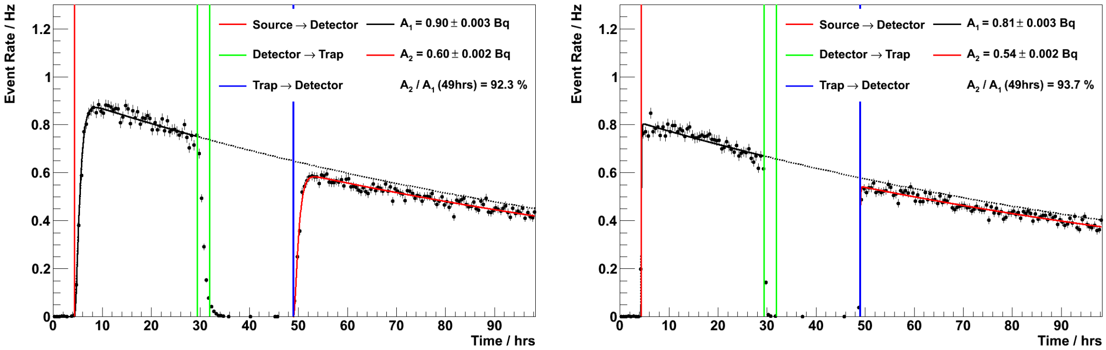

(a) ^{214}Po Activity **(b)** ^{218}Po Activity

Figure 11.13.: Typical ^{214}Po and ^{218}Po rates measured in the detector during a trapping and transfer efficiency measurement with helium as the carrier gas and a trap temperature of −26 °C.

Different configurations of carrier gas, trap temperature and trapping time have been investigated, all of which influence the outcome of the measurement. Some measurement results are presented in Table 11.2.

Initially, trapping was attempted at room temperature with helium as a carrier gas. For short trapping times, reasonably high trapping and transfer efficiencies of 70% were achieved which gives good sensitivity. However, at this temperature, the trapping efficiency is a strong function of the duration of the trapping run, as increasing the time to 2.5 hr reduces the efficiency to 20%.

It is hypothesised that this is because radon is initially adsorbed, then is repeatedly released and re-adsorbed until it propagates all the way through the trap. To improve the performance of the trap, it was cooled to −25 °C, where the trapping efficiency became an impressive $92 - 93\%$, which was stable over $0.8 - 2.5$ hr and two different flow rates of 5 and 10 lpm.

It is not always feasible to use helium as a carrier gas from a cost perspective and because it may damage the PMTs of the detector. Nitrogen is an obvious alternative, and so the trapping procedure was repeated using this gas. Further, a longer run of 20 hr was attempted which is closer to real trapping conditions. However, for this measurement, the trapping and transfer efficiency plummeted to $\sim 25\%$.

Two further tests were undertaken to ascertain the cause of this reduction. The first was a shorter nitrogen trapping run which measured 71%, confirming that performance is reduced with nitrogen compared to helium. The second test was a 20 hr helium run, which also saw a reduction to 65% so that the previously observed constancy of trapping efficiency with time does not continue up to this duration.

In an attempt to reduce the desorption of radon from the trap, a trapping run was conducted at a lower temperature. Dry ice was added to the isopropyl alcohol so that the trap temperature fell to −68 °C, which is between the melting and boiling points of radon. Using nitrogen for a 5 hr run, the trapping and transfer efficiency was measured as 72%. This is comparable to the performance at −23 °C but with a considerably more complicated experimental procedure and so this technique was not pursued further.

The trapping and transfer efficiency measurements described above confirm that, at the temperatures investigated, there is variation in the results as a function of trapping time. The trapping scenario used for this type of calibration is not equivalent to a typical gas sample measurement, which can be appreciated by considering the 20 hr running case. In the calibration, all the radon sample is transferred to the trap within the first hour of trapping, whereas in a real measurement the radon will be supplied continuously over the duration of the trapping run.

As a result, these calibration results must be used with care. They may be used when trapping conditions are identical, for example when measuring the radon content of the gas supply system for SuperNEMO which has a similar volume to the electrostatic

Meas. No.	Carrier Gas	Temp. °C	Time hr	Flow lpm	Efficiency / % ^{214}Po	 ^{218}Po
1	He	22	0.8	10	70.7	72.6
2	He	22	2.5	10	20.5	21.5
3	He	−22	0.8	10	93.1	92.1
4	He	−26	2.5	10	92.3	93.7
5	He	−26	2.5	5	92.1	94.4
6	N_2	−24	20.0	7	26.4	24.8
7	N_2	−23	2.5	10	71.6	71.1
8	He	−28	20.0	7	66.9	65.2
9	N_2	−68	5.0	7	71.7	67.1

Table 11.2.: Trapping and transfer efficiency measurement results for different gases, temperatures and trapping times.

detector. This measurement is detailed in Section 13.1. Additionally, the region of stable helium trapping measurements may be used. However, outside of this region, the above results represent lower bounds on the trapping efficiencies for the particular trapping conditions.

In order to provide more flexibility a further programme of measurements of trapping efficiency has been initiated. The premise is to supply a continuous radon activity to the trap to mimic real measurement conditions, which is achieved with a similar technique to the aforementioned flow-through detector calibration method.

The measurement begins in exactly the same way with gas flow through the source and detector. When this activity is stable, the output from the source is transferred through the trap, whilst maintaining flow through the detector. At the end of the trapping run, the trap is heated and the radon is purged into the detector.

A trapping measurement following this technique is shown in Figure 11.14. Figure 11.14a shows the beginning of the run, where initially there is a stable level in the detector. After 26 hours, the source output is diverted through the trap and the level in the detector falls. However, after $\sim$ 30 hours, the level in the detector begins to rise as the radon begins to escape the trap. Figure 11.14b shows the next stage of the measurement where the radon in the trap is moved to the detector to be measured. Unfortunately, in this measurement, the activity of the ^{214}Po does not behave as expected, taking an unusually long time to come into equilibrium. This uncertainty is taken into account with an increased systematic error on the transfer efficiency.

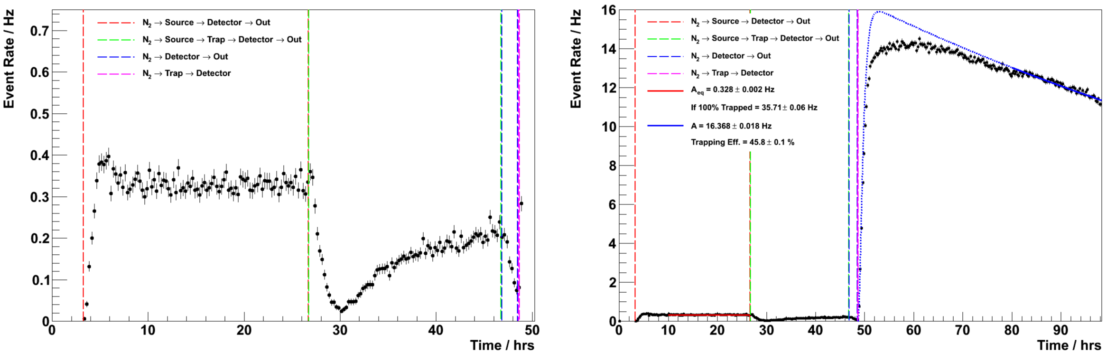

(a)

(b)

Figure 11.14.: ^{214}Po activity in the detector during a flow-through trapping efficiency measurement using nitrogen at 7 lpm. The curve in (b) has been fitted after 80 hr and extrapolated back.

A flow-through calibration allows the extraction of much more information than in the first calibration type. By monitoring the output of the trap, it is possible to infer the amount of radon contained within. The calculated trap activity is shown alongside the ideal case in Figure 11.15a. It can be seen that at the beginning of the run the trap activity is similar to that expected if all radon is trapped. However, as the gas flow continues, the radon activity in the trap becomes lower than expected as a result of the released radon.

The ratio of these quantities gives the trapping efficiency as a function of the trapping time, which is plotted in Figure 11.15b. It can be seen that at the beginning of trapping, the efficiency is in the region $90 - 100\%$ and there is a steady decrease in the trapping efficiency after ~ 3 hours. The amount of radon in the trap after 20 hours from Figure 11.15a can be compared with the measurement after transferring the radon to the detector to extract the transfer efficiency. As discussed above, there are large uncertainties associated with this value, placing it at $69 - 85\%$. This transfer efficiency has been used to calculate a combined trapping and transfer efficiency as a function of time which is also shown in Figure 11.15b.

It can be seen that for short trapping times, the trapping and transfer efficiency is $\sim 70\%$, in excellent agreement with measurement 7 in Table 11.2. This slowly

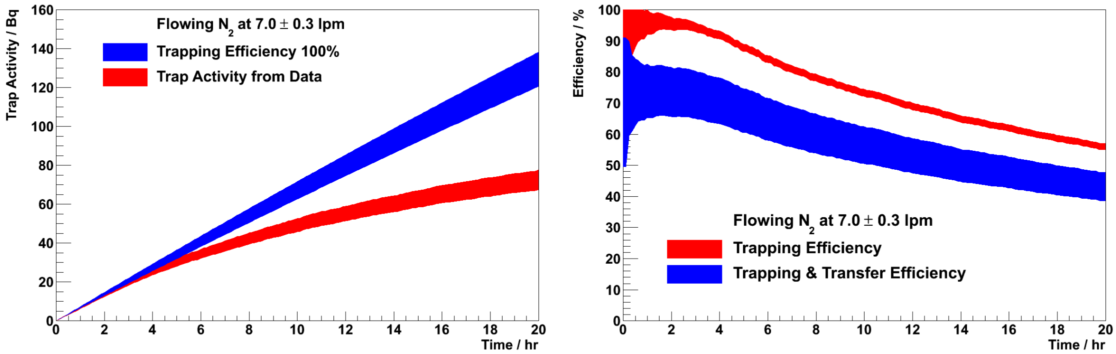

(a) (b)

Figure 11.15.: (a) Radon activity in the carbon trap during the flow-through calibration run shown in Figure 11.14, calculated by measuring the trap output (red) and in the ideal trapping efficiency case (blue). (b) Ratio of the two lines in (a) giving the trapping efficiency (red) and the trapping and transfer efficiency (blue).

decreases to a value of $\sim 45\%$ after 20 hours which is also in good agreement with the midpoint of measurements 6 and 7. These measurements can therefore be used in good confidence to read off the appropriate trapping and transfer efficiency for the particular trapping time.

11.2.3. Trap Background

The final measurement that must be made before the RnCL can be used is its intrinsic background. This is measured using “blank” runs where a measurement procedure is completed without actually sampling any gas.

An example of a blank run is shown in Figure 11.16. Initially, the trap is heated and flushed to clear any remaining radon. It is then purged into the detector with helium to confirm that it is free of radon. In this particular measurement, a small activity of radon is transferred into the detector at this point. Next, the trap is left sealed for $\sim$ 20 days to allow emanation of radon. After this time period, the trap is re-heated and radon is transferred into the detector. There is a low level of radon measured allowing a conservative estimate of the trap activity of 0.23 ± 0.11 mBq.

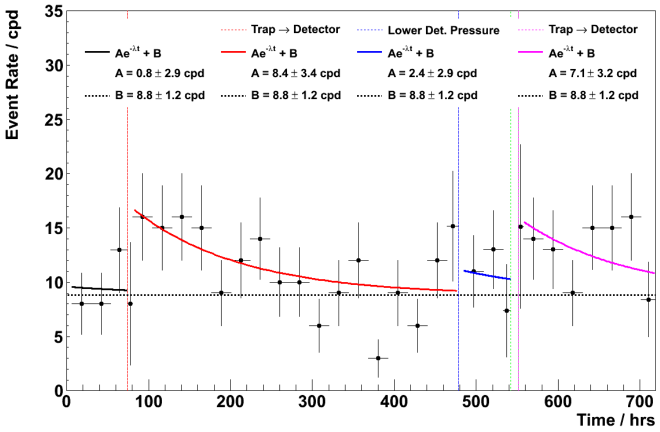

Figure 11.16.: Measurement of the intrinsic background of the carbon trap. The trap is initially cleared and purged into the detector (red). The detector is depressurised (blue) before the emanated radon from the trap is transferred into the detector (magenta).

Chapter 12.

Radon Concentration Line Sensitivity Estimates

The main aim of the research and development described in part II of this thesis is to measure radon at the low levels required for SuperNEMO. This chapter will assess whether the combination of radon concentration line (RnCL) and electrostatic detector, described in Chapter 11, have sufficient sensitivity to make a measurement at the level of ~ 150 µBq/m^3.

In the first section, a definition of the minimum detectable activity is introduced (Section 12.1). This will be used to quantify the sensitivity of the system in three different cases. Firstly, the detector-only sensitivity will be addressed (Section 12.2), which is shown to be insufficient for the required SuperNEMO radon level. A hypothetical measurement with the RnCL is then studied to find the sensitivity of the system to a supply of gas of uniform activity (Section 12.3). Finally, a realistic scenario for the measurement of a C-section is put forward to confirm that a measurement at the target level is indeed achievable (Section 12.4).

12.1. Minimum Detectable Activity

In order to quantify the sensitivity of the apparatus that has been developed, a stringent definition must first be found for the sensitivity of a measurement. In this work, the definition of Minimum Detectable Activity (MDA) given in 'Radiation Detection and Measurement' by G. F. Knoll is used [120].

This definition is based on a binary decision of whether the output of the detector is representative of background only or indicates the presence of a signal along with the background. The concept is that prior to any measurement, the probability of a false positive is identified, where signal is indicated when there is only background present, as is the probability of a false negative, where a signal that is present is misidentified as background only.

To decide whether there is a signal, a critical number of counts, n_c, is predefined and if more counts than this number are observed, it is concluded that there is a signal present. Firstly, n_c must be found for a well-known expected number of background events, B, and measurement confidence level, CL, such that the probability of a false positive is less than $1 - \mathrm{CL}$. If B is Poisson-distributed then to satisfy the above criterion, n_c must be increased until the following inequality is satisfied:

$$P_B(n \geq n_c) = \sum_{n=n_c}^{\infty} Pois(n; B) = 1 - \sum_{n=0}^{n_c-1} e^{-B}\frac{B^n}{n!} \leq 1 - \mathrm{CL} \tag{12.1}$$

Once n_c has been set high enough to reduce the false positive probability to $1 - \mathrm{CL}$, the probability for false negatives can be used to calculate the minimum expected number of signal events, S, that satisfies the MDA requirement. S is therefore increased until the following is true:

$$P_{S+B}(n < n_c) = \sum_{n=0}^{n_c-1} Pois(n; S+B) = \sum_{n=0}^{n_c-1} e^{-(S+B)}\frac{(S+B)^n}{n!} \leq 1 - \mathrm{CL} \tag{12.2}$$

These results are most readily understood graphically as shown in Figure 12.1. The black curve represents the Poisson distributed background expectation, from which n_c has been set so that the black shaded area corresponds to $1 - \mathrm{CL}$ as per Equation (12.1). The red line is the distribution for the minimum signal on the same background, where S has been set such that the red shaded area also corresponds to $1 - \mathrm{CL}$ as in Equation (12.2).

Once the minimum signal has been found, it can be converted into an activity. This minimum activity is what is referred to as the MDA.

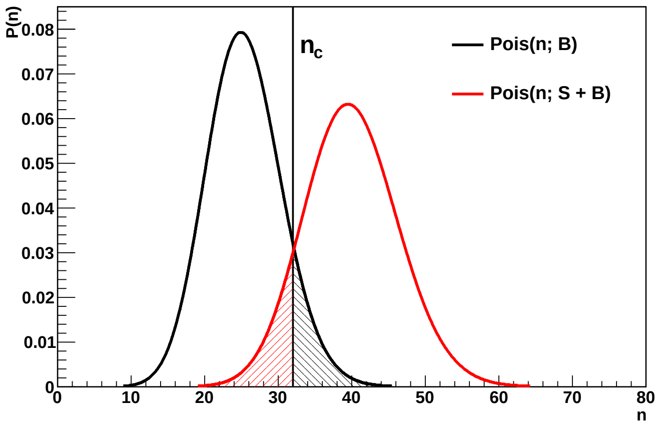

Figure 12.1.: Probability distributions for two Poisson distributed variables. n_c has been increased until the false positive result corresponding to the black shaded area has sufficiently low probability. Then S has been increased until the red shaded area corresponding to the false negative result also has area $1 - \mathrm{CL}$.

12.1.1. Normal Approximation

In this section, a simplification is introduced where the Poisson distributions described above are approximated so that all calculations can proceed analytically. It is well-known that for large enough λ, the Poisson distribution can be approximated as a normal distribution:

$$Pois(\lambda) \approx Norm(\mu = \lambda, \sigma = \sqrt{\lambda}) \tag{12.3}$$

This approximation can be further improved by applying the continuity correction $n_c \to n_c - \frac{1}{2}$. Therefore Equation (12.1), where $\lambda = B$, becomes

$$P_B(n \geq n_c) \approx \int_{n_c - \frac{1}{2}}^{\infty} \frac{1}{\sqrt{2\pi B}} e^{-\frac{(x-B)^2}{2B}} dx = \frac{1}{2} - \frac{1}{\sqrt{\pi}} \int_0^{\frac{n_c - \frac{1}{2} - B}{\sqrt{2B}}} e^{-t^2} dt \tag{12.4}$$

At this point, it is helpful to introduce the error function, which is defined as

$$\mathrm{erf}(x) = \frac{2}{\sqrt{\pi}} \int_0^x e^{-t^2} dt \tag{12.5}$$

Using this definition and Equations (12.1) and (12.4) it can be seen that

$$P_B(n \geq n_c) \approx \frac{1}{2}\left(1 - \operatorname{erf}\left(\frac{n_c - \frac{1}{2} - B}{\sqrt{2B}}\right)\right) \leq 1 - \mathrm{CL} \tag{12.6}$$

The equivalent procedure can be applied to Equation (12.2) to give

$$P(n < n_c) \approx \frac{1}{2}\left(1 + \operatorname{erf}\left(\frac{n_c - \frac{1}{2} - (S + B)}{\sqrt{2(S + B)}}\right)\right) \leq 1 - \mathrm{CL} \tag{12.7}$$

The MDA definition provides the smallest possible value of S for a given B, so n_c is not of direct interest and can be eliminated. Equations (12.6) and (12.7) can be combined to find

$$S - \sqrt{2B}E \geq \sqrt{2(S + B)}E \tag{12.8}$$

where E is a positive number defined as:

$$E = \operatorname{erf}^{-1}(2\mathrm{CL} - 1) \tag{12.9}$$

Therefore, discounting the unphysical $S \leq 0$ solution, it is found that

$$S \geq 2E(E + \sqrt{2B}) \tag{12.10}$$

The minimum value of S is when the inequality is equal, so under this approximation the MDA can be calculated from the minimum number of signal events that are detectable, S_0, which is given by

$$S_0 = 2E(E + \sqrt{2B}) \tag{12.11}$$

12.2. Electrostatic Detector Sensitivity

The simplest case to be considered is the detector-only sensitivity. The same measurement is imagined as in Section 10.4, where a signal activity, A_S, is introduced into a detector with intrinsic background activity, A_D, which detects ^{214}Po decays.

In this case, to find the number of signal events, S, expected to have been detected after a given time, T, in a detector with detection efficiency, ϵ_D, the detector background is set to zero in Equation (10.25) and it is found that

$$\begin{aligned} S = \epsilon_D \int_0^T \lambda_4 N_4 dt &= \epsilon_D \int_0^T \left(A_S \lambda_1 \lambda_2 \lambda_3 \lambda_4 \sum_{i=0}^{4} \frac{e^{-\lambda_i t}}{k_{i,4}^4} \right) dt \\ &= \epsilon_D A_S \lambda_1 \lambda_2 \lambda_3 \lambda_4 \sum_{i=0}^{4} \frac{(1 - e^{-\lambda_i T})}{\lambda_i k_{i,4}^4} \end{aligned} \tag{12.12}$$

Similarly, to find the number of expected background events, A_S is set to zero which gives

$$\begin{aligned} B &= \epsilon_D \int_0^T A_D \left\{ 1 - \sum_{i=0}^{4} \left[\left(\prod_{j=i+1}^{4} \lambda_j \right) \sum_{k=i}^{4} \frac{e^{-\lambda_k t}}{k_{k,4}^{4-i}} \right] \right\} dt \\ &= \epsilon_D A_D T - \epsilon_D A_D \sum_{i=0}^{4} \left[\left(\prod_{j=i+1}^{4} \lambda_j \right) \sum_{k=i}^{4} \frac{(1 - e^{-\lambda_k T})}{\lambda_k k_{k,4}^{4-i}} \right] \end{aligned} \tag{12.13}$$

These quantities are shown in Figure 12.2 alongside the equivalent values for ^{222}Rn. It can be seen that there is very little difference between the ^{214}Po and ^{222}Rn cases at any time during the measurement, and using only ^{222}Rn gives a very similar sensitivity.

To calculate the MDA, Equation (12.13) is used to find B, which is then combined with Equation (12.11) to extract the minimum number of signal events, S_0, for a given confidence level. Finally, Equation (12.12) is used to convert S_0 into the MDA, which is shown as a function of the measurement time in Figure 12.3.

As might be expected, at short measurement times there is very little sensitivity since there has been no time for any radon to decay. However, as time increases the MDA falls rapidly before reaching a shallow minimum at ∼3 days. After this it begins to increase again as the increasing number of background counts begins to take effect. As expected, there is very little difference between ^{214}Po and ^{222}Rn, with the two methods converging after a measurement time of ∼1 day.

From Figure 12.3, the minimum detectable activity for the electrostatic detector alone is 0.12 mBq or 1.7 mBq/m^3, which is an order of magnitude larger than the target value of 150 µBq/m^3.

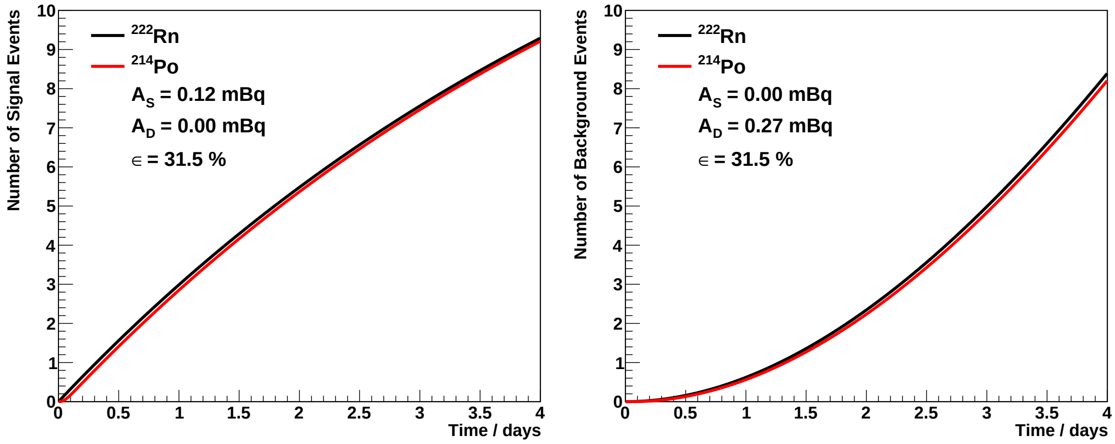

(a) Signal Events, S **(b)** Background Events, B

Figure 12.2.: (a) Expected number of signal events, S, for events from both ^{222}Rn and ^{214}Po decays with $A_D = 0.27$ mBq and $A_S = 0.12$ mBq. (b) Expected number of background events, B, for the same activities.

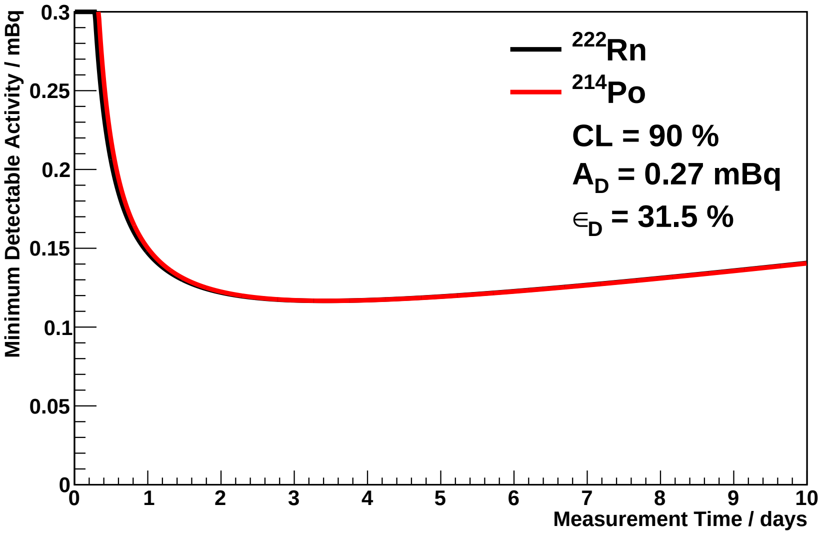

Figure 12.3.: MDA for the electrostatic detector as a function of the measurement time, showing the ^{222}Rn and ^{214}Po results.

12.3. Uniform Gas Measurement

As the required sensitivity is not achieved with the detector alone, the RnCL must be used. The simplest case involving the RnCL is where a gas is supplied with constant activity. This scenario is studied in this section.

If a gas with activity per unit volume, a_G, is supplied to the RnCL at a flow rate, f, the number of radon atoms in the carbon trap, N_C, is described by

$$\frac{dN_C}{dt} = A_C - \lambda N_C + \frac{\epsilon_T f a_G}{\lambda} \tag{12.14}$$

where A_C is the intrinsic activity of the carbon trap and ϵ_T is the trapping efficiency. If the conservative assumption is made that none of the intrinsic activity from the carbon trap is exhausted during the trapping run, then the above equation has a solution given by

$$N_C\left(T_f\right) = \left(\frac{A_C}{\lambda} + \frac{\epsilon_T\left(T_f\right) f a_G}{\lambda^2}\right)\left(1 - e^{-\lambda T_f}\right) \tag{12.15}$$

where T_f is the time that gas has been flowing. In this section, this is limited to 20 hr as this is the range over which the trapping efficiency has been measured. If after a trapping run of length, T_f, the radon is transferred to the detector, then the number of radon atoms is the same as was found before:

$$N_D = \frac{A_D}{\lambda}\left(1 - e^{-\lambda t}\right) + \epsilon_{tr} N_C\left(T_f\right) e^{-\lambda t} \tag{12.16}$$

where ϵtr is the transfer efficiency. To calculate the minimum detectable activity, the number of signal and background events must be calculated. As was seen above, there is little difference between using ^{222}Rn and ^{214}Po, so the simpler ^{222}Rn case is shown here. If the detector is left to measure for a time, T_m, the number of expected signal events is

$$S = \epsilon_{tr} N_C^S\left(T_f\right) \epsilon_D\left(1 - e^{-\lambda T_m}\right) \tag{12.17}$$

where a superscript has been added to N_C^S to shown that only the signal component of this number is included:

$$N_C^S\left(T_f\right) = \frac{\epsilon_T\left(T_f\right) f a_G}{\lambda^2}\left(1 - e^{-\lambda T_f}\right) \tag{12.18}$$

A similar process gives the number of expected background events as

$$B = \epsilon_D A_D T_m + \epsilon_D\left(\epsilon_{tr} N_C^B\left(T_f\right) - \frac{A_D}{\lambda}\right)\left(1 - e^{-\lambda T_m}\right) \tag{12.19}$$

where

$$N_C^B\left(T_f\right) = \frac{A_C}{\lambda}\left(1 - e^{-\lambda T_f}\right) \tag{12.20}$$

The same procedure is followed to calculate the MDA as with the detector-only case, and two distinct cases are considered here. In the first, the trapping and transfer efficiency flow-through measurement described in Section 11.2.2 is used and the sensitivity is therefore calculated for a measurement of nitrogen with a flow rate of 7 lpm. The minimum detectable activity under these assumptions is shown in Figure 12.4. As expected, the sensitivity improves with the volume of gas that has been collected, up to the maximum gas volume of 8.5 m^3 which the trapping efficiency measurement covers. The sensitivity that can be reached in this case is at the level of 40 µBq/m^3.

In the second case, the lowest trapping efficiency for helium of 67% is used and it is assumed that this efficiency remains constant as a function of trapping time, which may well be achieved if a lower trap temperature can be maintained. The minimum detectable activity under these assumptions is shown in Figure 12.5. A considerable improvement is seen and sensitivities as low as 5 µBq/m^3 can now be reached.

12.4. C-Section Measurement

The RnCL has been shown to be able to measure a supply of gas of uniform activity at a level below the SuperNEMO radon requirement, but the main quantity that the apparatus must be able to measure is the radon content of the SuperNEMO tracker. The tracker is built in four sections, known as C-sections, each of which must be

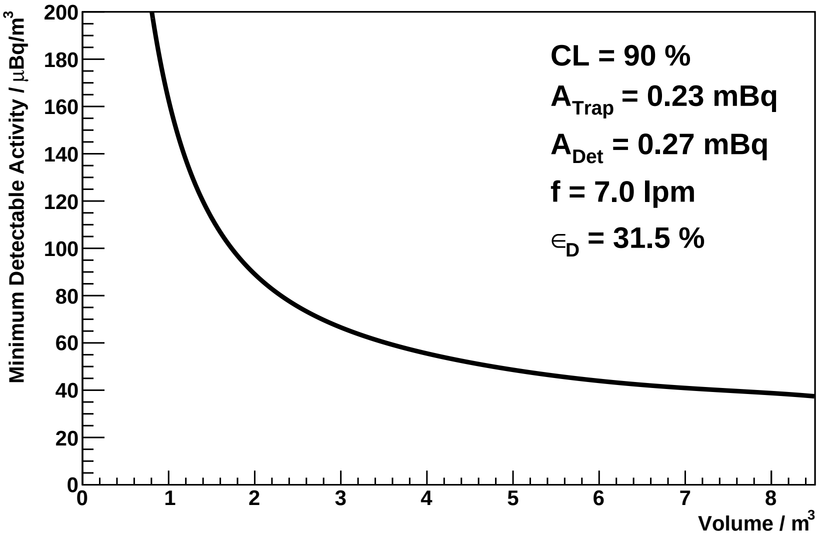

Figure 12.4.: Minimum detectable activity for a uniform supply of nitrogen as a function of volume supplied to the RnCL. A flow of 7 lpm is assumed so that the known trapping efficiency can be used.

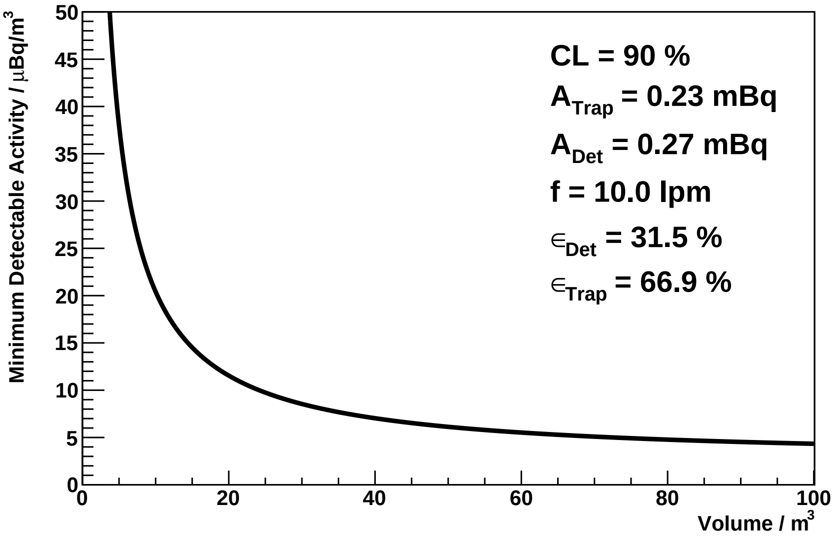

Figure 12.5.: Minimum detectable activity for a uniform gas supplied to the RnCL with a trapping efficiency constant over the duration of trapping.

measured prior to assembly. Therefore, the radon activity inside a C-section is the key measurement.

In an ideal scenario, the C-section would be left sealed for an extended period prior to the measurement to build up radon. However, in reality, a C-section is not a sealed unit and has small leaks. This means that it must be kept at a slight overpressure to prevent environmental radon from entering. Therefore, the number of radon atoms inside a C-section, N_T is given by

$$\frac{dN_T}{dt} = A_T - \lambda N_T - \frac{f_{in} N_T}{V_T} + \frac{f_{in} a_G}{\lambda} \tag{12.21}$$

where f_{in} is the flow rate of gas which is supplied to sustain an overpressure, $V_T = 3.8\ \mathrm{m}^3$ is the volume of one C-section and a_G is the activity of the supply gas per unit volume. Before starting a measurement, it is imagined that the C-section will be left to come into equilibrium such that it has an activity per unit volume of

$$a_T = \frac{\lambda N_T}{V_T} = \frac{A_T + f_{in} a_G / \lambda}{V_T + f_{in}/\lambda} \tag{12.22}$$

Once the C-section is in equilibrium, a trapping run can take place where the gas from the tracker is passed through the RnCL. The number of atoms in the trap, N_C, takes the same form as Equation (12.15), replacing $a_G \to a_T$ and distinguishing the flow through the trap as f_{RnCL}. The form of S and B are identical to Equations (12.17) and (12.19), where in this measurement, the signal relates to the activity of the C-section, A_T, so that

$$N_C^S\left(T_f\right) = \frac{\epsilon_T\left(T_f\right) f_{RnCL}}{\lambda^2} \frac{A_T}{V_T + f_{in}/\lambda} \left(1 - e^{-\lambda T_f}\right) \tag{12.23}$$

and the activity from the supply gas now becomes part of the background contribution:

$$N_C^B\left(T_f\right) = \frac{A_C}{\lambda}\left(1 - e^{-\lambda T_f}\right) + \frac{\epsilon_T\left(T_f\right) f_{RnCL}}{\lambda^2} \frac{f_{in} a_G}{\lambda V_T + f_{in}} \left(1 - e^{-\lambda T_f}\right) \tag{12.24}$$

The calculated minimum detectable activity for such a C-section measurement is shown in Figure 12.6 as a function of the activity of the supply gas. In this plot, nitrogen has again been assumed as the carrier gas and a flow suppression factor has been applied (Section 10.3). The target level is achievable, provided that the activity of the supply gas does not exceed 1.5 mBq/m^3.

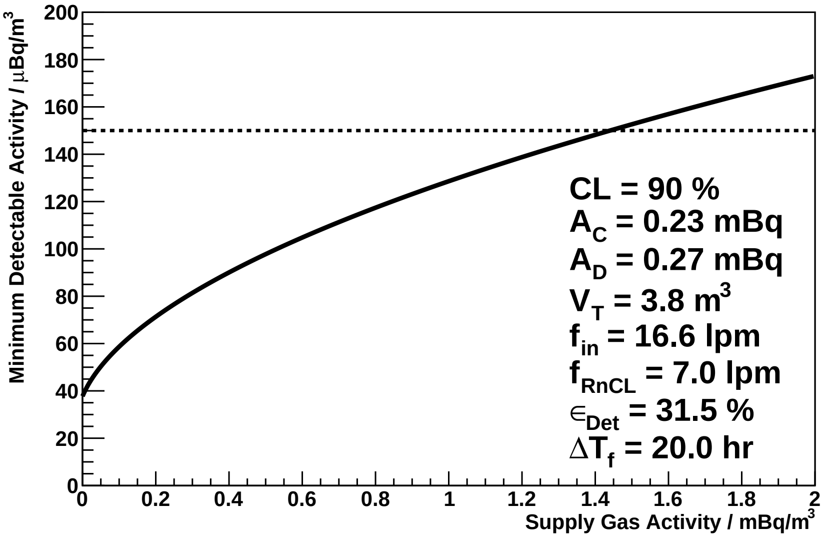

Figure 12.6.: Sensitivty of the RnCL for a C-section measurement as a function of the input gas activity. The sensitivity is presented as in Equation (12.22) with the reduction in activity from flow suppression already applied.

The sensitivity of this measurement may be improved further by a number of different measures. One of the most significant is a reduction of the input flow rate, which requires that the leak rate from the C-section is reduced. Other improvements may arise from changing to a new carrier gas with improved trapping efficiency, or by increasing the trapping time.

Having shown that the RnCL is capable of providing useful measurements of the radon activity inside a C-section, there is clearly good justification for performing a measurement such as that described here. This is the culmination of the next chapter, described in Section 13.3.

Chapter 13.

Low-level Radon Measurements

A substantial amount of work has gone into the development and commissioning of both the electrostatic detector and radon concentration line (RnCL), as described in Chapter 11. The new apparatus has been put to good use, making a series of measurements of low-level radon activities from large gas volumes, which are the subject of this chapter.

There have been three different types of measurements that will be presented herein. The first is of the intrinsic radon activity of the gas system, which has been developed to prepare the tracking gas mixture for SuperNEMO (Section 13.1). Next, the radon activity from off-the-shelf gas cylinders is considered, with measurements of both helium and nitrogen presented in Section 13.2. Finally, a measurement of the radon content of the first tracker C-section for the SuperNEMO demonstrator is introduced in Section 13.3.

13.1. Gas System

The tracking gas for SuperNEMO will be a mixture of helium, argon and ethanol in the same proportions as used for NEMO-3 (Section 5.2). In order to obtain the appropriate proportions, a dedicated gas supply system has been developed for the experiment. This design was based on the system used for NEMO-3, with the replacement of all components with more radiopure alternatives, with the exception of the large bubbler. This bubbler is a stainless steel cylinder with a length of 2 m and a diameter of 0.2 m. In operation, it is filled with alcohol and gas is passed through at high pressure to add approximately the right proportion of alcohol to the gas mixture.

As was shown in Section 10.3, due the small volume of the gas system compared to the required flow rates and radon half-life, there is no difference between radon emanating in the gas system and that emanating from the tracker. Furthermore, a carbon trap of the type used in the RnCL cannot be used to filter the output from the gas system since it will also remove the ethanol. As a result there are strict requirements on the radon emanation from the gas system with a target of 0.2 mBq, corresponding to 10% of the total radon budget.

The first measurement of the emanation from the gas system was undertaken with the RnCL in the early stages of its commissioning. The volume of the gas system is dominated by the large bubbler from NEMO-3, which is of comparable size to the electrostatic detector. As a result, the spike-type trapping efficiency calibrations can be reliably used if the same flow rate, trap temperature and timing conditions are replicated.

In this measurement, the gas system was thoroughly flushed with helium and then left for 4.1 days for radon to emanate. After this time, helium was flushed through the gas system and into the RnCL at 10 lpm. The trap was kept at room temperature for this run, which lasted 50 minutes, so that the measured trapping efficiency of 70.7% (Table 11.2) could be used.

After transferring the radon to the detector, 18.9 ± 4.0 cpd of ^{214}Po was seen, as shown in Figure 13.1a. The expected contribution from the intrinsic trap activity was 0.2 cpd, so that the activity from the gas system in the detector was 0.69 ± 0.15 mBq. When the trapping efficiency and radon build-up time are taken into account, the gas system activity is found to be 1.9 ± 0.4 mBq.

This value is an order of magnitude higher than the target level, so it was important to isolate the main cause of the emanation. The prime suspect was the large bubbler from NEMO-3 as not only is this the largest component from the gas system, it is also the only one not specifically designed for a low-level of radon emanation. As such, it has a glass window, welded seams and viton seals all of which may contribute to an elevated radon level. To reduce this contribution, the glass window was replaced with stainless steel and the viton seals were covered in SBR to reduce radon diffusion.

To assess whether the bubbler was the cause of the high radon level, it was sealed for a month and the measurement procedure was repeated on this section of the gas system separately. The resulting activity in the detector (Figure 13.1b) corresponds to an activity of 1.4 ± 0.2 mBq from the bubbler. This confirmed the suspicions that it was the main contributor and will now be replaced before re-testing the entire gas system.

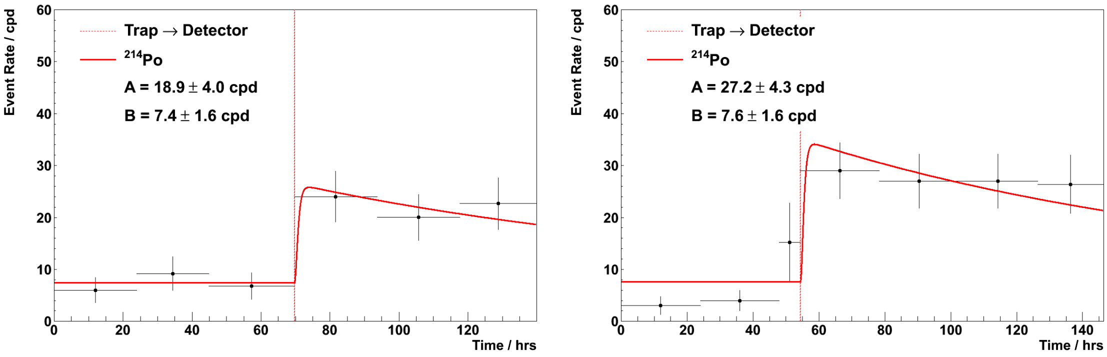

(a) Whole Gas System

(b) Bubbler Only

Figure 13.1.: Measurements of the radon emanation from the SuperNEMO gas system. (a) ^{214}Po activity in the detector after extracting radon from the whole gas system. (b) ^{214}Po activity from the large bubbler sub-component only.

13.2. Gas Cylinders

One of the most basic measurements that can be undertaken using the RnCL is to measure the activity of standard gas cylinders. This is also amongst the simplest measurements that can be made, so a programme of cylinder measurements has been undertaken as part of commissioning of the RnCL. The results of these measurements are presented in this section.

13.2.1. Modelling Cylinder Activity

Before discussing the experimental procedure, it is useful to consider what might be expected of the radon activity from a gas cylinder. If the cylinder has been allowed to equilibrate before being used, then any radon introduced in the filling stage will have decayed and the activity contained is purely from emanation from the cylinder itself.

The quantity of interest is usually the specific radon activity, that is, the radon activity per unit volume. As the bottle is emptied, radon is removed from the cylinder and replaced by newly emanated radon. However, the volume of gas contained within the cylinder will decrease and so the specific activity will increase. This can be seen by considering the differential equation that describes the number of radon atoms remaining in the gas cylinder:

$$\frac{dN_G}{dt} = A_G - \lambda N_G - \frac{f N_G}{(V_G - ft)} \tag{13.1}$$

where V_G is the total volume of gas (at STP) contained in the cylinder at the start of the measurement. It is clear that the radon in the bottle reduces more quickly as time increases, so the specific activity of its output must be higher. This equation can be solved using an integrating factor, to find

$$\frac{e^{\lambda t} N_G}{V_G - ft} = \int \frac{e^{\lambda t} A_G}{V_G - ft} dt = -\frac{A_G \lambda}{f} \int \frac{e^{\lambda t}}{\lambda t - \frac{\lambda V_G}{f}} dt = -\frac{A_G}{f} e^{\frac{\lambda V_G}{f}} \int \frac{e^x}{x} dx \tag{13.2}$$

This final integral has no analytic solution, but can be shown to be equal to the exponential integral defined as

$$\mathrm{Ei}(x) = \int_{-\infty}^{x} \frac{e^t}{t} dt \tag{13.3}$$

Assuming that the cylinder was in equilibrium at the start of the measurement, the constant of integration can be found, leading to the final form for N_G:

$$N_G = \frac{A_G}{\lambda V_G} (V_G - ft) e^{-\lambda t} + \frac{A_G}{f} (V_G - ft) e^{\frac{\lambda V_G}{f} - \lambda t} \left[\mathrm{Ei}\left(-\frac{\lambda V_G}{f} \right) - \mathrm{Ei}\left(\lambda t - \frac{\lambda V_G}{f} \right) \right] \tag{13.4}$$

The instantaneous specific activity at the output of the cylinder, a_G, is simply given by the specific activity in the bottle at that time:

$$a_G = \frac{\lambda N_G}{V_G - ft} = \frac{A_G}{V_G} e^{-\lambda t} + \frac{\lambda A_G}{f} e^{\frac{\lambda V_G}{f} - \lambda t} \left[\mathrm{Ei}\left(-\frac{\lambda V_G}{f} \right) - \mathrm{Ei}\left(\lambda t - \frac{\lambda V_G}{f} \right) \right] \tag{13.5}$$

This is plotted as a function of the volume remaining in the cylinder in Figure 13.2. As expected, the radon activity increases as the bottles are emptied, with a more severe effect for lower flow rates. This is simply because the faster flow rates empty the bottles before a significant amount of radon has had time to emanate.

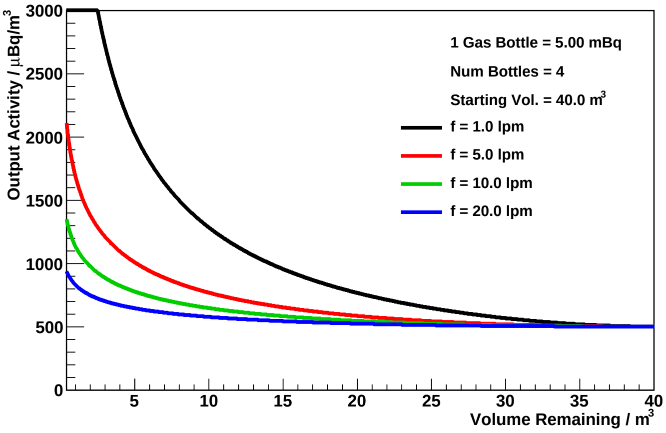

Figure 13.2.: Specific activity at the output of four cylinders as a function of the volume remaining, predicted by the model shown here. The cylinders are assumed to have a combined activity of 20 mBq and a starting volume of 40 m^3.

To simplify the measurements conducted, all bottles are drained at flow rates between $10 - 20$ lpm and never completely emptied such that, to a good approximation, their output activity is uniform over time.

13.2.2. Measuring Full Cylinders

In order to disentangle the low levels of activity in the output from gas cylinders from the background emanation from the gas supply line, the latter must be separately measured. The cylinder measurements shown here were undertaken at MSSL, where the gas supply line consists of 30 m of stainless steel pipe, which is expected to contribute very little radon, along with two regulators and a coloured plastic filter of unknown provenance. The latter is considered particularly likely to be a source of radon emanation.

A measurement was performed where the line was sealed for ~ 20 hours to allow radon to emanate, before flushing through the trap with 50 l of helium. The trap was heated and the radon purged into the detector with a further 25 l of helium. This

75 l produces a negligible contribution to the measurement as will be seen when the specific activity results are presented later. The resulting activity of 25.1 ± 3.3 cpd in the detector, corresponding to 0.92 ± 0.12 mBq, is shown in Figure 13.3a. Following the derivation in Section 12.3, the activity of radon in the detector immediately after transfer from the trap is given by

$$A_D = \epsilon_{tr} A_C \left(1 - e^{-\lambda T_C}\right) + \epsilon_{tr} \left(\epsilon_T \left(T_f\right) A_G + \frac{\epsilon_T \left(T_f\right) f a_G}{\lambda}\right) \left(1 - e^{-\lambda T_f}\right) e^{-\lambda T_{trans}} \tag{13.6}$$

where the relevant timings for this measurement are as follows

- T_C: time between clearing the trap and detector transfer (1449 min).
- T_f: time that the line is in contact with the trap (1163 min).
- T_{trans}: time between stopping collection and detector transfer (63 min).

In addition to neglecting the activity from the small volume of helium used, this volume also places the trapping and transfer efficiency firmly in the stable region for helium, with a value of 92%, such that the activity of the line is extracted as 7.4 ± 1.0 mBq.

Once the contribution of the line has been measured, it is possible to begin measurements of the gas from cylinders. The experimental procedure is simple – after clearing the trap, it is cooled and a sample of gas is collected for ~ 20 hours. At this point, the trap is heated and the radon transferred to the detector. A typical measurement of a nitrogen cylinder is shown in Figure 13.3b.

In order to extract the activity of the gas, Equation (13.6) is again applied. In the case shown here, 4.53 ± 0.25 mBq has been measured with $T_C = 1462$ min, $T_F = 1070$ min and $T_{trans} = 128$ min. Using the trapping and transfer efficiencies from the flow-through calibration, the specific radon activity of the gas is extracted as 957 ± 132 µBq/m^3, such that mean intrinsic activity of each bottle is 9.6 mBq.

A similar measurement of helium cylinders produced a result of $69 - 118$ µBq/m^3, where the range is due to uncertainties in the trapping efficiency and the bounding cases of 66% and 92% have been used. These cylinders were the same as those used in the line activity measurement, justifiying the declaration that their contribution of $\sim 5 - 10$ µBq could be neglected. The discrepancy between helium and nitrogen

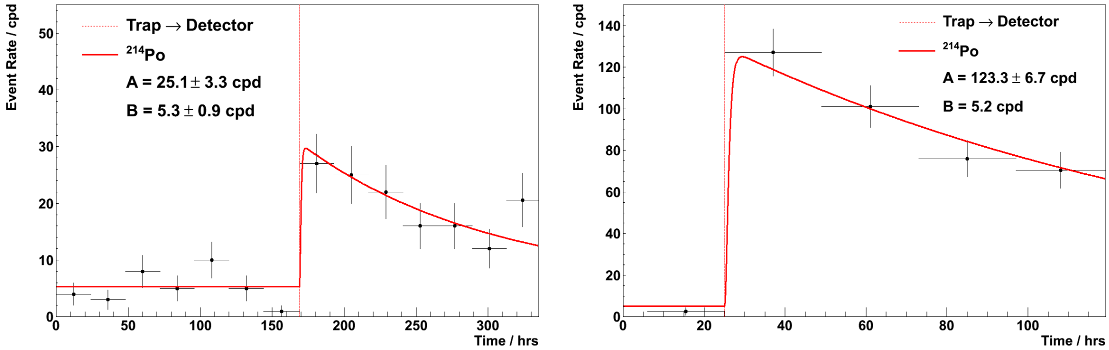

(a) Line Only **(b)** Line and Gas

Figure 13.3.: (a) ^{214}Po activity for supply line and 0.075 m^3 of helium. (b) ^{214}Po activity from line and 10.7 m^3 of nitrogen.

at this stage is intriguing, but more than two measurements are required before drawing any conclusions.

13.2.3. Measuring Used Cylinders

When measuring radon emanation from a C-section, as will be discussed in Section 13.3, the gas cylinders that are used to perform the measurement can contribute the largest background. Therefore it is important to measure the radon activity from the particular set of cylinders used for the measurement so that any internal variation may be taken into account.

The scenario of the measurement, as far as the cylinders are concerned, is that they are emptied down to $\sim 20\%$ and then left sealed whilst the radon from the C-section measurement is in the detector. After a typical period of ~ 5 days, a similar measurement to that described above for the full cylinders is carried out on the remaining gas in the cylinders.

The specific activity of the cylinders is extracted using the same technique as for the full cylinder measurements, but it is necessary to account for the radon build-up time and depleted gas volume in the cylinder when converting this measurement to the specific activity of the same cylinders when full. The modelling of a typical measurement is as follows.

At the start of use, the cylinders are assumed to be in equilibrium with total intrinsic activity, A_B. The flow rate is sufficiently fast that the specific activity from the cylinders is approximately constant and the activity in the cylinders at the end of this period is simply given by the the proportion of gas remaining.

$$A(T_1) = \frac{V(T_1)}{V(0)} A_B \tag{13.7}$$

After the cylinders are re-sealed, the radon level increases back towards equilibrium, so that when the next measurement starts at time, T_2, the radon activity in the bottles is given by

$$A(T_2) = \left((1 - e^{-\lambda(T_2 - T_1)}) + \frac{V(T_1)}{V(0)} e^{-\lambda(T_2 - T_1)} \right) A_B \tag{13.8}$$

As an example of this type of measurement, consider a C-section measurement where the volume in the cylinders is reduced from 38.5 m^3 to 11.5 m^3. The activity remaining in the bottles at the end of this flushing is therefore 29.9% of A_B. These cylinders were then left for 100 hours, rising to an activity of 67.0% of A_B, before being measured themselves. The measurement of 1.83 ± 0.22 mBq/m^3 from a starting volume of 11.5 m^3 can then be propagated to find the specific activity at the start of the C-section flushing:

$$a_G = \frac{A_B}{V(0)} = \frac{(1.83 \pm 0.22)\ \mathrm{mBq/m^3} \times V(T_1)}{V(0) \times (67.0 \pm 0.6)\%} = 815 \pm 105\ \mathrm{\mu Bq/m^3} \tag{13.9}$$

A number of measurements of gas cylinders are shown in Table 13.1. It is immediately clear that the measured nitrogen cylinders have considerably higher radon activity than those of helium. The reason for this difference remains unclear, as the cylinder supplier maintains that there is no material difference between them, although of course the cylinders may be manufactured from different batches of steel with different levels of radon contamination.

Even amongst the nitrogen cylinders, there is considerable variation in the bottle activities. This means it is imperative that each combination of bottles is measured after a C-section measurement so that this background can be accurately subtracted.

Gas	Num. Cylin.	Pressure bar	Volume Meas. m^3	Meas. Act. mBq/m^3	Full Cyl. Act. $\mu Bq/m^3$
He	2	190	11.4	-	$69 - 118$
He	4	15	2.5	0.84 ± 0.13	77 ± 13
N_2	2	200	10.7	-	957 ± 132
N_2	4	55	10.0	1.83 ± 0.22	815 ± 105
N_2	4	40	8.1	1.83 ± 0.23	583 ± 81
N_2	4	45	8.4	1.07 ± 0.18	373 ± 68

Table 13.1.: Measurements of gas cylinders of helium and nitrogen. The pressure at the start of the measurement is shown. Where both a measured activity and full cylinder activity is given, the latter is calculated from the former.

13.3. C-section

The main purpose of the development of the RnCL is to facilitate the measurement of the radon activity of the SuperNEMO tracker during construction. As described in Section 9.3, construction of the first C-section has begun and its frame has been populated with optical modules. In order to perform a radon test and to commission the performance of the tracking cells before full detector assembly, it must be possible to seal the C-section without the calorimeter walls. To this end, dedicated gas-sealing plates have been designed, which are fixed where the adjacent C-section and calorimeter walls will be in the final detector.

13.3.1. Measurement Starting Point

It is of interest, particularly with the first C-section, to measure the radon level of an empty frame without tracker cells. To perform this measurement, the gas seal plates were therefore attached to the C-section frame. As was previously mentioned, these sealing plates do not form a perfect seal and therefore the C-section must be continuously flushed prior to a radon measurement so that a known starting point for the measurement is reached.

Assuming that no radon enters the system externally, the number of radon atoms inside the C-section may be modelled by the following differential equation

$$\frac{dN_T}{dt} = A_T + A_G - \lambda N_T - \frac{f_{in} N_T}{V_T} + \frac{f_{in} a_G}{\lambda} \tag{13.10}$$

where A_T and A_G are the intrinsic activities of the C-section and gas supply line, f_{in} is the input flow rate of gas, with specific activity a_G, into the C-section volume, V_T. If, at the start of flushing, the activity in the C-section is A_0, then the activity after a time, t is given by

$$A(t) = \frac{A_T + A_G + f_{in} a_G / \lambda}{\lambda'_T / \lambda} \left(1 - e^{-\lambda'_T t}\right) + A_0 e^{-\lambda'_T t} \tag{13.11}$$

where

$$\lambda'_T = \lambda + \frac{f_{in}}{V_T} \tag{13.12}$$

The C-section activity in this envisaged scenario is plotted in Figure 13.4 for four different starting activities. It can be seen that for the maximum achievable flow rate of 16.7 lpm, a minimum of 50 hr of flushing is required to reach an equilibrium level in the C-section so that a measurement may start.

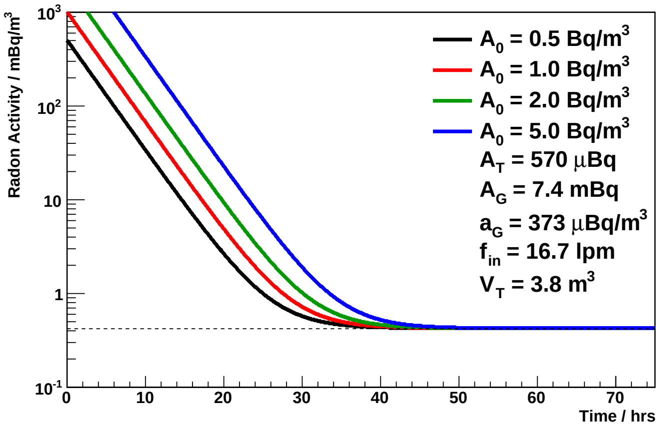

Figure 13.4.: Activity inside the C-section whilst flushing prior to a radon measurement, as modelled by Equation (13.11).

13.3.2. Extracting C-section Activity

For a typical C-section measurement, a certain degree of modelling is required to extract the radon activity from the C-section from the other background components. To illustrate this, a typical C-section measurement is shown here.

As described above, before starting any measurement, the C-section is flushed at ~ 20 lpm for 50 hr. At this point, the equilibrium activity inside the C-section is given by

$$a_T^{eq} = \frac{A_T + A_G + f_{in} a_G / \lambda}{V_T + f_{in}/\lambda} \tag{13.13}$$

The experimental procedure is identical to that used when measuring the gas cylinders and a_T^{eq} is extracted in the same way. Once a measurement of a_T^{eq} has been performed, the gas cylinders are separately measured to eliminate uncertainties from variation in a_G from bottle-to-bottle. Then it is straight-forward to extract the radon activity from the C-section as:

$$A_T = \left(1 + \frac{f_{in}}{\lambda V_T}\right) V_T a_T^{eq} - A_G - \frac{f_{in} a_G}{\lambda} \tag{13.14}$$

It is instructive to consider some measured values to see which terms dominate this equation. If the first measurement with nitrogen as a carrier gas is considered, the experimental values of $f_{in} = 16.7$ lpm and $a_G = (583 \pm 81)$ µBq/m^3 lead to a value of 77.4 ± 11.2 mBq for the final term. This significantly outweighs the contribution from A_G of 7.4 ± 1.0 mBq. The measured value of a_T^{eq} was 1.43 ± 0.18 mBq/m^3, which gives a value of $A_T = 109 \pm 27.7$ mBq, if the only unaccounted contribution to the radon activity comes from emanation from the C-section.

For a realistic flow rate of 0.5 m^3/hr into all four C-sections, a suppression factor of 5.35 is achieved, and the measured activity would lead to a specific activity of $a_T^{real} = 5.4 \pm 1.2$ mBq/m^3. This value is a factor ~ 35 larger than the target value, which is clearly unacceptable.

However, as mentioned previously, the C-section is known to leak and the measured activity corresponds to only 0.05% of the environmental radon activity. Therefore, it is plausible that a large fraction of this radon activity is from outside the C-section.

13.3.3. Anti-Radon Tent

In order to disentangle the possible origins of the observed high level of radon, an anti-radon tent was built around the C-section. This tent was constructed from a double layer of polythene which was heat-sealed to form an airtight cover as shown in Figure 13.5. The tent was flushed with nitrogen at 3.5 m^3/hr, and maintained a clear overpressure as can be seen from the bulging in the photograph.

Figure 13.5.: Photograph of the anti-radon tent covering the C-section.

In order to assess the efficacy of the tent, a commercial radon detector (Durridge RAD7) was used to measure the radon level inside. The ambient level in the room was measured to be $2 - 3$ mBq/m^3 over an extended period. The tent provided a significant reduction as can be seen from Figure 13.6a. The measured level is compatible with the intrinsic background of the RAD7, such that a limit on the activity of $a_{out} < 0.15$ Bq/m^3 (90% CL) may be set, confirming a reduction of a factor > 15. In addition, a measurement of the humidity inside the tent also shows a promising reduction as can be seen in Figure 13.6b.

13.3.4. C-section Results

Four measurements of the radon activity inside the first C-section have been made as detailed in Table 13.2. Three have been made with high environmental radon levels, giving results of tracker activities of ~ 100 mBq corresponding to ~ 5 mBq/m^3 inside SuperNEMO for nominal tracker flow conditions.

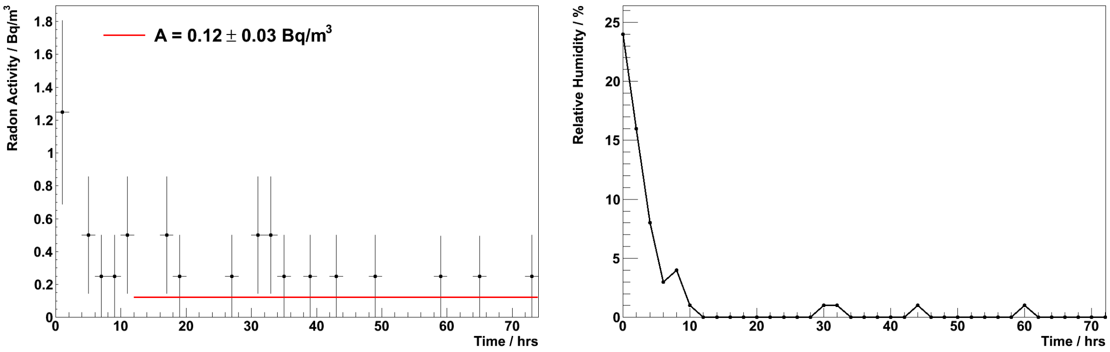

(a) Radon Activity **(b)** Humidity

Figure 13.6.: Measurements made by the RAD7 device inside the anti-radon tent during a C-section measurement. Radon activity and humidity measurements are shown.

The final measurement was performed with the anti-radon tent radon in place, so that the environmental radon level was < 0.15 Bq/m^3. This resulted in a reduction by a factor ~ 3 to $A_T = 38.5 \pm 11.1$ mBq or 1.9 ± 0.5 mBq/m^3 for nominal flow conditions. This result indicates that a large fraction of the radon measured inside the C-section was indeed coming from outside sources and not from internal contamination.

The nominal flow rate of ~ 0.5 m^3/hr is the baseline value, but tests of prototype cells have shown that it should be possible to operate the tracker up to flow rates of 1.0 m^3/hr. This increase has a significant influence on the radon level as was described in Section 10.3. If the nominal flow rate is replaced by the maximum, then the radon level inside SuperNEMO reduces to 1.0 ± 0.3 mBq/m^3.

Even with the anti-radon tent and maximum flow conditions, the measured value is still a factor $6 - 7$ higher than the target value of 0.15 mBq/m^3. However, before drawing firm conclusions, some key assumptions that were made in extracting the tracker activity must be scrutinised.

Firstly, there is a very large contribution to the measurement from the activity of the supply gas. Whilst these bottles have been re-measured after being used to flush the C-section, a considerable amount of modelling is required to extract the gas activity during the measurement. If the assumptions used to model this activity are not wholly correct and small errors are therefore made in measuring the activity of the cylinders, large differences in the radon activity of the C-section can occur. There is

Carrier Gas	a_{out} Bq/m^3	a_T^{eq} mBq/m^3	a_G µBq/m^3	A_T mBq	a_T^{nom} mBq/m^3	a_T^{max} mBq/m^3
He	2.1 ± 0.1	$0.50 - 0.79$	77 ± 13	$67 - 118$	$3.3 - 5.7$	$1.8 - 3.2$
N_2	2.94 ± 0.15	1.43 ± 0.18	583 ± 81	109 ± 28	5.4 ± 1.3	3.0 ± 0.8
N_2	0.67 ± 0.14	1.60 ± 0.20	815 ± 105	103 ± 29	5.1 ± 1.4	2.8 ± 0.8
N_2	< 0.15	0.66 ± 0.11	373 ± 68	38.5 ± 11.1	1.9 ± 0.5	1.0 ± 0.3

Table 13.2.: Four independent measurements of radon activity inside the first C-section. From left to right, the symbols denote: environmental radon level, measured level inside the C-section, separate measurement of activity from gas cylinders, extracted C-section activity and the specific activity inside SuperNEMO for nominal and maximum flow conditions.

a two-fold programme to investigate this area. In the short term, two measurements of the same bottles are being made with a build-up time in between to cross-check the modelling results. In the longer term an anti-radon trap will be installed on the gas supply line. This provides a more drastic solution of removing the radon contributions from the gas cylinders and supply line altogether.

Secondly, there is the implicit assumption that the radon activity is reduced approximately uniformly in the volume surrounding the C-section by the anti-radon tent. Whilst this is almost certainly the case for the bulk of the gas, there may be pockets that have a higher activity. A particular problem may occur if there are leaks between PMTs and the tracking volume, which are then sealed from the outside world. Despite being specifically chosen for their low radioactivity, each PMT may still contain up to 0.25 Bq of ^{226}Ra. Only a small fraction of this activity would be required to emanate into the tracking volume to account for the measured activity. Additionally, there may also be a possibility that some external welds in the gas sealing plates, which may be thoriated, are now in contact with the tracker gas. To counter these possible problems, a comprehensive re-design of the sealing process at all points of the C-section is being undertaken.

In parallel to these improvements, an extensive programme of individually testing components for radon emanation measurements has begun. The majority of components have already been tested and the observed level seems too high to be from any major component. However many measurements will still be repeated with more sensitive apparatus to exclude this possibility.

The detection of a radon level above what is acceptable for the final detector within a matter of months of beginning construction highlights the importance of the RnCL. The early warning from the apparatus, which was specifically designed for this purpose, will be crucial in re-visiting the prototype SuperNEMO design to ensure that the SuperNEMO demonstrator achieves its target background levels.

Chapter 14.

Conclusion

Neutrinoless double beta decay ($0\nu\beta\beta$) is a hypothesised, but as yet unobserved, process whereby a nucleus decays emitting two electrons without any accompanying neutrinos. It violates lepton number conservation and is forbidden in the standard model. If it were to be observed, it would imply that the neutrino is a Majorana particle and the associated decay rate would allow (model-dependent) extraction of the absolute mass scale of the neutrino. Its observation would therefore have far-reaching implications for the fields of particle physics, cosmology and astrophysics.

The most common mechanism for $0\nu\beta\beta$ is the neutrino mass mechanism, where the decay is mediated by a helicity flip of the exchanged neutrino. In addition, there are mechanisms mediated by a right-handed current or by the emission of a hypothetical particle known as a Majoron.

In addition to $0\nu\beta\beta$, there is the process of two neutrino double beta decay ($2\nu\beta\beta$). This decay is allowed in the Standard Model, although it is doubly weak and therefore heavily suppressed. Despite its rare nature, it has been directly observed in nine isotopes. It is important to measure the $2\nu\beta\beta$ process precisely as it may be used to tune nuclear models which are required to obtain useful information from $0\nu\beta\beta$. Furthermore, $2\nu\beta\beta$ is often one of the major backgrounds to a $0\nu\beta\beta$ search and so its rate must be precisely known.

The NEMO-3 detector, which operated between $2003 - 2011$ in the Souterrain de Modane (LSM), searched for $0\nu\beta\beta$ in seven different candidate isotopes with a total source mass of 10 kg. The experiment has also produced the most accurate measurements of the $2\nu\beta\beta$ half-life for each isotope that it contains. A detailed description of the main components of the detector is included in this thesis, with a particular focus on its ability to completely reconstruct the topology of an event.

The second largest mass of source isotope in the detector was 932g of ^{82}Se. The double beta decay analysis of this isotope forms a major part of this thesis. The only backgrounds to a $0\nu\beta\beta$ search with NEMO-3 come from those that can mimic events containing two electrons. A large analysis effort has gone into using the full capabilities of NEMO-3 to identify and measure all sources of background, the results of which are presented. There is good agreement between the measurements with NEMO-3 and independent measurements using HPGe.

After optimising a set of selection criteria, a $2\nu\beta\beta$ signal is clearly identified in 1918.5 days of data, with a signal-to-background ratio of 3.4. The resulting half-life is

$$T^{2\nu}_{1/2} = (9.93 \pm 0.14(\mathrm{stat}) \pm 0.72(\mathrm{syst})) \times 10^{19}\ \mathrm{yr}$$

The nuclear matrix element for ^{82}Se may then be extracted as

$$\left|M^{2\nu}\right| = 0.0484 \pm 0.0018$$

After measuring the $2\nu\beta\beta$ half-life, a $0\nu\beta\beta$ search is conducted in optimised channels for the mass mechanism, right-handed current and Majoron emission decay modes. No evidence for $0\nu\beta\beta$ is found for any modes, so limits on the signal strength for each decay mode are set. For the mass mechanism, the half-life limit is the world's strongest limit using ^{82}Se, with a value of

$$T^{0\nu}_{1/2} > 2.18 \times 10^{23}\ \mathrm{yr}\ (90\%\ \mathrm{CL})$$

corresponding to an effective Majorana neutrino mass of

$$\langle m_{\beta\beta}\rangle < 1.0 - 2.8\ \mathrm{eV}\ (90\%\ \mathrm{CL})$$

The asymmetry between the two electron energies was exploited in the right-handed current λ mode, to produce a half-life limit of

$$T^{0\nu\lambda}_{1/2} > 1.18 \times 10^{23}\ \mathrm{yr}\ (90\%\ \mathrm{CL})$$

with a corresponding lepton number violating parameter

$$\langle\lambda\rangle < (2.8 - 3.0) \times 10^{-6} \text{ (90\% CL)}$$

This limit is the best in ^{82}Se and only a factor $2-3$ weaker than the best results from the Heidelberg-Moscow experiment of $\langle\lambda\rangle < 1.1 \times 10^{-6}$ [100] and the NEMO-3 ^{100}Mo result of $\langle\lambda\rangle < 1.4 \times 10^{-6}$. The final $0\nu\beta\beta$ mode considered is the Majoron emission decay mode, where half-life limits were set for three different spectral indices as:

$$\begin{aligned}
n &= 1 \qquad T_{1/2}^{0\nu\chi^0} > 4.89 \times 10^{22} \text{ yr (90\% CL)}\\
n &= 2 \qquad T_{1/2}^{0\nu\chi^0} > 2.63 \times 10^{22} \text{ yr (90\% CL)}\\
n &= 3 \qquad T_{1/2}^{0\nu\chi^0} > 1.42 \times 10^{22} \text{ yr (90\% CL)}
\end{aligned}$$

The corresponding limits on neutrino-Majoron coupling are the strongest produced by NEMO-3, despite having less source mass than ^{100}Mo. This is a result of the disparity between the $2\nu\beta\beta$ half-lives of the two isotopes, with ^{100}Mo almost an order of magnitude shorter. These results are the strongest limits using ^{82}Se, however they have been superseded by recent results from KamLAND-Zen with an improvement of a factor ~ 3 [60].

SuperNEMO is a next-generation $0\nu\beta\beta$ experiment that will build on the success of the NEMO-3 experiment, using the same tracker-calorimeter technology. In its baseline design it will house 100 kg of ^{82}Se and achieve a half-life sensitivity of 10^{26} yr or an effective Majorana neutrino mass of $\langle m_{\beta\beta}\rangle < 50 - 100$ meV. In this thesis, the SuperNEMO detector design is introduced, with particular emphasis on the improvements that have been made to the NEMO-3 design.

Radon is a radioactive gas that is found in all materials as it is part of naturally occurring radioactive decay chains. It can enter the detector either through diffusion, contamination during detector construction or emanation from the detector materials themselves. Once inside, it can cause a significant background via its progeny ^{214}Bi. In order to reach its target sensitivity, the radon level inside SuperNEMO must be less than 150 µBq/m^3, which is significantly lower than the 5 mBq/m^3 level of NEMO-3. As a result, significant R&D effort has gone into reducing the level of radon inside the detector and measuring these low-levels of radon.

The latter part of this radon R&D is the focus of Part II of this thesis, where the development of a radon concentration line (RnCL) is described. The premise behind the operation of this apparatus is to adsorb radon in a cooled carbon trap so that it can be concentrated from large volumes and transferred to a smaller volume where it may be measured. The RnCL has been constructed and commissioned, with a measured sensitivity of 40 µBq/m^3 for a uniform supply of nitrogen and sensitivities down to 5 µBq/m^3 in helium if current measurements are extrapolated.

The first measurements using the RnCL have shown that typical activities for standard gas cylinders when full are $70 - 120$ µBq/m^3 for helium and $370 - 960$ µBq/m^3 for nitrogen with considerable variation in the latter measurements. This confirms that a cleaner gas supply is required for both SuperNEMO and future measurements using the RnCL, prompting the design of a radon removal trap, which is currently being constructed.

The main purpose of the development of the RnCL is to measure the four sub-modules of the SuperNEMO tracker, known as C-sections, as they are built. The first C-section is currently under construction and the RnCL has been used to measure its radon content. Initial measurements put the level at ~ 3 mBq/m^3 in SuperNEMO for maximum flow suppression. An anti-radon tent has subsequently been constructed around the C-section and the level has reduced down to 1.0 ± 0.3 mBq/m^3, confirming that a large proportion of the measured radon was coming from external sources.

The radon activity measured inside the first C-section is currently a factor $\sim 6 - 7$ above the target level. However, there are considerable systematic effects that must be addressed and the origin of the measured radon must be understood before any conclusions may be drawn. A programme of further work which will address these issues is outlined with the presentation of the measurements.

The RnCL has clearly served its main purpose to identify problematic levels of radon inside SuperNEMO at the earliest possible stages of construction, so that any sources of radon can be addressed to ensure that SuperNEMO reaches its target background levels.

Bibliography

[1] W. Pauli, *Dear radioactive ladies and gentlemen*, Phys.Today **31N9** (1978) 27.

[2] E. Fermi, *An attempt of a theory of beta radiation.*, Z.Phys. **88** (1934) 161–177.

[3] C. Cowan, F. Reines, F. Harrison, H. Kruse, and A. McGuire, *Detection of the free neutrino: A Confirmation*, Science **124** (1956) 103–104.

[4] G. Danby, J. Gaillard, K. A. Goulianos, L. Lederman, N. B. Mistry, et al., *Observation of High-Energy Neutrino Reactions and the Existence of Two Kinds of Neutrinos*, Phys.Rev.Lett. **9** (1962) 36–44.

[5] M. L. Perl, G. Abrams, A. Boyarski, M. Breidenbach, D. Briggs, et al., *Evidence for Anomalous Lepton Production in* e^+e^- *Annihilation*, Phys.Rev.Lett. **35** (1975) 1489–1492.

[6] DONUT Collaboration, K. Kodama et al., *Observation of tau neutrino interactions*, Phys.Lett. **B504** (2001) 218–224, `arXiv:hep-ex/0012035 [hep-ex]`.

[7] ALEPH Collaboration, DELPHI Collaboration, L3 Collaboration, OPAL Collaboration, SLD Collaboration, LEP Electroweak Working Group, SLD Electroweak Group, SLD Heavy Flavour Group, S. Schael et al., *Precision electroweak measurements on the Z resonance*, Phys.Rept. **427** (2006) 257–454, `arXiv:hep-ex/0509008 [hep-ex]`.

[8] MiniBooNE Collaboration, A. Aguilar-Arevalo et al., *Event Excess in the MiniBooNE Search for* $\bar{\nu}_\mu \to \bar{\nu}_e$ *Oscillations*, Phys.Rev.Lett. **105** (2010) 181801, `arXiv:1007.1150 [hep-ex]`.

[9] G. Mention, M. Fechner, T. Lasserre, T. Mueller, D. Lhuillier, et al., *The*

Reactor Antineutrino Anomaly, Phys.Rev. **D83** (2011) 073006, `arXiv:1101.2755 [hep-ex]`.

[10] J. Davis, Raymond, D. S. Harmer, and K. C. Hoffman, *Search for neutrinos from the sun*, Phys.Rev.Lett. **20** (1968) 1205–1209.

[11] B. Pontecorvo, *Mesonium and anti-mesonium*, Sov.Phys.JETP **6** (1957) 429.

[12] B. Pontecorvo, *Inverse beta processes and nonconservation of lepton charge*, Sov.Phys.JETP **7** (1958) 172–173.

[13] Z. Maki, M. Nakagawa, and S. Sakata, *Remarks on the unified model of elementary particles*, Prog.Theor.Phys. **28** (1962) 870–880.

[14] SNO Collaboration, Q. Ahmad et al., *Direct evidence for neutrino flavor transformation from neutral current interactions in the Sudbury Neutrino Observatory*, Phys.Rev.Lett. **89** (2002) 011301, `arXiv:nucl-ex/0204008 [nucl-ex]`.

[15] B. Kayser, *Neutrino physics*, eConf **C040802** (2004) L004, `arXiv:hep-ph/0506165 [hep-ph]`.

[16] Particle Data Group, J. Beringer et al., *Review of Particle Physics (RPP)*, Phys.Rev. **D86** (2012) 010001.

[17] F. T. Avignone, S. R. Elliott, and J. Engel, *Double Beta Decay, Majorana Neutrinos, and Neutrino Mass*, Rev.Mod.Phys. **80** (2008) 481–516, `arXiv:0708.1033 [nucl-ex]`.

[18] E. Majorana, *Theory of the Symmetry of Electrons and Positrons*, Nuovo Cim. **14** (1937) 171–184.

[19] T. Bowles and R. Robertson, *Tritium beta decay and the search for neutrino mass*, Los Alamos Sci. **25** (1997) 86–91.

[20] Troitsk Collaboration, V. Aseev et al., *An upper limit on electron antineutrino mass from Troitsk experiment*, Phys.Rev. **D84** (2011) 112003, `arXiv:1108.5034 [hep-ex]`.

[21] C. Kraus, B. Bornschein, L. Bornschein, J. Bonn, B. Flatt, et al., *Final results from phase II of the Mainz neutrino mass search in tritium beta decay*,

Eur.Phys.J. **C40** (2005) 447–468, `arXiv:hep-ex/0412056 [hep-ex]`.

[22] G. Drexlin, V. Hannen, S. Mertens, and C. Weinheimer, *Current direct neutrino mass experiments*, Adv.High Energy Phys. **2013** (2013) 293986, `arXiv:1307.0101 [physics.ins-det]`.

[23] J. Lesgourgues and S. Pastor, *Neutrino mass from Cosmology*, Adv.High Energy Phys. **2012** (2012) 608515, `arXiv:1212.6154 [hep-ph]`.

[24] WMAP Collaboration, G. Hinshaw et al., *Nine-Year Wilkinson Microwave Anisotropy Probe (WMAP) Observations: Cosmological Parameter Results*, `arXiv:1212.5226 [astro-ph.CO]`.

[25] S. A. Thomas, F. B. Abdalla, and O. Lahav, *Upper Bound of 0.28 eV on the Neutrino Masses from the Largest Photometric Redshift Survey*, Phys.Rev.Lett. **105** (2010) 031301, `arXiv:0911.5291 [astro-ph.CO]`.

[26] P. Bhupal Dev, S. Goswami, M. Mitra, and W. Rodejohann, *Constraining Neutrino Mass from Neutrinoless Double Beta Decay*, `arXiv:1305.0056 [hep-ph]`.

[27] M. Archidiacono, N. Fornengo, C. Giunti, S. Hannestad, and A. Melchiorri, *Sterile Neutrinos: Cosmology vs Short-BaseLine Experiments*, `arXiv:1302.6720 [astro-ph.CO]`.

[28] A. Sakharov, *Violation of CP Invariance, c Asymmetry, and Baryon Asymmetry of the Universe*, Pisma Zh.Eksp.Teor.Fiz. **5** (1967) 32–35.

[29] T. Ohlsson, H. Zhang, and S. Zhou, *Probing the leptonic Dirac CP-violating phase in neutrino oscillation experiments*, Phys.Rev. **D87** (2013) 053006, `arXiv:1301.4333 [hep-ph]`.

[30] C. Weizsacker, *Zur Theorie der Kernmassen*, Z.Phys. **96** (1935) 431–458.

[31] M. Goeppert-Mayer, *Double beta-disintegration*, Phys.Rev. **48** (1935) 512–516.

[32] G. Racah, *On the symmetry of particle and antiparticle*, Nuovo Cim. **14** (1937) 322–328.

[33] M. Hirsch, H. Klapdor-Kleingrothaus, and S. Kovalenko, *Supersymmetry and neutrinoless double beta decay*, Osaka 1995, Weak and electromagnetic

interactions in nuclei, 1995.

[34] J. Schechter and J. Valle, *Neutrino Masses in SU(2) × U(1) Theories*, Phys.Rev. **D22** (1980) 2227.

[35] W. Rodejohann, *Neutrinoless double beta decay and neutrino physics*, J.Phys. **G39** (2012) 124008, `arXiv:1206.2560 [hep-ph]`.

[36] M. Doi, T. Kotani, H. Nishiura, and E. Takasugi, *DOUBLE BETA DECAY*, Prog.Theor.Phys. **69** (1983) 602.

[37] SuperNEMO Collaboration, R. Arnold et al., *Probing New Physics Models of Neutrinoless Double Beta Decay with SuperNEMO*, Eur.Phys.J. **C70** (2010) 927–943, `arXiv:1005.1241 [hep-ex]`.

[38] Y. Chikashige, R. N. Mohapatra, and R. Peccei, *Spontaneously Broken Lepton Number and Cosmological Constraints on the Neutrino Mass Spectrum*, Phys.Rev.Lett. **45** (1980) 1926.

[39] C. Aulakh and R. N. Mohapatra, *Neutrino as the Supersymmetric Partner of the Majoron*, Phys.Lett. **B119** (1982) 136.

[40] G. Gelmini and M. Roncadelli, *Left-Handed Neutrino Mass Scale and Spontaneously Broken Lepton Number*, Phys.Lett. **B99** (1981) 411.

[41] P. Bamert, C. Burgess, and R. Mohapatra, *Multi-Majoron modes for neutrinoless double beta decay*, Nucl.Phys. **B449** (1995) 25–48, `arXiv:hep-ph/9412365 [hep-ph]`.

[42] N. Fatemi-Ghomi, *Measurement of the double beta decay half-life of* ^{150}*Nd and search for neutrinoless decay modes with NEMO-3 detector*, `arXiv:0905.0822 [hep-ex]`.

[43] NEMO-3 Collaboration, R. Arnold et al., *Limits on different Majoron decay modes of* ^{100}*Mo and* ^{82}*Se for neutrinoless double beta decays in the NEMO-3 experiment*, Nucl.Phys. **A765** (2006) 483–494, `arXiv:hep-ex/0601021 [hep-ex]`.

[44] C. D. Carone, *Double beta decay with vector majorons*, Phys.Lett. **B308** (1993) 85–88, `arXiv:hep-ph/9302290 [hep-ph]`.

[45] R. Mohapatra, A. Perez-Lorenzana, and C. de S Pires, *Neutrino mass, bulk Majoron and neutrinoless double beta decay*, Phys.Lett. **B491** (2000) 143–147, `arXiv:hep-ph/0008158 [hep-ph]`.

[46] J. Vergados, H. Ejiri, and F. Simkovic, *Theory of Neutrinoless Double Beta Decay*, Rept.Prog.Phys. **75** (2012) 106301, `arXiv:1205.0649 [hep-ph]`.

[47] A. Smolnikov and P. Grabmayr, *Conversion of experimental half-life to effective electron neutrino mass in $0\nu\beta\beta$ decay*, Phys.Rev. **C81** (2010) 028502.

[48] H. Klapdor-Kleingrothaus, A. Dietz, L. Baudis, G. Heusser, I. Krivosheina, et al., *Latest results from the Heidelberg-Moscow double beta decay experiment*, Eur.Phys.J. **A12** (2001) 147–154, `arXiv:hep-ph/0103062 [hep-ph]`.

[49] H. Klapdor-Kleingrothaus, I. Krivosheina, A. Dietz, and O. Chkvorets, *Search for neutrinoless double beta decay with enriched ^{76}Ge in Gran Sasso 1990-2003*, Phys.Lett. **B586** (2004) 198–212, `arXiv:hep-ph/0404088 [hep-ph]`.

[50] C. Aalseth, I. Avignone, F.T., A. Barabash, F. Boehm, R. Brodzinski, et al., *Comment on 'Evidence for neutrinoless double beta decay'*, Mod.Phys.Lett. **A17** (2002) 1475–1478, `arXiv:hep-ex/0202018 [hep-ex]`.

[51] C. Aalseth, F. Avignone, R. Brodzinski, W. Hensley, H. Miley, et al., *Recent results of the IGEX ^{76}Ge double-beta decay experiment*, Phys.Atom.Nucl. **63** (2000) 1225–1228.

[52] GERDA Collaboration, M. Agostini et al., *Results on neutrinoless double beta decay of ^{76}Ge from GERDA Phase I*, `arXiv:1307.4720 [nucl-ex]`.

[53] GERDA Collaboration, K. Knöpfle, *GERDA - Status and Perspectives*, Nucl.Phys.Proc.Suppl. **237-238** (2013) 31–33.

[54] Majorana Collaboration, N. Abgrall et al., *The Majorana Demonstrator Neutrinoless Double-Beta Decay Experiment*, `arXiv:1308.1633 [physics.ins-det]`.

[55] GERDA Collaboration, M. Barnabe Heider, *Semiconductor-based experiments for neutrinoless double beta decay search*, Nucl.Phys.Proc.Suppl. **229-232** (2012) 141–145.

[56] J. R. Wilson, *Double beta decay measurement with COBRA*, Nucl.Phys.Proc.Suppl. **221** (2011) 313–316.

[57] S. Umehara, T. Kishimoto, I. Ogawa, R. Hazama, H. Miyawaki, et al., *Neutrino-less double-beta decay of* ^{48}*Ca studied by* CaF_2*(Eu) scintillators*, Phys.Rev. **C78** (2008) 058501, `arXiv:0810.4746 [nucl-ex]`.

[58] S. Umehara, T. Kishimoto, M. Nomachi, S. Yoshida, K. Matsuoka, et al., *Search for neutrino-less double beta decay with CANDLES*, AIP Conf.Proc. **1441** (2012) 448–450.

[59] KamLAND-Zen Collaboration, A. Gando et al., *Limit on* $0\nu\beta\beta$ *Decay of* ^{136}*Xe from the First Phase of KamLAND-Zen and Comparison with the Positive Claim in* ^{76}*Ge*, Phys.Rev.Lett. **110** (2013) no. 6, 062502, `arXiv:1211.3863 [hep-ex]`.

[60] KamLAND-Zen Collaboration, A. Gando et al., *Limits on Majoron-emitting double-beta decays of* ^{136}*Xe in the KamLAND-Zen experiment*, Phys.Rev. **C86** (2012) 021601, `arXiv:1205.6372 [hep-ex]`.

[61] KamLand-Zen Collaboration, J. Shirai, *KamLAND-Zen: Status and Future*, Nucl.Phys.Proc.Suppl. **237-238** (2013) 28–30.

[62] J. R. Wilson, *Non-accelerator Neutrino Physics*, IoP HEPP & APP Group Meeting, 2013.

[63] E. Andreotti, C. Arnaboldi, F. Avignone, M. Balata, I. Bandac, et al., ^{130}*Te Neutrinoless Double-Beta Decay with CUORICINO*, Astropart.Phys. **34** (2011) 822–831, `arXiv:1012.3266 [nucl-ex]`.

[64] CUORE, L. Pattavina, *Status of the CUORE experiment*, J.Phys.Conf.Ser. **447** (2013) 012066.

[65] LUCIFER Collaboration, L. Pattavina, *LUCIFER: Neutrinoless double beta decay search with scintillating bolometers*, J.Phys.Conf.Ser. **335** (2011) 012047.

[66] EXO Collaboration, M. Auger et al., *Search for Neutrinoless Double-Beta Decay in* ^{136}*Xe with EXO-200*, Phys.Rev.Lett. **109** (2012) 032505, `arXiv:1205.5608 [hep-ex]`.

[67] D. J. Auty, *EXO-200 Experiment*, Implications of Neutrino Flavor

Oscillations, 2011.

[68] NEXT Collaboration, J. J. Gómez-Cadenas, *Present status and future perspectives of the NEXT experiment*, `arXiv:1307.3914 [physics.ins-det]`.

[69] NEMO-3 Collaboration, L. Simard, *The NEMO-3 results after completion of data taking*, J.Phys.Conf.Ser. **375** (2012) 042011.

[70] R. Saakyan, *Tracking-based Experiments in Double Beta Decay*, Nucl.Phys.Proc.Suppl. **229-232** (2012) 135–140.

[71] GERDA Collaboration, M. Agostini et al., *Measurement of the half-life of the two-neutrino double beta decay of* ^{76}*Ge with the Gerda experiment*, J.Phys. **G40** (2013) 035110, `arXiv:1212.3210 [nucl-ex]`.

[72] NEMO-3 Collaboration, J. Argyriades et al., *Measurement of the two neutrino double beta decay half-life of* ^{96}*Zr with the NEMO-3 detector*, Nucl.Phys. **A847** (2010) 168–179, `arXiv:0906.2694 [nucl-ex]`.

[73] NEMO-3 Collaboration, R. Arnold et al., *First results of the search of neutrinoless double beta decay with the NEMO-3 detector*, Phys.Rev.Lett. **95** (2005) 182302, `arXiv:hep-ex/0507083 [hep-ex]`.

[74] NEMO-3 Collaboration, R. Arnold et al., *Measurement of the Double Beta Decay Half-life of* ^{130}*Te with the NEMO-3 Detector*, Phys.Rev.Lett. **107** (2011) 062504, `arXiv:1104.3716 [nucl-ex]`.

[75] EXO-200 Collaboration, J. Albert et al., *An improved measurement of the* $2\nu\beta\beta$ *half-life of* ^{136}*Xe with EXO-200*, `arXiv:1306.6106 [nucl-ex]`.

[76] NEMO-3 Collaboration, J. Argyriades et al., *Measurement of the Double Beta Decay Half-life of* ^{150}*Nd and Search for Neutrinoless Decay Modes with the NEMO-3 Detector*, Phys.Rev. **C80** (2009) 032501, `arXiv:0810.0248 [hep-ex]`.

[77] F. A. Danevich, A. S. Georgadze, V. V. Kobychev, B. N. Kropivyansky, A. S. Nikolaiko, et al., *Search for double beta decay of cadmium and tungsten isotopes: Final results of the solotvina experiment*, Phys.Rev. **C68** (2003) 035501.

[78] R. Arnold, C. Augier, A. Bakalyarov, J. Baker, A. Barabash, et al., *Technical design and performance of the NEMO-3 detector*, Nucl.Instrum.Meth. **A536** (2005) 79–122, `arXiv:physics/0402115 [physics]`.

[79] NEMO-3 Collaboration, J. Argyriades et al., *Measurement of the background in the NEMO-3 double beta decay experiment*, Nucl.Instrum.Meth. **A606** (2009) 449–465, `arXiv:0903.2277 [nucl-ex]`.

[80] O. Ponkratenko, V. Tretyak, and Y. Zdesenko, *The Event generator DECAY4 for simulation of double beta processes and decay of radioactive nuclei*, Phys.Atom.Nucl. **63** (2000) 1282–1287, `arXiv:nucl-ex/0104018 [nucl-ex]`.

[81] R. Brun, F. Bruyant, M. Maire, A. McPherson, and P. Zanarini, *GEANT3*, CERN-DD-EE-84-1 (1987) .

[82] O. Helene, *Upper Limit of Peak Area*, Nucl.Instrum.Meth. **212** (1983) 319.

[83] G. J. Feldman and R. D. Cousins, *A Unified approach to the classical statistical analysis of small signals*, Phys.Rev. **D57** (1998) 3873–3889, `arXiv:physics/9711021 [physics.data-an]`.

[84] A. L. Read, *Presentation of search results: The CL(s) technique*, J.Phys. **G28** (2002) 2693–2704.

[85] T. Junk, *Confidence level computation for combining searches with small statistics*, Nucl.Instrum.Meth. **A434** (1999) 435–443, `arXiv:hep-ex/9902006 [hep-ex]`.

[86] S. Wilks, *The Large-Sample Distribution of the Likelihood Ratio for Testing Composite Hypotheses*, Annals Math.Statist. **9** (1938) no. 1, 60–62.

[87] M. Kauer, *Search for the double beta decay of ^{96}Zr with NEMO-3 and calorimeter development for the SuperNEMO experiment*. PhD thesis, University College London, 2010.

[88] NEMO-2 Collaboration, R. Arnold et al., *Double beta decay of ^{82}Se*, Nucl.Phys. **A636** (1998) 209–223.

[89] S. Elliott, A. Hahn, M. Moe, M. Nelson, and M. Vient, *Double beta decay of ^{82}Se*, Phys.Rev. **C46** (1992) 1535–1537.

[90] O. Manuel, *Geochemical Measurements of Double beta Decay*, J.Phys. **G17** (1991) S221.

[91] J. Suhonen and O. Civitarese, *Weak-interaction and nuclear-structure aspects of nuclear double beta decay*, Phys.Rept. **300** (1998) 123–214.

[92] E. Caurier, F. Nowacki, A. Poves, and J. Retamosa, *Shell Model Studies of the Double Beta Decays of* ^{76}*Ge,* ^{82}*Se and* ^{136}*Xe*, Phys.Rev.Lett. **77** (1996) 1954–1957.

[93] A. Staudt, K. Muto, and H. Klapdor-Kleingrothaus, *Calculation of* $2\nu\beta\beta$ *and* $0\nu\beta\beta$ *decay rates*, Europhys.Lett. **13** (1990) 31–36.

[94] J. Menendez, A. Poves, E. Caurier, and F. Nowacki, *Disassembling the Nuclear Matrix Elements of the Neutrinoless beta beta Decay*, Nucl.Phys. **A818** (2009) 139–151, `arXiv:0801.3760 [nucl-th]`.

[95] F. Ŝimkovic, V. Rodin, A. Faessler, and P. Vogel, $0\nu\beta\beta$ *and* $2\nu\beta\beta$ *nuclear matrix elements, QRPA, and isospin symmetry restoration*, Phys.Rev. **C87** (2013) 045501, `arXiv:1302.1509 [nucl-th]`.

[96] M. Kortelainen and J. Suhonen, *Improved short-range correlations and* $0\nu\beta\beta$ *nuclear matrix elements of* ^{76}*Ge and* ^{82}*Se*, Phys.Rev. **C75** (2007) 051303, `arXiv:0705.0469 [nucl-th]`.

[97] F. Iachello, J. Barea, and J. Kotila, *A compilation of* $0\nu\beta\beta$ *nuclear matrix elements in the interacting boson model*, Nucl.Phys.Proc.Suppl. **237-238** (2013) 21–23.

[98] T. R. Rodriguez and G. Martinez-Pinedo, *Energy density functional study of nuclear matrix elements for* $0\nu\beta\beta$ *decay*, Phys.Rev.Lett. **105** (2010) 252503, `arXiv:1008.5260 [nucl-th]`.

[99] M. Aunola and J. Suhonen, *Mean field effects on neutrinoless double beta decay*, Nucl.Phys. **A643** (1998) 207–221.

[100] M. Gunther, J. Hellmig, G. Heusser, M. Hirsch, H. Klapdor-Kleingrothaus, et al., *Heidelberg - Moscow beta-beta experiment with* ^{76}*Ge: Full setup with five detectors*, Phys.Rev. **D55** (1997) 54–67.

[101] F. Ŝimkovic, G. Pantis, J. Vergados, and A. Faessler, *Additional nucleon*

current contributions to neutrinoless double beta decay, Phys.Rev. **C60** (1999) 055502, `arXiv:hep-ph/9905509 [hep-ph]`.

[102] S. Stoica and H. Klapdor-Kleingrothaus, *Critical view on double-beta decay matrix elements within quasi random phase approximation-based methods*, Nucl.Phys. **A694** (2001) 269–294.

[103] O. Civitarese and J. Suhonen, *Light neutrino masses and hierarchies and the observability of neutrinoless double beta decay*, Nucl.Phys. **A729** (2003) 867–883, `arXiv:nucl-th/0208005 [nucl-th]`.

[104] C. Barbero, J. M. Cline, F. Krmpotic, and D. Tadic, *Exact evaluation of the nuclear form-factor for new kinds of majoron emission in neutrinoless double beta decay*, Phys.Lett. **B392** (1997) 419–425, `arXiv:hep-ph/9609421 [hep-ph]`.

[105] Heidelberg - Moscow-Collaboration, J. Bockholt et al., *Bounds on new Majoron models from the Heidelberg - Moscow experiment*, Phys.Rev. **D54** (1996) 3641–3644, `arXiv:nucl-ex/9511001 [nucl-ex]`.

[106] M. Hirsch, H. Klapdor-Kleingrothaus, S. Kovalenko, and H. Pas, *On the observability of majoron emitting double beta decays*, Phys.Lett. **B372** (1996) 8–14, `arXiv:hep-ph/9511227 [hep-ph]`.

[107] SuperNEMO Collaboration, H. Gómez, *BiPo: A dedicated radiopurity detector for the SuperNEMO experiment*, AIP Conference Proceedings **1549** (2013) no. 1, 94–97.

[108] SuperNEMO Collaboration, B. Soulé, *Radon emanation chamber: High sensitivity measurements for the SuperNEMO experiment*, AIP Conference Proceedings **1549** (2013) no. 1, 98–101.

[109] SuperNEMO Collaboration, F. Mamedov, I. Štekl, K. Smolek, and P. Čermák, *High sensitivity detectors for measurement of diffusion, emanation and low activity of radon*, AIP Conference Proceedings **1549** (2013) no. 1, 120–123.

[110] J. R. Partington, *Discovery of Radon*, Nature **179** (1957) 912.

[111] J. L. Marshall and V. R. Marshall, *Ernest Rutherford, the "True Discoverer" of Radon*, Bull.Hist.Chem. **28** (2003) 76.

[112] W. Ramsay and J. N. Collie, *The Spectrum of the Radium Emanation*, Proc.Roy.Soc.Lond. **73** (1904) 470–476.

[113] National Academy of Sciences, *Health Effects of Exposure to Radon: BEIR VI, Committee on Health Risks of Exposure to Radon (BEIR VI)*, ISBN-0-309-056454-4 (1999) .

[114] V. Vasiliev, *Radon in SuperNEMO*, Internal Note **DocDB:297** (2008) .

[115] E. Wellisch, *The distribution of the active deposit of radium in an electric field*, Philosophical Magazine Series 6 **26** (1913) no. 154, 623–635.

[116] P. Pagelkopf and J. Porstendörfer, *Neutralisation rate and the fraction of the positive* ^{218}*Po-clusters in air*, Atmospheric Environment **37** (2003) no. 8, 1057 – 1064.

[117] E. Choi, M. Komori, K. Takahisa, N. Kudomi, K. Kume, K. Hayashi, S. Yoshida, H. Ohsumi, H. Ejiri, T. Kishimoto, K. Matsuoka, and S. Tasaka, *Highly sensitive radon monitor and radon emanation rates for detector components*, Nucl.Instrum.Meth. **A459** (2001) 177–181.

[118] C. Mitsuda, T. Kajita, K. Miyano, S. Moriyama, M. Nakahata, et al., *Development of super-high sensitivity radon detector for the Super-Kamiokande detector*, Nucl.Instrum.Meth. **A497** (2003) 414–428.

[119] G. Heusser, W. Rau, B. Freudiger, M. Laubenstein, M. Balata, and T. Kirsten, ^{222}*Rn detection at the* $\mu Bq/m^3$ *range in nitrogen gas and a new Rn purification technique for liquid nitrogen*, Applied Radiation and Isotopes **52** (2000) no. 3, 691 – 695.

[120] G. Knoll, *Radiation Detection and Measurement*, ISBN-9780470131480 (2000) .